

**Major progress in radar technology development is making unprecedented contributions to aerospace platforms and national defense capability. Over the last decade, the creation of active electronically scanned array (AESA) radars by Northrop Grumman Corporation and other providers has enabled remarkable advances in fire control systems for fighter aircraft like the U.S. Air Force's F-22 Raptor, the joint services' F-35 Lightning II, and the U.S. Navy's F/A-18 Super Hornet—and also in surveillance systems both for airborne early warning and control (AEW&C) platforms like the Royal Australian Air Force's Wedgetail aircraft and for air-to-ground surveillance platforms like the Global Hawk and E-10 (which are being supported through the Multi-Platform Radar Technology Insertion Program—MP-RTIP).**

# AESA Radar:

*REVOLUTIONARY CAPABILITIES FOR MULTIPLE MISSIONS*

**F**or these and other aircraft, both manned and unmanned, AESA radars will increasingly be relied on to provide tremendous versatility and speed, as well as much greater range and resolution, for carrying out a multitude of searching, mapping and targeting missions. This groundbreaking technology will be used for other functions as well, including communications, detection of adversary emitters and jamming.

Key to the capabilities of the new system is an antenna consisting of hundreds or even thousands of small transmit/receive (T/R) modules instead of a central transmitter and receiver. Each module acts like a small individual radar. Unlike a conventional mechanically steered array (MSA), the AESA array of T/R modules is fixed, with no moving parts—an advance that increases system reliability.

In MSA radars, a circular or elliptical antenna plate in the nose of the aircraft is moved rapidly using a gimbal system to steer a beam across

an airspace or ground area. The AESA radar, in contrast, can steer its agile beams electronically—at nearly the speed of light—and redirect them instantaneously from one target to another. The modules may work together on a single task, or work in groups to do multiple tasks in parallel.

AESAs also represent an advance over the electronically scanned array (ESA) radar relied on, for instance, by the Air Force's E-3 Airborne Warning and Control System (AWACS) aircraft, B-1B Lancer bomber and E-8C Joint Surveillance Target Attack Radar System (Joint STARS).

ESA radars, like MSAs, use a central transmitter and receiver to feed their radiating elements, but steer the beam using an electronically controlled phase shifter placed immediately behind each radiating element. While these systems reap the benefits of electronic steering, the phase shifting and line losses lead to some reduction in radar performance. But the AESA radar, with its power distributed

among modules rather than emanating from a single high power transmitter, is not subject to this shortcoming.

"To populate a radar with many hundreds of these T/R modules and get them to act together is revolutionary," says Scott Porter, vice president of global field marketing at Northrop Grumman's Electronic Systems sector. "In fact, taking all the moving parts out of airborne radars is revolutionary."

The radar system's other fundamental enabling technologies are a multichannel receiver/exciter



with programmable waveforms; a very high-speed commercial-off-the-shelf-based common integrated sensor processor; and an advanced resource manager able to control the radar assets—array, receiver, waveform generator—to support a diversity of missions.

AESA's solid-state technology and elimination of mechanical moving parts will enable the radar to far surpass current standards for systems reliability. The radar system also features a "replaceable assemblies" design for faster, easier repairs or upgrades to hardware and software modules. For these reasons, AESA life-cycle costs are expected to be significantly lower than those of MSAs. The active arrays on the F-22 and F-35 should have almost twice the expected life of the airframe.

Among the diverse military activities likely to be major beneficiaries of AESA capabilities, four are especially important: surveillance, fighter aircraft fire control/targeting, electronic warfare and high-data-rate communications.

### Surveillance Systems

Northrop Grumman, which has been designing and manufacturing airborne radar systems longer than any other company, became the world leader in airborne electronic scanning surveillance systems with the fielding of radars for the E-3 AWACS and the Joint STARS platform in the 70s and 80s.

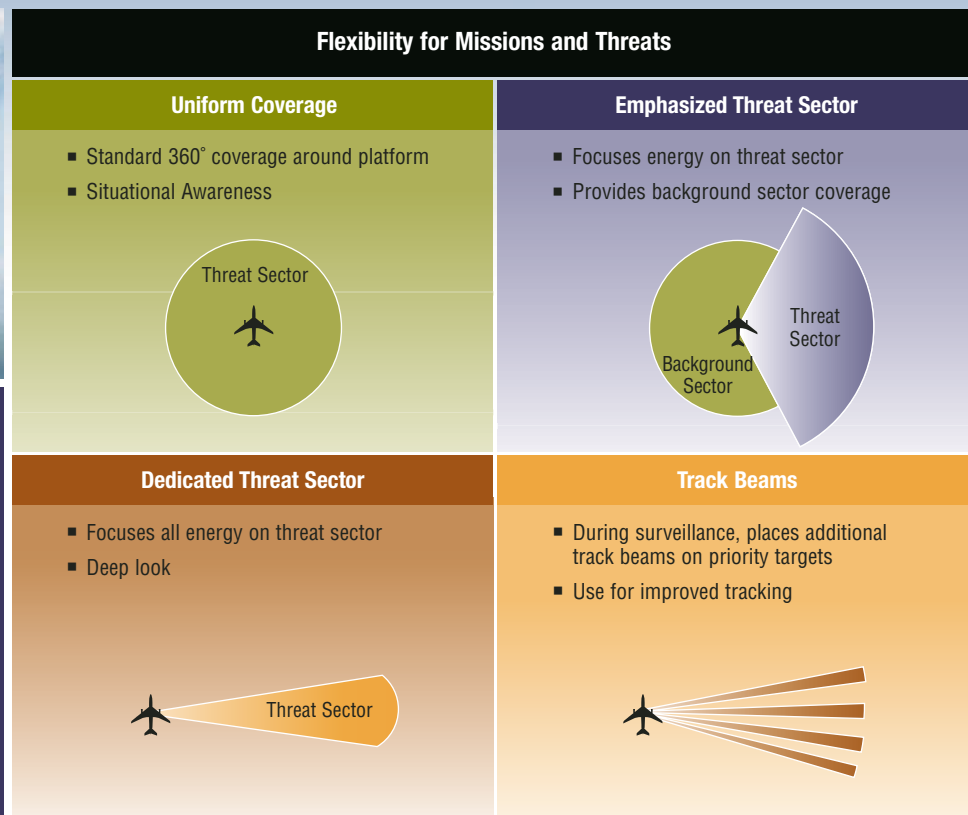
With the six AESA surveillance radars it is now producing for Australia's Wedgetail aircraft, the company has set a new standard for AEW&C capability. This 4th generation Multi-role Electronically Scanned Array (MESA), with its full 360 degree electronic scan and long detection range, delivers a wholly new level of situational awareness, flexibility and target update speed. The MESA radar is flying in the next-generation 737-700 series aircraft produced by The Boeing Company. This advanced AEW&C aircraft provides air-to-air coverage, air-to-surface coverage, integrated identification friend or foe (IFF), special track beams and focused sector operation.

The MESA radar hardware is currently in production and the system is completing integration and test. Four MESA-Boeing systems are also being produced for Turkey. In addition, Boeing and Northrop Grumman have proposed the AEW&C system for the Republic of South Korea's E-X early warning aircraft program.

The AEW&C aircraft is a high-value, stand-off system. It normally orbits far enough behind the forward edge of battle to remain in low-threat and friendly areas. Future advanced surface-to-air missiles will force the AEW&C to operate even farther back from the battle lines. To support offensive counter air missions, the AEW&C must be capable of detecting and tracking targets well past the battle lines into high threat areas. As a result, very long range radar detection is imperative for an airborne early warning radar system to function effectively in discerning enemy fighters, cruise missiles and future low cross section threats.



The Wedgetail's MESA system, mounted atop the fuselage to provide 360-degree coverage, can shift instantaneously among a variety of surveillance patterns, as shown at right.



The 737 AEW&C aircraft generates 360 kilowatts of electrical power to operate the MESA radar. In addition, the aircraft can carry radar antennas that are very large, approximately 6 x 18 feet for the side-looking antennas and 5 x 25 feet for the forward- and aft- looking antennas. This antenna size, plus the radar power, enable the AEW&C aircraft to survey great distances.

The MESA radar antennas are housed in a dorsal structure mounted on top of the fuselage. There are two back-to-back sideward looking arrays and a third antenna—called the “top hat” and positioned high in the dorsal fin—that looks front and back. These full coverage arrays, along with their component electronically steered T/R modules, enable MESA system operators to focus radar time and energy on the areas more likely to include hostile targets while simultaneously monitoring low threat areas with less radar energy.

Another major AESA surveillance system being designed and developed by Northrop Grumman is the next-generation radar for the Global Hawk and the E-10 aircraft. The design utilizes technology advances from development work on tactical aircraft for these surveillance platforms. The AESA system design allows for scalable antenna lengths to increase power and bandwidth. The array length for the Global Hawk is five feet—and more than 20 feet for the E-10, enabling both aircraft to concurrently provide the modes of synthetic aperture radar and ground moving target indication. The system will provide greatly improved air-to-ground capability and will also add air-to-air surveillance. The E-10 will have the ability to detect cruise missiles at tactically significant ranges.

### Targeting

The great range and exceptional agility that make AESA systems so well suited to the early warning mission also figure importantly in their effectiveness as fire control radars for fighter aircraft. An additional strength enhances fighter operations: the ability to achieve high-resolution imagery for air-to-ground targeting. AESA fighter radars, because they use X-band frequencies and synthetic aperture processing, are capable of such “targeting-quality” resolution. This is not the case for the AEW&C MESA radar: it uses lower, L-band frequencies, settling for lower resolution in order to achieve long range detection with less disruption from bad weather.

AESA fire control radars being built for fighter aircraft include Northrop Grumman’s AN/APG-77 for the F-22, AN/APG-81 for the F-35, and AN/APG-80 for the F-16E/F Block 60 Falcon. Northrop Grumman is now inserting its fourth-generation AESA technology into the F-22’s lot 5 of production—so this aircraft will have a radar that is highly common with that of the F-35.

The four AESA radars for U.S. fighter aircraft are in various stages of production, integration or testing. Those for the F-16 Block 60 and the F-22 are both operational, with



production ongoing, while the F-35 and F/A-18E/F AESAs are still in pre-operational stages of construction or upgrading.

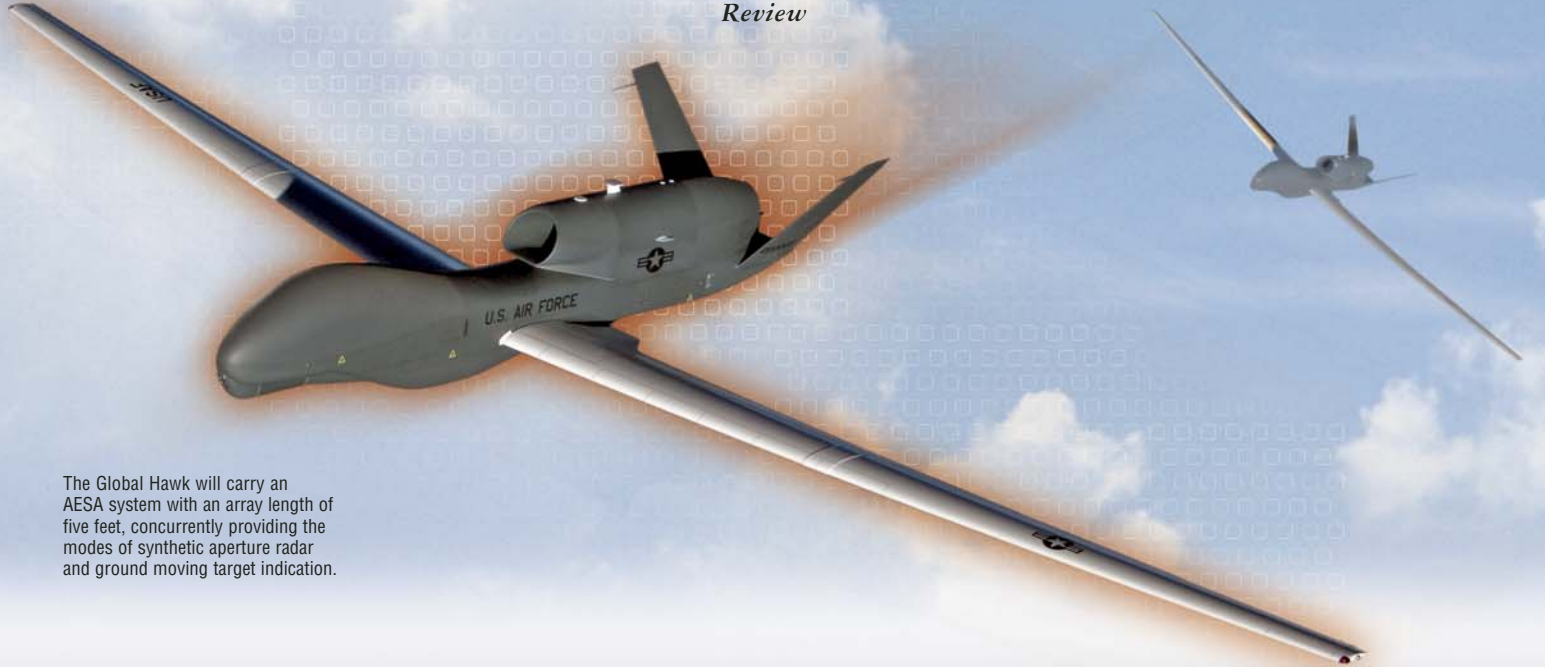
AESA radars also are being developed for the three latest European fighters—Sweden’s JAS-39 Gripen, the Eurofighter Typhoon and France’s Rafale. However, they are not expected to be ready until the next decade.

The AESA fire control radar provides fighter pilots with a number of new or greatly improved capabilities.

To begin with, pilots will have much greater functionality in air-to-air combat, being able to track and engage multiple threat aircraft.

The scanning movement of traditional mechanical radars limited the frequency of target updates the pilot could receive. To get a consistent enough picture to shoot a weapon, a pilot confronting several threats had to choose just one of the targets and focus all the radar’s energy on it.

However, the AESA radar changes this situation completely: because its agile beams move around so quickly, it can support the shooter by maintaining good quality tracks on multiple targets. In addition, the radar system automatically establishes tracking files for each detected target, reducing pilot workload.



The Global Hawk will carry an AESA system with an array length of five feet, concurrently providing the modes of synthetic aperture radar and ground moving target indication.

The radar also incorporates frequency hopping and other processing parameters that create a “low probability of intercept.” Thus, the AESA radar can detect an enemy aircraft without that target’s electronic warning systems becoming aware it is being scanned.

With an electronic beam that can look in different directions more than a thousand times per second, AESAs, in addition to tracking multiple airborne targets, can also carry out an entire range of tasks. For example, the radar can simultaneously perform air-to-air search-and-track, air-to-ground targeting, and aircraft terrain following.

AESA radars will also provide fighter pilots with much greater detection range than predecessor radars could offer. Because the power of transmission is now in the antenna, AESAs have three to four times the output energy of traditional mechanically scanned radars. This improved capability makes it possible, for the first time, to provide fire control that fully supports long range weapons like Advanced Medium-Range Air-to-Air Missile—giving these weapons the guidance they need to attack targets at their own maximum ranges.

Furthermore, AESA’s longer detection range enables it to spot and track small and stealthy cruise missiles at distances great enough for an aircraft’s defending missiles to hit them before they can reach their targets.

AESA radars’ synthetic aperture mode gives them another important advantage: they will have as much as

5 times the air-to-ground resolution of predecessor radars. Thus fighter aircraft radars will, for the first time, be capable of very accurate all-weather targeting for air-launched Global Positioning System-assisted weapons like the Joint Direct Attack Munition and Joint Standoff Weapon.

In fact, fighter pilots will now, on the strength of their radars alone, be self-sufficient in prosecuting targets. Previously, if they were not equipped with auxiliary infrared targeting pods, pilots had to do target planning before takeoff, or have the objective and its coordinates passed to them en route. Their fire control radars were simply not accurate enough to designate a hit point on the ground. But now an AESA-equipped aircraft can develop coordinates for a target of opportunity, pass the data to its own weapon and destroy the target. No external help is needed.

As a recent Northrop Grumman Analysis Center study points out [Command and Control Arrangements for the Attack of Time-Sensitive Targets; [www.analysiscenter.northropgrumman.com](http://www.analysiscenter.northropgrumman.com)], of the various ways in which the sensor, decider and shooter elements can be integrated by battle management in a network centric warfighting operation, this approach in which a single platform has both the authorization and capability to handle all three functions is the simplest, fastest and, therefore, often the best for time-sensitive targeting.

Finally, an AESA-equipped aircraft can use the radar’s agility and acuity to rapidly develop targets for non-AESA equipped aircraft—for example, when working with multiple warplanes to identify, target and destroy the enemy’s integrated air defense system at the beginning of a conflict. Such collaborative operations can be made even faster and more accurate by planned future enhancements for fighter aircraft targeting systems—for instance, improved synthetic aperture radar; automatic target detection/cueing, better access to geo-location tools like Northrop Grumman’s RainStorm and, of course, more high-bandwidth data links.

In future network centric operations, AESA’s ability to provide this kind of force multiplication will be extendable to any platform on the evolving Global Information Grid.

### **Electronic Warfare**

Because AESA radars have high power, speed and sensitivity, they are also ideal tools for electronic warfare. Threat jamming, protection and countermeasures can be an integral part of the AESA mission suite, rather than a separate system provided by the host platform. Because of the high bandwidth, rapid scanning and response times of the AESA, electronic warfare modes become a natural aspect of Northrop Grumman’s multifunctional architectures.

## Communications

The multimission AESA can make key contributions in another role as well. In September 2005, a team comprised of Northrop Grumman, L-3 Communications and Lockheed Martin Corporation, after a two year internal research and development effort, successfully demonstrated an innovative use of AESA radars for high-bandwidth communications.

The team transmitted and received high-data-rate communications signals over the air using an AN/APG-77 radar aperture and a common data link modem that L-3 had created in connection with its development work for the U-2 spy plane program. Tests proved that the modem-equipped AESA can deliver long distance line-of-sight communications for both air-to-air and ground-to-ground applications.

Researchers demonstrated the transfer of a 72 megabyte synthetic aperture radar image in 3.5 seconds at a data rate of 274 megabytes per second (mbps). By comparison, the transfer would take 48 minutes on today's standard Link 16. Company

researchers ultimately demonstrated laboratory transmission rates of 548 mbps using the F-22 radar array—and received data rates of up to 1 gigabyte per second.

"Normally, you would equip a platform with a directional aperture that enables you to download your data rapidly," says Joe Ensor, vice president, Combat Avionic Systems, Northrop Grumman's Electronic Systems sector. "But here, with the F-22 AESA, we already had a great aperture onboard—so it made sense to try to use that to get very high-capability communications off the aircraft."

The effort has been successful enough to attract the interest of U.S. Air Force Air Combat Command, and the company hopes eventually to turn its internal initiative into an Air Force or Navy contract.

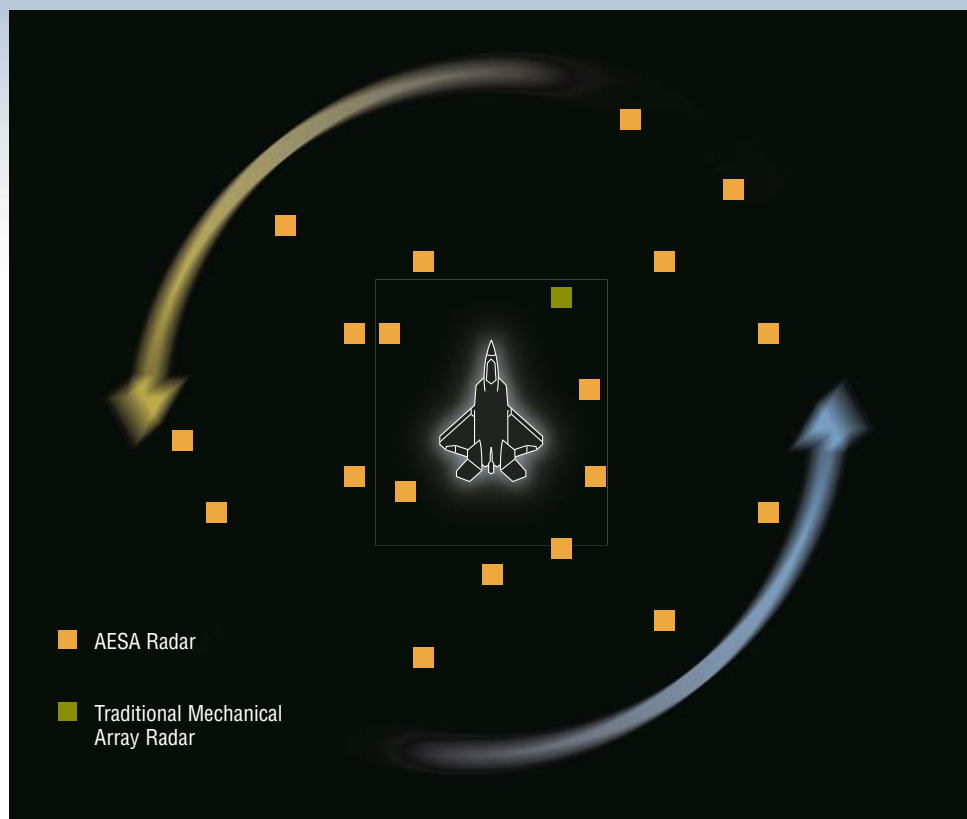
So, it may not be long before new-generation fighters will be able to use their AESA radars not only to collect sizeable amounts of intelligence and targeting data, but also to communicate those hefty packages of information around the battlefield in

seconds instead of the tens of minutes required by current data links.

While the AESA radar has many remarkable capabilities, perhaps the most striking is that most directly associated with its array of T/R modules, its ability to perform multiple tasks simultaneously as well as to shift at almost the speed of light from task to task.

This ability to be everywhere at once or move rapidly between modes makes AESA, more than any other sensor, the apt partner for the other speed-of-light defense systems now being developed—directed energy strike systems, or command and control systems that make actionable intelligence instantly available to forces, even those on the move, throughout the battlespace (see articles beginning pp.8 and 22).

Because they fit so naturally into the most futuristic sensor-decider-shooter triads conceivable, AESA radars are certain to be at the heart America's warfighting vision for many years to come. □



**Multiple Targeting Capability**  
Traditional mechanical radars are limited to tracking one target at a time; AESA radars, in contrast, can track multiple targets simultaneously.

# REVIEW OF THE STATE OF THE ART OF UK AESA TECHNOLOGY AND THE FUTURE CHALLENGES FACED

Dr Stephen Moore\*

\* Radar Lead, Dstl, UK. EMAIL: samoore1@dstl.gov.uk, TEL: +44 1252 45 5063

**Keywords:** AESA, MFR, radar, TRM, architecture, sub-arrays.

## Abstract

The UK Ministry of Defence is starting to introduce in to service the next generation of radar technology. This technology brings with it the potential for significant improvements in performance for airborne, ground based and naval applications as well as benefits for through life capability maintenance. However there are a number of challenges facing the implementation of advanced radar technology that can make these benefits difficult to realise. To address these challenges, the UK MoD is currently undertaking a number of advanced research and technology demonstration programmes aimed at in-service equipment and future upgrade programmes. This paper summarises the current state of UK MoD funded next generation radar programmes and highlights the key challenges faced. These challenges represent opportunities which the wider community can address.

## 1 Introduction

The UK Ministry of Defence is starting to introduce in to service the next generation of radar technology. The principal radar technology being introduced is active electronically scanned array (AESA) technology. This AESA technology is likely to become the main form of UK radar technology in the years to come.

Next generation radar technology is being introduced through a number of platforms including: COBRA (ground based), SAMPSON (naval), and ASTOR (airborne). It is also the subject of a number of key MoD technology demonstrator programmes (TDPs): AMSAR, CECAR (both airborne) and ARTIST (naval). These radars will be briefly described in Section 3 and 4. Section 2 will discuss the benefits of this technology, whilst Section 5 will highlight the challenges faced and the opportunities that such technology can offer if these challenges are addressed. Finally Section 6 will summarise the UK position.

## 2 Benefits of AESA technology

AESA technology in land, sea and airborne environments brings a number of advantages over traditional mechanically scanned radar systems.

The ability of AESA based radars to utilise rapid electronic inertialess scanning allows fast reaction times. This enables rapid scanning within the field of regard, including intelligent, random, or adaptive search modes. It also facilitates rapid track formation (through the use of rapid look-backs) and can greatly increase track formation range over that of mechanically scanned radar. These tracks can be highly adaptive to permit high accuracy tracking of multiple, fast manoeuvring targets. With intelligent radar control, a radar system can utilise these tracking benefits to enable multiple target engagement whilst maintaining other functionality. These benefits of rapid electronic inertialess scanning result in a more capable radar system that can out perform mechanically scanned radar in both search and track modes.

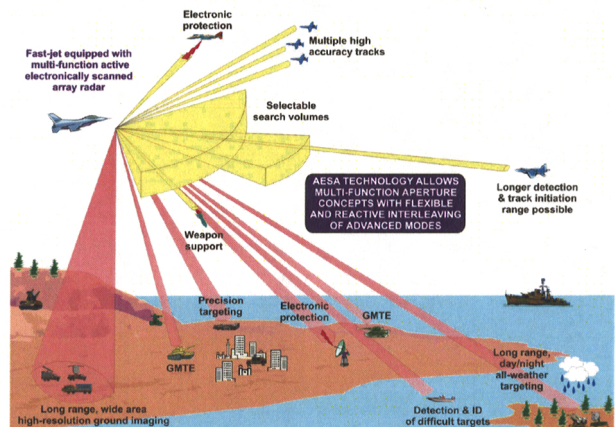


Figure 1 – Airborne AESA benefits

AESA technology also brings with it a more efficient method of generating transmit power. For a given platform with limited power available, AESA technology can make best use of that power and achieve longer detection ranges than an equivalent mechanically scanned system. This increase in efficiency is due to the introduction of a large number of transmit / receive modules (TRMs) at the array face. These TRMs each have an efficient power amplification stage, rather than a centralised power amplifier and a power feed network. Amplification in TRMs is typically through the use of a Gallium Arsenide (GaAs) power amplifier, though future systems may exploit Gallium Nitride or diamond technology. The downside to use of many TRMs is that the cooling load is greatly increased behind the array face, often requiring a

mixture of air and liquid cooling (depending on power density and available resources). This is less of a problem for surface based radar systems, but represents a significant challenge for airborne radars. In an airborne platform where the available cooling and power is limited, AESA radar must be designed to make best use of available resources. However given these limitations in airborne platforms, it is still possible to design AESA radar which can provide significantly higher transmit power (both peak and mean) over a mechanically scanned radar solution.

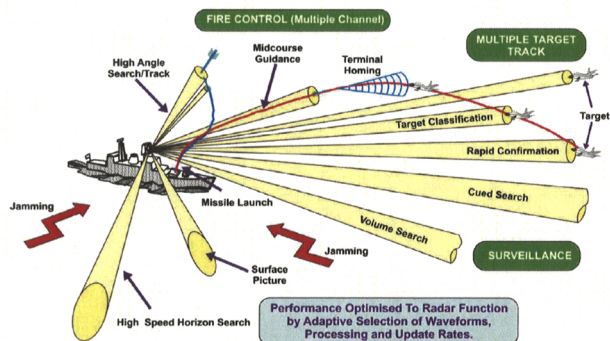


Figure 2 – Shipborne AESA benefits

The architecture of AESA radars can be designed to provide multiple receive channels, facilitating a number of advanced radar modes, including: adaptive beamforming (ABF) to counter jamming (sidelobe and mainbeam) and space-time adaptive processing (STAP) to remove clutter and to detect and track slow moving air and ground targets. The challenge is to optimise the number of channels to the required performance of the radar and then to fully exploit these for ABF, STAP and other advanced radar and non-radar modes (e.g. the use of the radar as a high accuracy emitter locator). The use of AESA radar for non-radar modes is an area of increased interest for the UK. The radar is often situated in the prime sensing location for a platform, therefore if the technology can be adapted to provide a multi-function aperture (MFA) solution, this can yield high performance solutions for comms (e.g. provision of guidance messages to weapons), emitter location, electronic surveillance, target illumination, and bi- or multi-static modes.

AESA radars with advanced antenna architectures (multiple channels) and designs (wide tuneable frequency range and wide instantaneous bandwidths), state of the art TRMs (with improved element control of amplitude, phase and transmitted waveforms), and with advanced digital waveform generators provide the user with a large number of parameters with which to optimise the radar to improve performance in a given scenario. This large trade space gives the ability for levels of dwell and mode optimisation not previously possible. The challenge is to intelligently optimise these parameters and coordinate this through sophisticated sensor control.

A final key benefit of AESA radar design is that it yields a highly reliable radar. The large number of TRMs and the design of the antenna architecture mean that the radar can tolerate a significant number of TRM failures, with individual TRM failures only marginally affecting antenna performance (beamwidth, sidelobes, gain, TX/RX power). This graceful degradation of antenna performance means that AESA radars have a large mean time between critical failure (MTBCF). New AESA radar concepts promise reliability levels comparable to the platform lifetime – “fit and forget” technology. This increase in reliability and MTBCF leads to whole life cost savings which benefits through life capability management (TLCM).

Figure 1 and Figure 2 summarise the key performance benefits of AESA technology for airborne and shipborne applications.

### 3 UK AESA radar

Next generation radar technology is only recently beginning to be introduced in to UK forces in the surface and airborne domains. The first AESA radars currently in or soon to be in-service with UK forces are: COBRA (ground based), SAMPSON (naval), and ASTOR (airborne).

This section briefly outlines these AESA radars, before Section 4 goes on to discuss some of the research upon which these systems are based and which is developing future AESA radar systems.

#### 3.1 Surface based AESA radar

COBRA and SAMPSON are two examples of the latest breed of surface based phased array radars. They build upon extensive UK and European funded research programmes and represent world leading multi-function radars.

COBRA (Counter Battery Radar, Figure 3), built for the UK, France and Germany by the EuroArt consortium comprising Lockheed Martin, EADS (Germany), and Thales (France and UK) is a ground based, highly mobile weapon location radar.



Figure 3 – COBRA (built by EuroArt consortium)

COBRA is currently in service with UK forces and demonstrating the advantages of advanced radar technologies.

SAMPSON (Figure 4), built by BAE Systems Insyte, is a shipborne multi-function radar which is part of the PAAMS system for the new T45 ships the Royal Navy is procuring. It provides both self and local area defence.

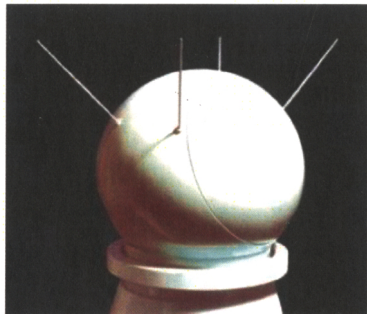


Figure 4 – SAMPSON MFR (built by BAE Systems Insyte), part of the PAAMS system fitted to the Type 45 ship

SAMPSON is based upon MoD funded research and the MESAR and MESAR2 TDPs and will shortly enter into service.

### 3.2 Airborne AESA

There are currently few examples of airborne AESAs around the world, with fully AESA based solutions only recently being introduced.

ASTOR (Airborne Stand-Off Radar, Figure 5) is an airborne ground surveillance system designed to provide detailed information regarding the movement and disposition of enemy forces. Its Dual-Mode Radar (DMR) is a large phased array radar capable of Ground Moving Target Indication (MTI) and high resolution Synthetic Aperture Radar (SAR) ground imaging modes.



Figure 5 – ASTOR aircraft (built by Raytheon Systems Ltd)

This platform will provide a step-change in performance over previous solutions in its ISTAR role (Intelligence, Surveillance Target Acquisition and Reconnaissance). ASTOR will soon be in-service with the Royal Air Force.

## 4 Current UK technology demonstrator and research programmes

Current UK technology demonstrator and research programmes are working hard to take the technology to the next step and create truly multi-function AESA based radar

systems to meet the requirements of ground, sea and air platforms.

These R&D programmes broadly fall into two categories: surface based and airborne technology demonstrator programmes (TDPs). These will be described in this Section, before Section 5 goes on to discuss the challenges facing these TDPs.

### 4.1 Surface based TDPs

ARTIST is a four year programme of UK/US collaboration currently underway aiming to design and demonstrate the next generation of surface based radar technology. Within the UK it involves Dstl, BAE Systems Insyte, QinetiQ, and Roke Manor Research; whilst in the US it involves the US Navy, Lockheed Martin, MIT Lincoln Labs, and Johns Hopkins University APL.

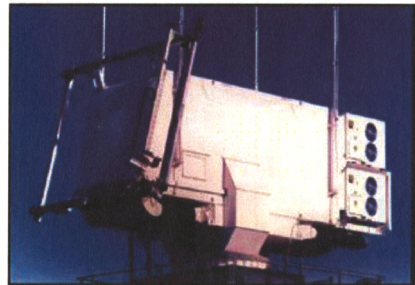


Figure 6 – UK ARTIST TDP (involves Dstl, BAE Systems Insyte, QinetiQ, Roke Manor Research)

The ARTIST programme builds upon the highly successful UK MESAR and MESAR2 TDPs (and other associated research programmes) which previously de-risked key technologies for the soon to be in service SAMPSON MFR (e.g. ABF, RRM).

ARTIST is an advanced multiple sub-arrayed AESA MFR which is addressing the key technology areas of: high fidelity waveform generation, digital antenna processing, signal processing, radar control, and sensor integration.

It is leveraging lessons learnt from previous UK and US programmes (e.g. on COTS processing and open architecture issues) to help with the de-risking of these key technology areas. Technology developments from the UK part of this programme are initially aimed at future upgrades to the SAMPSON radar.

### 4.2 Airborne TDP's

The UK is currently involved in two key airborne TDPs which are de-risking AESA technology for fast-jet applications. These are the AMSAR and CECAR TDPs.

The AMSAR TDP is a UK, French and German collaboration de-risking key technologies for a generic airborne fast-jet platform (e.g. Typhoon or Rafale) through a series of ground

based trials and flight trials on a BAC 1-11. AMSAR represents the first generation of European airborne AESA technology and has led to a burgeoning AESA MFR capability within UK, France and Germany.



Figure 7 – AMSAR (involves UK, French and German MoDs and also SELEX SAS, Thales France and EADS Ulm)

AMCAR is a multiple sub-arrayed antenna which is developing advanced adaptive beamforming (ABF) and space-time adaptive processing (STAP) techniques as part of the de-risking of advanced air-to-air modes.

The CECAR TDP is a second generation AESA TDP between UK and Germany aimed at de-risking key technologies for a possible future upgrade to the Typhoon fast-jet platform. CECAR builds upon the significant technical achievements of the AMSAR programme to address Typhoon specific issues.



Figure 8 – CECAR on a BAC 1-11 trials aircraft (involves UK and German MoDs and also SELEX SAS and EADS)

CECAR is de-risking advanced air-to-air and air-to-ground radar modes through flight trials on a BAC 1-11. It is also de-risking a possible future upgrade to Typhoon fast-jets through detailed radar system design using representative hardware and through integration, fit and trial on a Typhoon development aircraft (Typhoon DA5).

## 5 Challenges for the future

The existing or soon to be in-service AESA radars described in Section 3 and the TDPs described in Section 4 both face a number of key challenges to enable capability maintenance in a continually changing military environment. This need is

driven by through life capability management (TLCM) which requires in its broadest sense the maintenance of both initial operating capability as well as capability as the environment changes beyond that originally envisaged (e.g. due to the changing nature of the threat, a differing concept of employment, or a more challenging environment).

These challenges are broadly similar in nature for both surface based and airborne radars due to the similarities in their basic technologies and their approaches to solve the problems faced (though of course there remain fundamental differences in the implementation of any solutions and in the nature of the environment in which they operate).

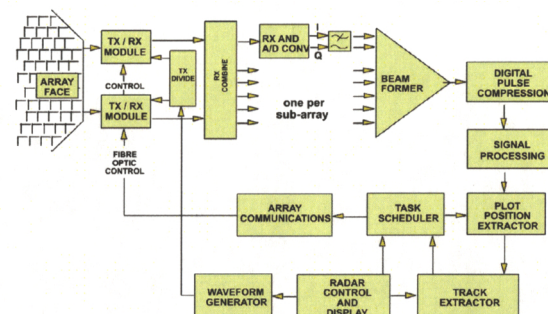


Figure 9 – Generic shipborne AESA architecture

The similarities between surface based and airborne radars can be seen in the typical architecture designs shown in Figure 9 and Figure 10 (as well as in Figure 1 and Figure 2).

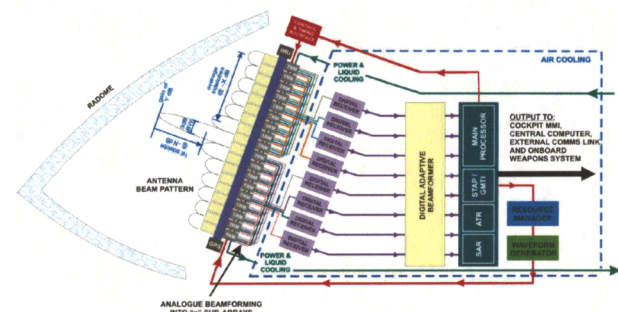


Figure 10 – Generic airborne AESA architecture

The challenges faced are described in the following subsections.

### 5.1 Transmit / receive modules

As discussed earlier, AESA technology brings with it a more efficient and robust method of generating transmit power (as well as a lower receiver noise figure) through the use of many parallel power amplification stages at the antenna within TRMs. This can enable an AESA to make best use of the limited power available on a given platform. The downside being that the cooling load is greatly increased behind the array face, often requiring a mixture of air and liquid cooling (depending on power density and available resources).

There are a number of challenges facing the design of these TRMs (see Figure 11 for an example of a TRM). There are the continual challenges of reducing the size, weight, complexity and cost of TRMs. There are also a number of other challenges to improve the efficiency, increase the peak and mean output power, reduce the receive noise figure, increase the instantaneous and tuneable bandwidths. These latter challenges are driving the design of the antenna elements and the design of the power amplifier.

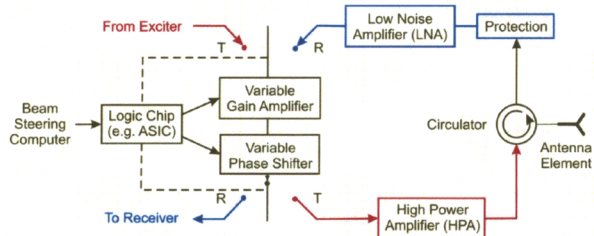


Figure 11 – Typical Transmit/Receive Module design

Designing an antenna element that can meet the requirement of a wide tuneable bandwidth whilst being able to transmit a wide instantaneous bandwidth (e.g. for high resolution imaging or air target recognition modes) is difficult and challenging. Within the UK, research is continuing to develop and improve antenna element design to meet these stressing design goals (hand in hand of course with radome design).

Power amplification within TRM is typically through the use of a Gallium Arsenide (GaAs) power amplifier. Research is continuing to improve their design, efficiency and power amplification capabilities. However future systems may well exploit Gallium Nitride (GaN) or diamond technology to yield a step change in performance of TRMs. To de-risk future TRM designs, the UK MoD is initially investing in GaN technology through the European KORRIGAN programme.

## 5.2 Multiple channels

The UK is actively researching multiple channel AESA radar for applications to ground based, naval and airborne platforms. This technology can provide the enhanced performance and functionality needed to meet the UK's future requirements.

Higher levels of array digitisation can result in multiple sub-arrays which can yield multiple channels and/or degrees of freedom (depending on the nature of the RF and digital combination network). These can be exploited to give a radar an advanced electronic counter counter measure (ECCM) capability against multiple advanced jamming sources (within both the sidelobe and main beam – see Figure 12), advanced STAP modes, and for airborne radars, improved ground moving target indication (GMTI).

Research is continuing within the UK to improve the design and technology readiness level (TRL) of radars with high levels of digitisation.

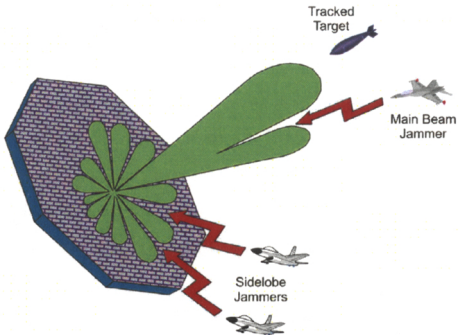


Figure 12 – Electronic counter counter measure (ECCM) adaptive beamforming (ABF) capability of AESAs

Very high levels of digitisation (see Figure 13) remain challenging on both a cost and technical implementation level.

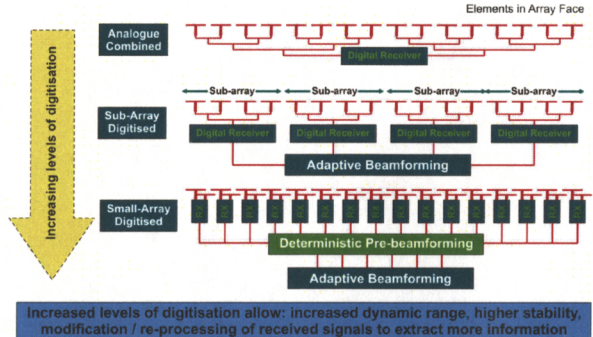


Figure 13 – Increasing levels of digitisation and ECCM

Exploiting high levels of digitisation is also challenging. Research is continuing, aiming at further developing ABF, STAP and GMTI techniques as well as looking at other ways this advanced AESA radar capability can be exploited for other modes / techniques.

## 5.3 Multi-function aperture concepts

The UK, in common with many other nations, is beginning to become interested in looking at other ways advanced AESA radar technology can be exploited.

Typically radars (by definition a high gain RF device) occupy a prime location on a platform. It is possible that this prime location and advanced RF functionality may be able to be exploited for a number of other functions, including communications, passive surveillance, or possibly active RF applications (maybe in a return to the UK's 1935 Daventry experiment!).

The field of multi-function aperture concept research is however currently still in its infancy. Whilst a challenging area, it offers the promise of much more flexible sensor solutions which can yield significant military utility and offer increased performance for a number of complementary RF

modes. Instigating research and development in this emerging area represents an interesting opportunity.

#### **5.4 Intelligent radar control**

The next generation of AESAs must fully harness their multi-function benefits through the use of next generation radar task schedulers and mode optimisation – i.e. intelligent radar control (IRM).

Current and future AESA radar systems have (or will have) significant multi-parameter diversity (e.g. in transmit frequency, waveforms, transmit power, beamwidth, antenna pattern optimisation / adaptation, mode interleaving etc) which allow a radar to be dynamically optimised for a wide range of scenarios (see Figure 1 and Figure 2 for examples).

This optimisation requires an efficient radar resource manager (RRM) working with a sensor, platform and force resource manager / mission planner to fully exploit the maximum potential that such AESA technology offers.

Without such intelligent radar control, the many benefits that AESA offers will be difficult to realise.

The UK MoD is continuing its active research into RRM / IRM for both surface based and airborne AESA radar applications. However there remains need still for significant further development of advanced techniques and work is continuing to look at new methods and algorithms.

#### **5.5 Ground moving target engagement**

Finally, as research continues on air-to-ground targeting from airborne platforms, there remains the key challenge of ground moving target engagement (GMTE). This encompasses: moving target indication, detection, tracking, geolocation, recognition, collateral damage assessment, engagement and finally battle damage assessment – i.e. all stages required to successfully engage a moving ground target from an airborne platform.

GMTE is a mode specific to airborne platforms designed to attack moving targets. It is a technically challenging mode which can benefit greatly from the benefits that advanced AESA radars can bring (e.g. STAP, GMTI, advancing tracking, high resolution imaging modes, flexible employment) as well as the benefits of networked operation (outside the scope of this paper).

The challenge of GMTE is included in this paper as an example of a capability requirement that is technically difficult and which relies upon the previous challenges to be addressed. Further R&D is vital in this area.

### **6 Summary**

This paper has summarised the current UK state of art in AESA radar systems technology, the research underway to further advance it, and the challenges faced in the future.

The driving challenge remains the ability to enable capability maintenance in a continually changing military environment. This need is driven by through life capability management (TLCM) which requires in its broadest sense the maintenance of both initial operating capability as well as capability as the environment changes beyond that originally envisaged (e.g. due to the changing nature of the threat, a differing concept of employment, or a more challenging environment).

To address this radar TLCM challenge, given the important role radar will retain as a key means of day / night all weather long range surveillance and targeting, the UK must continue to actively pursue advanced radar research and development

A key enabler to tackle radar TLCM is advanced AESA radar system design. Radars with high reliabilities, multiple parameter diversity and high levels of digitisation offer the potential to greatly increase radar longevity. These degrees of adaptability / flexibility can be exploited by algorithms and techniques produced by future research programmes to maintain performance against a changing threat, method of employment or a more challenging environment. High reliability (i.e. high MTBCF) means that the main radar hardware becomes effectively “fit and forget”, with hardware upgrades restricted to mission computing upgrades to combat obsolescence and to exploit newly developed algorithms and techniques to make better use of the inherent radar capabilities. Such a solution provides significant cost savings, performance advantages, and opportunities to exploit.

Whilst the AESA radar programmes discussed face a number of challenges, the technologies to face these challenges also present a number of opportunities to provide a step change in military capability. These opportunities can be realised through exploitation of recent and planned advances in AESA radar technology and through the optimal and intelligent usage of the many degrees of adaptation these systems offer to tune a radar systems capability to maximise performance in a given role/mode.

### **Acknowledgements**

I would like to acknowledge all of the extensive research and development, both MoD and industry funded, that is referenced within this paper. Without the efforts of the many UK and international companies and individuals involved, these programmes would not have achieved their many successes. It is through the continued efforts of these people that we can continue this success and address the challenges discussed within this paper.

### **References**

UK MoD Defence White Paper 2003 “Delivering Security in a Changing World” (2003)

UK MoD “Defence Industrial Strategy” (Dec 2005)

UK MoD “Defence Technology Strategy” (Nov 2006)

# UK Airborne AESA Radar Research

Dr Stephen Moore\*

\*Radar Team Leader, Dstl, UK. samoore1@dstl.gov.uk

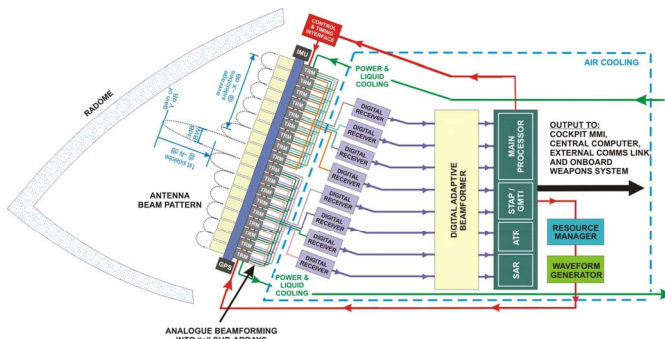
**Keywords:** AESA, radar, multiple sub-arrays, airborne.

## Abstract

This paper reviews current UK airborne active electronically scanned array (AESA) designs, discusses current trends towards higher digitisation and multi-function aperture concepts, and details the key future challenges that this technology faces. Specifically the paper discusses applications to fast-jets. Key requirements are for higher levels of digitisation to provide the performance required in ECCM, STAP, GMTI and ESM modes. Building radar systems with the key basic building blocks to as a minimum enable future realisation of these advanced modes will help to "future proof" the systems. This design philosophy is integral to the concept of through life capability management (TLCM) – i.e. a system designed to support the ability to sustain capability through incremental, spiral upgrade of signal processing, line replaceable items (LRIs), firmware and advanced modes.

## 1 Introduction

The UK Ministry of Defence is starting to introduce in to service the next generation of airborne radar technology. The principal airborne radar technology beginning to be introduced is active electronically scanned arrays (AESA) (see Figure 1). This could become the main form of UK airborne radar technology in the years to come.



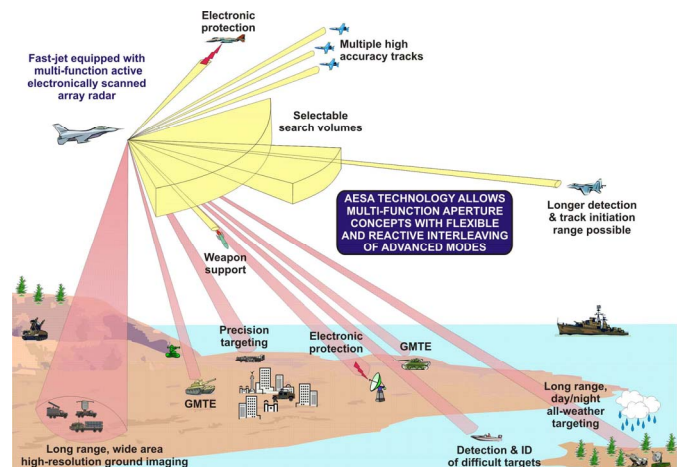
The first AESA system the UK has brought in to service is the ASTOR airborne ISTAR platform. Following on from this there are a number of key MoD technology demonstrator programmes (TDPs) (e.g. AMSAR, CECAR) which are developing and de-risking technology for possible

exploitation on platforms such as the Eurofighter Typhoon fast-jet or future UAV concepts.

The challenge facing these new and next generation AESA based radar systems is initially in their fundamental design to enable full exploitation and then in realising the many benefits that the multi-function aperture technology provides through its inherent flexibility and parameter diversity. This is the challenge that is currently exercising the UK MoD and the UK AESA radar community. This paper outlines these challenges, highlights the benefits in meeting them, and then discusses current research and development and future plans which aim to tackle the issues.

## 2 Benefits of airborne AESA technology

AESA technology in airborne environments brings a number of advantages over traditional mechanically scanned radar systems (Figure 2).



The ability of AESA based radars to utilise rapid electronic inertialess scanning allows fast reaction times. This enables rapid scanning within the field of regard, including intelligent, random, or adaptive search modes. It also facilitates rapid track formation (through the use of rapid look-backs) and can greatly increase track formation range over that of mechanically scanned radar. These tracks can be highly adaptive to permit high accuracy tracking of multiple, fast manoeuvring targets. With intelligent radar control, a radar system can utilise these tracking benefits to enable multiple target engagement whilst maintaining other functionality.

These benefits of rapid electronic inertialess scanning result in a more capable radar system that can out perform mechanically scanned radar in both search and track modes.

AESA technology also brings with it a more efficient method of generating transmit power. For a given platform with limited power available, AESA technology can make best use of that power and achieve longer detection ranges than an equivalent mechanically scanned system.

A key benefit of AESA radar design is that it yields a highly reliable radar. The large number of transmit / receive modules (TRMs) and the design of the antenna architecture mean that the radar can tolerate a significant number of TRM failures, with individual TRM failures only marginally affecting antenna performance (beamwidth, sidelobes, gain, TX/RX power). This graceful degradation of antenna performance means that AESA radars have a large mean time between critical failure (MTBCF). New AESA radar concepts promise reliability levels comparable to the platform lifetime – “fit and forget” technology. This increase in reliability and MTBCF leads to whole life cost savings which benefits through life capability management (TLCM).

Finally, AESA radars with advanced antenna architectures (multiple channels) and designs (wide tuneable frequency range and wide instantaneous bandwidths), state of the art TRMs (with improved element control of amplitude, phase and transmitted waveforms), and with advanced digital waveform generators provide the user with a large number of parameters with which to optimise the radar to improve performance in a given scenario. This large trade space gives the ability for levels of dwell and mode optimisation not previously possible. The difficulty is to intelligently optimise these parameters and coordinate this through sophisticated sensor control.

### 3 Key challenges

Airborne AESA radar systems all face a number of key challenges to both implement and exploit the advanced AESA radar technology in addition to the extant problem of enabling capability maintenance in a continually changing military environment. This later need is driven by through life capability management (TLCM) which requires in its broadest sense the maintenance of both initial operating capability as well as capability as the environment changes beyond that originally envisaged (e.g. due to the changing nature of the threat, a differing concept of employment, or a more challenging environment).

The key challenges currently exercising the UK MoD and the UK AESA radar community are:

- (i) AESA architectures
- (ii) Transmit / receive modules
- (iii) Multiple channels and their implementation
- (iv) Level of digitisation required
- (v) Multi-function aperture concepts

### (vi) Intelligent radar control

All of these broadly fall into two categories: (a) implementing advanced AESA technology; and (b) exploiting this technology. Both of these categories will be discussed in the following sections.

This list does not imply that these are the only issues facing the implementation and exploitation of this technology. There are a number of other driving issues (e.g. the integration of such systems into existing or new platforms). However these represent the most significant challenges facing the airborne radar community which are being addressed by significant research & development funding whose ultimate aim is to enable the many benefits of AESA to be realised.

## 4 Architecture issues

There are a number of architecture issues affecting the implementation of AESA technology. Key current drivers are discussed in this section.

### 4.1 Transmit / receive modules

There are a number of challenges facing the design of TRMs (Figure 3). There are the continual challenges of reducing the size, weight, complexity and cost of TRMs. There are also a number of other challenges to improve the efficiency, increase the peak and mean output power, reduce the receiver noise figure, increase the instantaneous and tuneable bandwidths. These latter challenges are driving the design of the antenna elements and the design of the power amplifier.

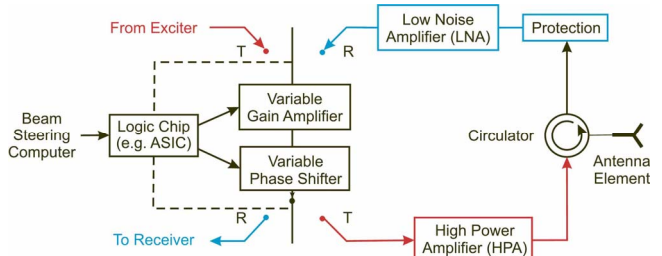


Figure 3: Typical Transmit/Receive Module design

As discussed earlier, AESA technology brings with it a more efficient and robust method of generating transmit power (as well as a lower receiver noise figure) through the use of many parallel power amplification stages at the antenna within TRMs. These TRMs each have an efficient power amplification stage, rather than a centralised power amplifier and a power feed network (as in e.g. passive ESAs). Power amplification within a TRM is typically through the use of a Gallium Arsenide (GaAs) power amplifier. The design and efficiency of TRMs in an AESA allow it to make best use of the limited power available on a given platform. The downside being that the cooling load is greatly increased behind the array face, often requiring a mixture of air and liquid cooling (depending on power density and available resources). Research is continuing to improve their design, efficiency and power amplification capabilities. However

future systems may well exploit Gallium Nitride (GaN) or diamond technology to yield a step change in performance of TRMs. To de-risk future TRM designs, the UK MoD is initially investing in GaN technology through the European KORRIGAN programme.

The downside to use of many TRMs is that the cooling load is greatly increased behind the array face, often requiring a mixture of air and liquid cooling (depending on power density and available resources). In an airborne platform where the available cooling and power is limited, AESA radar must be designed to make best use of available resources. However given these limitations in airborne platforms, it is still possible to design AESA radar which can provide significantly higher transmit power (both peak and mean) over a mechanically scanned radar solution.

Designing an antenna element, transmit / receive module and antenna architecture that can meet the requirement of a wide tuneable bandwidth whilst being able to transmit a wide instantaneous bandwidth (e.g. for high resolution imaging or air target recognition modes) is difficult and challenging. Within the UK, research is continuing to develop and improve designs to meet these stressing design goals (hand in hand of course with radome design). There is also continued interest in exploring the implementation and benefits of multiple polarisations (though this remains at present at a low technology readiness level).

## 4.2 Array manifold design

Array manifold design is an area which can easily be underestimated but whose design and performance is critically important to the overall performance of an AESA radar.

The design of the array manifolds behind the AESA antenna is closely linked with the state of the art in digital receiver technology. These factors drive the level of digitisation possible in the radar. High levels of digitisation will improve the performance of key modes such as digital adaptive beamforming (ABF) to counter jamming (sidelobe and mainbeam) and space-time adaptive processing (STAP) to remove clutter and to improve the detection and tracking of slow moving air and ground targets. The array manifold design is also integral to the utility of the radar in other modes (e.g. ESM) and in its future upgradeability. Therefore it is important to design the array manifold to meet the performance and function requirements in the near term and also for flexibility to support future upgrades (either hardware or software) to maintain capability (essentially to support TLM).

Figure 4 shows an example of a simplified AESA manifold design. This shows multiple analogue beamforming networks optimised to support different modes. The analogue beamforming networks feed into digital receivers which then in turn feed into a digital processing stage which includes digital beamforming. In this example there is an analogue

beamforming network which combines RF output from each antenna element and forms 4 channels: a sum beam, two difference beams (elevation and azimuth), and a guard channel (all optimised to produce low sidelobe antenna patterns). There is also a separate analogue beamforming network which combines RF output from each antenna element into 16 sub-arrays and similarly a separate network optimised to support other modes (e.g. comms or ESM).

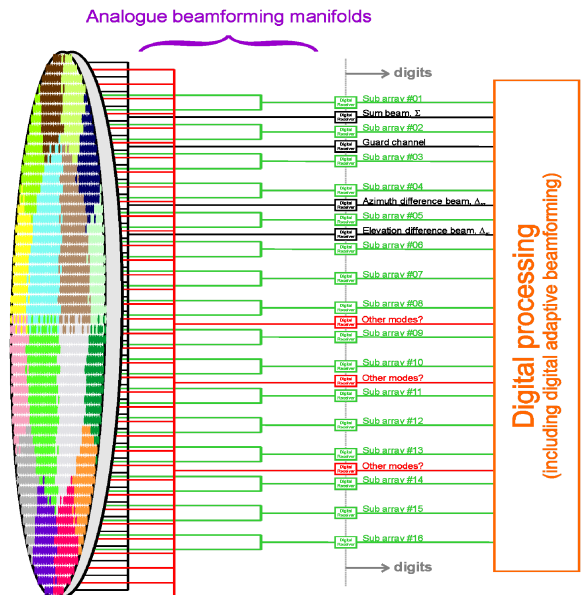


Figure 4: Example AESA manifold design

The analogue beamforming networks can either consist of a single stage of combination from the element level down to the chosen stage at which digitisation will occur, or they can consist of two or more stages of combination before digitisation (e.g. to a layer of small arrays before further combination into larger sub-arrays). Multiple stages offer the prospect of future upgradeability to higher degrees of digitisation through the removal of one or more stages and their replacement with digital receivers and an improved digital beam former.

As can be seen from this “simplified” AESA manifold, it is complex to design a radar which is optimised for multiple functions and with even moderate numbers of degrees of freedom to support modes such as ABF. Add to this the challenge of engineering and calibrating the array. This design would be greatly complicated if polarisation diversity were also required. Its optimisation would also be made more challenging if it were required to operate over a wide range of frequencies (e.g. over one or more octaves).

Of course it would be preferable to digitise at element level and remove the need for such complicated analogue beamforming networks. However the current state of the art for airborne radars does not support this. Therefore the array manifold must be a compromise between realisability and mode optimisation.



Figure 5: X Band digital receiver with a single layer construction (RF in, Digits out) [1]

Figure 5 shows an example of a current state of the art X-band digital receiver for an airborne radar application. Research is developing compact receivers which will support high levels of digitisation whilst maintaining the high levels of performance required (e.g. the challenging spurious free dynamic range requirements for digital receivers in airborne radars).

Research is continuing on designing future array manifolds and architectures to support the increasingly challenging requirements being placed on radar systems (e.g. multi-function aperture concepts). One such avenue of research is the soon to commence EDA funded SIMCLAIRS programme.

## 5 Exploitation issues

The key exploitation issue to consider is the level of digitisation required to support the exploitation of advanced modes to meet the performance aims of the radar system.

Earlier Section 4.2 talked about array manifold design and the limitations imposed by current digital receiver technology – but what degree of digitisation is required?

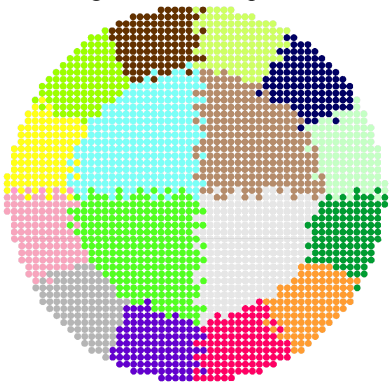


Figure 6: Example of an AESA antenna with 16 digitised sub-arrays (each sub-array is indicated by a different colour)

Higher levels of array digitisation (e.g. Figure 6) yield multiple degrees of freedom which can be exploited to give a radar an advanced electronic counter counter measure (ECCM) capability against multiple advanced jamming sources (within both the sidelobe and main beam), advanced STAP modes, and improved ground moving target indication (GMTI).

Figure 7 shows the design trades to be considered for an AESA antenna with an ECCM mode.

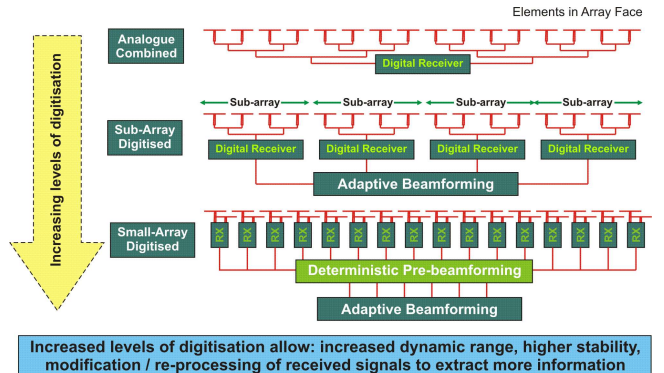


Figure 7: Increasing levels of digitisation and ECCM

Optimising the level of digitisation for each mode will depend upon the requirements for that mode (e.g. number and location of jammers to be cancelled, nature of target to be detected and its environment, and the minimum detectable velocity). In the example shown in Figure 8 the level of digitisation will be driven by the numbers of degrees of freedom required to digitally adapt the antenna beam on receive to null out the jamming power received from a given number of sidelobe and mainbeam jammers.

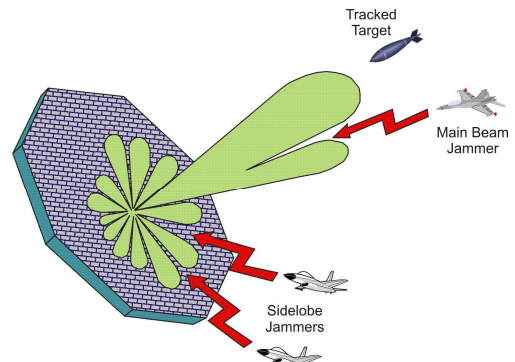


Figure 8: Electronic counter counter measure (ECCM) adaptive beamforming (ABF) capability of AESAs

It is therefore important to consider all the modes of the radar, the scenarios in which they will typically be utilised in and the subsequent performance requirements. These requirements then need to be balanced with the hardware limitations (i.e. section 4.2) and with the signal processing limitations (e.g. the computational limit on the numbers of channels that can be processed in real time). Note that it is important to correctly balance these requirements as it is inefficient to implement a design which requires numbers of degrees of freedom reduction in the digital domain due to a lack of computing resources to fully exploit them.

The UK has considered each of the factors described above, the relative benefits, the state of the art of technologies, as well as the requirements for: detection of difficult targets,

minimum detectable velocity, robustness to clutter, anti-jamming, and maintenance of performance in challenging environments. This has led the UK to concentrate on the realisation of the levels of digitisation best matched to its needs. This research will benefit the next generation of airborne AESA radars.

## 6 How to realise benefits of AESA

The next generation of AESAs must fully harness their multi-function benefits through the use of next generation radar task schedulers and mode optimisation – i.e. intelligent radar control (IRM).

Current and future AESA radar systems have (or will have) significant multi-parameter diversity (e.g. in transmit frequency, waveforms, transmit power, beamwidth, antenna pattern optimisation / adaptation, mode interleaving etc) which allow a radar to be dynamically optimised for a wide range of scenarios and environments.

This optimisation requires an efficient radar resource manager (RRM) working with a sensor, platform and force resource manager / mission planner to fully exploit the maximum potential that such AESA technology offers.

Without such intelligent radar control, the many benefits that AESA offers will be difficult to realise.

The UK MoD is continuing its active research into RRM / IRM for both surface based and airborne AESA radar applications. However there remains need still for significant further development of advanced techniques and work is continuing to look at new methods and algorithms.

## 7 Current AESA R&D

Current UK technology demonstrator and research programmes are working hard to take the technology to the next step and create truly multi-function AESA based radar systems to meet the requirements of air platforms.

The UK is currently involved in two key airborne technology demonstrator programmes (TDPs) which are de-risking AESA technology for fast-jet applications. These are the AMSAR and CECAR TDPs.

The AMSAR TDP is a UK, French and German collaboration de-risking key technologies for a generic airborne fast-jet platform (e.g. Typhoon or Rafale) through a series of ground based trials and flight trials on a BAC 1-11. AMSAR represents the first generation of European airborne AESA technology and has led to a burgeoning AESA MFR capability within UK, France and Germany.



Figure 9: AMSAR (involves UK, French and German MoDs and also SELEX SAS, Thales France and EADS Ulm)

AMSAR (see Figure 9) is a multiple sub-arrayed antenna which is developing advanced adaptive beamforming (ABF) and space-time adaptive processing (STAP) techniques as part of the de-risking of advanced air-to-air modes.

The CECAR TDP is a second generation AESA TDP between UK and Germany aimed at de-risking key technologies for a possible future upgrade to the Typhoon fast-jet platform. CECAR builds upon the significant technical achievements of the AMSAR programme to address Typhoon specific issues.



Figure 10: CECAR on a BAC 1-11 trials aircraft (involves UK and German MoDs and also SELEX SAS and EADS)

CECAR (see Figure 10) is de-risking advanced air-to-air and air-to-ground radar modes through flight trials on a BAC 1-11. It is also de-risking a possible future upgrade to Typhoon fast-jets through detailed radar system design using representative hardware and through integration, fit and trial on a Typhoon development aircraft (Typhoon DAS).

The UK is currently developing plans for follow on programmes to develop third generation AESA technology for future exploitation in near, medium and far term air platforms.

## 8 Future areas for airborne AESA R&D

What next for AESA R&D? The UK continues to develop and de-risk key AESA technologies with the aim to pull

through this work to benefit current and future platforms. The UK is also researching new applications, concepts and modes that can enhance the performance in existing scenarios as well as introduce new abilities which have the potential to increase the capability of the host platform. Two example future areas of research are briefly described in this section.

### 8.1 Multi-function aperture concepts

The UK, in common with many other nations, is beginning to look at other ways advanced AESA radar technology can be exploited (e.g. for non-radar modes).

Typically radars (by definition a high gain RF device) occupy the prime sensing location for a platform, therefore if the technology can be adapted to provide a multi-function aperture (MFA) solution, this can yield high performance solutions for comms (e.g. provision of guidance messages to weapons), emitter location, electronic surveillance, target illumination, and bi- or multi-static modes.

The field of multi-function aperture concept research is however currently still in its infancy. Whilst a challenging area, it offers the promise of much more flexible sensor solutions which can yield significant military utility and offer increased performance for a number of complementary RF modes. Instigating research and development in this emerging area represents an interesting opportunity.

### 8.2 Ground moving target engagement

As research continues on air-to-ground targeting from airborne platforms, there remains the key challenge of ground moving target engagement (GMTE). This encompasses: moving target indication, detection, tracking, geolocation, recognition, collateral damage assessment, engagement and finally battle damage assessment – i.e. all stages required to successfully engage a moving ground target from an airborne platform.

GMTE is a mode specific to airborne platforms designed to attack moving targets. It is a technically challenging mode which can benefit greatly from the benefits that advanced AESA radars can bring (e.g. STAP, GMTI, advancing tracking, high resolution imaging modes, flexible employment) as well as the benefits of networked operation (outside the scope of this paper). Further R&D in this area and in future weapons promises the potential to upgrade existing AESA radar based platforms to provide an ability to undertake this challenging role.

## 8 Summary

This paper has summarised the current UK state of art in airborne AESA radar systems technology, the research underway to further advance it, and the challenges faced in the future.

The driving challenge remains the ability to enable capability maintenance in a continually changing military environment. This need is driven by through life capability management (TLCM) which requires in its broadest sense the maintenance of both initial operating capability as well as capability as the environment changes beyond that originally envisaged (e.g. due to the changing nature of the threat, a differing concept of employment, or a more challenging environment).

To address this radar TLCM challenge, given the important role radar will retain as a key means of day / night all weather long range surveillance and targeting, the UK must continue to actively pursue advanced radar research and development

A key enabler to tackle radar TLCM is advanced AESA radar system design. Radars with high reliabilities, multiple parameter diversity and high levels of digitisation offer the potential to greatly increase radar longevity. These degrees of adaptability / flexibility can be exploited by algorithms and techniques produced by future research programmes to maintain performance against a changing threat, method of employment or a more challenging environment. High reliability (i.e. high MTBCF) means that the main radar hardware becomes effectively “fit and forget”, with hardware upgrades restricted to mission computing upgrades to combat obsolescence and to exploit newly developed algorithms and techniques to make better use of the inherent radar capabilities. Such a solution provides significant cost savings, performance advantages, and opportunities to exploit.

Whilst the AESA radar programmes discussed face a number of challenges, the technologies to face these challenges also present a number of opportunities to provide a step change in military capability. These opportunities can be realised through exploitation of recent and planned advances in AESA radar technology and through the optimal and intelligent usage of the many degrees of adaptation these systems offer to tune a radar systems capability to maximise performance in a given role/mode.

## Acknowledgements

I would like to acknowledge all of the extensive research and development, both MoD and industry funded, that is referenced within this paper. Without the efforts of the many UK and international companies and individuals involved, these programmes would not have achieved their many successes. It is through the continued efforts of these people that we can continue this success and address the challenges discussed within this paper.

## References

- [1] C. Tarran. “Advances in affordable Digital Array Radar”, IET/SEE Conference on “Waveform Diversity and Digital Radar 2008”, (2008).
- [2] S.A.W. Moore. “Review of the State of the Art of UK AESA Technology and the Future Challenges Faced”, RadarCon08, (2008).

## **Acronyms**

ABF	Adaptive Beam-Forming
AESA	Active Electronically-Scanned Antenna
AMSAR	Airborne Multi-role Solid-state Active array Radar
CAESAR	CAPTOR AESA Radar
ARTIST	Advanced Radar Technology Integrated System Testbed
CAR	Core Antenna Radar
CECAR	Captor EsCAN Risk reduction
ECAR	Enhanced Core Antenna Radar
ECCM	Electronic Counter Counter Measures
E-scan	Electronically-Scanned radar
GaAs	Gallium Arsenide
GMTI	Ground Moving Target Indication
GMTE	Ground Moving Target Engagement
GTDAR	GEC Thomson DASA Airborne Radar
MFA	Multi-Function Aperture
MFR	Multi-Function Radar
MoD	Ministry of Defence
MTBCF	Mean Time Between Critical Failure
NFTR	Near Field Test Range
PAAMS	Principal Anti-Air Missile System
R&D	Research & Development
RRM	Radar Resource Management
RX	Receive
SAR	Synthetic Aperture Radar
SEA	Single Element Adjustment
STAP	Space Time Adaptive Processing
TDP	Technology Demonstrator Programme
TLCM	Through Life Capability Management
TRL	Technology Readiness Level
TRM	Transmit / Receive Module
TX	Transmit

# AMSAR - A EUROPEAN SUCCESS STORY IN AESA RADAR

Jean-Luc Milin  
DGA/DET/CELAR  
Bruz, France,  
jean-luc.milin@dga.defense.gouv.fr

Stephen Moore  
DSTL, Porton Down  
Salisbury, United Kingdom,  
samoore1@dstl.gov.uk

Wolfram Bürger  
FGAN/FHR,  
Wachtberg, Germany,  
buerger@fgan.de

Pierre-Yves Triboulloy  
Thalès Airborne Systems,  
Elancourt, France,  
pierre.triboulloy@fr.thalesgroup.com

Mike Royden  
SELEX,  
Edinburgh, United Kingdom,  
mike.royden@selex-sas.com

Joachim Gerster  
EADS,  
Ulm, Germany,  
joachim.gerster@eads.com

**Abstract— DGA, BWB and D&ES initiated a radar programme, called AMSAR (Airborne Multi-role Solid-state Active-array Radar) to demonstrate the enormous potential of Active Electronically Scanned Array (AESA) radar. This paper describes all the stages of the AMSAR project and the results obtained. The AMSAR demonstrator is still the only European, forward-looking multichannel active array radar with the capability of recording the outputs of more than 4 quadrants.**

**Keywords-AESA, Airborne Radar, Fighter, ABF, STAP**

## 1. INTRODUCTION: THE AMSAR PROJECT

DGA, BWB and D&ES initiated a radar programme, called AMSAR (Airborne Multi-role Solid-state Active array Radar) to demonstrate the enormous potential of Active Electronically Scanned Array (AESA) radar. AMSAR was designed and built in co-operation with Thales (France), SELEX (UK) and EADS (Germany). Throughout the program, industries results were assessed by CELAR, CEV, FGAN, WTD61, DSTL and QinetiQ.

The AMSAR programme started in 1993 between UK and France, with Germany joining in 1995. AMSAR's objective was a flying airborne AESA technology demonstrator with real time operation, including Adaptive Beam Forming (ABF) techniques. The target platform for the technology was a fast jet aircraft.

1. Uhlmann, M.; Tanner, J.S.; Albarel, G., "Design characteristics of the AMSAR airborne phased array antenna" *IEE Colloquium On Electronic Beam Steering - 98/481*, vol., no.pp.3/1-3/5, 28 Oct 1998

The first purpose was to mature E-scan technology and demonstrate all operationally significant attributes and functions of an AESA airborne radar system focusing on air-to-air performance, including Electronic Counter-Counter Measure (ECCM), but also on Ground Moving Target Indication (GMTI).

Work was contracted to GTDAR, a company owned by Thales (France), SELEX Sensors and Airborne Systems Ltd (UK) and EADS (Germany). GTDAR is under contract to the French Authorities, who act on behalf of the French, German and UK Ministries of Defence.

The AMSAR demonstrator is an X-band active electronically scanned adaptive radar with a circular 1000 element antenna. Each element is connected to a high-power low-noise transmit / receive module (TRM) mounted on a vertical plank to ease mechanical integration. Each TRM has a phase shifter with attenuation control that allows precise phase and amplitude control. Thus the demonstrator is capable of inertia-less electronic scanning out to wide angles. See Refs 1,2. Furthermore, the array architecture provides 8 digitised channels to support digital adaptive beamforming. Adaptation is possible across a large trade space, e.g. AMSAR can adapt transmit / receive pattern, waveforms, update rates, mode interleaving, etc.

2. Arnold, E. , "A radiating element for an active airborne antenna" *Antennas and Propagation Society International Symposium, 1999. IEEE* , vol.1, no.pp.134-137 vol.1, Aug 1999

Integration, adjustment and evaluation of the AESA Antenna were carried out between early 2005 and spring 2006 at EADS Defence Electronics in Ulm. In 2006 / 2007 the radar system was integrated in EADS Ulm and then intensively evaluated on the ground in France – both on the Bruz CELAR facility BEDYRA (hardware-in-the-loop test bench) against simulated targets and jammers, and also against real targets and jammers at the CEV flight test centre at Cazaux. The AMSAR system was then installed in the QinetiQ BAC 1-11 test bed aircraft. A total of 22 flights were subsequently performed in 2008 over land and sea in France, Germany and the UK. The radar performances for air-to-air and air-to-ground modes were assessed against real targets like Falcon 20, Tornado, Alpha jets and Ground Targets.

A huge amount of real data was collected at the outputs of the antenna sub-arrays in presence of not only real targets, but also real jamming signals. The data collected during ground and flight trials permitted the performance of numerous different Digital Beam Forming (DBF) techniques to be established, including:

- Adaptive Beam Forming (ABF) for sidelobe and mainlobe anti-jamming,
- Jammer mapping by means of super-resolution,
- Deterministic nulling using weighting at TRM level,
- Ground Moving Target Indication (GMTI) and air-to-air clutter rejection by Space Time Adaptive Processing (STAP),
- Simultaneous multiple beamforming on receive.

### 3. THE AMSAR ACTIVE ARRAY MULTICHANNEL ANTENNA

The well-known major advantages of an AESA with respect to a mechanical scanned array are:

- Rapid electronic inertia-less scanning,
- High average transmit power possible due to high efficiency of array architecture,
- E-scan array architecture with multiple receive channels facilitates a number of advanced modes,
- AESA can be adapted to number of other functions,
- AESA share a highly reliable radar design:

The principal architecture of the AMSAR antenna is shown in figure 1. The RF Interface (RF-IF) is the interface between Receiver / Exciter and the RF Manifold. In transmit it amplifies the Exciter signal to provide the required input power for each Transmit and Receive Module (TRM).

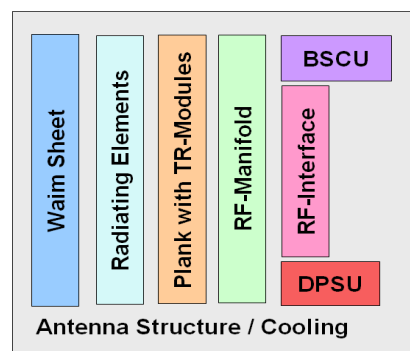


Figure 1. Block diagram of the AMSAR

In receive the RF Interface generates the Sum, DiffAz (difference pattern in azimuth) and DiffEl (difference pattern in elevation) channel from the Quadrant Subarrays.

The RF Manifold distributes the RF from / to the RF Interface to / from the TRMs. The TRMs (see figure 2) weight the signal in amplitude and phase to achieve the desired aperture distribution to produce the requested far field pattern.

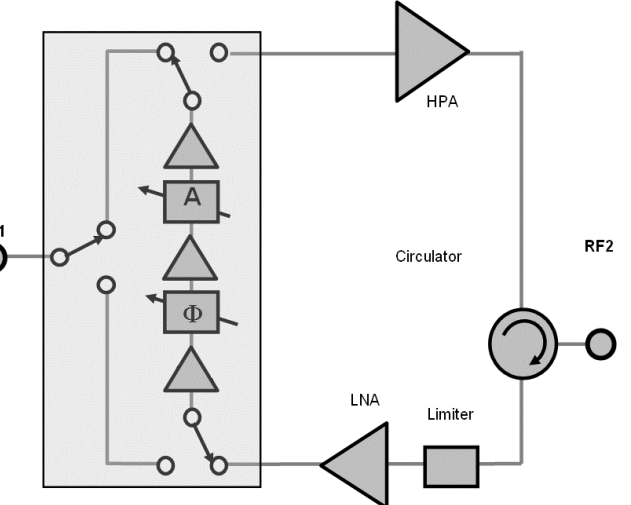


Figure 2. Block Diagram of an AMSAR TRM.

The radiating element and the WAIM (Wide Angle Impedance Matching) sheet ensure that the array can scan to wide angles with low reflections. The BSCU (Beam Steering Control Unit) and DPSU (Distributed Power Supply Unit) supply the TRMs with control and power. The antenna structure is responsible for mechanical positioning accuracy, stiffness and liquid cooling of the TRMs.

The sub-array architecture second level, consisting of a Side Lobe Blanking (SLB) guard channel, the 8 digitised sub-arrays and the monopulse four quadrants is shown on figure 3.

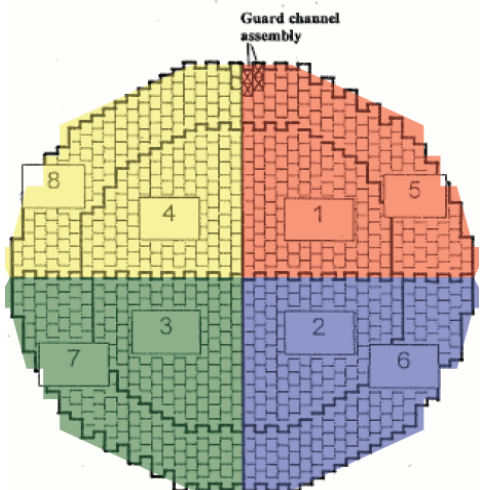


Figure 3. 8 Sub-array Architecture

Before evaluation, the antenna must be adjusted. Amplitude and phase are adjusted for each Radiating Element, to compensate for manufacturing tolerances of the sub-units (RF combiners, manifold, cables, etc.). In this single element adjustment process each radiating element is measured for some TRM states. The amplitude / phase deviations are corrected to get a uniform amplitude / phase distribution on the antenna aperture. Figure 4 shows the farfield pattern of the AESA without single element adjustment.

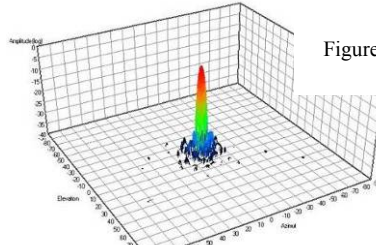


Figure 4. Farfield pattern before single element adjustment

Amplitude and phase deviations on individual elements result in high side lobes of the main beam. Fig 5 shows the improved farfield pattern after single element adjustment.

Figure 5. Farfield pattern after single element adjustment

After single element adjustment, the challenging performance requirements set at the beginning of the project were fulfilled - in particular, the average far sidelobe level.

During evaluation the cardinal pattern requirements of the antenna were measured in a Near Field Test Range (see figure 6) and a Far Field Test Range (see figure 7 and 8).

Measurements included directivity, beamwidth, peak side lobe level, average far sidelobe level and beam pointing accuracy. The liquid cooling system made it easy to study temperature effects.

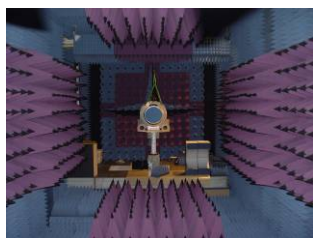


Figure 7. AMSAR antenna in the Far Field Test Range

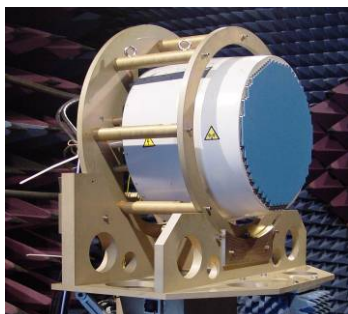


Figure 8. AMSAR antenna in the roll frame used on the Far Field Test Range

Figure 9 shows the Standard Rx Beam. (Red trace shows cross-polarisation rejection > 35 dB.

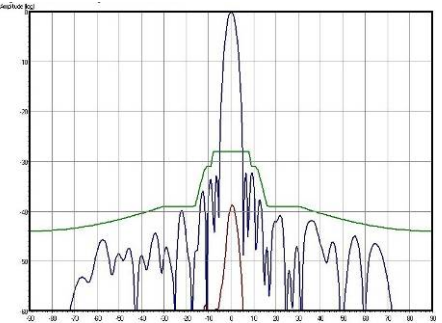


Figure 9. Standard Beam Rx

Figure 10 shows the standard beam scanned to 70°.

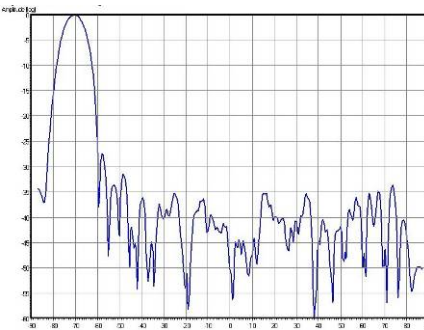


Figure 10. Standard Beam Rx @ 70°

Directivity is only 4dB less than the boresight pattern.

This validates the design of the radiating element and the WAIM sheet.

The far sidelobe levels of an AESA are determined by the residual random errors in amplitude and phase after adjustment.

A very low sidelobe beamshape (Hamming - 40dB) is shown in figure 11. Such low sidelobes are the result of a very accurate single element adjustment.

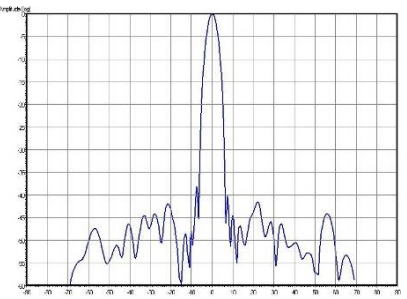


Figure 11. Hamming - 40dB Beam

SAR mode performance is shown in figure 12. This pattern was measured with the frequency offset 500 MHz from the frequency used for single element adjustment. There is only a slight increase of the sidelobes, showing that a broad SAR chirp is possible without losing the quality of the farfield pattern.

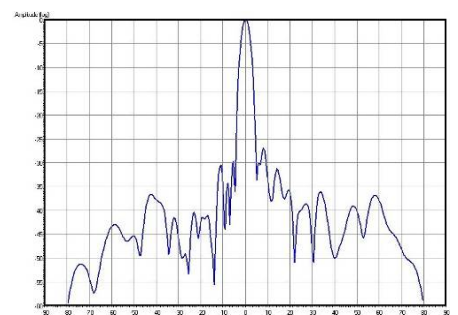


Figure 12. Standard Beam @ f + 500MHz

Finally, the AMSAR antenna was measured in free space, with and without a fighter radome.

#### 4. THE AMSAR SYSTEM

Figure 13 shows the AMSAR radar system block diagram.

An exciter generates the signal to be transmitted to the RF-IF in the antenna. The output of the 4 conventional

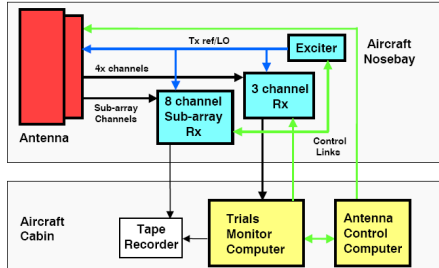


Figure 13. The AMSAR radar system block

channels: sum, DiffAz, DiffEl and guard channel for SLB, formed in the antenna RF-IF, are connected to the 3 channel receiver (DiffAz and Guard channel are multiplexed). This 3 conventional channel receiver performs real time signal digitisation. The outputs of the 8 sub-arrays are also digitised in real time, by routing the 8 outputs from the antenna RF-IF to an 8 channel Sub-Array receiver.

The Antenna Assembly was designed to be installed in the nosebay of the QinetiQ BAC 1-11. It is supported by a heat exchanger mounted in the forward cargo bay, and a primary power supply in the cabin. Also in the cabin is:

- The Antenna Control Computer, for command and control of the antenna.
- A digital recorder which captures signals on the radar bus and the high bandwidth signals from the two receivers (12 channels total, capacity 3 TB)
- The Trials Monitor Computer which comprises Engineering Display, Signal Processor, Data Processor and Radar Display. The Engineering Display provides system control and the HMI. The Signal Processor uses data from the 3-channel receiver to provide classical radar processing for target detection, and the Data Processor is responsible for computation of range, velocity and bearing, as well as track formation. Finally, the Radar Display shows the antenna beampointing, target range, velocity and tracks.

The AMSAR radar system is able to detect and track multiple targets simultaneously, using these air-to-air modes:

##### Velocity search only

- SO1 (HPRF detection and confirmation)  
SO2 (HPRF detection and MPRF confirmation).

##### Search and Track

- ST1 (HPRF search, MPRF track),  
ST2 (MPRF search and track)  
ST3 (ST1 and ST2 interleaved).

#### 5. THE CEV FLIGHT TEST CENTRE CAMPAIGN

After its integration and acceptance in EADS Ulm Germany, the AMSAR system went to Centre d'Essais en Vol (CEV) flight test centre in Cazaux near Bordeaux in France. Fitted on a ground trolley (see figure 14), the system was exercised with combinations of real targets such as Falcon 20, Hunter, Mirage 2000 and Alpha Jet (see figure 15). Some runs were recorded with the Falcon 20 and/or the Hunter emitting jamming signals in presence of a target. Different configurations were tested with sidelobe jamming, mainlobe jamming, or both. This campaign was mainly dedicated to radar parameter adjustment and data recording with real targets and jammers.



Figure 14. The AMSAR radar system during ground trials in Cazaux



Figure 15. The AMSAR radar system during ground trials in Cazaux facing different targets

#### 6. THE BEDYRA TEST CAMPAIGN

After the CEV test campaign, the AMSAR demonstrator moved to CELAR in Bruz near Rennes in France for intensive characterisation of the system. This used the hardware-in-the-loop dynamic test bed BEDYRA (Banc d'Evaluation DYnamique pour Radars et Autodirecteurs électromagnétiques). BEDYRA is a French MoD facility dedicated to evaluation of real radars and missile seekers.

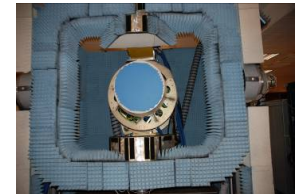


Figure 16. The AMSAR radar system on the 3-axis table of BEDYRA CELAR

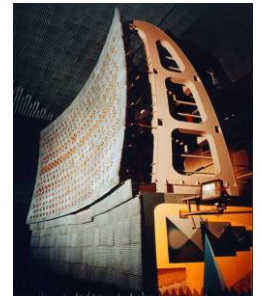


Figure 17. BEDYRA horn wall

The material under test is mounted on a 3 axis table (see figure 16), facing a wall of horns which reproduce an RF environment which simulates different types of targets and jammers, including real ones plugged into a horn. (see figure 17). The BEDYRA Campaign was mainly used to finalise radar parameter adjustment and assess the radar performances in terms of detection range and track formation range against various targets. It was also used to perform scenarios impossible in flight such as crossing targets. A huge amount of data was recorded with multiple targets, mainlobe jamming, sidelobe jamming, both simultaneously, false targets, etc.

- but without any clutter...

## 7. THE FLIGHT TRIALS TEST CAMPAIGN

Flight trials are needed to assess the radar performance in a real environment and to record data with sea or ground clutter. The AMSAR radar system was consequently installed on the QinetiQ BAC 1-11 aircraft (see figure 18).



Figure 18. QinetiQ BAC 1-11

A total of 22 flights have been performed. The first ones, over UK, from Boscombe test centre, were mostly dedicated to radar adjustment in the BAC 1-11 environment followed by air-to-air mode performance assessment. Multiple targets were detected and tracked at the expected ranges.

The next flights, over Germany, from the Manching WTD 61 test centre, were dedicated to air-to-ground modes using a STAP / GMTI waveform. The outputs of the 8 sub-arrays were recorded for further offline signal processing on a ground moving target equipped with GPS and reflectors (see figure 19) was driving in circles.

Finally, the last flights were over French ground and sea clutter, from Cazaux CEV. Dedicated mostly to ABF and air-to-air STAP, the AMSAR system faced high ground clutter (with the target going through the clutter notch); or up to two simultaneous jammers trying to mask an Alpha jet.

The outputs of the 8 sub-arrays were again recorded in various configurations including multiple sidelobe jamming, mainlobe jamming and simultaneous sidelobe and mainlobe jamming with real clutter and real masked target. The hundreds of Terabits of data recorded have then been analysed using different types of multichannel antenna processing.



Figure 19. Ground moving target for GE flights

## 8. THE COLLECTED DATA ANALYSIS

The AMSAR program proved the feasibility of an airborne AESA radar, and showed that all the benefits of such a system were achievable in real time. In addition, the AMSAR program aimed to support the evaluation of multichannel antenna processing techniques. All the data recorded during trials has been used for this purpose. Among the techniques evaluated were:

- Jammer mapping using angular super-resolution,
- Non-adaptive Jammer Rejection using spatial processing applied to the total degrees of freedom of the antenna by means of deterministic nulling,

- Adaptive Jammer Rejection by spatial Adaptive Beam Forming using the 8 sub-array channels,
- Probability of Detection improvement for Air-to-Air mode by means of ground clutter rejection using STAP,
- Minimum Detectable Velocity improvement for Air-to-Ground modes by means of STAP GMTI,
- Rapid reacquisition of lost under-track targets by means of simultaneous multiple Beam Forming on Receive and a broadened Transmission.

### 1) Digital sum channel construction

The first challenge was to prove that it was possible to accurately calibrate the 8 subarrays, i.e. compensate for differences in phase and amplitude between the 8 channels, to reconstruct a sum beam. AMSAR achieved this to the extent that the sum beam reconstructed off line using the 8 subarray outputs was even better than the conventional sum beam. The holes between adjacent sidelobes in the reconstructed sum beam were deeper than in the conventional one, proving that the aperture illumination was closer to the ideal.

### 2) Digital Adaptive Beamforming

The aim of digital adaptive beamforming is to:

- Form nulls (i.e. points of zero return) in jamming direction,
- Cancel multiple jammers (numbers dependent on degrees of freedom),
- Adapt the antenna pattern to the environment in real-time.

Different ABF Algorithms under different constraints were tested on real data recorded during the trials. With ground trials data recorded in BEDYRA it proved possible to reject the jammer down to the noise power level floor in all cases.

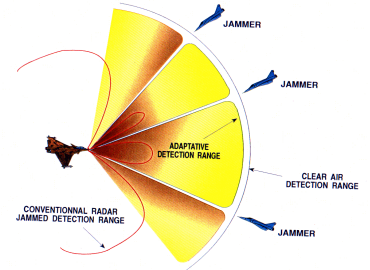


Figure 20. ABF for anti-jamming

The target masked by the jamming signal was always detected after ABF processing. Adapted radiating patterns were plotted and the degradation caused by countering sidelobe jamming was so small that having ABF on, even when no jamming is present, would not be unreasonable. For mainlobe jamming, the angular limit of acceptable adapted pattern degradation was established. Up to this limit the masked target was always detected after ABF processing. Results obtained were in line with textbook predictions.

With data recorded on flight trials, results obtained were nearly as good as during ground trials. In this case, the influence of clutter prevented jammer rejection from reaching the noise floor.

### 3) Space-Time Adaptive Processing for air-to-air modes

The aim of STAP for air-to-air modes is an improvement in probability of detection by means of Ground Clutter rejection. Figure 21 shows the influence of the antenna beam pattern on the range/Doppler map.

Clutter intercepted by the main beam prevents detection of targets flying with the same velocity as the aircraft. Furthermore, sidelobes of the antenna also create a «cactus» that degrades the target detection in range and velocities close to the main beam region.

As presented on figure 22, STAP counters this effect and the result is a range Doppler map with virtually no cactus and with a main beam clutter area that spreads much less in velocity. The actual performance of STAP processing was assessed using data collected during special flight trials from Cazaux. These trials used a lookdown configuration, with high clutter and a target going through the clutter notch. Good results were obtained, proving the practical benefit of STAP.

### 4) GMTI: Space-Time Adaptive processing for air-to-ground modes

The aim of STAP here is to ensure the detection of slow moving ground targets. What is expected is a reduction in the Minimum Detection Velocity (MDV) for various scan angles. Ground clutter filtering by STAP permits detection of targets that were masked by the clutter without any adaptive processing, as shown on Figure 23. The resulting detection can be superposed on SAR maps as shown on Figure 24. To assess the performance of STAP in this application, data was collected using lookdown configuration during dedicated flight trials from Manching with a GPS equipped, ground-moving target. Results were very good proving that slow moving targets can be detected in real environment. The specified MDV was surpassed.

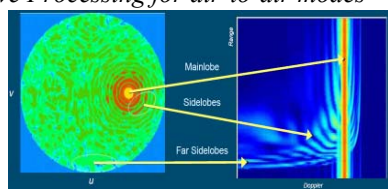


Figure 21. Antenna radiating pattern influence on the Range-Doppler map

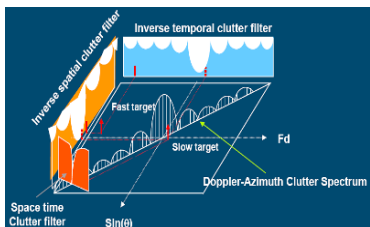


Figure 22. The STAP ground clutter-filtering concept

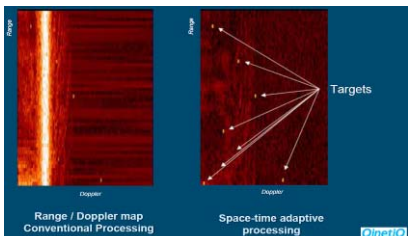


Figure 23. The STAP ground clutter-filtering result on slow ground moving targets

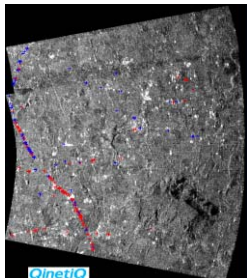


Figure 24. GMTI detection on a SAR map

### 5) Jammer mapping

Data collected in flight and in BEDYRA with crossing jammers have been used to assess the capability of AMSAR to perform jammer mapping. Jammer mapping uses data from a total scan of the entire space surrounding the radar. In regions where signals are high, spectral processing is applied for super-resolution. Although the real limit of the angular separation of 2 close jammers has not been assessed, results obtained were better than expected and show that such a mode is very promising.

### 6) Deterministic nulling

When the position of the jammer is known with precision *a priori*, for example using jammer mapping, one can in theory form a null in the jammer direction using the total degrees of freedom of the antenna - i.e. the number of TRMs. This technique is known as deterministic nulling. This non-adaptive concept can be used on antennas that are not equipped with ABF. Radiating patterns with deterministic nulling were recorded in the BEDYRA anechoic chamber proving the feasibility of this concept.

### 7) Simultaneous multiple Beams Forming on receive.

Even for an AESA radar, losing a target under track usually means spending time going back into search mode for reacquisition and confirmation. To avoid these time losses, it is possible to form, on receive, multiple beams around the latest known target position. The beam giving the detection indicates where the target has gone. Reinitializing the Kalman filters with this value avoids having to go back to search mode. AMSAR was evaluated in the BEDYRA anechoic chamber, forming two simultaneous Receive beams in azimuth, and a broadened Transmit beam. The expected performances were reached.

## 9. CONCLUSION: THE FUTURE OF AMSAR

The technological progress made on AESA architecture and Transmit and Receive Modules (TRMs) in the early years of the AMSAR program permitted the companies involved to confidently invest in a number of operational products. Two of these products are the RBE2AA (Radar à Balayage Electronique 2 plans à Antenne Active) for the Rafale fighter and Captor-E for the Eurofighter. Furthermore, this program allowed the testing of a large family of multichannel antenna processing techniques. Their performances now being known in a real environment, they will be soon implemented in operational modes. The data recorded during these trials has created a large library of data covering a diverse set of scenarios that can be used for algorithm development for many years. Finally, by a combination of antenna testing in BEDYRA and antenna simulation the ‘graceful degradation’ assumption has been confirmed by showing minimal effect on performance even with a random selection of 10% of TRMs inhibited.

At the time of writing, the AMSAR demonstrator is still the only European, forward-looking multichannel active array radar with the capability of recording the outputs of more than 4 quadrants in flight.



# Active Phased Array Antenna Development for Modern Shipboard Radar Systems

Ashok K. Agrawal, Bruce A. Kopp, Mark H. Luesse, and Kenneth W. O'Haver

**C**urrent and future Navy radar requirements are driven by rapidly evolving threats, including both cruise missiles and tactical ballistic missiles. To address these threats, array antennas will have to operate over wider bandwidths with enhanced sensitivity, higher radiated power levels, improved stability, and improved electronic protection to address reduced target radar cross-sections. In addition, there is a growing need for reduced array signatures and a practical need to control costs, including acquisition, operational, and support costs. Active phased array antennas have emerged as a fundamental technology for addressing these evolving Navy radar system needs. APL's Air Defense Systems Department has long been at the forefront of phased array antenna development for shipboard radar systems, and the Department is contributing to the development of active array antennas for the new generation of Navy radar systems currently under development. This article provides an overview of the emerging active array antenna technology.

## INTRODUCTION

Shipboard radar systems typically must provide surveillance of thousands of angular locations and track hundreds of targets and guided missiles, all within relatively short reaction times. These requirements can be met only with phased array antennas that allow electronic repositioning of radar beams to widely diverse angular locations within microseconds. Over a 40-year span, APL's Air Defense Systems Department has participated in the development of phased array antennas for Navy radar systems.<sup>1</sup>

In addition to enhanced sensitivity, improved system stability will be required to detect low-flying cruise missiles in sea or land clutter. Wider bandwidths will be

required to perform discrimination and target identification functions. At the same time that radar demands are increasing, there is a practical need to reduce acquisition and operation and support (O&S) costs, improve reliability, and reduce manning requirements. Active phased array antennas are emerging as a fundamental technology for addressing this evolving Navy radar system need, and APL's Air Defense Systems Department is playing a major role in these development efforts.

Although the concepts of phased array antennas are fairly straightforward, the factors that determine the design are extensive and even somewhat complex.

Design factors such as aperture sizing, pattern synthesis, and beamswitching speeds have changed little. On the other hand, solid-state component technology development has exploded over the last decade, exhibiting a continuing and significant impact on the design and performance of phased array antennas. The heart of an active phased array antenna is the transmit/receive (T/R) module. A T/R module at each radiating element provides power amplification during transmit and low-noise amplification during receive, as well as phase shift control for beamsteering. The emergence of gallium arsenide (GaAs) monolithic microwave integrated circuit (MMIC) technology has enabled the development of T/R modules with the required performance, excellent reliability, and acceptable cost in quantity production.

An active phased array radar can provide orders of magnitude performance improvement over its predecessor passive phased array radar, while at the same time improving reliability and reducing total ownership costs. Virtually all high-performance radars under development today employ an active array antenna. Navy radar development programs for which active phased arrays are a key enabling technology include the AN/SPY-3 multi-function radar, volume search radar for long-range surveillance, and advanced radars for Navy Theater Wide Ballistic Missile Defense. Other active array radars include the Theater High-Altitude Area Defense, National Missile Defense, and High Power Discriminator radars and the F-22 and Joint Strike Fighter fire control radars. Active array technologies have been used in commercial communications applications, including Iridium and Globalstar systems; however, these systems have not so far proven to be economically viable.

## ACTIVE PHASED ARRAY ANTENNA OVERVIEW

To fully appreciate what active array technology has to offer, it is useful to first review the conventional, or passive, array approach currently deployed in several fielded

military radar systems. A radio-frequency (RF) block diagram of a typical passive phased array antenna is shown in Fig. 1a. A centralized transmitter, which generally consists of high-power microwave tubes (e.g., traveling wave tubes) or cross-field amplifiers, provides the power to the radiating elements through a high-power beamformer network. High-power ferrite or diode phase shifters are controlled at each radiating element to electronically steer the beam to the desired angle. In receive mode, the outputs of the radiating elements and phase shifters are combined using a low-power beamforming network. Typically, three simultaneous receive beams are provided to support monopulse tracking. Low-noise amplifiers (LNAs) are used to amplify the signal at the output of the beamformers. One of the

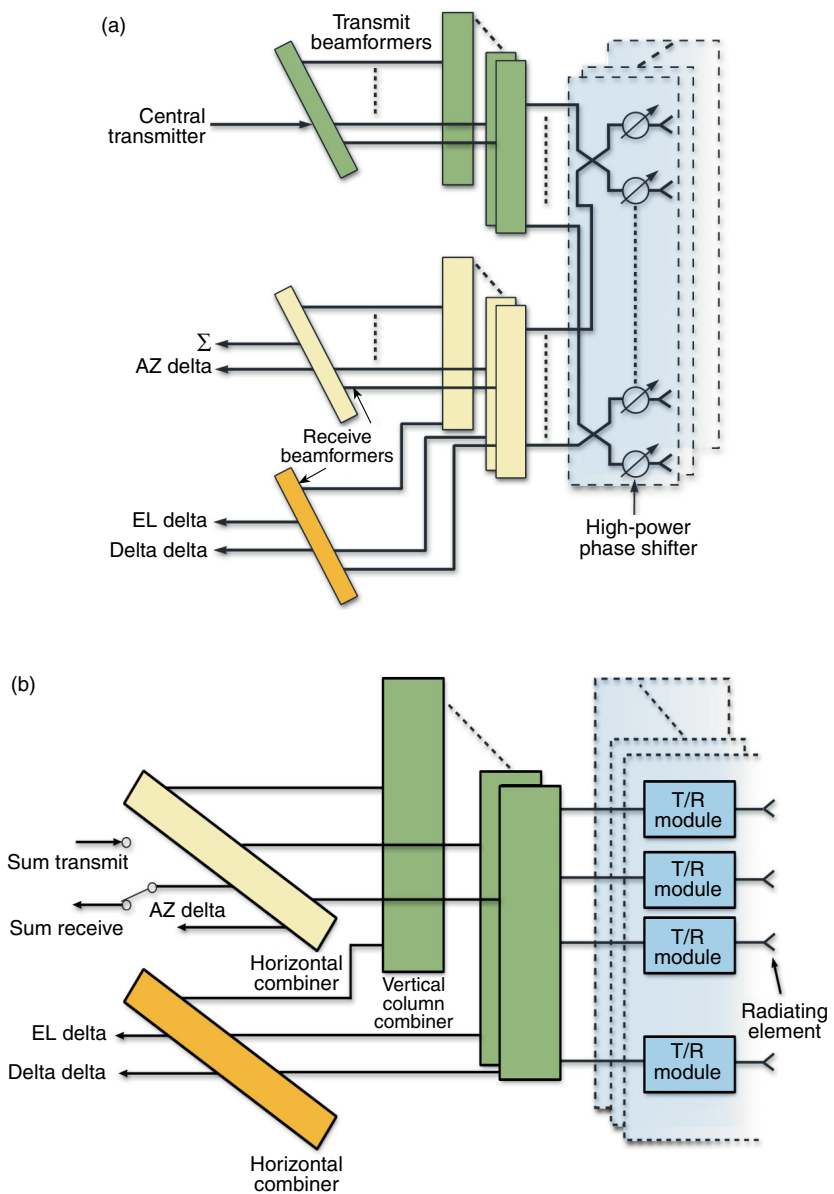


**Figure 1.** (a) RF block diagram of a passive phased array antenna. (b) Beamformer architecture of an active phased array antenna.

best examples of passive phased array radars is the AN/SPY-1 radar (Fig. 2), which has been in service for more than 20 years and is the Navy's highest-performing fielded radar.

Passive array systems have several inherent performance limitations and inefficiencies. For example, the transmit beamformer typically has significant losses, and the transmitter must generate a large amount of power to overcome these losses. In essence, a significant portion of the RF power generated by the transmitter is dissipated as heat before being radiated. High-power centralized transmitters usually employ microwave tube-based technologies, operate at lower duty factors, and have limited waveform flexibility. High receive beamformer losses, particularly when low sidelobes are required, significantly degrade receive sensitivity. Also, transmit noise from a centralized source is often a limitation in clutter-driven radar applications. Finally, high-power tube-based transmitters and their attendant high-voltage power supplies have lower reliability and higher maintenance and replacement costs than solid-state technology. This last issue is particularly important for shipboard applications that involve relatively long missions and a strong desire to avoid at-sea maintenance.

Evolving threats are driving the need for order-of-magnitude improvements in radar performance. Active array technology offers the capability of achieving the required performance improvements while at the same time offering improvements in reliability, maintainability, availability, and life-cycle costs. In active arrays, both transmit and receive functions are moved to the aperture by placing a T/R module at each radiating element (Fig. 1b). The T/R modules provide power amplification during transmit and low-noise amplification during receive, as well as amplitude and phase control for beamsteering and sidelobe reduction. Because this configuration places the power amplifiers and LNAs at the aperture, transmit and receive losses are significantly

reduced, resulting in increased radar sensitivity for a given amount of generated microwave power.

Key radar system-level advantages of active phased arrays over passive phased arrays are summarized as follows:

- **Increased sensitivity.** Lower transmit and receive beamformer losses, coupled with the ability of solid-state T/R modules to operate at higher duty cycles than conventional tube-based transmitters, generally enables order-of-magnitude improvements in radar sensitivity.
- **Improved target detection in clutter.** In an active array, key sources of transmit noise and instabilities (e.g., T/R modules and power supplies) are distributed at the aperture. Consequently, their noise contributions do not add coherently in the same fashion as the transmitted signal, and their contributions to pulse-pulse variations undergo an averaging effect. The result is a significant improvement in the ability of an active array radar to detect small moving targets in sea or land clutter.
- **Improved waveform and pattern flexibility.** The multiple functions of detection, tracking, target identification, illumination, kill assessment, and missile communications can be better optimized by the waveform flexibility that the solid-state active array technology facilitates. Also, because both amplitude and phase control are provided by the T/R modules at the element level, radiation patterns are more readily optimized for the radar mode of operation, including the use of null synthesis techniques.
- **Improved wideband operation.** The solid-state technology employed by active arrays can support inherently wideband microwave frequency operation. In addition, active array architectures are conducive to the implementation of practical true time delay devices, which support wide-bandwidth, high range resolution waveforms and target imaging capability.
- **Reliable operation.** Solid-state technology and the associated low-voltage power supplies have inherently good reliability. In addition, the distributed nature of the T/R modules and power supplies allows the array to be designed so that operational performance requirements can be met when a few percent of the modules fail. Active arrays can be designed to be serviced at long periodic intervals, avoiding the need for at-sea maintenance. The increased reliability of active arrays is projected to result in significantly lower O&S costs over the lifetime of the array.



**Figure 2.** SPY-1/D phased array antenna on DDG 51.

## ACTIVE PHASED ARRAY SUBSYSTEMS

The following key parameters are typically specified for an active array:

- Operating frequency and bandwidth
- Effective isotropic radiated power
- Scan coverage
- Beamwidths
- Sidelobe levels (all monopulse receive channels)
- Tracking accuracy
- Waveform parameters (duty, pulse width)
- System noise figure
- Third-order intercept
- Stability and phase noise
- Harmonic and spurious output
- Reliability, maintainability, and availability
- Manufacturing and life-cycle costs
- Prime power requirements and cooling
- Shipboard environmental requirements

The operating frequency, waveform parameters, and array performance requirements will vary depending on the particular applications served by the radar. The effective isotropic radiated power and beamwidth determine the number of elements and the required T/R module output power. The sidelobe levels determine the amplitude and phase characteristics of the T/R modules, aperture, and transmit and receive beamformers. The phase noise, stability, reliability, and maintainability requirements all influence the array architecture as well as the characteristics of the T/R modules and power supplies. The antenna cost and weight dictate the selection of technologies for different components

and, in conjunction with the environmental requirements, the array structure. The antenna cost, weight, and performance typically form a critical design trade space.

A block diagram of an active phased array radar system is shown in Fig. 3. An active phased array consists of a transmit and receive antenna aperture that includes the radiating elements, radome, and structure; T/R modules and associated control circuitry; RF beamformers; DC power distribution; and a beamsteering controller. Key features and fundamental design trades of these active array subsystems are addressed in the following paragraphs.

### Transmit/Receive Modules

The fundamental building block and key enabling technology for active array radar antennas is the T/R module. Depending on the application, active arrays can contain hundreds or, more typically, thousands of T/R modules. These T/R modules have an important role in determining array performance; they drive many aspects of the packaging design and can account for as much as 50% of the cost of the active array antenna. GaAs MMIC technology is key to realizing the required microwave circuit density in the small footprint available at each antenna element. Semiconductor batch-processing production of GaAs MMICs is key to achieving the active array performance advantages at desired

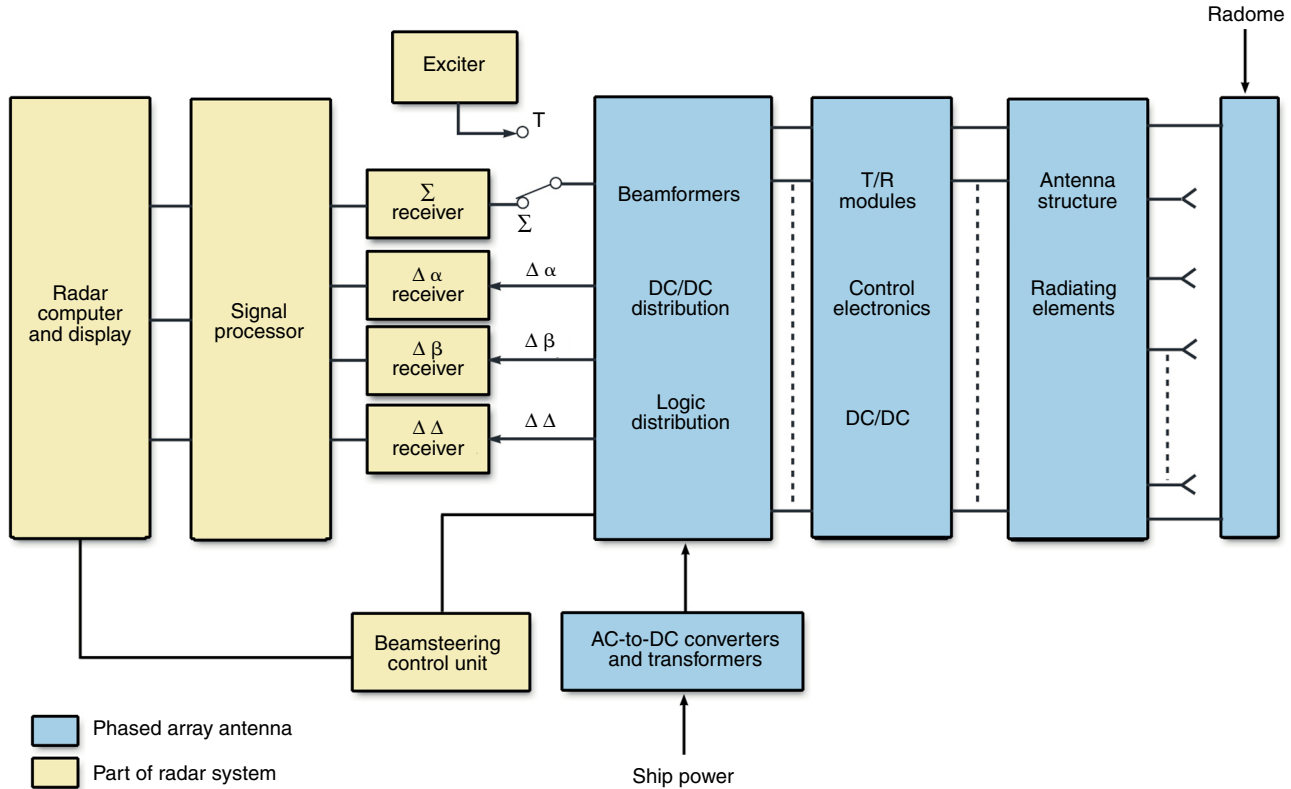


Figure 3. Block diagram of an active phased array radar system.

array acquisition costs. A typical T/R module is shown in Fig. 4.<sup>2</sup>

Figure 5 shows a block diagram of a typical T/R module. Each module contains a transmit path and a receive path. The transmit path consists of a phase shifter, a variable gain amplifier or attenuator (VGA), a driver amplifier, and a power amplifier. The power amplifier section may consist of several power amplifiers, typically two or four, where the output power of these amplifiers is combined to obtain the required output power for the radiating element. A circulator is used to provide the duplexing function and isolation between transmit and receive paths and to prevent load pulling of the power amplifier caused by variations in the antenna element's input impedance changes during beamscanning.<sup>3</sup> The receive path consists of a limiter, an LNA, a phase shifter, and a variable amplifier or attenuator. This module architecture provides an optimum performance compromise with respect to module noise figure, third-order intercept, and dynamic range.<sup>4</sup>

Voltage regulation and digital control circuitry are also often included in the T/R module. Local energy storage can be used to maintain transmit pulse current levels and satisfy rise-time requirements. Also, series regulators can be used for some or all internal voltages to reduce power supply ripple and noise to acceptable

levels to meet increasingly severe spectral purity requirements.<sup>5</sup> Low-resistance HEXFET switches are typically used to control the bias currents to the various amplifiers. Digital signals to control the phase shifter and attenuator are typically fed serially into the T/R module to reduce packaging complexity. This serial data stream is converted to parallel data with a shift register and clock signal. Memory may also be contained in the module to reduce the time required to switch between predetermined beam positions.

T/R module requirements are derived from the phased array antenna requirements and can vary significantly depending on the application. The following key parameters are typically specified for a T/R module:

- Operating frequency and bandwidth
- Output power
- Power-added efficiency
- Spurious and harmonic output
- Duty cycle and pulse characteristics
- Receive noise figure
- Receive gain and third-order intercept
- Number of amplitude and phase bits
- Amplitude and phase root-mean-square (rms) errors
- Mean time between failure (MTBF)
- Cost

The frequency, bandwidth, and output power are driven by the system application. A typical nominal output power for an X-band module, achievable with commercially available power MMICs, is around 10 W. Higher power levels are typical at lower frequencies. Power-added efficiency is an important parameter for minimizing the prime power requirements and cooling load of the active array. Depending on the technology used, transmit-power-added efficiencies on the order of 20 to 25% are typically achieved. LNA MMIC noise figures in the microwave regime typically range from 1 to 2 dB. Including losses and other effects, module noise figures in the 3- to 4-dB range are generally achievable. Modules used in low sidelobe applications require a higher number of phase control bits and lower amplitude and phase rms errors. Third-order intercept is an important parameter in mitigating interference from surface Navy radars where the radars, and thus the modules, are often operating in the vicinity of high-power radars on nearby ships. Because of the relatively long operating missions of surface Navy radars, module reliability is a critical factor in achieving low O&S costs and minimal maintenance actions. A T/R module should typically have an MTBF in the hundreds of thousands of hours.

Because of the large number of T/R modules in an active array, module production costs are critical to active array affordability. Module production costs can vary depending on performance, design complexity, production quantities, and other factors. Although

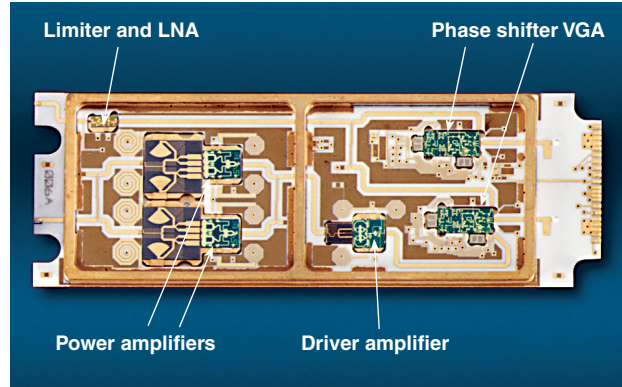


**Figure 4.** Photograph of a typical T/R module.

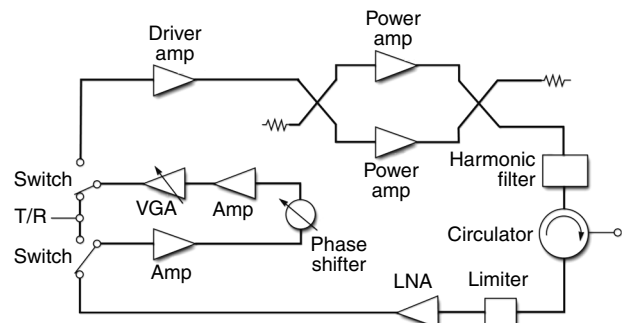


**Figure 5.** Block diagram of a typical T/R module.

the module cost breakdown can vary depending on the application, the typical cost breakdown of an X-band module (Table 1) is representative of current state-of-the-art X-band T/R modules. The cost of a T/R module consists of the cost of the semiconductors (MMICs), packaging, other components, assembly, and test. The MMICs are typically the most significant cost element. A more detailed T/R module cost discussion is provided in Refs. 6 and 7. The MMIC cost will increase with higher module output power.

Semiconductor cost is determined by wafer processing cost, wafer diameter, MMIC area, and yield. The wafer processing cost for GaAs is highly dependent on the volume of wafers produced by a foundry. Foundries typically can produce more than 20,000 wafers per year. However, production rates of at least 10,000 wafers per year are desirable to maintain low foundry overhead costs. Typical X-band T/R module production rates do not require a sufficient number of wafers to provide high foundry loading. One 4-in. wafer has enough area to supply the GaAs needed for more than 50 typical X-band modules. The production of 100,000 X-band modules per year would thus require less than 2000 4-in. wafers per year or less than 1000 6-in. wafers per year. Commercial volume using similar personnel and facilities is required to provide the low-overhead structure for cost-effective production of X-band T/R modules. Some GaAs producers have successfully achieved this product mix through high-volume sales to support wireless handset products.

### Radiating Elements and Antenna Aperture

The critical design task for the radiating element is designing one that radiates efficiently, with good impedance match, over the operating frequency band and the scan volume of the array. Cost is a significant consideration because of the large number of radiating elements typically present. Because the performance of a radiating element is affected by mutual coupling with other radiating elements, the radiating element must be designed for the radiating environment rather than as an isolated element. The design process is usually iterative and consists of simulation using numerical electromagnetic modeling tools, fabrication of a waveguide simulator to verify performance at a selected scan angle,

and fabrication of a small test array (generally consisting of up to 100 elements) to verify full performance. A well-designed element will provide an element pattern on the order of  $\cos^{1.25}\theta_s$  over the intended scan volume, where  $\theta_s$  is the scan angle from array broadside.

The list of the different kinds of elements that have been used in array systems includes dipoles, microstrip patches, microstrip and waveguide slots, waveguides, horns, and flared notches (Fig. 6).<sup>8</sup> The choice of element depends on several factors, such as power handling, polarization, bandwidth, environmental conditions, feeding arrangement, and manufacturing cost.

Dipoles and patches generally have narrow bandwidth. The element bandwidth is defined in terms of loss in gain with respect to the center frequency. A flared notch element<sup>9</sup> (Figs. 6a and 6b), where an open circuited orthogonal central conductor excites the notches in the outer conductors, is typically used for wideband arrays. Bandwidths up to 6:1 have been demonstrated.<sup>10</sup> For a microstrip slot antenna, a cavity must be used behind each slot to restrict radiation to the front hemisphere. A microstrip slot radiator is shown in Figs. 6c and 6d.

For high-power radar arrays, variants of the rectangular or cylindrical waveguide radiating elements (Fig. 6e) are generally used. Waveguide arrays, though heavy, tend to have low loss and graceful scan degradation. Ridged waveguides can be used for wide-bandwidth applications. Single, double, and quad-ridged waveguides are shown in Fig. 6e. Quad-ridged waveguides extend these features to circularly polarized phased arrays. Often, the waveguide element is dielectrically loaded to match its impedance to free space. A wide-angle impedance matching (WAIM) sheet can be used to produce susceptance variation with the scan angle that partially cancels the array scan mismatch. WAIM sheets are less practical for shipboard environments because ice formation at the aperture is not permitted, and some kind of heating arrangement is required. For example, in the SPY-1 antenna, ice is inhibited by placing alumina windows on the individual waveguide radiators and heating these windows through conduction heating.

Microstrip patch elements (Fig. 6f) can be fabricated with low-cost lithographic techniques. The two most common feed techniques are an in-line microstrip feed and a coaxial probe feed. Patch elements are narrowband. For electromagnetically coupled patches in a phased array, the bandwidth can be increased to more than 15% by choosing patch dimensions, substrate thickness, and dielectric materials. Using double-stacked patches, essentially providing a double-tuned element, can increase the bandwidth further.

### Radio-Frequency Beamformer Architectures

The RF beamformer plays a critical role in determining the radiation patterns, particularly the sidelobe

**Table 1. Typical T/R module cost breakdown.**

Cost element	Percentage of T/R module cost
MMICs	45%
Package/substrates	25%
Digital/analog circuitry	15%
Assembly	10%
Test	5%

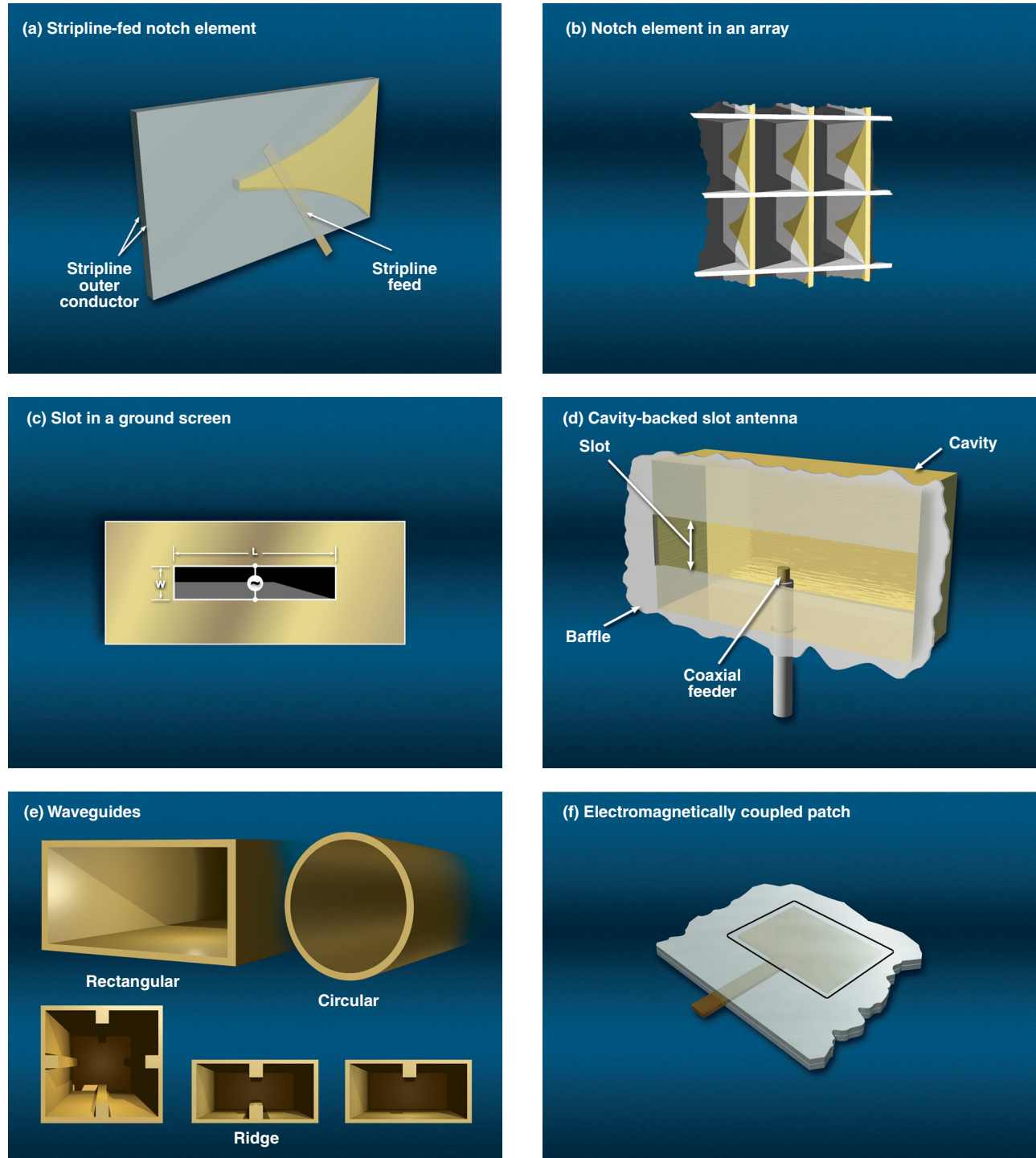


Figure 6. Radiating elements for phased-array antennas.

levels, of an array radar. On transmit, the RF beamformer distributes the input signals to the individual T/R modules. Typically, this is done so that each T/R module receives an identical input power level. Equal amplification in each T/R module then produces a uniform transmit aperture distribution that maximizes the transmit antenna gain.

In the receive mode, amplitude tapering across the aperture is typically applied to reduce the receive

sidelobe levels. Active array radars generally require low receive sidelobes to minimize susceptibility to jamming. The amplitude and phase error levels that can be maintained at the aperture determine the achievable sidelobes. The primary sources of error include the T/R modules and the RF beamformers. Phase shift control in the T/R module provides a mechanism for calibrating the module and beamformer phase errors. To obtain low residual and quantization phase errors to

support low sidelobe performance, as many as 7 bits are used in the digital phase shifter MMIC within the T/R module.

Passive array radars have similar requirements for low sidelobes. The amplitude control can be applied only in the receive beamformers in passive arrays, while the amplitude taper can be applied either in the beamformers or in the T/R modules in active arrays, as described next.

To obtain sufficient tracking accuracy, radars typically employ monopulse tracking techniques that require separate receive channels, or RF beamformer arrangements, for the receive sum, delta azimuth, delta elevation, and delta-delta channels. Each channel has an optimum amplitude distribution for low sidelobe performance. Also, because the channels are employed simultaneously, a single phase shifter in the T/R module cannot simultaneously correct phase errors in all monopulse channels, and often some compromise is made in the difference channel sidelobes relative to the sum channel sidelobes. There are many trade-offs in developing beamformer architectures for active array radars. Two common examples are discussed in the following paragraphs.

Figure 1b shows a simplified beamformer architecture of a monopulse active phased array antenna. In the receive mode, the radiating elements' outputs are first combined using column beamformers. The outputs of the column beamformers are then combined using horizontal beamformers to form the sum, azimuth delta, elevation delta, and delta-delta beams. The receive aperture weighting is applied in the T/R modules by using the attenuators or variable-gain amplifiers. Because the receive amplitude weighting is applied in the T/R modules, the transmit sum and receive sum beamformers have uniform distribution and are shared for the transmit and receive functions. The order of column and row combining can be interchanged.

The amplitude taper for an active array can also be applied in the beamformers rather than in the T/R modules, as shown in Fig. 7. Because transmit and receive amplitude tapers are different for this architecture, separate beamformers are required for the sum receive and transmit beams. Although the array with separate transmit and receive beamformers is more complex, it has a slightly lower receive noise figure. A lower antenna noise figure

is desired if the radar is to detect small returns. These two architectures have been analyzed,<sup>11</sup> and the results show that for a large active phased array antenna, the difference in the noise figure for the two is approximately 0.5 dB. The choice of common or separate beamformers is a function of beamformer complexity and antenna noise figure.

## DC Power Distribution

Below-deck AC-to-DC converters convert a ship's AC power into DC power that is supplied to the arrays. The voltage into an active array typically ranges from 200 to 500 VDC and, as such, is stepped down to voltage levels required by the T/R modules (around 10 VDC or less) by DC-to-DC converters. The requirements for a DC-to-DC converter include voltage and current requirements of the T/R modules, output voltage droop and ripple, random noise, efficiency, dynamic step response, and enough input and output energy storage capacitors that the maximum droop due to load change during the longest transmit period meets requirements.

DC power can be distributed in an array using either a distributed or a centralized system. In a distributed system, a single DC-to-DC converter (power

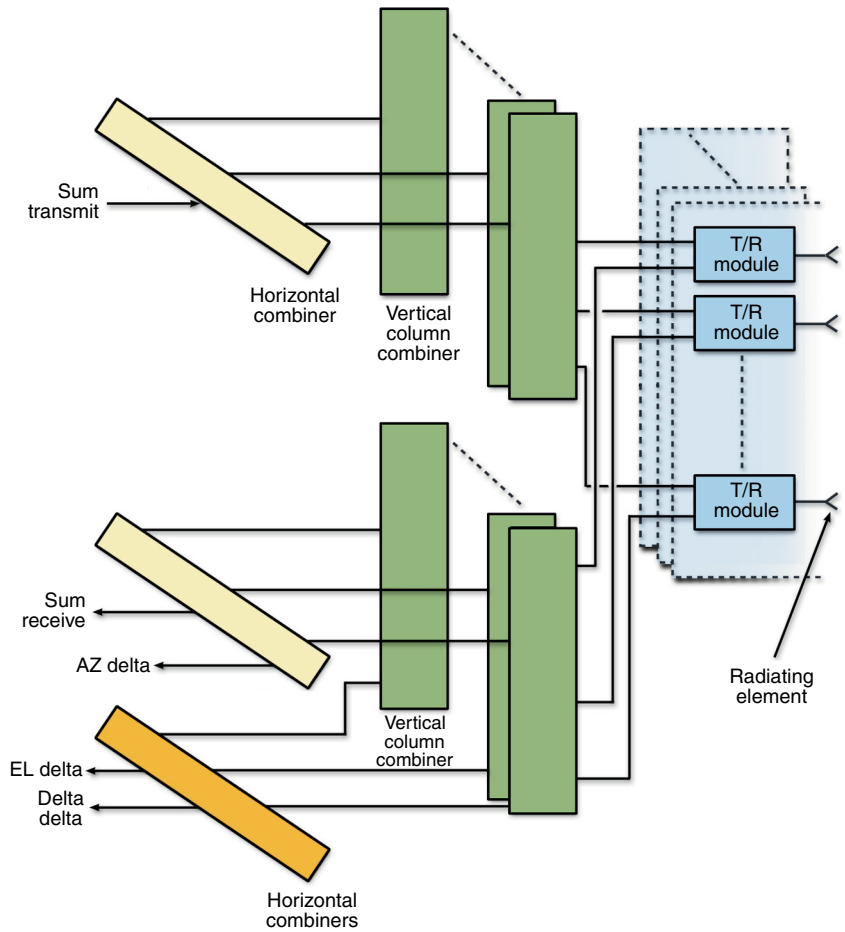


**Figure 7.** Beamformer architecture with separate transmit and receive beamformers.

supply) feeds a small group of T/R modules (typically two to eight) and DC-to-DC converters are distributed throughout the array, as shown in Fig. 8a. The DC-to-DC converters can be mounted on the same baseplate as the T/R modules. In the centralized power distribution system, a group of DC-to-DC converters are combined to feed a large section of the antenna. Redundancy is provided in each group of power supplies to increase reliability. The centralized power distribution is shown in Fig. 8b.

In both cases, the high-voltage DC is delivered to the converters using a low-current, high-voltage bus. In the centralized system, the low-power DC voltages are distributed throughout the array, requiring low-voltage, high-current buses. The converters convert high-voltage DC to low voltages required by the T/R modules, and voltage regulation is provided to generate voltages with very small ripple. Both approaches provide for improved clutter performance because of the uncorrelated random noise.<sup>12</sup> However, the DC-to-DC converters for the centralized system can be significantly larger than those of the distributed system and, to compensate for the impact of a smaller number of DC-to-DC converters on clutter performance, higher voltage regulation would be required.

The DC-to-DC converters can be either average power or peak power switching frequency converters. The switching frequency determines the size of the converter, as the converter size decreases with increasing frequency. The average power converters require storage capacitors to maintain the desired voltage droop. As the pulse width increases, the storage capacitance requirement increases, putting a physical limit on the length of the pulse. The other approach is to use a peak capacitor multiplying DC-to-DC converter. This converter has the unique advantage that the pulse energy can be stored on the primary high-voltage side of the converter, thereby resulting in a substantially smaller

energy storage capacitor. Both converters are comparable, and the choice of converter depends on pulse width, cost, and volume.

### Beamsteering Controller

Transmit and receive beams in an active phased array antenna are steered by changing the insertion phase of the phase shifters contained in the T/R modules. An antenna beamsteering controller (BSC) generates the phase shift commands for all of the T/R modules. Generation of the phase shift commands can either be distributed throughout the array or performed in a centralized location. These two architectures are referred to as a distributed BSC and a centralized BSC, respectively.

In the distributed BSC architecture (Fig. 9a), a central controller generates simple commands such as scan angle, frequency, and timing.<sup>13</sup> The T/R module control electronics contain an application-specific integrated circuit (ASIC), electrically erasable programmable read-only memory (EEPROM), field effect transistor (FET) switches, etc. The phase settings for each T/R module are calculated by the ASIC, given the simple input commands and the module location. EEPROMs may contain linearization amplitude and phase tables for each T/R module. These data are module specific, stored in EEPROMs on the basis of module factory test results, and can be erased and reloaded with new data at any time. The data transfer rate from ASIC to T/R modules can be of the order of 20 Mbps.

In addition to sending the scan angle and frequency, the central controller sends a command to set the antenna in either transmit or receive mode by setting switches appropriately in the T/R modules. A local crystal oscillator generates the clock at each local group of modules. The clock speed determines the time it takes for commands to reach all T/R modules. Distributing the clock at the local level minimizes the noise, because the clocks are not synchronized. Because many

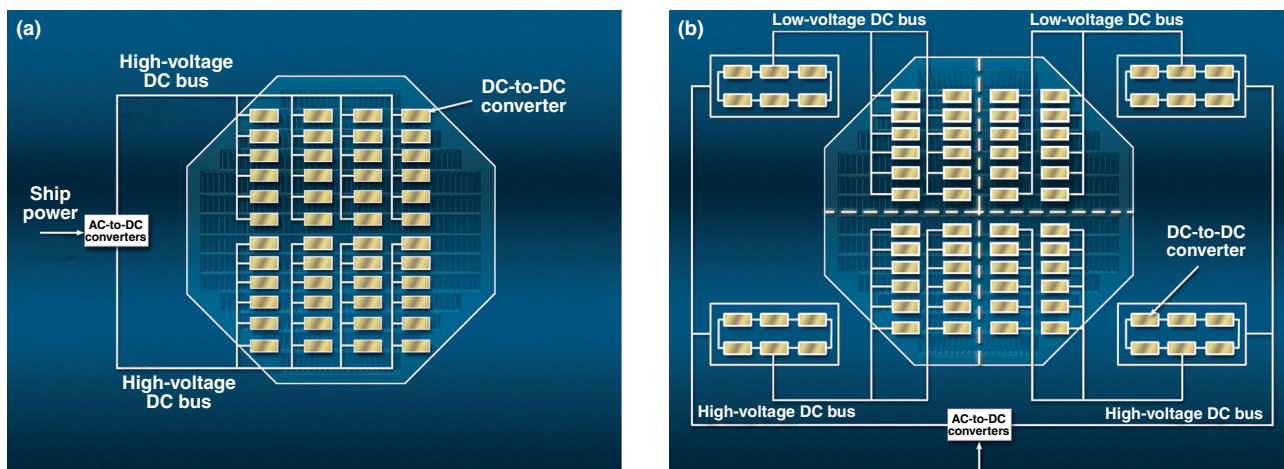


**Figure 8.** (a) Distributed and (b) centralized power distribution architecture.

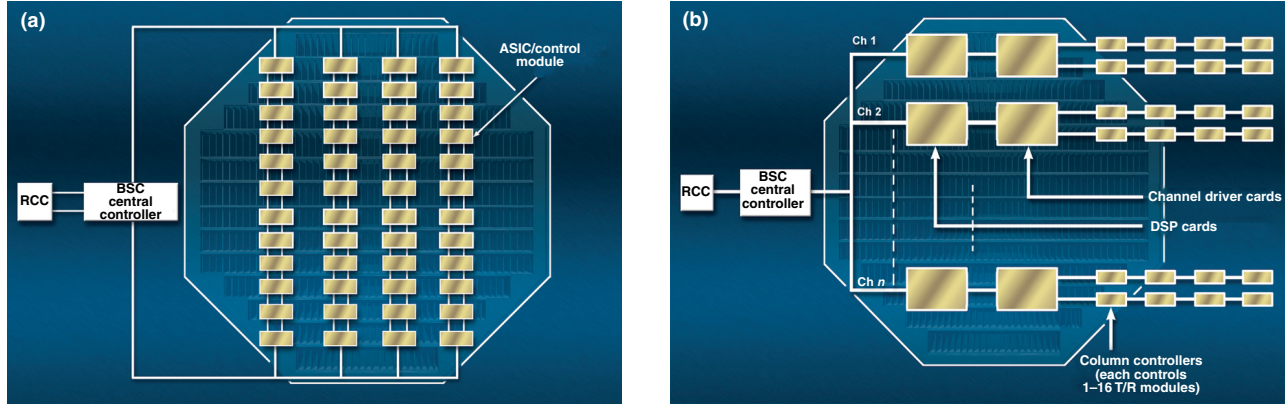


**Figure 9.** (a) Distributed and (b) centralized beamsteering controller architecture.

different beam-direction/gain-phase combinations can be stored in memory in advance, switching can readily be accomplished among various beams without recalculation within a single dwell.

In the centralized BSC architecture (Fig. 9b), most of the computations are performed in a central location and the data required by each T/R module are sent directly to the T/R modules or groups of T/R modules, such as lowest replaceable units (LRUs), using parallel buses. The central beamsteering controller may contain a number of digital signal processor (DSP) cards; each card is assigned responsibility for a specific group of T/R modules and stores all calibration values (linearization tables) for that group of modules. Each DSP card performs a set of beamsteering calculations for each T/R module in its group within a minimum pulse repetition interval (PRI). The PRI and the number of modules determine the total computation requirement. Several parallel processors may be needed to meet the requirements. The data that contain the phase and gain bits and that are sent over the control lines must be manipulated for final delivery to the T/R module. For the centralized BSC architecture, this function can be implemented in field-programmable gate arrays that can easily be reprogrammed to meet the requirements of a new T/R module.

The advantages of the centralized BSC include central processors that can be purchased commercially and reconfigured for different radar systems. The central control location requires a substantial data flow between the central control unit and the T/R modules. For a large active phased array, the data rates can range between 100 and 500 Mbps, requiring similar clock speeds. Fiber-optic data links may be appropriate at these speeds.

Either the distributed or the centralized BSC architecture can be adopted for a large active phased array system. Preliminary estimates show that the cost of these two architectures is very similar.

### Mechanical Packaging

The predominant packaging considerations associated with the mechanical design of active phased array

antennas include design for ease of maintenance, thermal management, packaging the DC power distribution system, RF beamformers, radiating aperture design/interface, and structural design. The overriding driver in what packaging options are available to the designer is the antenna operating frequency. As the frequency increases, element spacing decreases, requiring tighter spacing of the supporting electronics. Fortunately for the designer, higher-density arrays tend to have lower T/R module output power requirements; hence, the worst-case thermal design problems typically do not correlate with the worst-case packaging densities.

To optimize an array design for ease of maintenance, most of the active electronics are configured as LRUs, which can include T/R modules, DC-to-DC power converters, and various control/processor assemblies (Fig. 10). Reliability and system impact in the event of failure determine whether an assembly is designed as an LRU. System architecture, LRU reliability, and LRU cost define what is included within a given LRU. Fault isolation down to at least the LRU level is provided to minimize service time required during maintenance actions. Structural components, the coolant distribution system, RF beamformers, DC power distribution, and cabling are typically considered of sufficient reliability to be nonrepairable at sea.

Thermal design is critical for maintaining junction temperatures of the electronics at desired levels to support reliability requirements and maintain control of temperature-induced module-to-module phase errors. The T/R modules account for 70–80% of the heat generated within an array. Because of ever-increasing power density heat dissipation in modern shipboard active phased arrays, liquid cooling is normally required. The predominant cooling techniques in use today employ conduction away from the T/R module into liquid-filled coldplates or direct liquid flow-through cooling on individual LRUs. If the spacing allows electronics to be contained on one side of the LRU, the LRUs can be directly attached to the coldplates conducting across the large surface area opposite the components. Alternatively,

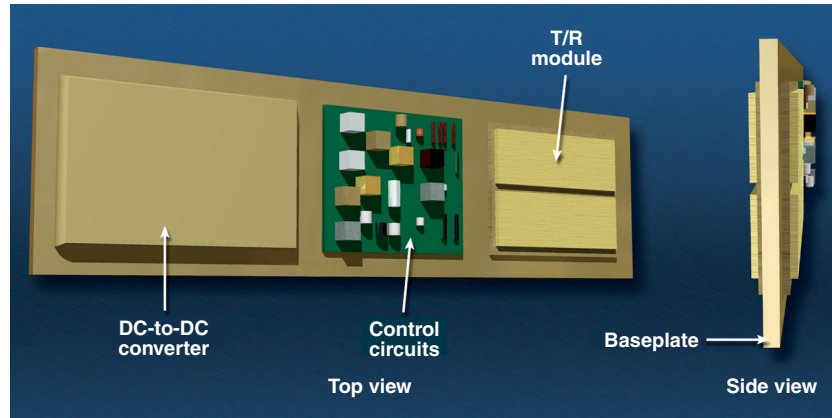


**Figure 10.** T/R module LRUs: components on both sides of a baseplate.

LRUs can be edge cooled. Figure 10 shows a typical edge-cooled LRU. As component power densities continue to increase, it may become necessary to mount the T/R modules directly to liquid-filled coldplates.

Because T/R modules exhibit phase changes with temperature variations, tight thermal control of the modules must be maintained across an array. Phase errors can be actively compensated for if the MMIC temperature is known. However, because of the difficulty in measuring the actual gate temperatures during various operational modes and duty cycles, this has not been shown to be practical. Current techniques focus on maintaining uniform coolant temperatures across the array and calibrating each element during one or more operating modes.

Maintenance requirements usually dictate that components not require removal to replace an LRU. In addition, maintenance must be performed from the back side (deckhouse interior) of the array, and therefore LRUs are inserted and extracted from the back of the array. It is imperative that RF beamformers, power distribution systems, control signal distribution systems, and their associated cabling be installed in a manner that allows ready access to the LRUs, and these elements must be designed to fit between the T/R module LRUs. This requires blind mate connections to the LRUs from the control, power, and RF distribution (and to liquid connections on liquid-cooled LRUs).

Two packaging configurations are shown in Fig. 11. In Fig. 11a, the T/R modules are mounted on a thermally conductive baseplate attached to the liquid-cooled mounting structure. This design is similar to the technique employed in air transportable rack equipment and allows components to be mounted to both sides of the baseplate. This technique offers a simple, easy-to-maintain packaging design that can accommodate tight element spacing. In addition, the coldplates become part of the antenna structure. Because of the increased thermal path length, the power dissipation capacity is somewhat power limited.

In the configuration shown in Fig. 11b, the T/R modules are mounted to one side of an LRU baseplate. The single-sided LRUs are mounted on a large vertical, fixed coldplate using wedge locks to press the baseplate against the coldplate. This configuration provides a large contact area to the coldplate and allows easy access to the LRUs; however, it tends to be better suited to larger element spacing, which allows LRU attachment by insertion on one side. The primary difficulty in this approach comes from the LRU-to-coldplate

interface. To readily accommodate sliding insertion and extraction, the interface needs to be free of filler material. This requires tight tolerance control of both surfaces and makes achieving repeatable thermal resistance from module to module difficult. Alternatively, a phase-change-type interface material could be employed that would require heating the interface prior to extraction.

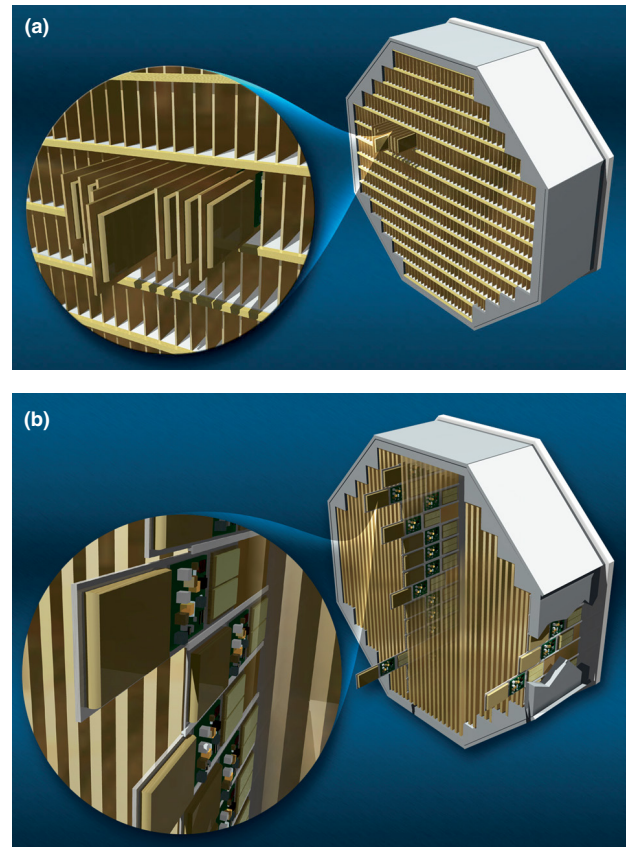


**Figure 11.** Antenna packaging assembly with (a) horizontal manifolds (edge-cooled LRUs) and (b) fixed vertical coldplates (one-sided LRUs mounted directly on both sides of the coldplates).

LRUs either must contain the radiating elements or must blind mate to the radiating elements on the array face. For low-sidelobe radar arrays, the latter is typically the case when the radiating elements are machined out of a faceplate to maintain tight element location tolerances. Overall mechanical alignment between the LRU and the radiating element requires tight control of large-tolerance stackups, and the resulting misalignment must be absorbed in the RF connector. There can easily be 15 to 25 tolerances, which combine to determine the radial float required in the RF connector. Because most floating RF connectors offer no more than 0.030 in. of radial float, it is necessary to use a combination of tight tolerances, statistical tolerancing methods, and occasionally specialized assembly fixtures to ensure proper alignment.

Structural design is a significant issue for shipboard active array radars. Traditionally the shipboard shock requirement (Mil-Std-901) has been the predominant structural design driver. For most antenna systems, floating platform barge testing is required. These tests impart a shock pulse on the order of 70 g at 11–14 Hz. A secondary consideration is to maintain adequate stiffness in the radiating aperture to ensure that array flatness requirements are maintained during operational sea states and shipboard structural vibrations. This flexural stiffness directly contributes to the array error budget and must be accounted for. Maintaining adequate flatness, particularly in larger, high-frequency arrays, will become increasingly difficult. One technique being explored is active measurement and compensation for deflection. In addition, error budgets must account for large-scale deflections of the ship's structural movement such as deckhouse or mast deflections.

## RELIABILITY AND LIFE-CYCLE COST

Achieving life-cycle cost requirements is critical to the acquisition of any new active array radar system for the U.S. Navy. Life-cycle cost consists of development, acquisition, installation, O&S, and disposal costs, of which the acquisition and O&S costs are the main contributors. The keys to reducing life-cycle costs are minimizing the cost of spares and, through fault-tolerant design of the antenna architecture, minimizing the frequency of maintenance actions.

The reliability of the antenna is measured in two ways: MTBF and mean time between critical failures (MTBCF). The MTBF of a large phased array is quite low because of the large number of components. It therefore becomes critical to incorporate fault tolerance into the design.<sup>14,15</sup> Because of the redundancy of the electronics supporting each radiating element, active phased array antennas are inherently fault tolerant and can be readily designed to degrade gracefully.

Consequently they are projected to achieve an MTBCF sufficient to support ship deployment periods with no scheduled maintenance.

The key to reducing O&S cost is the reliability and redundancy of the individual LRUs. The LRUs must be optimally sized to minimize cost, parts count, and performance impact in the event of failure, yet be of sufficient size for array packaging and maintenance access considerations. Antenna acquisition costs are primarily driven by the T/R module; however, LRU assembly and DC-to-DC converter costs can also be significant. Key to reducing these costs is attention to producibility and elimination of touch labor in the assembly. Because of the highly redundant nature of the architecture, many LRUs are produced in sufficient quantities to warrant true design for production.

Because of the combination of an inherently redundant architecture and highly reliable solid-state electronics (notably T/R modules), active arrays are projected to provide improved reliability and reduced O&S costs relative to conventional array radar systems.

## CONCLUSION

Active array antennas have emerged as a fundamental technology for addressing evolving surface Navy radar system needs. New shipboard active array radars currently under development include the AN/SPY-3 multifunction radar, volume search radar for long-range surveillance, and developmental radar concepts for Navy Theater Wide Ballistic Missile Defense. Largely as a result of active array technology, these new radars are projected to provide dramatic performance improvements as well as improved reliability and reduced O&S costs relative to conventional radar systems.

This article presented an overview of the key aspects of an active array and its various subsystems. The current state of the art was described, with particular emphasis on the critical T/R module technology. T/R module cost considerations were also addressed, given the significant focus on achieving affordable radar acquisition costs.

## REFERENCES

- <sup>1</sup>Frank, J., and O'Haver, K., "Phased Array Antenna Development at the Applied Physics Laboratory," *Johns Hopkins APL Tech. Dig.* **14**(4), 339–347 (1993).
- <sup>2</sup>Komiak, J., and Agrawal, A., "Design and Performance of Octave S/C-Band MMIC T/R Modules for Multifunction Phased Arrays," *IEEE Trans. Microwave Theory Tech.* **39**(12), 1955–1963 (Dec 1991).
- <sup>3</sup>Jones, R., and Kopp, B., "Duplexer Considerations for X-Band T/R Modules," *Microwave J.* **43**, 348–352 (May 2000).
- <sup>4</sup>Agrawal, A., Clark, R., and Komiak, J., "T/R Module Architecture Trade-offs for Active Phased Array Antennas," 1996 IEEE MTT-S Int. Microwave Symp., San Francisco, CA, pp. 995–998 (17–21 Jun 1996).

- <sup>5</sup>Moore, C., and Kopp, B., "Phase and Amplitude Noise Due to Analog Control Components," *Microwave J.* **41**, 64–72 (Dec 1998).
- <sup>6</sup>Kopp, B., "X-Band Transmit/Receive Module Overview," *IEEE MTT-Symp.*, Boston, MA, pp. 705–708 (Jun 2000).
- <sup>7</sup>Cordner, T., "GaAs Cost Drivers and an Approach to Achieving Low Cost Products," *Int. Conf. of GaAs Manufacturing Technol.*, pp. 153–159 (1997).
- <sup>8</sup>Mailloux, R. J., *Phased Array Antenna Handbook*, Artech House (1994).
- <sup>9</sup>Lewis, L. R., Fasset, M., and Hunt, J., "A Broadband Stripline Array Element," *IEEE AP-S Symp. Dig.*, Atlanta, GA, pp. 335–337 (Jun 1974).
- <sup>10</sup>Monser, G. J., "Performance Characteristics of Notch Array Elements Over 6:1 Frequency Band," *1987 Antenna Application Symp.*, University of Illinois (1987).
- <sup>11</sup>Agrawal, A., and Holzman, E., "Beamformer Architectures for Active Phased Array Radar Antennas," *IEEE Trans. Antennas Propag.* **AP-47**, 432–442 (Mar 1999).
- <sup>12</sup>Holzman, E., and Agrawal, A., "Active Phased Array Design for High Clutter Improvement Factor," *IEEE Int. Symp. Phased Array Technol.*, Boston, MA, pp. 44–47 (15–18 Oct 1996).
- <sup>13</sup>Deluca, A., Gentry, J., Thomas, D., Landry, N., and Agrawal, A., "Phased Array Antenna with Distributed Beamsteering," U.S. Patent No. 5339086 (16 Aug 1994).
- <sup>14</sup>Agrawal, A., and Holzman, E., "Active Phased Array Architectures for High Reliability," *IEEE Int. Symp. on Phased Array Technol.*, Boston, MA, pp. 159–162 (15–18 Oct 1996).
- <sup>15</sup>Agrawal, A., and Holzman, E., "Active Phased Array Design for High Reliability," *IEEE Trans. Aerosp. Electronic Sys.* **35**, 1204–1210 (Oct 1999).

## THE AUTHORS



ASHOK K. AGRAWAL received a Ph.D. in electrical engineering in 1979 from the University of New Mexico. He worked as a research scientist at Mission Research Corporation in Albuquerque, New Mexico, from 1976 to 1982 and as a Principal Engineer at Lockheed Martin Corporation in Moorestown, New Jersey (previously RCA, GE, and Martin Marietta), from 1983 to 1999. At Lockheed Dr. Agrawal was involved in research and development programs on various phased array antennas and also led the development of several active phased array antenna programs. In 1999 he joined APL and is continuing research and development work on active phased array antennas. Dr. Agrawal has published numerous papers in IEEE and other journals and holds five patents on phased array antenna topics. His e-mail address is ashok.agrawal@jhuapl.edu.



BRUCE A. KOPP received a B.S.E.E. from Arizona State University in 1986 and an M.S.E.E. from Stanford University in 1988. He was employed at Avantek in Milpitas, California, as a microwave and RF component and subsystem design engineer from 1986 to 1990, working on passive and control circuit development using printed lumped elements. Mr. Kopp is a member of the Principal Professional Staff at APL where he has been employed since 1990 developing T/R modules and associated packaging and solid-state technologies for phased array radar and communications systems applications. Mr. Kopp has participated in the development of 30 different T/R modules and has been the author or co-author of 17 papers related to T/R modules and related technologies. In addition, he teaches a 3-day short course on T/R module cost, performance, and reliability. His e-mail address is bruce.kopp@jhuapl.edu.



MARK H. LUESSE, a member of the APL Senior Professional Staff in the Air Defense Systems Department, received a B.S. in mechanical engineering from the University of Maryland. Before joining APL in 1989, he worked at AAI Corporation in Hunt Valley, Maryland, as a design engineer developing simulation and test equipment. At APL, he has designed, analyzed, and managed various hardware development and field test site efforts. Mr. Luesse joined ADSD's Radar Systems Development Group in 1996, working primarily on the mechanical design and packaging oversight of active phased array radar and communications antennas. His e-mail address is mark.luesse@jhuapl.edu.



KENNETH W. O'HAVER is a member of APL's Principal Professional Staff and is Supervisor of the Air Defense Systems Department's Radar Development Group. He received a B.S. in electrical engineering from Virginia Tech in 1981 and an M.S. in electrical engineering from The Johns Hopkins University in 1984. Mr. O'Haver joined APL in 1984 and has been engaged in the development of phased array and active aperture antenna systems and technologies for shipboard radar applications and shipboard and airborne communications applications. He is the lead engineer at APL for antenna development for the Navy's Cooperative Engagement Capability Program and is the Navy Integrated Product Team lead for SPY-3 radar array antenna equipment development. His e-mail address is kenneth.ohaver@jhuapl.edu.

# CHALMERS



## Simulation and Evaluation of an Active Electrically Scanned Array (AESAs) in Simulink®

***JENNY HILBERTSSON  
JOSEFINA MAGNUSSON***

*Signal Processing Group  
Department of Signals and Systems  
Chalmers University of Technology  
Göteborg, Sweden, 2009*

EX033/2009

# CHALMERS



## Simulation and Evaluation of an Active Electrically Scanned Array (AESA) in Simulink®.

Jenny Hilbertsson  
Josefina Magnusson

Antenna Group & Signal Processing Group  
Department of Signals and Systems  
CHALMERS UNIVERSITY OF TECHNOLOGY  
GOTHENBURG 2009

Supervisors at Saab Microwave Systems:  
Maria Lanne, Ph. D.  
Peter Nilsson Drackner, M.Sc.E.E

Examiners at Chalmers:  
Professor Mats Viberg  
Professor Per-Simon Kildal

EX033/2009



## **ABSTRACT**

An *Active Electronically Scanned Array* (AES) is an active antenna consisting of a large number of radiating elements and is commonly used in today's radar systems. One of the major advantages with this kind of antenna system is the ability to steer the beam electronically from one direction to another without any mechanical motion.

The assignment of the master thesis project is to create a model of an AES in Simulink® with the main purpose to evaluate whether Simulink® is a satisfying tool when simulating these large complex systems. Furthermore, the idea was to make a simulation using the Simulink® model with as many features of the Saab Microwave Systems antenna demonstrator (a 96 element receiver antenna) as possible.

A basic model is developed and then piece by piece upgraded to a more realistic antenna system model. The model is built using predefined Simulink® blocks where the block parameters are set by the user. One limitation with this model is the difficulty to implement a system with an arbitrary dimension since every box needs to be connected to the other boxes by hand.

To overcome this problem, a similar system model is developed using Embedded Matlab™ Function blocks. The two system models are designed to have the same functionality and since the first version is fixed to 96 elements, the comparison of the system models is performed with the same amount of elements. The difficulty with the Embedded Matlab™ version is the handling with large matrixes. The magnitude of the problem, that is, the number of array elements and the number of evaluation angles in the far-field, needs to be kept low enough to not run out of memory.

The two models both have strengths and weaknesses. A combination of the two models would probably result in the best outcome, the advantage of being able to study large and detailed system models combined with the possibility of having a flexible and arbitrary number of array elements.



## PREFACE

This thesis is a part of a Master of Science program at Chalmers University of Technology and has been performed at the Department of Signals and Systems between September 2008 and April 2009. The work has taken place at, and in cooperation with, Saab Microwave Systems in Lackarebäck, Gothenburg.

Moreover, this master thesis is a part of the strategic research centres *Strategic Research Center on Microwave Antenna Systems* (Charmant) and *Chalmers Antenna Systems VINN Excellence Centre* (Chase), where the first is sponsored by the *Swedish Foundation for Strategic Research* (SSF) and the second is sponsored by the *Swedish Governmental Agency for Innovation Systems* (VINNOVA) and Chalmers.

First, we would like to thank our supervisors Maria Lanne and Peter Nilsson Drackner for their explanations and guidance throughout the difficulties and obstacles during the work. We are particularly grateful to Maria for the effort she has put on reviewing grammar and offering suggestions for improvement in our thesis. A special thank to Sören Johansson for his interest and support to our thesis and for given us the opportunity to do this work at DD/UX and Saab Microwave Systems.

We would like to express our gratitude to Andreas Wikström who helped us regarding simulations of the large system in Simulink®. A grateful thank to Ulf Carlberg at *SP Technical Research Institute of Sweden* (SP) for the help regarding Simulink® and for being indulgent towards spam. We would also like to thank Mats Viberg and Per-Simon Kildal for being our examiners.

Thank to all co-workers that has shown interest in our work and contributed to making this an enjoyable time, especially Lars Erhage, Magnus Eriksson, Hanna Isaksson, Johan Jönsson, Mikael Pedersen, Elin Rönnnow, Jesper Skogsberg and Jonas Wingård.

Last, but not least, we would like to thank our families and friends for supporting and encouraging us during this thesis and the time of study.

Gothenburg, April 2009  
Jenny Hilbertsson & Josefina Magnusson



## **ABBREVIATIONS AND ACRONYMS**

AESA	Active Electrically Scanned Array
Charmant	Strategic Research Centre on Microwave Antenna Systems
Chase	Chalmers Antenna Systems VINN Excellence Centre
ESA	Electrically Scanned Array
GENA	Generic AESA Demonstrator
GUI	Graphical User Interface
HPA	High Power Amplifier
IFF	Identification Friend or Foe
LNA	Low Noise Amplifier
M-AESA	Multirole AESA
MSA	Mechanically Scanned Array
PA	Power Amplifier
PESA	Passive Electrically Scanned Array
RAM	Random Access Memory
RF	Radio Frequency
SLL	Side Lobe Level
SNR	Signal-to-Noise Ratio
SSF	Swedish Foundation for Strategic Research
T/R module	Transmit Receive module
VINNOVA	Swedish Governmental Agency for Innovation Systems



# CONTENTS

<b>1</b>	<b>INTRODUCTION</b>	<b>11</b>
1.1	Background .....	11
1.2	Purpose.....	12
1.3	Literature Search .....	12
1.4	Limitations and Simplifications .....	12
<b>2</b>	<b>THEORY</b>	<b>14</b>
2.1	Array Antennas .....	14
2.1.1	<i>Linear Arrays</i> .....	16
2.1.2	<i>Planar Arrays</i> .....	18
2.2	Scanned Arrays .....	19
2.2.1	<i>ESA vs MSA</i> .....	19
2.2.2	<i>AESA vs PESA</i> .....	19
2.3	Simulink® .....	20
2.4	Drutten, the Demonstrator.....	20
<b>3</b>	<b>METHOD</b>	<b>22</b>
3.1	Model Based on Drag-and-Drop Boxes .....	22
3.1.1	<i>Antenna Element and T/R Module</i> .....	22
3.1.2	<i>Modelling of Linear Array</i> .....	23
3.1.3	<i>Modelling of Planar Array</i> .....	27
3.2	Model Composed by Embedded Matlab™ Function Blocks .....	29
3.2.1	<i>Information Matrix</i> .....	29
3.2.2	<i>Plane Wave</i> .....	30
3.2.3	<i>Antenna Element</i> .....	30
3.2.4	<i>Transmit Receive Module</i> .....	31
3.2.5	<i>Combining Network</i> .....	32
3.3	Implementation of the Demonstrator .....	32
<b>4</b>	<b>RESULTS</b>	<b>33</b>
4.1	Outcome from the Embedded Matlab™ Function Block Model .....	33
4.2	Implementation from Drutten .....	41
<b>5</b>	<b>DISCUSSION</b>	<b>44</b>
5.1	Advantages and Disadvantages.....	44
5.2	Further Work .....	45
<b>6</b>	<b>CONCLUSIONS</b>	<b>46</b>
<b>REFERENCES</b>		<b>47</b>
<b>APPENDIX A: SIMULINK® BLOCKS</b>		<b>48</b>
<b>APPENDIX B: DRAG AND DROP 'GENERATE_PARAMETERS.M'</b>		<b>50</b>
<b>APPENDIX C: DRAG AND DROP 'EDIT_PARAMETERS.M'</b>		<b>52</b>
<b>APPENDIX D: EMBEDDED MATLAB™ FUNCTION BLOCKS</b>		<b>53</b>
<b>APPENDIX E: EMBEDDED MATLAB™ 'EDIT_PARAMETERS.M'</b>		<b>58</b>
<b>APPENDIX F: EMBEDDED MATLAB™ 'GENERATE_PARAMETERS.M'</b>		<b>59</b>
<b>APPENDIX G: MATLAB SCRIPT 'TAYLORTAP_LIN'</b>		<b>61</b>

## TABLE OF FIGURES

<i>Figure 1. Topology of a linear array.</i> .....	15
<i>Figure 2. Geometry of a linear array antenna.</i> .....	16
<i>Figure 3. Criteria for non-radiating grating lobes.</i> .....	17
<i>Figure 4. A periodic rectangular two dimensional array geometry.</i> .....	18
<i>Figure 5. Scheme of the antenna elements in Drutten.</i> .....	21
<i>Figure 6. Simple diagram of the antenna unit.</i> .....	21
<i>Figure 7. T/R module in receiver mode consisting of an LNA, a varying phase shifter and an attenuator.</i> ..	23
<i>Figure 8. The three components, LNA, phase shifter and attenuator, grouped into a subblock called T/R module.</i> .....	23
<i>Figure 9. Ten identical antenna elements, their T/R modules and a combining network.</i> .....	24
<i>Figure 10. Content in the Receiver phase subbox.</i> .....	24
<i>Figure 11. A linear array with ten indexed antenna elements.</i> .....	25
<i>Figure 12. The steering value for element (1,1) are multiplied with the incoming signal in the subblock Phase shifter.</i> .....	26
<i>Figure 13. The tapering value for element (1,1) are multiplied with the incoming signal in the subblock Attenuator.</i> .....	27
<i>Figure 14. Structure of the planar array.</i> .....	28
<i>Figure 15. The first element in the planar array.</i> .....	28
<i>Figure 16. Model composed by Embedded Matlab<sup>TM</sup> Function blocks.</i> .....	29
<i>Figure 17. Two-dimensional matrix with <math>16 \times 6</math> elements and <math>181 \times 181</math> points in different directions.</i> ..	30
<i>Figure 18. Configuration of the elements in Drutten, seen from the front.</i> .....	32
<i>Figure 19. Radiation pattern for an ideal, uniform planar array with <math>16 \times 6</math> isotropic antenna elements.</i> ..	34
<i>Figure 20. The cross-sections of the radiation pattern from the incoming field.</i> .....	34
<i>Figure 21. The cross-sections of the radiation pattern for an untapered planar array of <math>16 \times 6</math> antenna elements with cosine-shaped element patterns.</i> .....	35
<i>Figure 22. The radiation pattern when the beam is scanned to <math>\theta=30^\circ</math> and <math>\phi=45^\circ</math>.</i> .....	36
<i>Figure 23. The cross-sections when the beam is scanned to <math>\theta=30^\circ</math> and <math>\phi=45^\circ</math>.</i> .....	36
<i>Figure 24. The radiation pattern using a Taylor tapering of -45 dB in x-direction and a -30 dB in y-direction.</i> .....	37
<i>Figure 25. The cross-sections after a Taylor taper has been applied in the attenuator block.</i> .....	37
<i>Figure 26. A 3D plot of the Embedded Matlab<sup>TM</sup> system when steering the main beam into <math>(30^\circ, 170^\circ)</math> having a Taylor tapering of 30 dB in x-direction and a Taylor tapering of 20 dB in y-direction.</i> .....	38
<i>Figure 27. A 3D plot of the Drag-and-Drop system when steering the main beam into <math>(30^\circ, 170^\circ)</math> having a Taylor tapering of 30 dB in x-direction and a Taylor tapering of 20 dB in y-direction.</i> .....	38
<i>Figure 28. The radiation pattern when having a low number of bits in attenuators and phase shifters, a Taylor tapering of -45 dB in x-direction and -30 dB in y-direction is applied.</i> .....	39
<i>Figure 29. The cross-sections when having a low number of bits.</i> .....	40
<i>Figure 30. The cross-sections for <math>\sigma=0.07</math>.</i> .....	40
<i>Figure 31. Grating lobes caused by a change in distance, from <math>0.5\lambda</math> to <math>0.8\lambda</math> in both x- and y-directions, between the elements in the array.</i> .....	41
<i>Figure 32. Element patterns from five elements in the demonstrator, the cosine shaped and the adjusted diagram.</i> .....	42
<i>Figure 33. Radiation pattern for cross-section v after antenna element with isotropic, cosine and measured element diagram.</i> .....	43
<i>Figure 34. Radiation pattern for cross-section u using an antenna element with isotropic, cosine and measured element diagram.</i> .....	43

# 1 INTRODUCTION

In this thesis, a specific type of antenna system, called *Active Electrically Scanned Array* (AESA), is studied. The basic principle as well as the structure of the system is presented where the latter is modelled and simulated in a program called Simulink®.

The assignment is to model an antenna system where all the fundamental parts are included such as antenna aperture, receiver and combining network. A simple and ideal *transmit receive module* (T/R module) is modelled as a first step and piece by piece developed into a larger and more complex planar array system.

## 1.1 BACKGROUND

Ever since Christian Hülsmeyer got his patent for the *Telemobilescope* 1904, where he calculated the distance for an electro-magnetic wave to travel back and forth between a metal object and his scope, the development of radar technology has progressed.<sup>1</sup> In 1935 Great Britain launched research activities regarding air defence. The radar technology in particular was a question of vital importance for the defence of Britain but it took some years before the technique was exploited to the utmost. The new radar technology was integrated with radiotelephony and direction finding, which made it possible to achieve both early warnings and the positions for hostile planes in the battle of Britain during World War II.<sup>2</sup>

As many times before, military purposes have precipitated the technical development which later on has proven useful also for civil applications. With more advanced antennas, the radar can perform more sophisticated search and track pattern but the technique is also used for non military applications, such as air traffic control, weather monitoring and road speed control.

The radar technology can briefly be described as follows. Electromagnetic radiation is transmitted and propagates through the air and when it reaches a target, or some other obstacle, the wave is reflected. The reflection returns as a weak signal, also known as an echo, and from this signal useful information of the target can be extracted, for example the distance, the position and the rate of speed (in case of a moving target).

Today, radar technology is a widely spread technique for different fields of applications. Several systems have been designed, for instance the Erieye and the Giraffe, two radars developed by Saab Microwave Systems. Both are surveillance radars, but the first one is air-borne radar and the second is ground-based radar. Among others, SAMPSON and APAR radars can be mentioned as phased array naval systems, the MESA and THAAD as surveillance systems and AMSAR and Gripen PS-05 as fighter radars.<sup>3</sup>

The next step in systems for radar and electronic warfare is the development of the *Multirole AESA* (M-AESA), which is a development program between Saab Microwave Systems, Selex Sistemi Integrati S.p.A and Elettronica S.p.A by order of the Swedish and Italian Armed Forces. The goal is to create a system for radar, electronic warfare and communication, used for land-, sea- and air-based applications. Radar systems of today usually have one main function, but the main idea of the M-AESA is a multifunction system where *Identification Friend or Foe* (IFF), missile warnings and jamming of hostile radars are some of the functions. The existing hardware cannot manage the requirements for the future

<sup>1</sup> Skolnik, Merrill I. *Introduction to Radar Systems*. 3<sup>rd</sup> ed. New York: McGraw-Hill. 2001. p. 15

<sup>2</sup> <<http://www.foi.se>> (17 December 2008)

<sup>3</sup> Nilsson Drackner, Peter. M.Sc.E.E. personal communication (8 October 2008)

but new semiconductor components and materials might be the solution to this problem. With multithread capacity and multifunction, a system will, depending on the tactical situation, be used for different applications.<sup>4</sup>

## 1.2 PURPOSE

The main purpose of this thesis is to design a model, which consists of the essential parts of an AESA system, in Mathworks™ Simulink®. An AESA consists of a large quantity of components which together constitute a large complex system. To understand and predict its performance knowledge about the different parts is needed, as well as an overview and understanding of the entire system. By modelling the system in a simulation program, it is possible to increase the understanding for how the different parts act together and affect the system performance.

Furthermore, a goal is to evaluate whether Simulink® is a satisfying tool to use when modelling these types of large, complex systems and if it can be useful for similar types of systems. As the work proceeds, the model will become more and more realistic and aspects like maladjustments and interference from internal as well as external factors will be taken into consideration.

Another goal is to extract information from an authentic AESA model and implement the features into the Simulink® model to get a more realistic model.

## 1.3 LITERATURE SEARCH

Information concerning antennas, essential components and AESA principles are procured during the first weeks. For the main part the literature consists of articles from IEEE Xplore, previous thesis and books about array antennas and radar technology.

This thesis work has, as mentioned, been performed as part of the strategic research centres Chase and Charmant which implicate an opportunity to take advantage of the knowledge and experience of the centres, especially concerning programming in Simulink®. Since Saab Microwave Systems holds a large amount of information and knowledge itself, several rewarding discussions and conversations with co-workers have taken place and given a clearer vision of the subject.

## 1.4 LIMITATIONS AND SIMPLIFICATIONS

Since AESA systems are complex and contains a large amount of components, a true model is hard to achieve. In this thesis several limitations have been done, some due to complexity and others because of time limitation.

The antenna elements are modelled as isotropic elements where losses, mutual coupling and maladjustments are disregarded. In the model using Embedded Matlab™ Function blocks there is a possibility to take radiation losses into consideration.

In this thesis, the focus is on the AESA operating in receive mode, where the main purpose for this decision is to be able to compare the simulated results with existing measurement data as the model is developed.

---

<sup>4</sup> <etn.se> (2 February 2009)

The T/R module has been limited to contain the three most important components; a *low noise amplifier* (LNA), a phase shifter and an attenuator, where the LNA has been modelled as an ideal component, described by a constant. The combining network, which in reality is a complicated net due to mismatches are in this thesis represented by a summation net which add up all signals without any losses.

## 2 THEORY

This section contains some basic antenna theory that is used within the work. Along with informative text and pictures some equations are presented in order for the simulation work to appear more comprehensive. The theory is divided into some general antenna theory, a Simulink® introduction and a short presentation of a demonstrator. Together they contribute to give the reader a brief theoretical introduction to this thesis work as well as insight in what the reality can look like. The terms used, are considered as an antenna in either transmitting or receiving mode, depending on which is more convenient for explaining a particular antenna property.

### 2.1 ARRAY ANTENNAS

Some antenna sources can be seen as isotropic elements, which mean that they radiate equally well in all directions. This is just a theoretical assumption which is used to simplify calculations. Many antenna elements, especially small ones, are often radiating similar to isotropic elements with a wide radiation beam. This is not always a desired feature, several field of antenna applications require a more directive radiation characteristic.

The ability to focus energy in a certain direction is called *directivity* and for an antenna with physical area  $A$  this is calculated according to *Equation 1*, where lambda ( $\lambda$ ) is the free space wavelength. One way to achieve higher directivity is to enlarge the electrical size of the antenna which can be done by combining several antennas into a so called array antenna.

The relation between the directivity and the *gain* of an antenna is given according to *Equation 2*, where  $G$  is the gain,  $D$  is the directivity and  $e_{rad}$  is the radiation efficiency. (The radiation efficiency is always less or equal to unity.) As can be seen in the two equations below, an array antenna has higher gain than an element of a single antenna, which makes it possible to transmit a signal longer distances. Therefore are arrays more suited for applications like tracking radar and search radar where transmitting over long distances is a desired property.<sup>5</sup>

$$D_{\max} = \frac{4\pi}{\lambda^2} A \quad [-] \quad \text{Equation 1}^6$$

$$G = e_{rad} D \quad [-] \quad \text{Equation 2}^7$$

An array antenna can be designed in many ways using different kinds of antenna elements, but in most cases the same type of antenna element is used over the whole antenna aperture. Depending on which properties that are desired, the elements can be located in different ways, which means the elements are placed in a row or in a grid of elements placed on a linear or a planar surface, respectively. Other configurations, such as circular arrays are also possible, where circular arrays are one specific case of conformal arrays, that is, arrays placed on non-

<sup>5</sup> Stimson, George W. *Introduction to Airborne Radar*. 2<sup>nd</sup> ed. Mendham, USA. SciTech Publishing. 1998 pp. 473-479.

<sup>6</sup> Kildal, Per-Simon. *Foundations of Antennas: A Unified Approach*. Lund, Studentlitteratur. 2000 p. 69

<sup>7</sup> Pozar, David M. *Microwave and RF design of wireless systems*. John Wiley & Sons. 2001 p. 118

planar surfaces. This provides the possibility to tailor-made array antennas with certain properties.

Array antennas can be divided into two main groups, *broadside* and *endfire*, depending on how their main beam is designed to radiate. An *endfire array* has its main beam in the direction along the array, while the *broadside array* radiate perpendicular to the arrays orientation, see *Figure 1*. If the array is phase steered, the direction of the beam can be changed without rotating the antenna platform.<sup>8</sup>

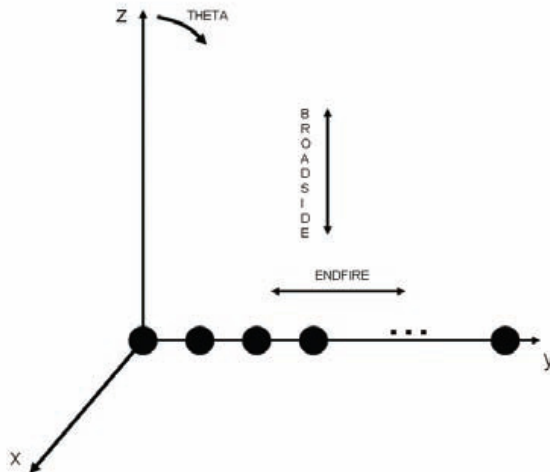


*Figure 1. Topology of a linear array.*<sup>9</sup>

Not all the radiated power from an array is concentrated to the main lobe direction as desired; some of the power will leak into so called *side lobes*. The amount of this misdirected power is measured relative to the main beam power and is called the *side lobe level* (SLL). Side lobes occur since the surface of the array is finite, which means radiation from less than -90° and more than 90° are received and affect the radiation pattern. In a radiation pattern where losses are neglected, the first side lobe has a relative level of -13.2 dB. To reduce the side lobes and decrease the SLL a method called *tapering* can be used. This method changes the radiation pattern by lowering the signal amplitude in the elements close to the edges. Using this technique the main beam will be less focused, meaning that the main beam will be wider.

The radiation field from an array antenna (or a single antenna element) has different properties depending on how far away from the array it is measured. The region surrounding the antenna can be divided into two different main parts, *near field* and *far field*, where the transition between them depend of the wavelength and the diameter of the antenna. The far field is defined as the area where the spherical wave front, radiated by the antenna or array, becomes a close approximation to the ideal planar phase front of a plane wave. The definition of the far field is described by the radius distance,  $r$ , from the antenna according to *Equation 3*, where  $D$  is the largest dimension of the antenna and  $\lambda$  is the wavelength.<sup>10</sup>

---

<sup>8</sup> <[www.orbanmicrowave.com](http://www.orbanmicrowave.com)> (2 October 2008) pp. 1-15

<sup>9</sup> <[www.orbanmicrowave.com](http://www.orbanmicrowave.com)> (2 October 2008) p. 1

<sup>10</sup> Kildal, pp. 37-42.

$$r \geq \frac{2D^2}{\lambda} \quad [\text{m}]$$

Equation 3<sup>11</sup>

## 2.1.1 LINEAR ARRAYS

The elements in a linear array are distributed over a one dimensional straight line and are often equidistantly positioned to achieve a desired radiation pattern. If a plane wave is incident towards an equidistantly array where all elements are identical and the antenna elements are omnidirectional, the received wave will diverge only by a phase difference at each element. This phase difference can be calculated according to *Equation 4*, where  $x$  is the extra distance the wave has to travel from one element to the next,  $dx$  is the distance between two elements and  $\theta$  is the direction of the incident wave. An illustration of these parameters can be seen in *Figure 2*.<sup>12</sup>

$$\Delta\phi = \frac{x}{\lambda} 2\pi = \frac{dx \sin \theta}{\lambda} 2\pi \quad [\text{rad}]$$

Equation 4<sup>13</sup>

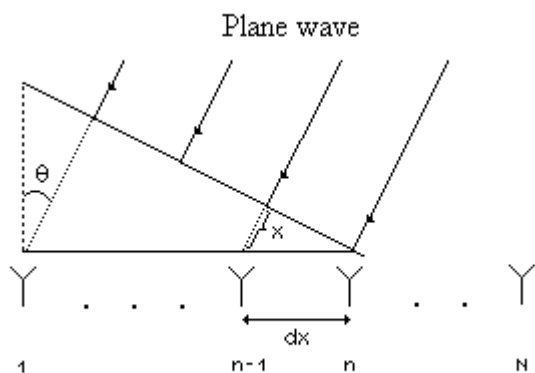


Figure 2. Geometry of a linear array antenna.

To achieve a more definite radiation pattern, the field from the elements need to interfere positively in the desired direction and have negative interference in all other directions. This is possible by phase steering the radiation from each antenna element.<sup>14</sup>

The far field radiation pattern from an  $N$ -element linear equally spaced array is a summation of the radiation of each element according to *Equation 5*, where  $j$  is the imaginary unit,  $k$  is the wave number ( $2\pi/\lambda$ ) and  $V_n$  is the complex excitation of the element  $n$ . Further,  $dx$  represent the distance between two elements while  $\theta$  are the angle of the incident wave. Assuming identical element patterns, the equation (for the radiation pattern) can be rewritten and divided into two parts, the *element pattern* and the *array factor*, according to *Equation 6*.

<sup>11</sup> Kildal, p. 38.

<sup>12</sup> Visser, Hubregt J. *Array and Phased Array Antenna Basics*. Chichester, England. John Wiley & Sons. 2005 pp. 123-135

<sup>13</sup> Visser, p. 124

<sup>14</sup> Visser, p. 124.

$$\mathbf{E}(\theta, \phi) = \sum_{n=1}^N V_n \mathbf{E}_{ele}(\theta, \phi) e^{jkn dx \sin \theta} \quad [\text{V/m}] \quad \text{Equation 5}^{15}$$

$$\mathbf{E}(\theta, \phi) = \underbrace{\mathbf{E}_{ele}(\theta, \phi)}_{\text{Element pattern}} \underbrace{\sum_{n=1}^N V_n e^{jkn dx \sin \theta}}_{\text{Array factor}} \quad [\text{V/m}] \quad \text{Equation 6}$$

The element pattern,  $\mathbf{E}_{ele}$ , describes the radiation of a single antenna element and will therefore change appearance depending on what kind of antenna element is used. The array factor is dependent of the element spacing  $dx$ , the number of antenna elements in the array,  $N$ , and the amplitude and phase excitation of each element.<sup>16</sup> The bigger element spacing the larger directivity is obtained, as long as there are no visible *grating lobes*. Grating lobes are maxima in the radiation pattern in other directions than the main beam. To avoid these often undesired maxima (they can be mistaken for the response of a target in the main beam) the requirement on the element spacing for non-radiating grating lobes can be calculated according to *Equation 7*, where  $\lambda_{min}$  is the wavelength at the highest frequency. Furthermore,  $\theta_{max}$  is the position of the main lobe and  $\sin(\theta_{00}/2)$  corresponds to the half null depth beam width of the grating lobe. An illustration of the parameters can be seen in *Figure 3*.

Having small element spacing, approximately half a wavelength, makes it possible to theoretically design the antenna for full scan, which means the antenna can scan up to almost  $\pm 90^\circ$  from broadside. In reality, the radiation impedance changes with scan, which means the useful scan region becomes limited to  $\pm 60^\circ$ .<sup>17</sup>

$$d \leq \frac{\lambda_{min}}{1 + \sin \theta_{max} + \sin(\theta_{00}/2)} \quad [\text{m}] \quad \text{Equation 7}^{18}$$

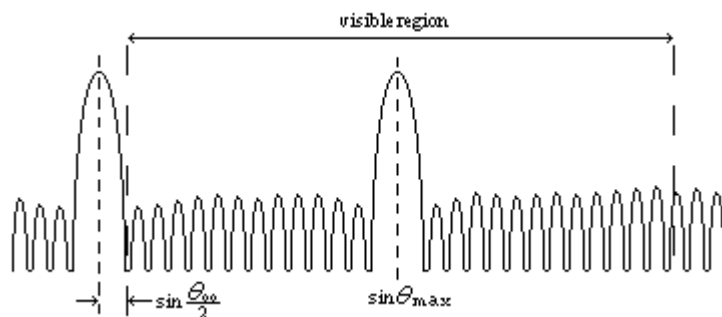


*Figure 3. Criteria for non-radiating grating lobes.*

<sup>15</sup> Lanne, p. 8.

<sup>16</sup> Lanne, Maria. *Antenna Arrays System: Electromagnetic and Signal Processing Aspects* Lic. Chalmers University of Technology. Gothenburg, Chalmers Reproservice. 2005 pp. 7-10.

<sup>17</sup> Kildal, pp. 341-378.

<sup>18</sup> Kildal, p. 354.

## 2.1.2 PLANAR ARRAYS

A planar array consists of antenna elements spread over two dimensions where the positions compose a planar lattice. A planar array can be described as a linear array of linear arrays if the grid on the planar array is of rectangular shape and all the elements are equally spaced, this does not mean they need to have same spacing in the two orthogonal directions, see *Figure 4*. The radiation field from a planar array is a summation of the radiation from each element, just like for the linear array. Since the planar array is distributed over two dimensions the equation will be described by both *theta* ( $\theta$ ) and *phi* ( $\phi$ ), according to *Equation 8*.  $V_{mn}$  describe the complex excitation for the element in the  $m^{\text{th}}$  row,  $n^{\text{th}}$  column.  $E_{\text{ele}}$  implicate the element pattern,  $k$  the wave number and  $dx$  respectively  $dy$  represent the distance between two elements in the different dimensions.

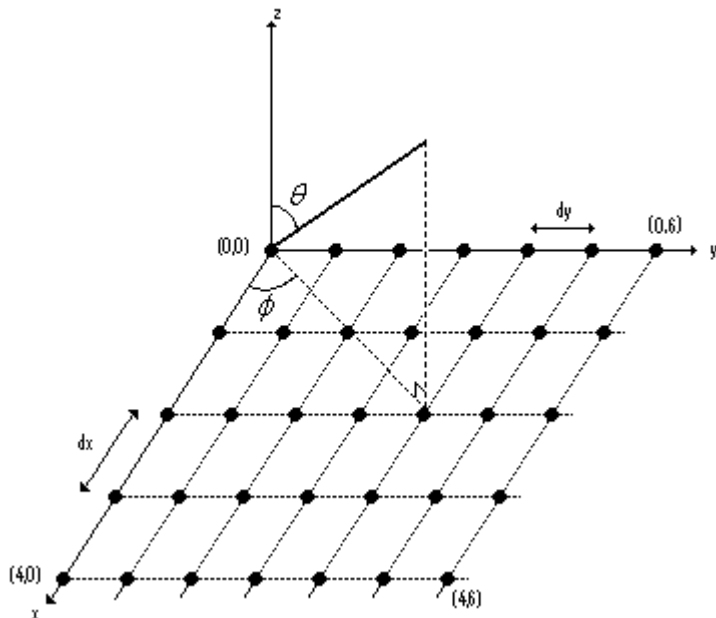


*Figure 4. A periodic rectangular two dimensional array geometry.*

$$E(\theta, \phi) = \sum_{m=1}^M \sum_{n=1}^N V_{mn} E_{\text{ele}}(\theta, \phi) e^{jk \sin \theta (mdx \cos \phi + ndy \sin \phi)} \quad [\text{V/m}] \quad \text{Equation 8}^{19}$$

Using planar arrays makes it possible to shape the radiation pattern in two dimensions and to control the radiation pattern in both  $\theta$ - and  $\phi$ -direction. Further, the side lobes can be lowered in both directions as well and can be beam steered toward any point in space.<sup>20</sup>

Radiation diagrams are one way to present the result from an array antenna. The diagrams represent the radiation from the antenna and can be plotted in  $\theta$  and  $\phi$ -plane or in  $u$ - and  $v$ -plane. The most common way is to plot the radiation in  $u$ - and  $v$ -plane which is a transformation from the  $(\theta, \phi)$ -coordinates using *Equation 9* and *Equation 10*.

<sup>19</sup> Lanne, p. 14.

<sup>20</sup> Balanis, Constantine A. *Antenna Theory: Analysis and Design*. 3<sup>rd</sup> ed. Hoboken, New Jersey. John Wiley & Sons. 2005 pp. 349-362

$$u = \sin\theta \cdot \cos\phi \quad [-] \quad \text{Equation 9}$$

$$v = \sin\theta \cdot \sin\phi \quad [-] \quad \text{Equation 10}$$

## 2.2 SCANNED ARRAYS

This section will introduce and briefly describe and compare different scanned arrays as well as a comparison between them, where advantages and disadvantages will be listed. The first section will introduce and compare the two main groups of scanned arrays, *Electronically Scanned Array* (ESA) and *Mechanically Scanned Array* (MSA). In the last section there will be a comparison between *Passive ESA* (PESA) and *Active ESA* (AESAs) which are two subgroups to the ESA.

### 2.2.1 ESA vs MSA

Some of the technologies today require the array antenna to have a moveable main beam, for instance many radar applications. Scanned arrays are the solution to this requirement since they have the ability to scan large areas instead of only using a fixed beam.

As mentioned earlier, the MSA is a scanned array which uses mechanics to change the direction of the main beam. This is achieved by mounting the array on a turn-table and then tilts the entire antenna to point in the desired direction. The largest disadvantage of this method is the force of inertia which limits the speed of the mechanical movement. Therefore scanning between two far off angles is time consuming, but it is a good operative method considering the financial aspects, due to the fact that MSAs only uses one central transmitter and receiver for the entire system. These kind of mechanical arrays are commonly used in both land-based and air-based applications.

In contrast to the MSA, the ESA is mounted on a fixed plane and instead of mechanical movement the beam is steered using electronics. By adjusting the amplitude and phase of the element excitations, the direction of the main beam can be changed. Phase shifters are used to change the phase while the amplitude adjustment is done by amplifiers. Since this technique is based on electronic signals, the time to scan the main beam from one point into another far off point is identical with scanning to the nearest possible. This is a desirable advantage and one of the main reasons why many MSAs are replaced by ESAs even though the latter is more expensive due to its complexity.<sup>21</sup>

### 2.2.2 AESA vs PESA

The ESAs can be divided into the two groups, passive and active ESAs, both having the feature to steer the main beam using the combination of phase shifters and amplifiers. The main difference with the PESA is the use of only one central transmitter and receiver for the entire system, while the AESA has one power amplifier behind each antenna element. This makes the AESA more complex and therefore is it also more expensive than the PESA. Both the PESA and the AESA have one electronically controlled phase shifter placed behind each radiating element of the array.

---

<sup>21</sup> Stimson, pp. 473-479.

The AESA is commonly designed with one T/R module behind each element in the array. In addition to phase shifters and attenuators, T/R modules commonly include *high power amplifiers* (HPA), circulators or switches (to switch between reception and transmission), limiters and LNA for the received signals. All T/R modules are in transmit mode fed with a RF-signal via a RF feed network. The use of array antennas with a large number of elements and T/R modules makes it possible to operate the antenna even when some T/R modules are broken. This advantage is called *graceful degradation*. Since the T/R module makes it possible to individually steer the amplitude and phase excitation of each element, superior beam shape agility is also provided.<sup>22</sup>

## 2.3 SIMULINK®

Simulink® is a *Graphical User Interface* (GUI) extension to Matlab®, containing several tools for modelling and simulation of multidomain dynamic systems. It supports linear and nonlinear systems, modelled in continuous time, sampled time, or a combination of the two. Since Simulink® is an integrated part of Matlab®, data can easily be transferred between the programs which make it possible for the user to take full advantage of the features offered by both environments. In Simulink® the user can build hierarchical models as block diagram, with predefined blocks using drag-and-drop mouse operations. The program has an extensive block library containing sources, sinks, math functions and many other useful blocks which altogether is over two hundred pieces. Some of the boxes are underframes in which the user has the possibility to create own properties using operation code as for instance C++ and Embedded Matlab® code.<sup>23</sup>

Since a large amount of boxes might cause the system to be difficult to lucid, the model can be simplified by grouping blocks into subsystems. Besides the lucidness, subsystems make it easy to keep blocks with related functionality together and establish a hierarchical block diagram with different layers. Subsystems are either executed conditionally or unconditionally, where the latter are always executed. Depending on the input signal, the conditionally executed subsystem may or may not be executed.<sup>24</sup> As there are coding algorithms better suited for the textual language instead of the graphical, the *Embedded Matlab™ Function* block is a useful tool. Working with the Embedded Matlab™ subset makes it possible to perform embedded software design as well as implementation and testing completely within the Matlab® workspace.<sup>25</sup>

## 2.4 DRUTTEN, THE DEMONSTRATOR

Saab Microwave Systems, earlier Ericsson Microwave Systems, has, as part of the *Generic AESA Demonstrator* (GENA) program, worked with an active antenna demonstrator which consists of a rectangular phased array antenna. The demonstrator is only built to work in receive mode.

The demonstrator consists of a planar array with 200 dipole elements set up in a rectangular grid with 10×20 antenna elements. The elements are equidistantly spaced in *x*-direction as well as in *y*-direction, but do not have the same spacing in the two orthogonal dimensions. The 96 elements in the middle, placed 6×16, are connected to one receive module each whereas the

---

<sup>22</sup> Stimson, pp. 473-491.

<sup>23</sup> <www.mathworks.com> b (29 September 2008)

<sup>24</sup> <www.mathworks.com> c (9 February 2009) pp. 198-199

<sup>25</sup> <www.mathworks.com> a (9 February 2009) p.15

104 elements on the border are terminated into matched loads, see *Figure 5*. The receive path for each of the 96 elements consists of, as can be seen in *Figure 6*, a limiter, an LNA, an eight bit phase shifter and a nine bit attenuator.

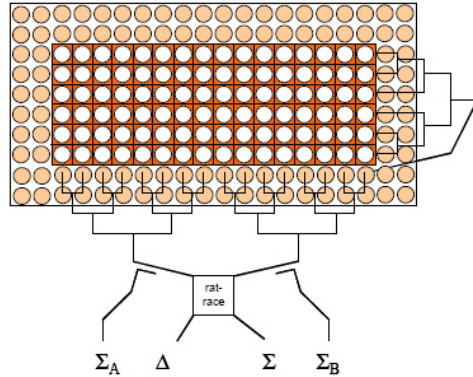


*Figure 5. Scheme of the antenna elements in Drutten.*<sup>26</sup>

The GENA program focus was on developing basic equipments necessary for next generation of prototypes and products within the field of active antennas for modern radar. It concentrated on technologies and antenna architectures that could be used for different radar applications at different frequencies, where the demonstrator works at S-band (2-4 GHz). The demonstrator has been used to get practical experience in areas like antenna system design, T/R module production, antenna system calibration and evaluation. Some of the goals have been to demonstrate a stable active antenna function with an active receive array and to evaluate a calibration scheme based on factory characterization.<sup>27</sup>

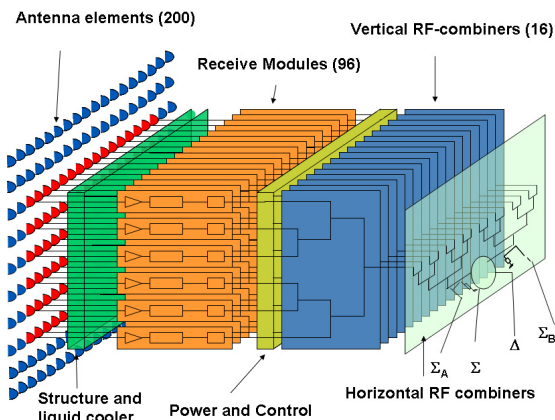


*Figure 6. Simple diagram of the antenna unit.*<sup>28</sup>

<sup>26</sup> Nilsson Drackner, Peter and Engström, Björn. *An Active Antenna Demonstrator for Future AESA- Systems*. In: IEEE International, *Proceedings of the International Radar Conference 2005*. 2005. p. 227.

<sup>27</sup> Nilsson Drackner and Engström, pp. 226-231

<sup>28</sup> Nilsson Drackner, Peter. M.Sc.E.E. E-mail. (25 March 2009)

## **3      METHOD**

In this section the implementation of the AESA system is presented. Since the assignment of the thesis work is to evaluate whether Simulink® is a good simulation tool for large arrays, two different modelling approaches are evaluated and compared. This is done to explore as many of the features in Simulink® as possible.

The first modelling approach presented is almost pure Simulink® programming with boxes linked to each other where the idea is to avoid intervention of Matlab® to the greatest possible extent, whereas the second is built up with boxes of Embedded Matlab™ programming complemented with Matlab® scripts. The first modelling approach is called *Model Based on Drag-and-Drop Boxes*, while the second modelling approach is called *Model Composed by Embedded Matlab™ Function Blocks*.

Some of the predefined Simulink® blocks used have functionalities that are quite easy to understand, while others need an explanation. The boxes used in the models and a short summary about how they work can be found in *Appendix A*.

### **3.1    MODEL BASED ON DRAG-AND-DROP BOXES**

In this modelling approach the focus is to model an AESA system based on the drag-and-drop boxes method that the Simulink® library offers. First the system is built in a way where each component is ideal and then the components are modified step by step into a more complex and realistic model. As a start an antenna element and a T/R module are modelled, these are modified and copied into a linear and finally a planar array.

#### **3.1.1    ANTENNA ELEMENT AND T/R MODULE**

The first step in the modelling of the AESA is to create a model of the T/R module, where all the parts in the module are ideal and linear. In receive mode the first component in the module is an LNA which in this stage corresponds to a multiplication factor. The phase shifter, which follows after the LNA, is modelled as an exponential function where the phase is manually change by the user. The last component in the T/R module is an attenuator and like the LNA this part is represented by a multiplication factor. In this initial model the antenna is lossless and therefore the received signal of the antenna is transmitted unchanged into the LNA. When simulating the model, it is assumed that a plane wave impinges on the antenna. Complex base band representation is used, which means that the signals received by the antenna elements are modelled as complex numbers. This signal is transported through the simulation model and then, using a *Scope block*, the user is able to watch the result, see *Figure 7*.

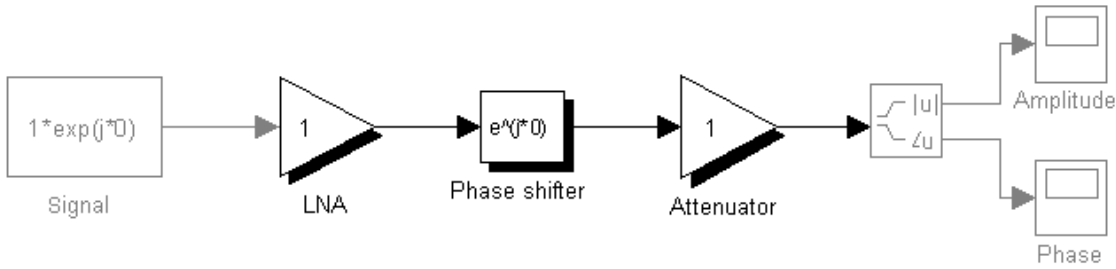


Figure 7. T/R module in receiver mode consisting of an LNA, a varying phase shifter and an attenuator.

As mentioned in the theory part (section 2.3), there is a possibility in Simulink® to group different boxes into so called subblocks. This provides the opportunity to divide the model into different subsystems and thereby make the model more apprehensible. The three components; the LNA, the phase shifter and the attenuator are representing a T/R module and are therefore placed in a subblock with the same name, see *Figure 8*.

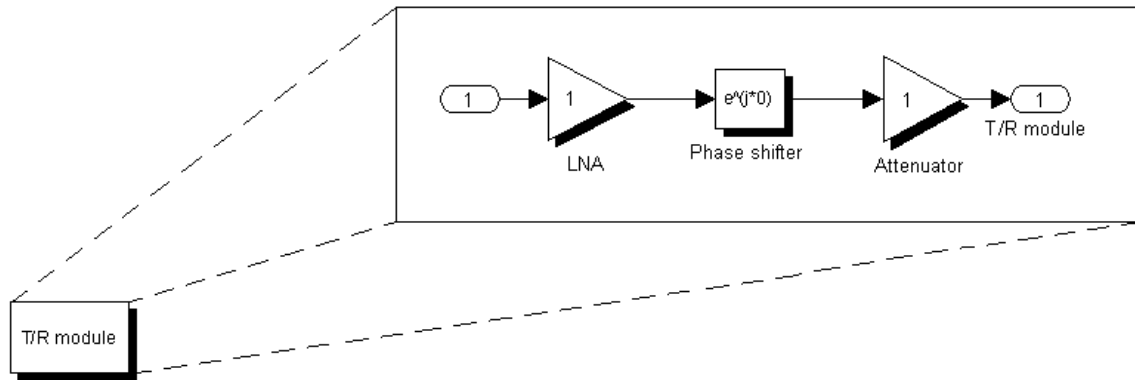


Figure 8. The three components, LNA, phase shifter and attenuator, grouped into a subblock called T/R module.

The input signal to the T/R module comes from the antenna element. The antenna element is modelled under the assumption that there is no mismatch, losses or coupling between the elements and consequently, everything received by the element is thereby transmitted unchanged into the T/R module.

### 3.1.2 MODELLING OF LINEAR ARRAY

To model an array of ten antenna elements and T/R modules, the model with an antenna element and a T/R module, is copied into ten identical versions and then their signals are added in a combining network, see *Figure 9*. The combining network is at this stage a summation network, where all signals are added disregarding losses and mismatches.

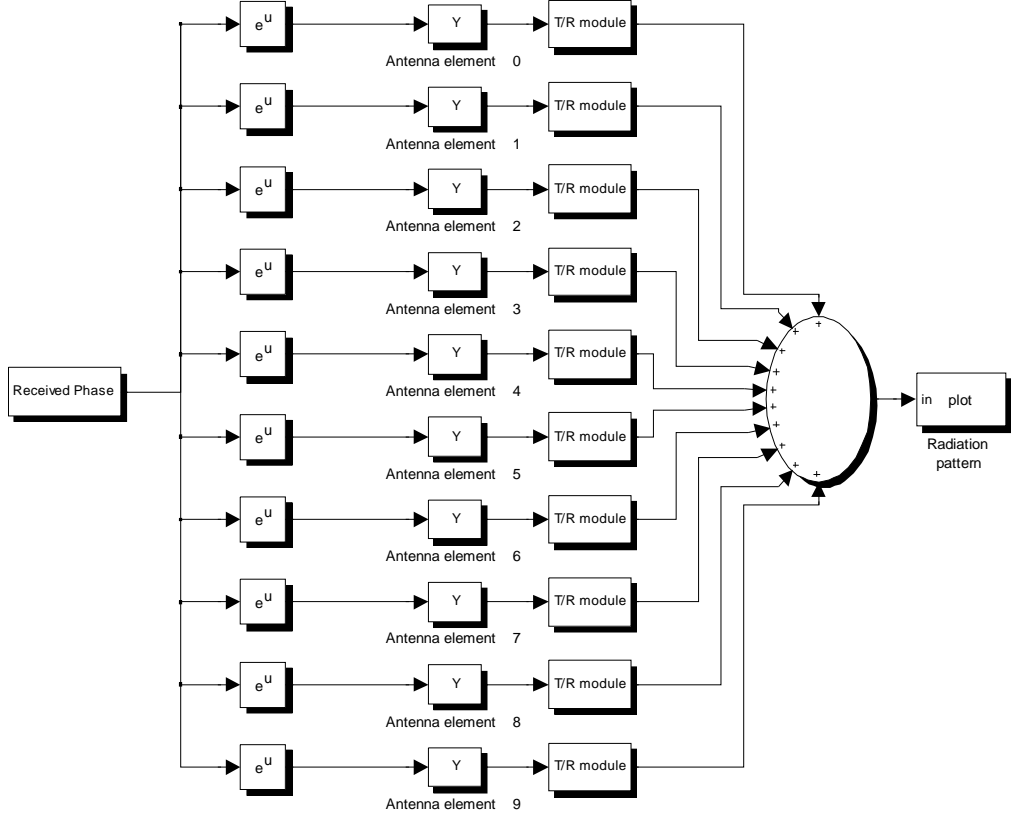


Figure 9. Ten identical antenna elements, their T/R modules and a combining network.

The signals received by the antenna elements are modelled as a vector of complex numbers representing the received plane wave. The received signals are a function of the direction of the incident plane wave relative to the normal of the array antenna aperture. To model how the array receives signals from all angles of incident in the  $\theta$ -plane, the vector with plane wave directions contains angles from  $-\pi/2 - \pi/2$  radians with 180 steps. This is placed in a subsystem called *Received Phase*, see Figure 10. Since the angles from  $-\pi/2 - \pi/2$  radians equals the angles from  $-90^\circ - 90^\circ$ , there will be 181 points representing all integers in the interval.

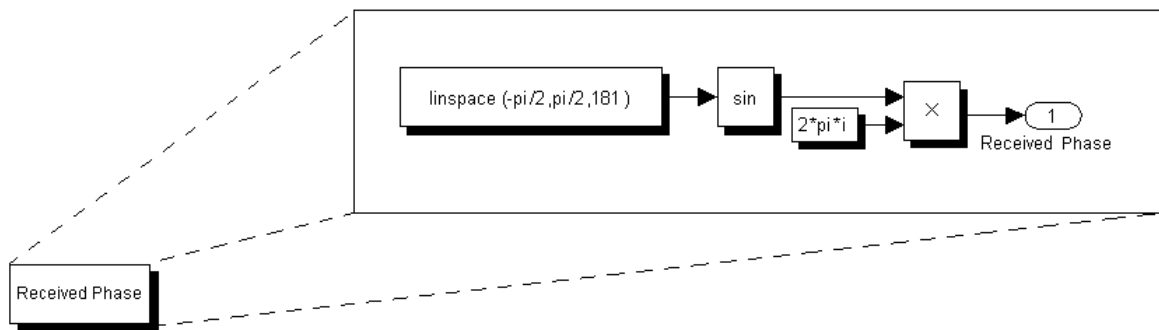
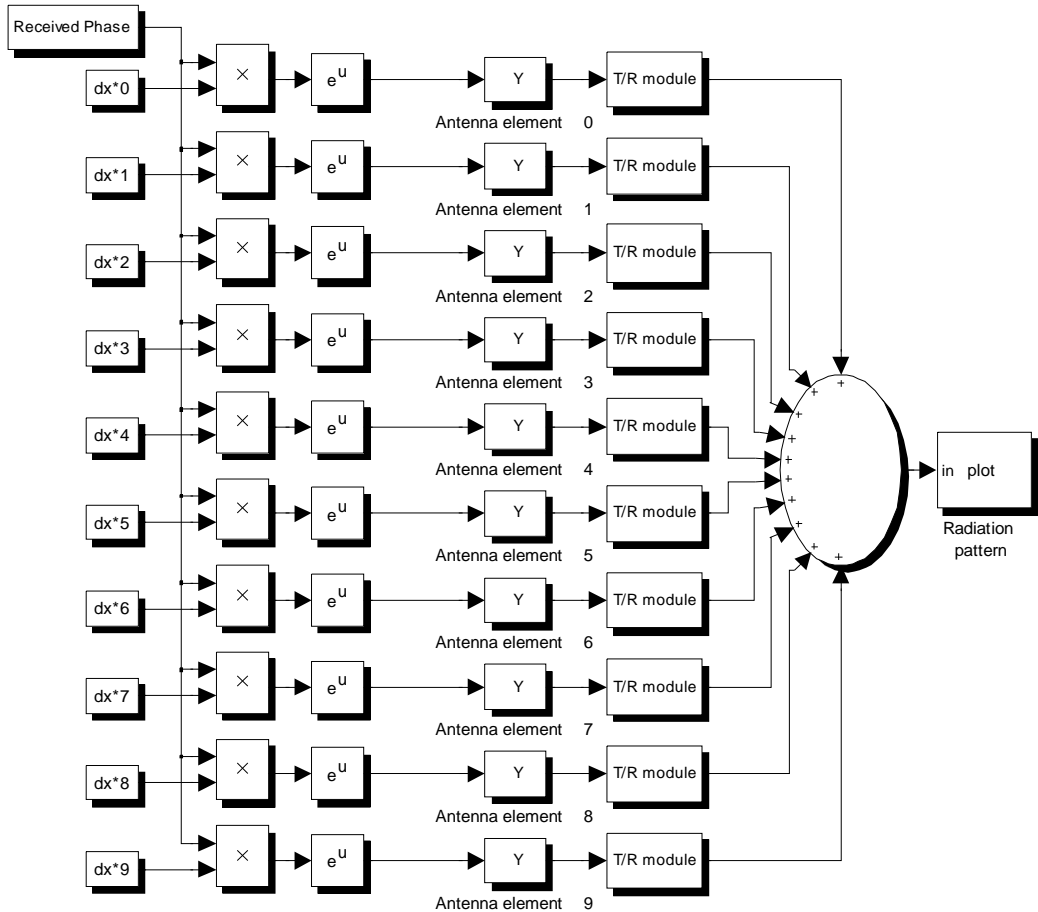


Figure 10. Content in the Receiver phase subbox.

In an array antenna there are physical distances between the antenna elements. Because of these distances an incoming signal will not be received at all elements on the same time,

unless the signal is incident perpendicular to the array aperture surface. The incoming signal corresponds to a narrow band plane wave and the difference in the received signal between two elements can therefore be described as a phase shift instead of a time shift. When implementing this in the model, each element needs to have an index corresponding to its position in the array, see *Figure 11*. This index is multiplied with a phase constant which represents the physical distance between two adjacent elements, according to *Equation 11*. Where  $k$  represents the wave number,  $n$  describes the index of the element and  $dx$  the distance between two elements. The angle of the incident wave is described by  $\theta$ .



*Figure 11.* A linear array with ten indexed antenna elements.

$$\text{signal into element } n = e^{-jkndx \sin \theta} \quad [-] \quad \text{Equation 11}$$

Both phase shifters and attenuators are created with a predefined scale of values. This scale describes the values that the component can adopt and is limited by a maximum and a minimum value. Phase shifters and attenuators are manufactured with a certain number of bits which is a measure of how many states the scale of values are divided into. If the component for example is an eight bit attenuator the scale is divided equally into 256 different states, according to *Equation 12*. Since there is a limited amount of states in this type of component it is not always possible to set the desired attenuation value. This results in a small residual for each component setting. In this model the number of bits is defined by the user and can be changed from one simulation to another.

$$8\text{-bit component} \Rightarrow 2^8 = 256 \quad [-]$$

Equation 12

When these bit components are manufactured it is not possible to make them identical since there always will be small variations between the components. This is the reason why two components do not have identical states of scale even though they are designed and manufactured in the same way. The uneven states are described in this model using a *Gaussian normal distribution*, according to *Equation 13*, where *mu* ( $\mu$ ) and *sigma* ( $\sigma$ ), represent the mean value and standard deviation. These parameters determine the magnitude of the variation between the phase shifters and attenuators respectively and are set by the user.

The equation is implemented in a Matlab® script, see *Appendix B*, and calculated for each component when running the program. In the script, the function *randn* is used to return pseudorandom, scalar values drawn from a normal distribution with the specified mean value and standard deviation. This implies that a unique variation between each component will occur.

$$f(x | \mu, \sigma) = \frac{1}{\sigma\sqrt{2\pi}} \cdot e^{-\frac{(x-\mu)^2}{2\sigma^2}} \quad [-] \quad \text{Equation 13}$$

This description is used in this model for both phase shifters and attenuators with the difference that the states of the attenuators are divided between 0 – 1 while the phase shifters are divided between 0 –  $2\pi$ . It is possible for the user to have different  $\mu$ - and  $\sigma$ -values for the phase shifters and the attenuators.

The phase shifter as well as the attenuator is represented by one subsystem each. The phase shifter is a subblock containing an exponential to steer the main lobe into a, by the user predefined direction, see *Figure 12*. The desired phase shift is depending on where in the geometry of the array the element is placed. Since the incoming signal is received with a time shift between the elements this needs to be reversed by the phase shifters to make sure the signals adds up in phase (constructively). Consequently, the phase shifters must have knowledge about where in the array they are placed by knowing the positions of their interconnected antennas. The exponential that can be seen in the figure is varying dependent on the index of the antenna element.

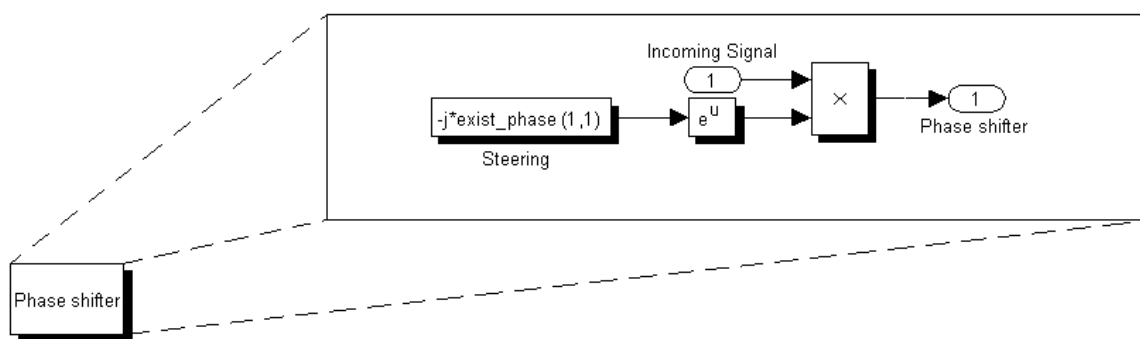


*Figure 12. The steering value for element (1,1) are multiplied with the incoming signal in the subblock Phase shifter.*

The attenuators are the components that are used when tapering an array. In this thesis a *Taylor tapering* is applied to the elements in the array. For example, a *30 dB Taylor* distribution corresponds to a beam pattern where the highest side lobes are 30 dB below the main lobe maximum. A Matlab® script, see *Appendix B*, is used to calculate the attenuation for each element to achieve a specific tapering. The script calculates the ideal values for a linear array with a specified number of elements. From these values the nearest existing value in the scale of the attenuator is chosen and a small error of attenuation arises (corresponding to the difference between the desired and actual attenuation value). The resulting tapering value is multiplied with the incoming signal in the attenuator, see *Figure 13*.

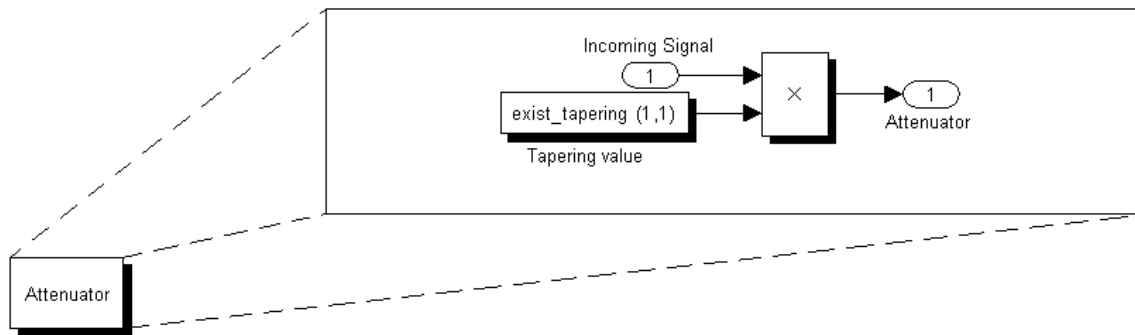


*Figure 13.* The tapering value for element (1,1) are multiplied with the incoming signal in the subblock Attenuator.

The simulation of the ten different antennas and their T/R modules is done for 181 different angles of incidence which in the end of the simulation is combined and presented in a radiation pattern. When the simulation of the linear array is done, an Embedded Matlab™ Function block is programmed to automatically present a radiation pattern which completes the simulation of the linear array.

### 3.1.3 MODELLING OF PLANAR ARRAY

To model the planar array the previously modelled linear array is used. Since the model should be comparable to *Drutten* (the antenna demonstrator) having a size of  $6 \times 16$  elements, the linear array is increased to 16 elements. These are copied into six different subsystems, representing six linear arrays, see *Figure 14*. To let the six linear arrays represent a planar array, the indexation of the elements are increased to contain two numbers corresponding to the two dimensions. The signal received at the elements in a planar array are also dependent on two directions and the equation describing the radiation will be expanded as described in the theory, according to *Equation 8*.

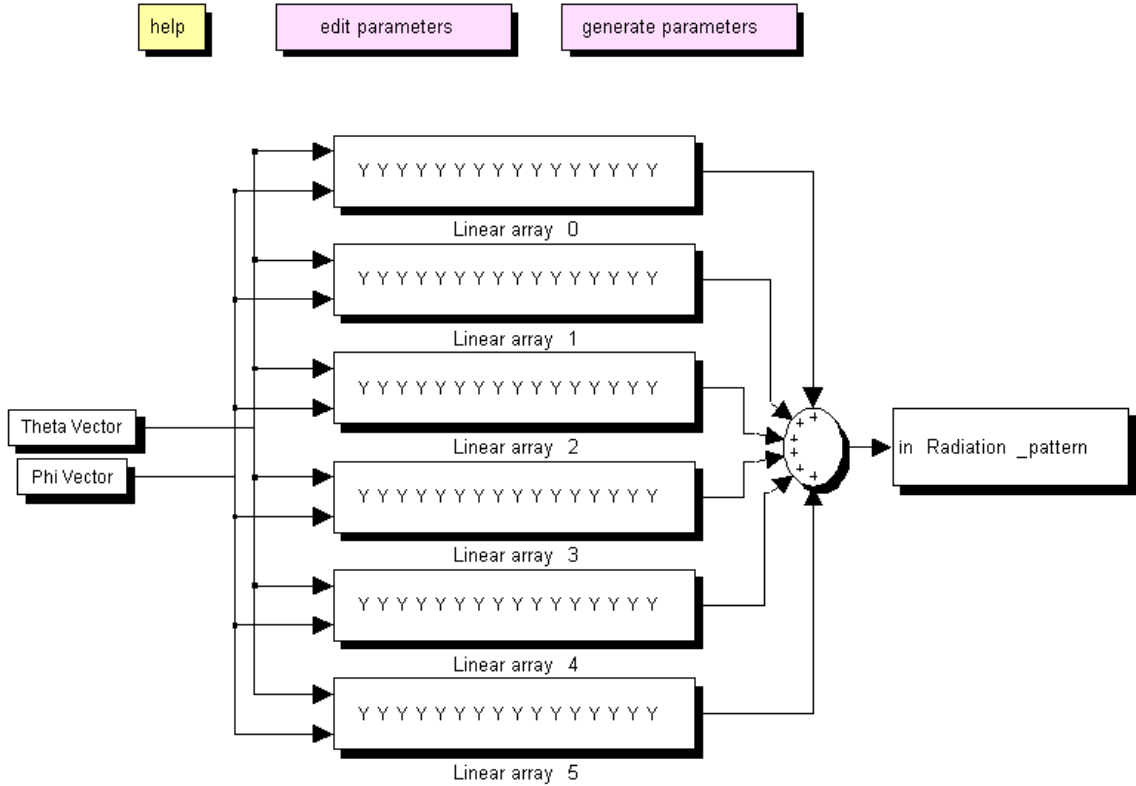


Figure 14. Structure of the planar array.

When having a planar array new aspects must be taken into consideration. The array is two dimensional which means, the beam can be scanned in two dimensions. Therefore is the antenna system modelled as a function of both  $\theta$  and  $\phi$ , which can be seen in *Figure 15*.

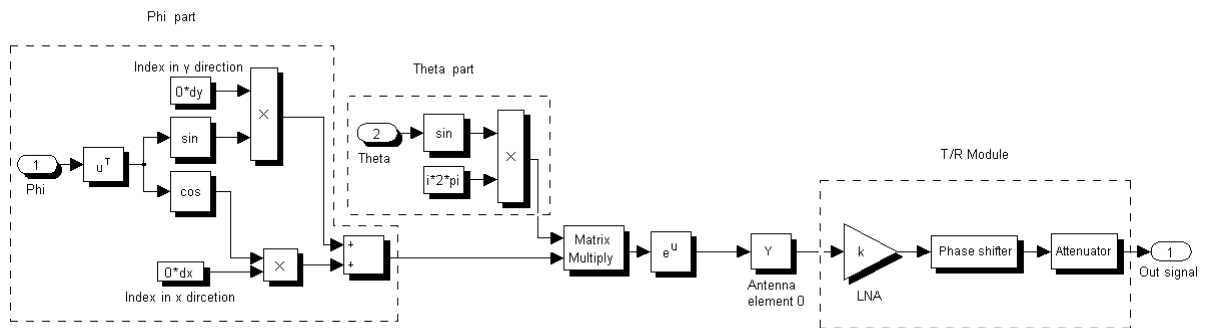


Figure 15. The first element in the planar array.

The simulation of the planar array is done using 181 different angles of incidence in both  $\theta$ - and  $\phi$ -plane, where  $\theta$  goes from  $0 - \pi/2$  and  $\phi$  goes between  $0 - 2\pi$ . The signals from the different elements are added and presented in a three dimension radiation pattern.

The system is complemented with two Matlab® scripts, one containing the different adjustable parameters for the system and one containing calculations based on the modified parameters. The first script, see *Appendix C*, contains the parameters for the antenna geometry, the phase shifter, the attenuator and other variables needed for the simulation. The user should only get in touch with this first script and make changes suited for the wanted simulation since the

second script is called upon automatically from the first. The second script, which has been mentioned before, contains calculations of values required for the phase shifters and the attenuators, see *Appendix B*.

### 3.2 MODEL COMPOSED BY EMBEDDED MATLAB™ FUNCTION BLOCKS

The previously designed model was created with a fix number of elements in the antenna system. It also used one box for each operation in the model, which lead to a substantially large amount of boxes. Knowing this, the second model is made with the intention of having an arbitrary number of elements and having all components with the same functionality modelled in same block. One way to create these blocks is to use Embedded Matlab™ Function blocks in which the properties for the blocks are programmed by the user. This makes it possible to create blocks containing many components of the same type, but where each of the components has unique performance.

The previous model was built as an ideal antenna element with a connected T/R module, which subsequently was extended into a large more complex planar array. The *Model Composed by Embedded Matlab™ Function Blocks* is intended to be equal to the final result of the *Model Based on Drag-and-Drop Boxes* system and therefore a planar array is designed without the intermediate steps of a single antenna element and a linear array. Since this AESA model is based on Embedded Matlab™ Function blocks, see *Figure 16*, the system consists of coding algorithms in textual language. The code for the different component blocks used in the system can be seen in *Appendix D*.

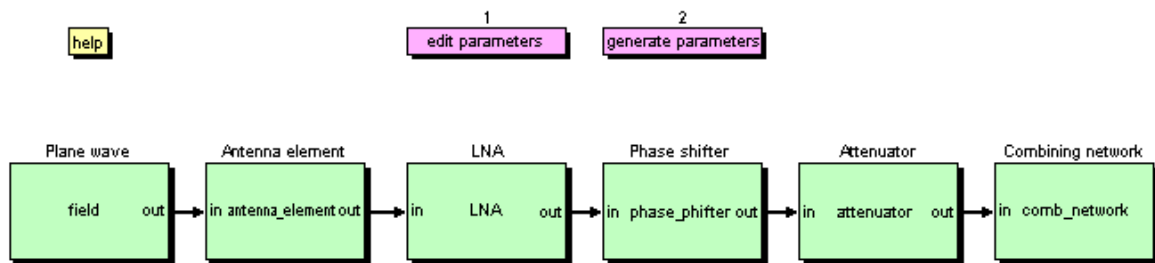


*Figure 16. Model composed by Embedded Matlab™ Function blocks.*

#### 3.2.1 INFORMATION MATRIX

The model is built using six Embedded Matlab™ Function blocks, where each of the blocks is programmed to represent a component or a function in the AESA system. Since each antenna element can receive signals from arbitrary directions specified by the two dimensions,  $\theta$  and  $\phi$ , the information at each element will be represented by a matrix. The matrix is sent throughout the whole system and modified in every box before it is summed up in the last block. This is done by storing the matrixes of each element after each other, in the order in which their antenna elements are positioned. Altogether, the columns in the large matrix contain the amount of elements in  $x$ -direction times the number of scanned  $\theta$ -values and the rows contain the amount of elements in  $y$ -direction multiplied with the number of  $\phi$ -values to be scanned. A visualization of a matrix can be seen in *Figure 17*.

The code used in the Embedded Matlab™ Function blocks are similar to the one used in Matlab®, but with a smaller number of functions. The command *cell*, which is a function that creates matrix arrays, is one example of a function that would facilitate the handling of these

large matrixes. The cell array allows the programmer to store matrixes at each position in a matrix but this command is not supported by Simulink®.

$$\begin{matrix} & 1 & 2 & \dots & 16 \\ 1 & \left[ \begin{matrix} [181 \times 181] & [181 \times 181] & \dots & [181 \times 181] \end{matrix} \right] \\ 2 & \left[ \begin{matrix} [181 \times 181] & [181 \times 181] & \dots & [181 \times 181] \end{matrix} \right] \\ \vdots & \vdots & \vdots & \ddots & \vdots \\ 6 & \left[ \begin{matrix} [181 \times 181] & [181 \times 181] & \dots & [181 \times 181] \end{matrix} \right] \end{matrix}$$

Figure 17. Two-dimensional matrix with  $16 \times 6$  elements and  $181 \times 181$  points in different directions.

One of the criterions for the Embedded Matlab™ Function block is the requirement of having the size of the output independent of the size of the input. For this reason, the size of the matrix is predefined in the script with the eligible variables, see Appendix E.

### 3.2.2 PLANE WAVE

The first block in this model is called *Plane wave* and contains the equation describing the appearance of the signal received at each element of the antenna, according to *Equation 14*. Where the equation is calculated from *Equation 8* for element  $(x, y)$  and where the amplitude of the received field is set to one. The signal depends on the position of each antenna element which is described by the integers  $x$  and  $y$  and where  $dx$  and  $dy$  represent the spacing between the elements expressed in wavelengths. Furthermore,  $\theta$  and  $\phi$  symbolize the angles from where the plane wave has been transmitted. If both angels are zero, which means that the signal is incident perpendicular towards the antenna aperture, the signal at each antenna element will be identical. As previously, the received signals are described by a matrix of received values, reflecting the position of the transmitted signal scanned. The received signals are stored together and then transmitted into the next block called *Antenna element*.

$$\text{signal into element } (x, y) = 1 \cdot e^{2\pi \cdot j \sin \theta ((y-1)dy \cdot \sin \phi + (x-1)dx \cdot \cos \phi)} \quad [-] \quad \text{Equation 14}$$

### 3.2.3 ANTENNA ELEMENT

The antenna elements in the previous model had the features of an isotropic antenna, which means that the antenna was assumed to radiate equally in all directions. This assumption is a common simplification and requires that mutual coupling, losses and maladjustments are neglected.

In this model the antenna element is developed one step further as an element pattern is implemented. The element pattern describes the radiation of an antenna element and is in this model approximated using a cosine function, according to *Equation 15*, where the equation is expressed in normalized amplitude and  $m$  describes the value which the cosine factor is superscript to. This equation will attenuate the radiation in near edge angles of the antennas. If the  $m$ -factor is set to zero, the model will be identical to the previous model since the cosine term will become equal to one. Furthermore, the equation is independent of scanning angles in

$\phi$ -direction, which makes the appearance of the element diagram to be the same for all angles of  $\phi$ . Since the appearance of the diagram is independent of the position of the elements in the antenna, they will have identical pattern for each element. The values for the element pattern are calculated and placed in a vector, which is multiplied with the received matrix using two for-loops and then transmitted into the next block.

$$\text{element diagram} = \sqrt{\cos^m \theta} \quad [\text{V}] \quad \text{Equation 15}^{29}$$

### 3.2.4 TRANSMIT RECEIVE MODULE

As described in the theory part (section 2.2.2), the T/R module is one of the key elements for the AESA system and even though different architectures are possible the three most important parts; LNA, phase shifter and attenuator, are included in this model. In contrast to the previous model this one has no block named T/R module, since all the components in the T/R modules are placed directly in the model.

In real systems, the function of the LNA is to amplify a weak signal before sending it into the rest of the system. The LNA is the first component in receive channel in the T/R module and can therefore amplify the signal before noise has been added from the rest of the components. In this way the *Signal-to-Noise Ratio* (SNR) is kept high and the signal can more easily be distinguished. The function of the LNA is identical with the foregoing model and since the models are created with a high input signal where the noise is neglected the function of the LNA is not as important as in real systems.

The LNA block, transfers the incoming matrix without modification further to the next block. If the user wants to add maladjustments or losses, the block can be reprogrammed to include them, using two for-loops with a describing equation in the middle.

When the matrix is sent through the system and arrives at the phase shifter box, this block repeat the influence of the distances between the antenna elements. As been described in the drag-and-drop model, the phase shifter should reverse the phase shift that is applied on the received signal due to the distances between the antenna elements. It is the phase shifters that steer the antenna beam into a, by the user, predefined direction as well.

The phase shifter is one of the components which is most developed. In this model, both manufacturing variations and bits are taken into consideration, which makes each phase shifter unique and the result from one simulation to another can include having a small difference. Since there were problems to create an equivalent phase shifter in the drag-and-drop model, the script used in this model, see *Appendix F*, was also implemented in the first system model but with some modifications.

The attenuators are similar to the phase shifters since both have bits and manufacturing variations that are taken into consideration. A Matlab® script, see *Appendix G*, is used to calculate the ideal attenuation values for each antenna element using three parameters defined by the user; the number of elements in the particular array, the SLL and the desired number of side lobes having the same height. To create unique attenuators to this model the ideal attenuation values are modified using the same Matlab® script as for the phase shifters, see *Appendix F*. Each unique tapering value is multiplied into the received matrix on all places

---

<sup>29</sup> Mailloux Robert J. *Phased Array Antenna Handbook*. 2<sup>nd</sup> ed. Norwood, USA. Artech House. 2005. p. 305

representing its position in the array, for example, the tapering value at element  $(1,1)$  is multiplied at the first  $181 \times 181$  places in the incoming matrix. This is done for each antenna element in the array using a double for-loop and then the matrix is transmitted to the combining network block.

### 3.2.5 COMBINING NETWORK

In the previously described model the combining network corresponds to a summation block which adds up the signals from all elements and transmits the final signal into a plotting embedded box. The *Combining network* block is programmed to have the same functions as the previous system model, but with both the summation network as well as the automatic plotting function in the same box. The block is adding all signals having the same angel of incident, which results in a matrix having a size equal to the number of points in the  $(\theta, \phi)$ -directions. The measured data of the matrix is illustrated in three different ways; the 3D far field pattern and the far field cross sections for both  $u$  and  $v$ .

## 3.3 IMPLEMENTATION OF THE DEMONSTRATOR

Measurement data from the demonstrator has been extracted and implemented in the model to get one step closer to a true antenna system. The implementation is done using the *Model Composed by Embedded Matlab™ Function Blocks*, even though the *Model Based on Drag-and-Drop Boxes* could be developed to handle this implementation as well. The measurement data come from the 200 antenna elements in the demonstrator and their positions can be seen in *Figure 18*. As mentioned in section 2.4, the 96 elements in the middle are the ones not terminated into matched loads. Five of the element patterns, corresponding to the elements positioned at place 4, 43, 46, 48 and 94 in the figure, are used to create an average function corresponding to the diagram. The function is implemented in the antenna elements in the model and is therefore representing a model one step closer to a real antenna system.

191	181	177	173	169	165	161	157	153	149	145	141	137	133	129	125	121	117	107	97
192	182	178	174	170	166	162	158	154	150	146	142	138	134	130	126	122	118	108	98
193	183	91	85	79	73	67	61	55	49	43	37	31	25	19	13	7	1	109	99
194	184	92	86	80	74	68	62	56	50	44	38	32	26	20	14	8	2	110	100
195	185	93	87	81	75	69	63	57	51	45	39	33	27	21	15	9	3	111	101
196	186	94	88	82	76	70	64	58	52	46	40	34	28	22	16	10	4	112	102
197	187	95	89	83	77	71	65	59	53	47	41	35	29	23	17	11	5	113	103
198	188	96	90	84	78	72	66	60	54	48	42	36	30	24	18	12	6	114	104
199	189	179	175	171	167	163	159	155	151	147	143	139	135	131	127	123	119	115	105
200	190	180	176	172	168	164	160	156	152	148	144	140	136	132	128	124	120	116	106

Figure 18. Configuration of the elements in Drutten, seen from the front.

## 4 RESULTS

In this chapter, results from the simulated models are presented and analysed. The outcome from the different models, *Model Based on Drag-and-Drop Boxes* and *Model Composed by Embedded Matlab™ Function Blocks*, are compared and explained. As described in the theory (section 2.1.2), one way to present the performance of an array antenna is to present its radiation pattern. Most commonly, this pattern is presented in spherical coordinates and the results for the models are therefore plotted like this throughout the whole chapter. The simulations are done to show how the performance of the components influences the radiation pattern for the whole system. To distinguish characteristics easier, the cross-sections of the radiation pattern are presented as well.

During all simulations presented in this chapter, the parameter *regenerate\_modules* is set to *true* which imply that the T/R modules are unique, not only compared with the other modules, but also from one simulation to another. As long as the standard deviations are set to relatively low values, the regeneration of modules should not affect the outcome considerably.

### 4.1 OUTCOME FROM THE EMBEDDED MATLAB™ FUNCTION BLOCK MODEL

To demonstrate how the different parameters and components influence the system, figures illustrating the outcome from each block in the model are plotted. The first figure, representing the outcome from the *Field* block, illustrates the radiation pattern for an ideal untapered (uniform) planar array consisting of  $16 \times 6$  isotropic antenna elements, see *Figure 19*. The cross-section of this pattern is illustrated in *Figure 20* and shows a SLL of -13.2 dB, which is correct according to theory, see section 2.1. If counting the number of peaks between  $u = 0$  and  $u = 1$  (corresponding to half a period of the periodic array factor for this array with element separation  $\lambda/2$ ), including the main beam as one peak and multiplying it with two, the product represents the number of elements in the  $x$ -direction. The same can be performed for the  $v$ -plane resulting in the number of elements in the  $y$ -direction.

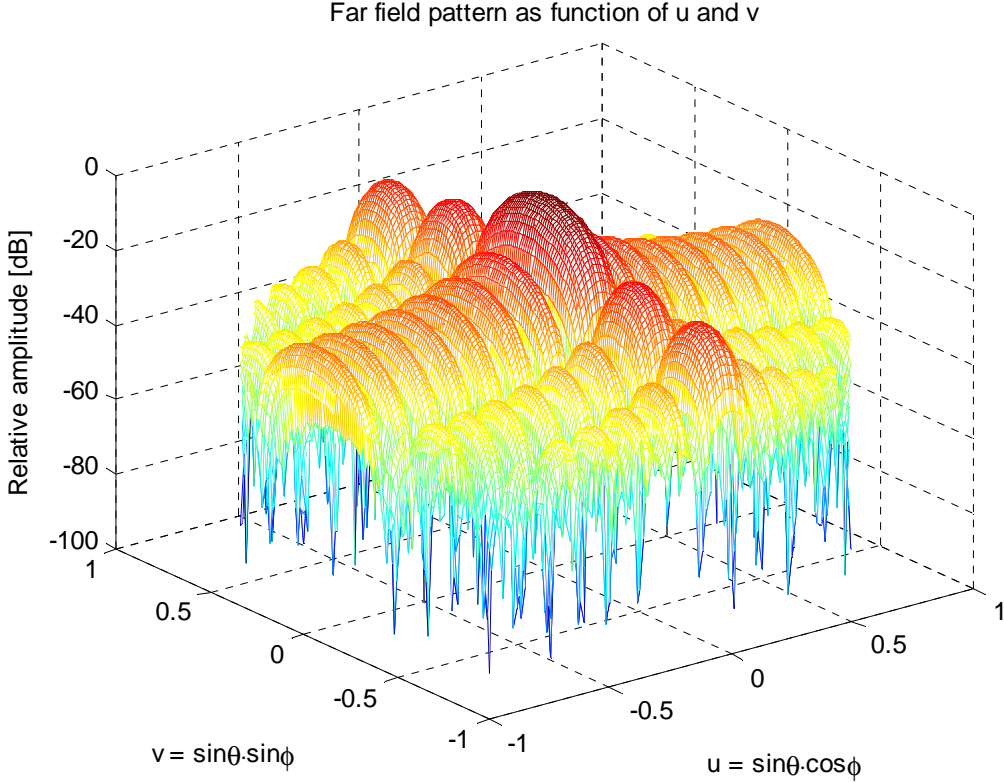


Figure 19. Radiation pattern for an ideal, uniform planar array with  $16 \times 6$  isotropic antenna elements.

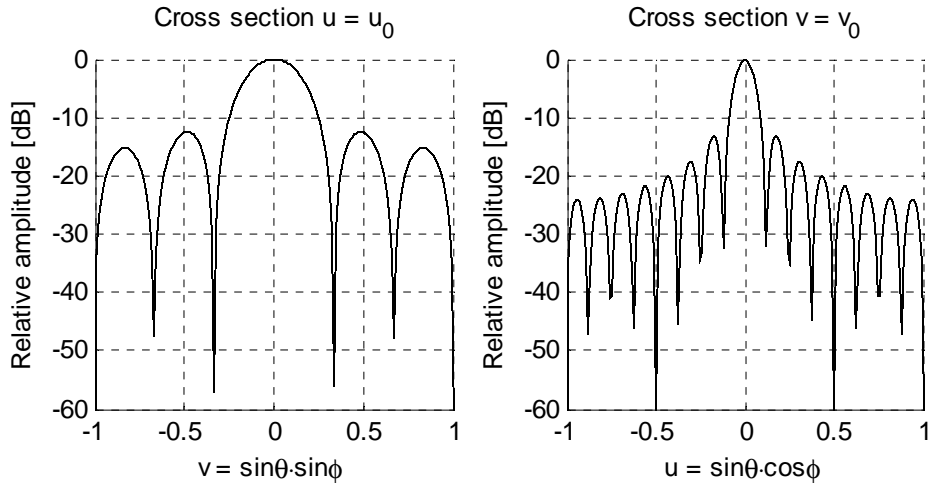
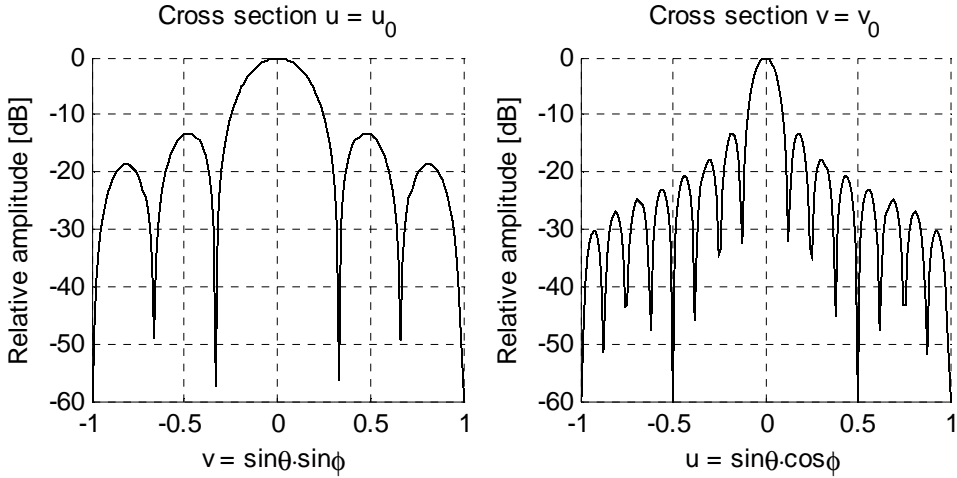


Figure 20. The cross-sections of the radiation pattern from the incoming field.  
Left:  $u=0, v=\sin\theta \sin\phi$     Right:  $u=\sin\theta \cos\phi, v=0$

To give a more realistic description of how the antenna elements radiate an element diagram is applied using a cosine shape in both  $u$ - and  $v$ -direction, according to *Equation 15* in section 2.6.3. The factor which cosine is superscript to is in this case 1.4 and result in a decreasing radiation for angles further away from zero. If the cosine factor is superscript to zero, the elements become isotropic which represent the case of the *Model Based on Drag-and-Drop Boxes*. The outcome with isotropic element patterns would be the same as in previous figure, since there is no contribution from the elements.

When the field has been received by the antenna elements and weighted by the element pattern, the radiation pattern has changed and can be seen in *Figure 21*. The difference with

the previous figure can be seen in the cross-section for  $u$ , where the level of the second side lobe has attenuated an extra 3 dB, at  $v = 0.81$ , compared to the left diagram in *Figure 20*. In the cross-section for  $v$ , every side lobe from the second one and further is attenuated, more or less, compared to the right diagram in *Figure 20*. The largest difference can be seen in the last side lobe where the attenuation has increased by more than 4 dB. The cosine factor is a projection and mismatch factor which increases with the angle and is the reason why the outer side lobes are affected the most.



*Figure 21. The cross-sections of the radiation pattern for an untapered planar array of  $16 \times 6$  antenna elements with cosine-shaped element patterns.*

*Left:  $u=0, v=\sin\theta\sin\phi$       Right:  $u=\sin\theta\cos\phi, v=0$*

If the antenna is electronically tilted, the phase shifters counteract the phase shifts which arise when the radiation is not incident perpendicular to the aperture. This means that the phase shifters are changed so the array is receiving in another direction than the main lobe. As can be seen in *Figure 22*, the main beam is pointed in  $u$  and  $v$  equal to 0.3536 which means the antenna is electronically tilted into  $\theta_0 = 30^\circ$  and  $\phi_0 = 45^\circ$ , according to *Equation 9* and *Equation 10* from the theory part (section 2.1.2). The cross-sections of  $u$  and  $v$  of the radiation pattern give a clearer view and can be seen in *Figure 23*.

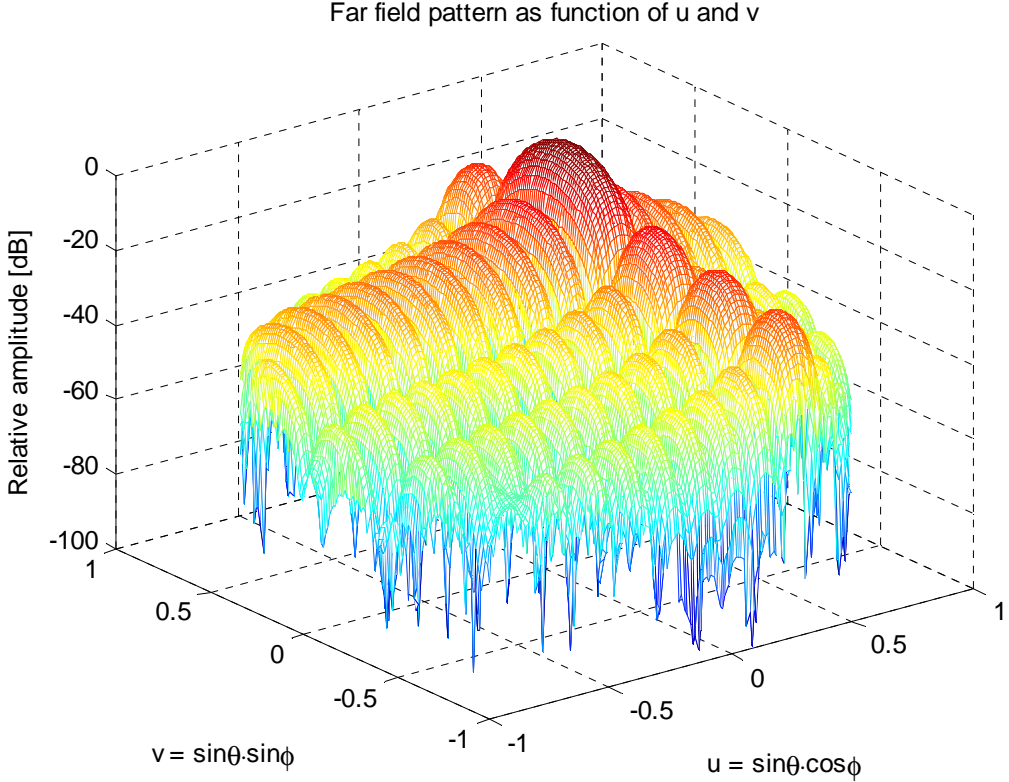


Figure 22. The radiation pattern when the beam is scanned to  $\theta=30^\circ$  and  $\phi=45^\circ$ .

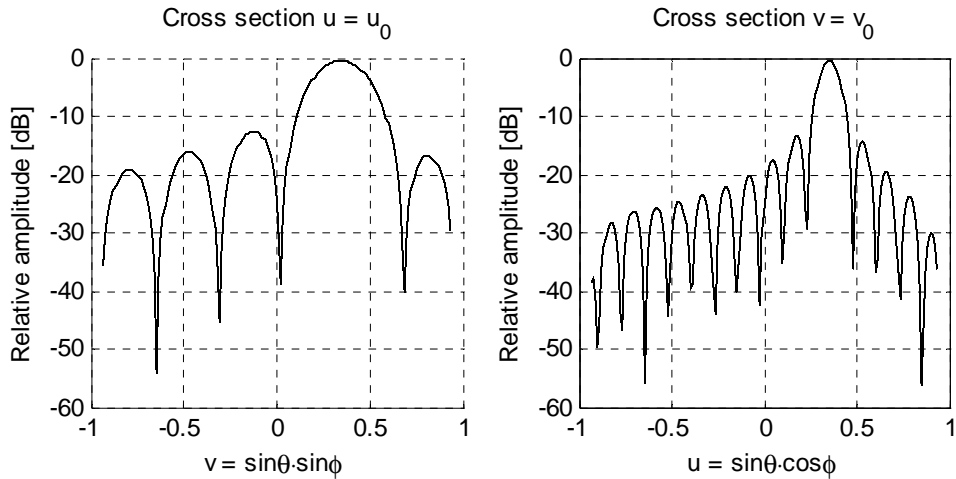


Figure 23. The cross-sections when the beam is scanned to  $\theta=30^\circ$  and  $\phi=45^\circ$ .

Left:  $u=0.3536$ ,  $v=\sin\theta \sin\phi$       Right:  $u=\sin\theta \cos\phi$ ,  $v=0.3536$ .

As mentioned in the theory (section 2.1), finite antennas cause side lobes and to decrease the side lobes a tapering can be applied to reduce the radiation from the elements near the edges. This result in lower side lobes but contributes to widen the main beam. To indicate the affect of tapering, a *Taylor 45 dB* tapering in  $x$ -direction and a *Taylor 30 dB* tapering in  $y$ -direction is applied and simulated. For both taperings, the number of side lobes with the same height is set to four and the result of the simulation can be seen in *Figure 24*. In the figure significant changes have occurred compared to *Figure 22*; the SLL has decreased and the main beam has become wider. In the left image in *Figure 25*, the cross-section of  $u$  is presented and since all the side lobes are lowered below -30 dB the desired tapering is obtained. In the right image the cross-section of  $v$  is presented, showing that the values for the first side lobes are adjusted to

the desired tapering value. The outer side lobes, further away from the main beam, are not tapered below -45 dB since the combination of the low tapering level and letting four side lobes have the same height is too hard to achieve. This result in a combination of the two criterions where all side lobes have been attenuated but the ones closest to the main beam are affected the most.

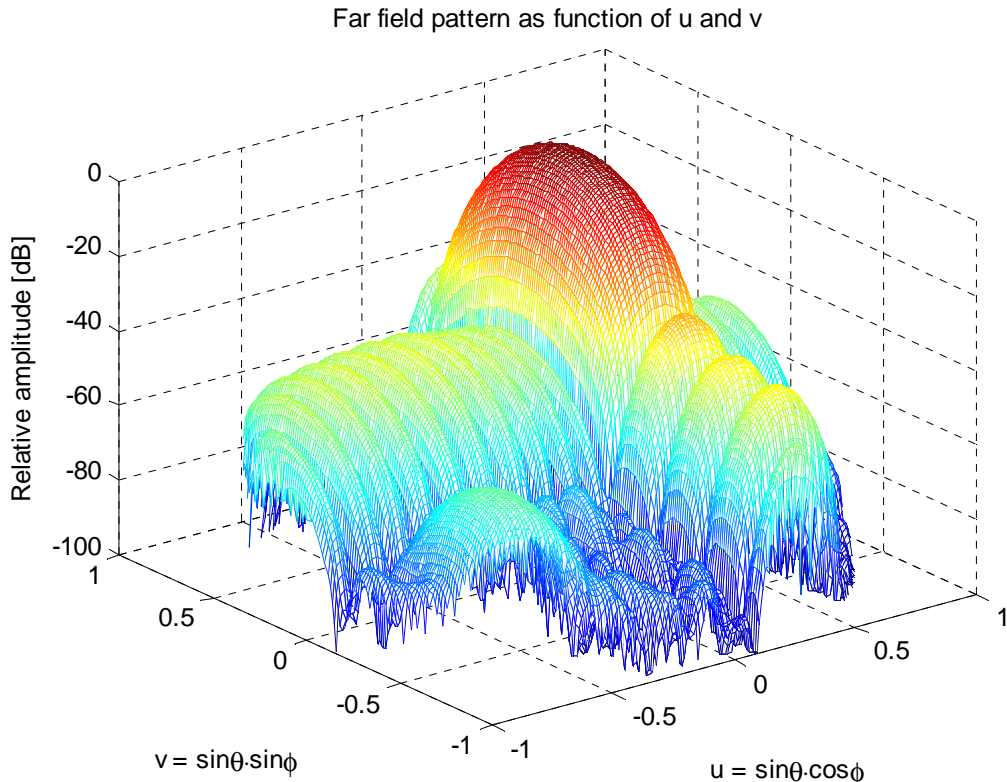


Figure 24. The radiation pattern using a Taylor tapering of -45 dB in x-direction and a -30 dB in y-direction.

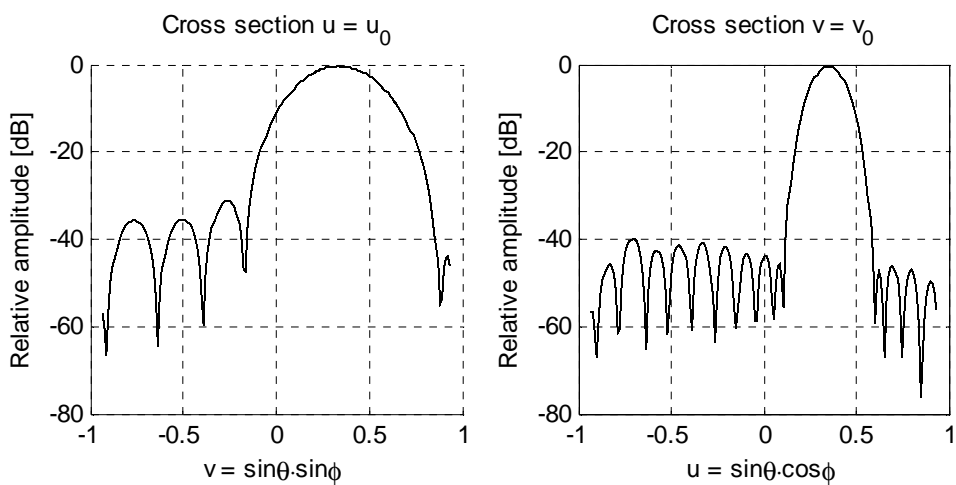
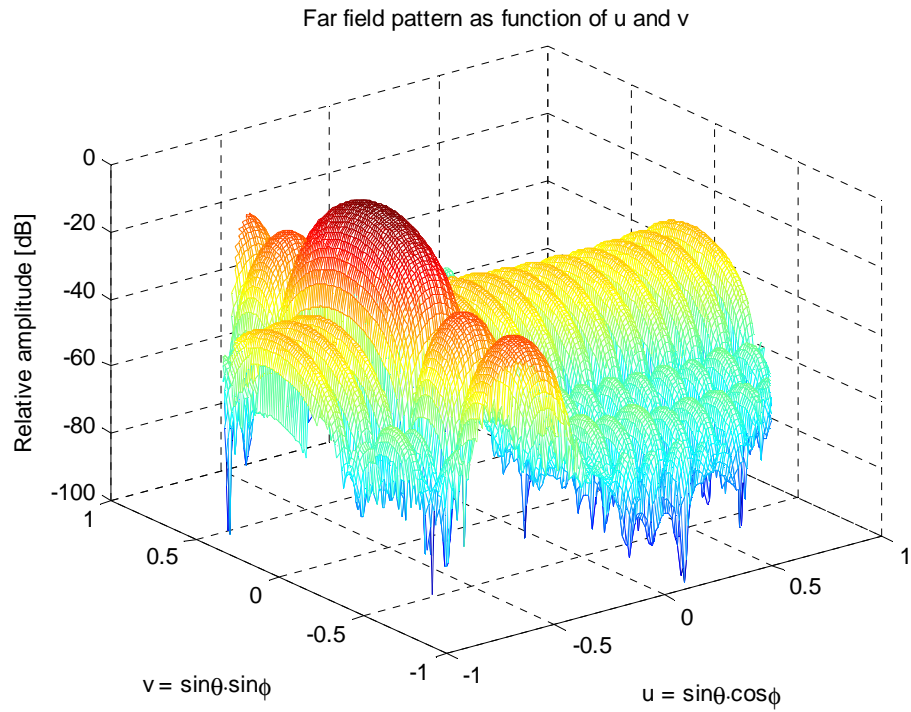


Figure 25. The cross-sections after a Taylor taper has been applied in the attenuator block.

Left:  $u=0.3536$ ,  $v=\sin\theta\sin\phi$ , with a Taylor tapering of -30 dB  
 Right:  $u=\sin\theta\cos\phi$ ,  $v=0.3536$ , with a Taylor tapering of -45 dB

To establish the fact that the two models, *Model Based on Drag-and-Drop Boxes* and *Model Composed by Embedded Matlab™ Function Blocks*, can be equally comparable a simulation

is done where the two models have the same values of their variables. If comparing *Figure 26* with *Figure 27* they are identical, which means the models are comparable.



*Figure 26.* A 3D plot of the Embedded Matlab™ system when steering the main beam into  $(30^\circ, 170^\circ)$  having a Taylor tapering of 30 dB in x-direction and a Taylor tapering of 20 dB in y-direction.

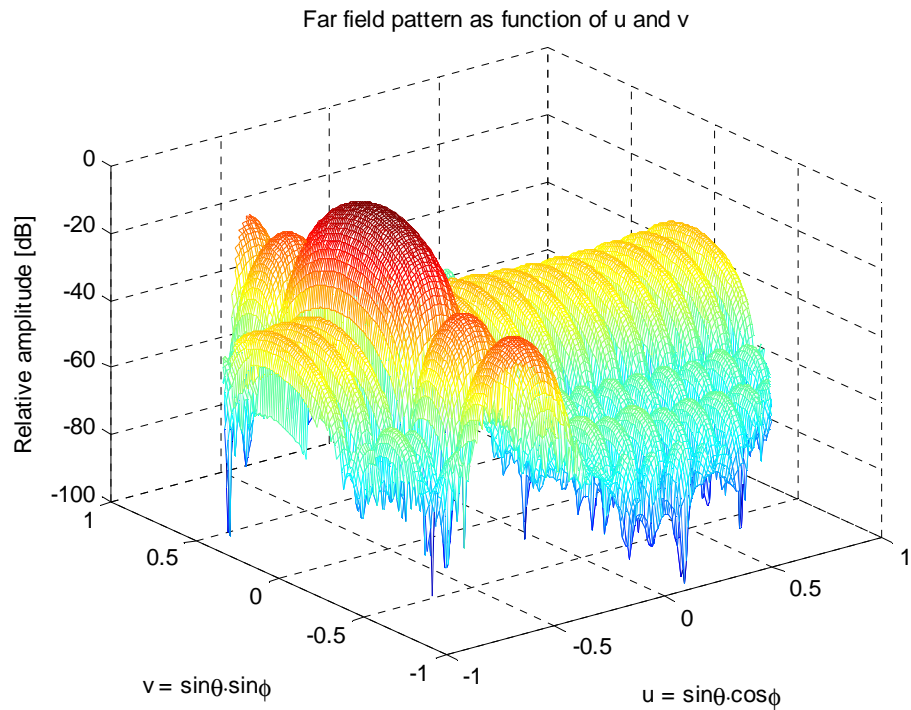


*Figure 27.* A 3D plot of the Drag-and-Drop system when steering the main beam into  $(30^\circ, 170^\circ)$  having a Taylor tapering of 30 dB in x-direction and a Taylor tapering of 20 dB in y-direction.

The performance and accuracy of phase shifters and attenuators depend on the number of bits which the components are manufactured for. In previous simulations, the number of bits was selected to nine, but to illustrate how a small number of bits affect the system, a simulation using five bits for both types of components is done. This low number of bits causes a larger space between each level that the phase shifter can adapt, according to *Equation 16*.

$$\text{phase level step} = \frac{360}{2^{\text{number of bits}}} \Rightarrow \frac{360}{2^5} = 11.25 \text{ } [^\circ] \quad \text{Equation 16}$$

When the main beam is directed into  $\theta_0 = 30^\circ$  and  $\phi_0 = 45^\circ$ , the phase at each antenna element is close to a multiple of the phase level step. Therefore will the influence on the radiation pattern not be so distinct, but as can be seen in *Figure 28*, the small amounts of bits have generated a high side lobe at approximately  $u$  and  $v$  equal to -0.5. Having low side lobes makes it easier to distinguish errors, since the magnitude of the errors is more comparable to the levels of the side lobes.

As can be seen in *Figure 29*, the performance of the attenuation of the side lobes is reduced. The tapering is set to attenuate 45 dB for the cross-section of  $v$ , but the outcome corresponds not even to *Taylor 30*. Since the figures are plotted in dB, errors at lower levels is much more prominent than for higher side lobes, therefore are the phenomena not as prominent in the cross-section of  $u$  compared to  $v$ .

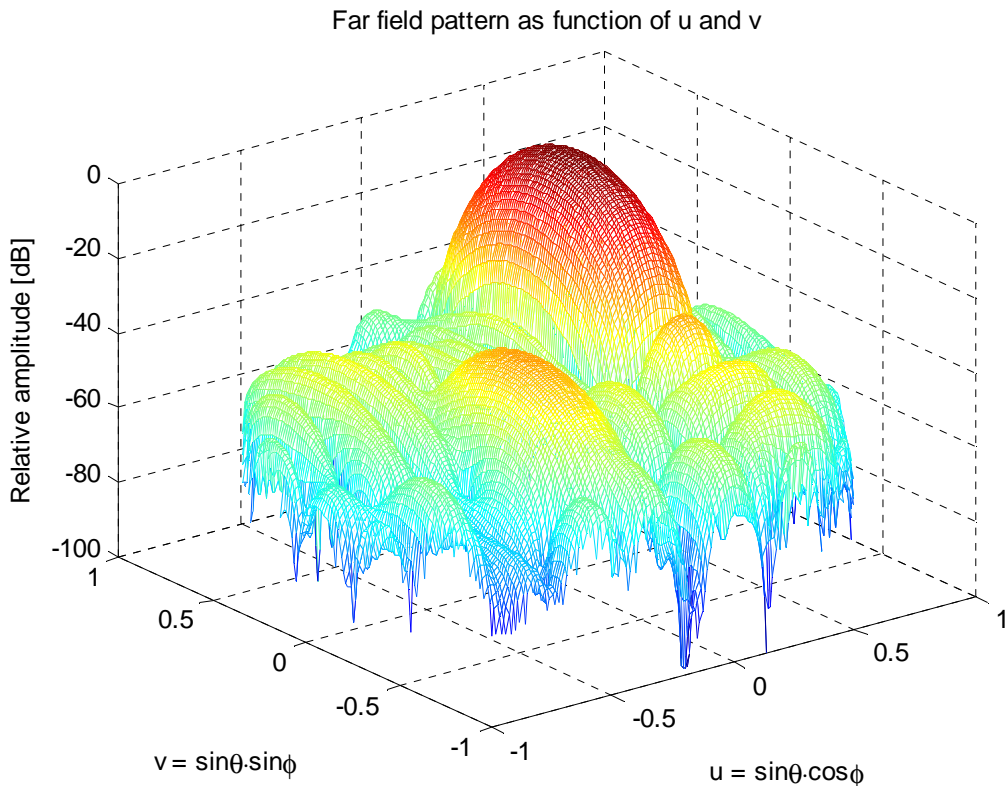


*Figure 28. The radiation pattern when having a low number of bits in attenuators and phase shifters, a Taylor tapering of -45 dB in x-direction and -30 dB in y-direction is applied.*

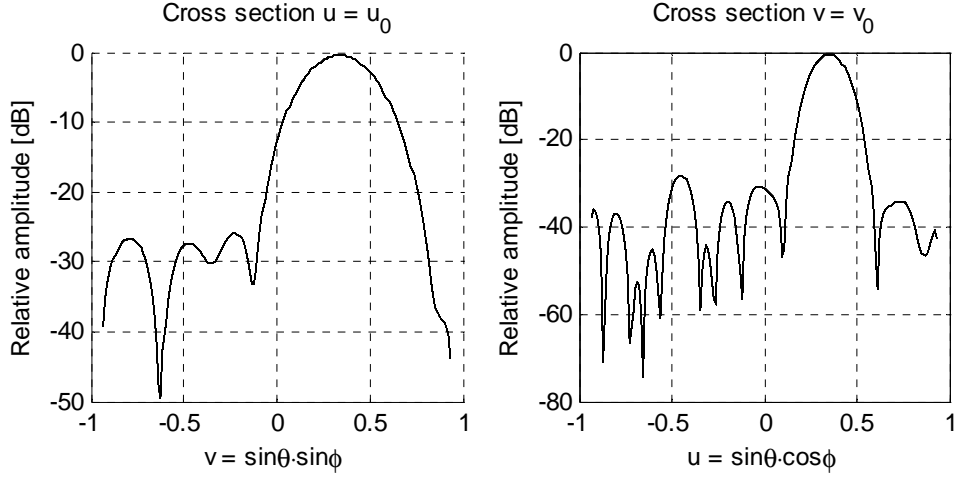


Figure 29. The cross-sections when having a low number of bits.

Left:  $u=0.3536$ ,  $v=\sin\theta \sin\phi$ , with a tapering of -30 dB

Right:  $u=\sin\theta \cos\phi$ ,  $v=0.3536$ , with a tapering of -45 dB.

Another issue that affects the performance of the phase shifters and the attenuators are the variation of the components when they are manufactured. To give a clear view of how these fluctuations affects the radiation results the number of bits is reset to nine and instead the standard deviation ( $\sigma$ ) of the phase and attenuation for the phase shifters and attenuators, respectively, is selected to 0.07. This standard deviation corresponds to a phase of  $4^\circ$  and an attenuation of 0.59 dB. The result of the variations can be seen in *Figure 30* and apart from the  $\sigma$  parameter all the variables have the same values as in *Figure 25*.

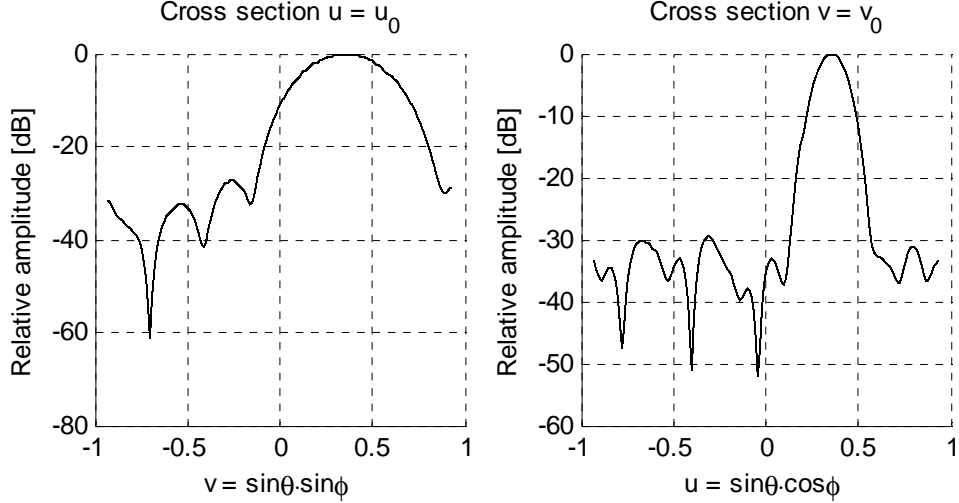
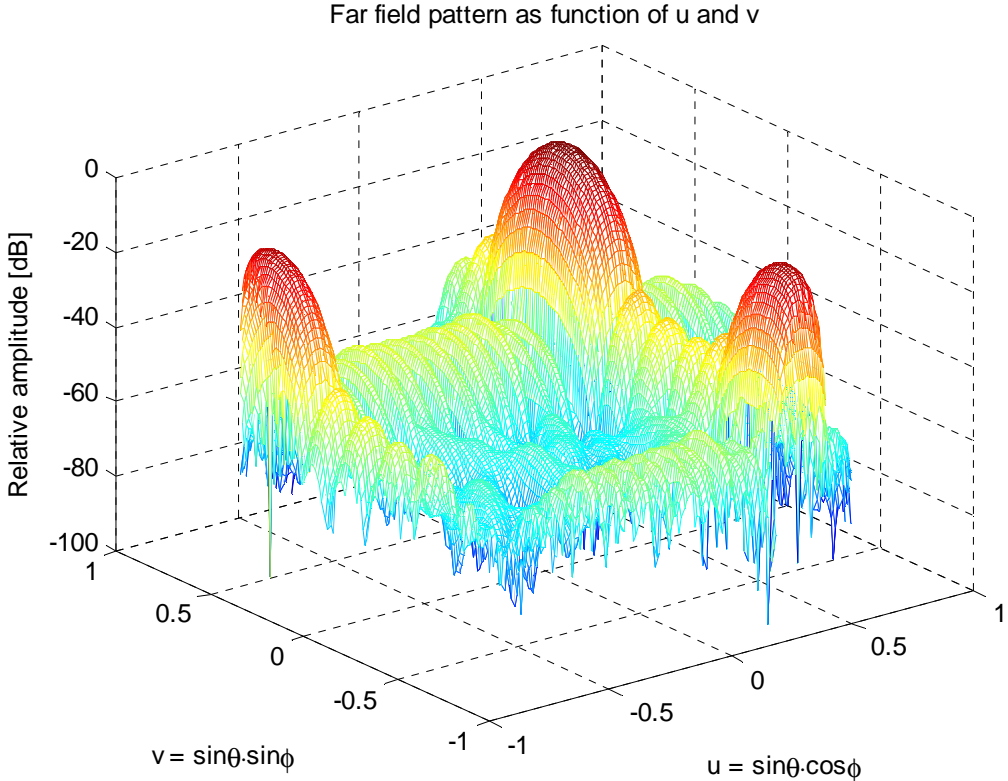


Figure 30. The cross-sections for  $\sigma=0.07$ .

Left:  $u=0.3536$ ,  $v=\sin\theta \sin\phi$ , with a Taylor tapering of -30 dB

Right:  $u=\sin\theta \cos\phi$ ,  $v=0.3536$ , with a Taylor tapering of -45 dB.

A simulation having an element spacing of  $0.8 \lambda$  in both  $x$ - and  $y$ -direction is done to illustrate the importance of having a not too big distance between the elements in the array (see section 2.1.1). These large distances between the elements cause grating lobes and as can be seen in *Figure 31*, two have appeared in the visible region when changing the distance from  $0.5 \lambda$  to  $0.8 \lambda$ .



*Figure 31. Grating lobes caused by a change in distance, from  $0.5 \lambda$  to  $0.8 \lambda$  in both x- and y-directions, between the elements in the array.*

## 4.2 IMPLEMENTATION FROM DRUTTEN

In this subchapter, the outcome of the model adapted to the receiver antenna demonstrator Drutten is presented. As mentioned earlier, the implementation is made using measurement data from the antenna elements in the demonstrator.

Measurement data from five of the active elements in Drutten, one in the middle and four at the edges, are used to estimate a common element pattern, see *Figure 18*. Since Drutten is built to have its best element pattern in the azimuth angle this is the one used for all of the five elements. The diagrams of the five elements and the estimated function are almost identical and can be seen in *Figure 32*. The patterns from the elements in the middle are very similar to the ones at the edges and therefore are a simplification of using the same diagram for all the elements a good approximation of the true antenna element performance.

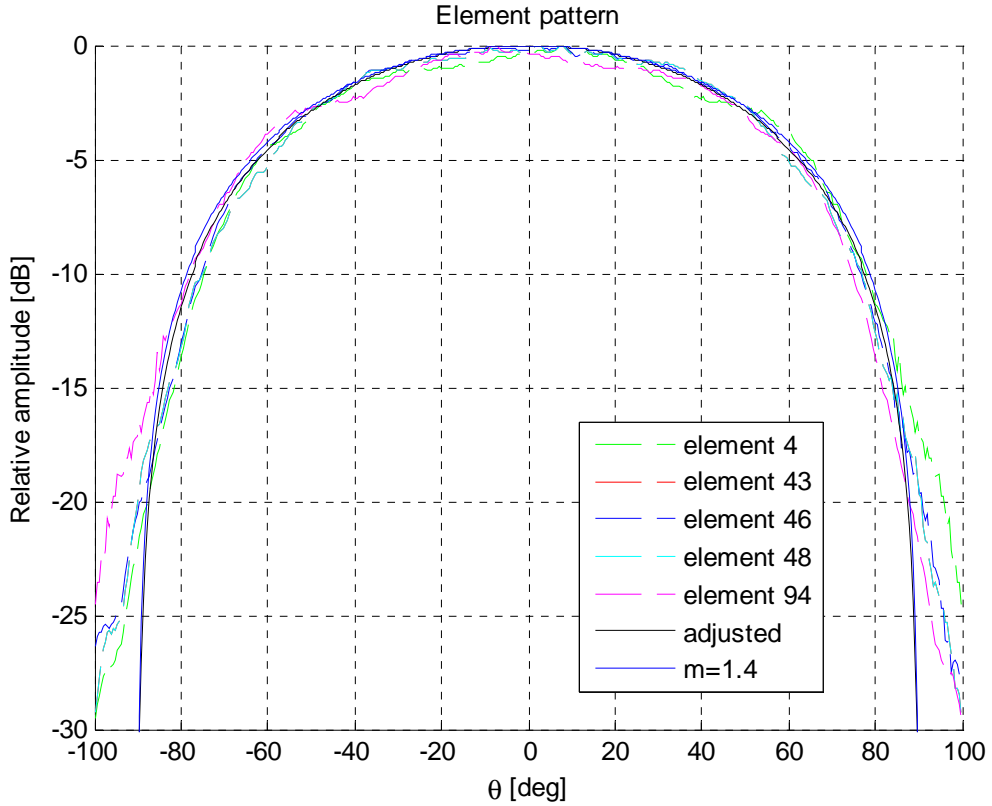


Figure 32. Element patterns from five elements in the demonstrator, the cosine shaped and the adjusted diagram.

The outcome of the *Antenna element* block is illustrated for three different element patterns; isotropic, cosine and adjusted. The latter is the one using the adapted diagram representing the element pattern from the elements in the demonstrator. It can be seen that the radiation pattern using the adjusted element is closer to the radiation pattern using the cosine shaped pattern than the isotropic one, see *Figure 33* and *Figure 34*. The largest difference, between the three different element patterns, can be distinguished at the last side lobes whereas the main beams of the three patterns are identical.

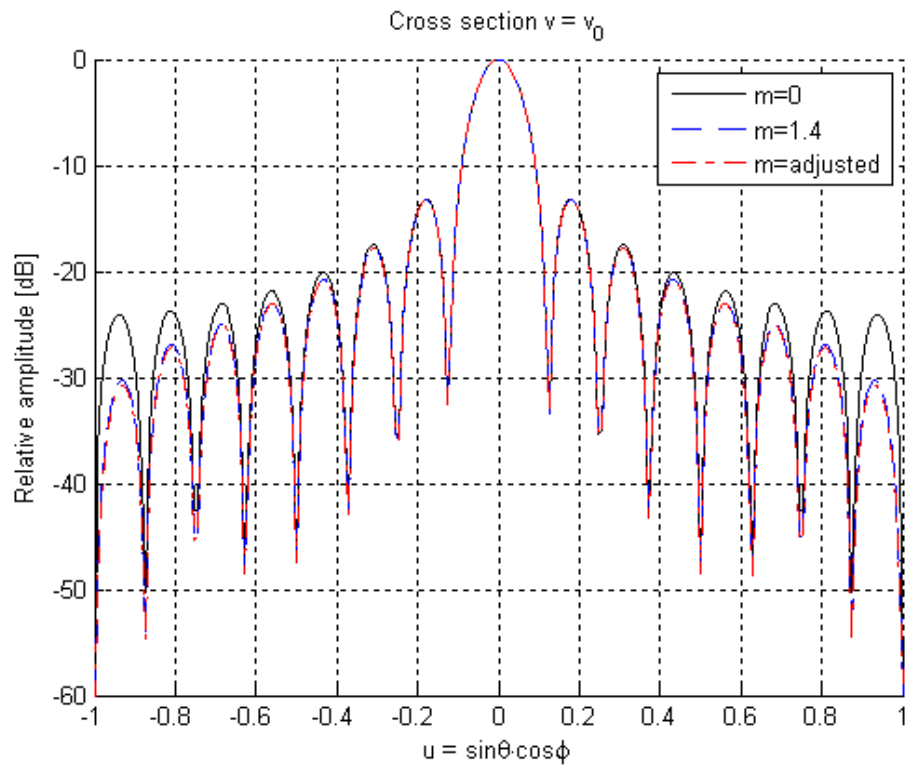


Figure 33. Radiation pattern for cross-section  $v$  after antenna element with isotropic, cosine and measured element diagram.

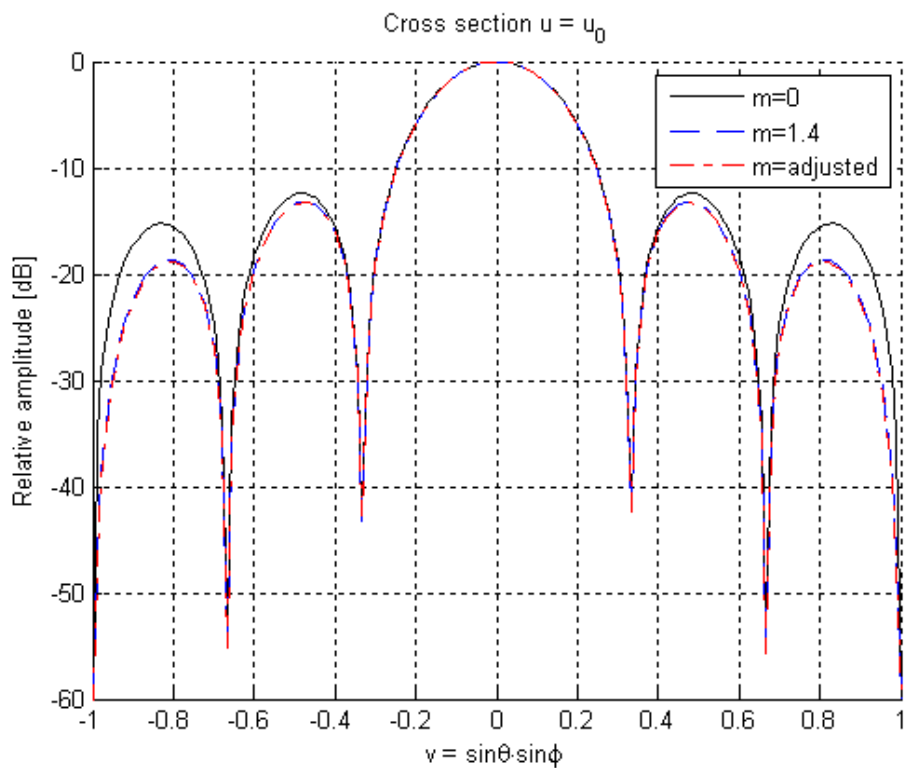


Figure 34. Radiation pattern for cross-section  $u$  using an antenna element with isotropic, cosine and measured element diagram.

## 5 DISCUSSION

In this work, an AESA system is implemented in two ways, both using Simulink<sup>®</sup> for simulations. The first, *Model Based on Drag-and-Drop Boxes*, is build with graphical code while the latter, *Model Composed by Embedded Matlab<sup>TM</sup> Function Blocks*, is implemented with textual scripts.

This chapter is made with the purpose to discuss the outcome of the simulations as well as present a comparison between the two different models. There is also a part that brings up the discussion about whether Simulink<sup>®</sup> is a good simulation tool for these kind of systems and how to continuing in a possible future work.

### 5.1 ADVANTAGES AND DISADVANTAGES

Even though Simulink<sup>®</sup> is a user-friendly tool and easy to understand for the first-time user, there are many functions and settings that might complicate things for the user before appreciating the benefits. For the simulations with drag-and-drop boxes, one limitation is the difficulty to implement an arbitrary size  $m \times n$  system since every box has to be connected to another and the parameters in these boxes are changed by hand. This can be made relatively easy and quickly for a small system with few components, but as the system grows, it becomes more time consuming and the risk for mistakes becomes substantial.

The model with Embedded Matlab<sup>TM</sup> Function blocks on the other hand is less complicated in the sense of giving a better overview of the system and is easier to change the size of the antenna systems. At first sight, the Embedded Matlab<sup>TM</sup> Function block gives the impression of having a code identical to the one used in Matlab<sup>®</sup> and even though there are many resemblances there are several differences as well. The Embedded Matlab<sup>TM</sup> Function block requires for instance that the size of the output is independent of the input and once a variable is defined, it can not be redefined to any other type or size. Furthermore, a difference from the regular Matlab<sup>®</sup> program is that the subset does not support matrix deletion. This might be seen as a drawback, but it opens up to reuse of matrixes and the user becomes encouraged to write more efficient code. The feature, the new way of writing code, might seem inconvenient for the experienced Matlab<sup>®</sup> programmer, since a part of the capacity in Matlab<sup>®</sup> functions can not be utilized.

Due to the fact that the Embedded Matlab<sup>TM</sup> Function block does not support some of the common Matlab<sup>®</sup> functions, alternative solutions to problems have been necessary. The command *cell* is one of the functions not supported by Embedded Matlab<sup>TM</sup> Function. Instead an alternative solution was created, where a matrix was used to give the impression of functioning as the command cell. In each element position another matrix was positioned, containing the scanned angles in both directions.

Another problem with the drag-and-drop concept has been to create realistic phase shifters and attenuators equal to the ones created in the model composed by embedded blocks. The idea was to use the textual script created for the model with Embedded Matlab<sup>TM</sup> Function and translate it into graphical code. In this way the drag-and-drop system would be modelled without intervention of Matlab<sup>®</sup>. Difficulties came up when trying to determine the closest possible phase value compared to the correct phase value. So far, a solution to the graphical translation has not been conceived and therefore, the textual script is used in both models.

One advantage with Simulink® is the generation of error message windows that appears when something in the model is incorrect. The message gives a short description on what is wrong and sometimes even gives a solution to the problem. For the simulations belonging to this thesis there have been error messages often related to *running low on memory* in the Embedded Matlab™ Function version, which can be described as one of the larger problems with this model. The model uses one matrix that is modified throughout the whole system. The size of this matrix depends on the number of elements and the amount of scanned values, which means that it becomes large for arrays with many elements and for radiation patterns with fine resolution. The running low on memory issue is an essential problem since array antennas often are composed by a large number of elements and requires a large amount of values to give an accurate result. To solve the problem, the Embedded Matlab™ Function version was modelled on a computer with higher *Random Access Memory* (RAM).

One of the key features with Simulink® is the ability of sampling. This feature has so far not been taken into consideration, but if, for instance, the angles of  $\theta$  are sampled and the outcome for each sample is saved, the result can be added together in the end. By using sampling this way, a possible result for the Embedded Matlab™ Function model is that a better and more refined model can be achieved since more values for the angles of  $\theta$  as well as  $\phi$  can be used without the problem of running low on memory. For the model based on the drag-and-drop concept, this use of sampling can result in, among other things, smaller matrixes.

## 5.2 FURTHER WORK

Since the model of the AESA is focused on the receive mode, one continuation of this work could be to develop the system such that a simulation in both receive and transmit mode are possible. Furthermore, another step could be to simulate the whole process of a radar; a signal from transmitting mode into receiving mode where the reflecting part is modelled using time sampling.

It is possible to continue to update the model in several ways. In particular all those parts, which have been modelled assuming ideal performance. The model of the antenna elements could for example be expanded to including mismatch, manufacturing differences and mutual coupling to give a more realistic result. The combining network is another part which could be further developed.

There is a possibility to expand the model and implement more components and their features, for example mixers and filters. Further more, aspects like noise temperature can be taken into consideration. Another possibility is to compare more of the measurement data from the demonstrator to see how close to reality the model can get. The model could also be expanded to take into account realistic noise figures, amplifier gain and system losses in order to evaluate the overall noise figure and S/N-ratio.

## **6 CONCLUSIONS**

There are many possibilities when using Simulink<sup>®</sup> to build models. The program has several different ways to create models and the numerous supplies of tools to perform the modelling are various. During the work, when modelling this large and complex AESA system, there are parts that have been hard to solve. If this is due to restrictions in Simulink<sup>®</sup> as a program, or if the knowledge about the software is too limited, cannot be firmly declared.

Two models were simulated, one based on the drag-and-drop concept and one composed by Embedded Matlab<sup>TM</sup> Function blocks, with the intention of having the same functionality. The models have several features that demonstrate the concept of a true AESA system, even though the system could be further developed. The two most important drawbacks with the latter model, is the insufficient flexibility and the large memory requirements. These questions need to be addressed during further developments of the model. Since the first model had problem-free simulations regarding the memory issue, a combination of the two models is likely to result in the best outcome.

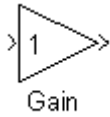
Simulink<sup>®</sup> makes it easy to focus on one component at a time and to develop and improve the functionality gradually. Furthermore, Simulink<sup>®</sup> is considerably easier to overview than a large Matlab<sup>®</sup> script because of the feature that the system can be divided into subboxes or Embedded Matlab<sup>TM</sup> Functions. The larger problems that have arisen so far have been solved, either in Simulink<sup>®</sup> or by contribution of Matlab<sup>®</sup>, so generally speaking, the software is a good tool for implementations of this kind.

## REFERENCES

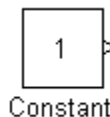
- Axberg, Stefan. (2005). *Tekniken skriver krigshistorien*. (Electronic) <[http://www.foi.se/FOI/templates/Page\\_\\_\\_\\_3930.aspx](http://www.foi.se/FOI/templates/Page____3930.aspx)> (17 December 2008)
- Balanis, Constantine A. (2005). *Antenna Theory: Analysis and Design*. 3<sup>rd</sup> ed. Hoboken, New Jersey. John Wiley & Sons.
- Kildal, Per-Simon (2000). *Foundations of Antennas: A Unified Approach*. Lund, Studentlitteratur.
- Lanne, Maria. (2005). *Antenna Arrays System: Electromagnetic and Signal Processing Aspects* Lic. Chalmers University of Technology. Gothenburg, Chalmers Reproservice.
- Mathworks™. (2008a). *Embedded MATLAB™ Getting Started Guide*. (Electronic) PDF: <[http://www.mathworks.com/access/helpdesk/help/pdf\\_doc/eml/eml\\_gs.pdf](http://www.mathworks.com/access/helpdesk/help/pdf_doc/eml/eml_gs.pdf)> p. 15 (9 February 2009)
- Mathworks™. (2008b). *Simulink® 7.2*. (Electronic) <<http://www.mathworks.com/products/simulink/description1.html>> (29 September 2008)
- Mathworks™. (2008c). *Simulink® 7 User's Guide*. (Electronic) PDF: <[http://www.mathworks.com/access/helpdesk/help/pdf\\_doc/simulink/sl\\_using.pdf](http://www.mathworks.com/access/helpdesk/help/pdf_doc/simulink/sl_using.pdf)> pp. 172-178. (9 February 2009)
- Mailloux Robert J. (2005) *Phased Array Antenna Handbook*. 2<sup>nd</sup> ed. Norwood, USA. Artech House
- Moernaut, Gerald J.K. & Orban, Daniel L. (2006). *The Basics of Antenna Arrays*. (Electronic) PDF: <[http://www.orbanmicrowave.com/The\\_Basics\\_of\\_Antenna\\_Arrays.pdf](http://www.orbanmicrowave.com/The_Basics_of_Antenna_Arrays.pdf)> (2 October 2008)
- Nilsson Drackner, Peter & Engström, Björn. (2005) An Active Antenna Demonstrator for Future AESA- Systems. In: IEEE International, *Proceedings of the International Radar Conference 2005*. Arlington, VA, USA. 9-12 May, 2005.
- Pozar, David M. (2001). *Microwave and RF design of wireless systems*. John Wiley & Sons.
- Skolnik, Merrill I. (2001). *Introduction to Radar Systems*. 3<sup>rd</sup> ed. New York. McGraw-Hill.
- Stimson, George W. (1998). *Introduction to Airborne Radar*. 2<sup>nd</sup> ed. Mendham, USA. SciTech Publishing.
- Visser, Hubregt J. (2005). *Array and Phased Array Antenna Basics*. Chichester, England. John Wiley & Sons.
- Wennberg, Anna. (2007). *Se, snacka och stör med samma antenn*. (Electronic) <<http://etn.se/22546>> (2 February 2009)

## APPENDIX A: SIMULINK® BLOCKS

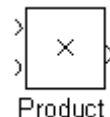
A short presentation of the different block used in the drag-and-drop model.



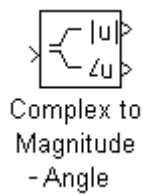
*Gain:* The gain block multiplies the input by a constant value and accepts a real or complex scalar, vector, or matrix of any data type supported by Simulink® software. If the input of the gain block is real and the gain is complex, the output will also be complex.



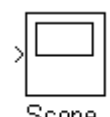
*Constant:* The constant block generates a real or complex constant value. This can be done with a scalar, vector, or matrix output, depending on the dimensionality of the constant value parameter and the setting of the interpret vector parameters as 1-D parameter. The output of the block has the same dimensions and elements as the constant value parameter.



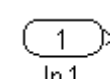
*Product:* The product block performs multiplication or division of its inputs. This block produces outputs using either element-wise or matrix multiplication, depending on the value of the multiplication parameter. The product block accepts real or complex signals of any data type supported by Simulink® software including fixed-point data types.



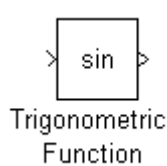
*Complex to Magnitude - Angle:* The complex to magnitude-angle block accepts a complex-valued signal of type double or single. Its outputs, the magnitude and/or phase angle of the input signal, depend on the setting of the output parameter and are real values of the same data type as the block input. The input can be an array of complex signals, in which case the output signals are arrays. The magnitude signal array contains the magnitudes of the corresponding complex input elements, while the angle output contains the angles of the input elements.



*Scope:* The scope block displays its input with respect to simulation time. The scope block can have multiple axes (one per port) and all axes have a common time range with independent y-axes. The scope block allows you to adjust the amount of time and the range of input values displayed.



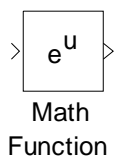
*Inport:* Inport blocks are the links from outside a system into the system are common in subboxes.



*Trigonometric function:* The trigonometric function block performs numerous common trigonometric functions as: sin, cos, tan, asin, acos, atan, atan2, sinh, cosh, tanh, asinh, acosh, and atanh. The output of the block is a result of the function using one or more inputs. The trigonometric function block accepts input signals as real or complex of type double.

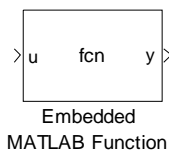


*Sum block:* The sum block performs addition or subtraction on its inputs. This block can add or subtract scalar, vector or matrix inputs, it can also collapse the elements of a signal.



Math Function

*Math function:* The Math Function block performs numerous common mathematical functions using exponential, transpose, square root, reciprocal and many more. The block output is the result of the operation of the function on the input or inputs and both real and complex inputs are accepted, except for reciprocal and square root.



Embedded MATLAB Function

*Embedded Matlab Function:* An Embedded Matlab™ Function block lets the user compose a Matlab function within a Simulink model. The user can specify input and output data to the Embedded Matlab Function block in the function header as arguments and return values. The Embedded Matlab Function block supports a subset of the language for which it can generate efficient embeddable code.<sup>30</sup>

---

<sup>30</sup> <<http://www.mathworks.com/access/helpdesk/help/toolbox/simulink/index.html?/access/helpdesk/help/toolbox/simulink/>> (31 mars 2009)

## APPENDIX B: DRAG AND DROP 'GENERATE\_PARAMETERS.M'

```

for y = 1:elem_y
    [rte,index] = min(abs(ideal_vec - wanted_phase(y,x)));
    error_vec = mu_phase_shifter + sigma_phase_shifter.*randn(1);
    exist_phase(y,x) = ideal_vec(index) + error_vec;
end
end

pos = [find(exist_phase < 0)];
for z = 1:length(pos)
    exist_phase(pos(z)) = 0;
end
pos = [find(exist_phase > 2*pi)];
for z = 1:length(pos)
    exist_phase(pos(z)) = 2*pi;
end

clear ideal_vec error_vec x y pos;

% Attenuator
% Create one unique attenuator for each antenna element using a normal
% distributed random function

exist_tapering = zeros(length(elem_y),length(elem_x));
wanted_tapering = tap_y_vec'*tap_x_vec;
ideal_vec = linspace(0,1,2^attenuation_bit+1);

for x = 1:elem_x
    for y = 1:elem_y
        [rte,index] = min(abs(ideal_vec - wanted_tapering(y,x)));
        error_vec = mu_attenuator + sigma_attenuator.*randn(1);
        exist_tapering(y,x) = ideal_vec(index) + error_vec;
    end
end

pos = [find(exist_tapering < 0)];
for z = 1:length(pos)
    exist_tapering(pos(z)) = 0;
end
pos = [find(exist_tapering > 2*pi)];
for z = 1:length(pos)
    exist_tapering(pos(z)) = 2*pi;
end

clear ideal_vec error_vec x y pos;
end

exist_tapering = exist_tapering';
exist_phase = exist_phase';
clear bits attenuator x y p circular_attenuator min_value max_value;
clear wanted_tapering;

```

## APPENDIX C: DRAG AND DROP 'EDIT\_PARAMETERS.M'

```
clc;

% Edit parameters for simulation
% Press SAVE before returning to the simulink model.

% Antenna geometry
dx = 0.5; % Element separation in x direction [lambda]
dy = 0.5; % Element separation in y direction [lambda]
p_theta = 181; % The number of points in theta direction
p_phi = 181; % The number of points in phi direction
m = 0; % Factor used to raise cosinus, in this model it has to be zero

% Phase shifter
theta_0 = 0; % Steering in theta direction, range: 0-90 [degrees]
phi_0 = 0; % Steering in phi direction, range: 0-360 [degrees]
mu_phase_shifter = 0; % Mean for normal distribution
sigma_phase_shifter = 0.00; % Standard deviation for normal distribution
phase_bit = 9; % Number of bits

% Attenuator
mu_attenuator = 0; % Mean for normal distribution
sigma_attenuator = 0.00; % Standard deviation for normal distribution
attenuation_bit = 9; % Number of bits
sll_x = 0; % Reduce side lobe level in x direction, set to zero if
untapered [dB]
sll_y = 0; % Reduce side lobe level in y direction, set to zero if
untapered [dB]
nn_x = 4; % Number of affected nulls
nn_y = 4; % Number of affected nulls

% Set 'true' if new receiver modules are wanted, 'false' if latest modules
% should be used. First time the parameter should be set to 'true'.
regenerate_modules = 'true';

% SAVE and return to the Simulink model

%%
% Fixt in the drag-and-drop model
elem_x = 16; % The total number of antenna elements in x direction
elem_y = 6; % The total number of antenna elements in y direction
run('H:\Simulink\Slutgiltiga Simulinkmodeller\phase_attenuation.m');
```

## APPENDIX D: EMBEDDED MATLAB™ FUNCTION BLOCKS

```

m = parameter_vec(5);
% theta_0 = parameter_vec(6);
% phi_0 = parameter_vec(7);

% Two eligible element patterns where the second is the adjusted
% an = sqrt(cos(theta).^complex(m));
% approximated element pattern
an = 1.7*sqrt((cos(theta)).^(2.2));

antenna = ones(length(phi),1) * an;

a = 0;
b = 0;
for y = 1:tot_y
    for x = 1:tot_x
        matrix_in(b+(1:length(phi)),a+(1:length(theta))) =
matrix_in(b+(1:length(phi)),a+(1:length(theta))).*antenna;
        a = a + length(theta);
    end
    a = 0;
    b = b + length(phi);
end

out = matrix_in;

% ~ ~ ~ ~ ~ ~ ~ ~ ~ ~ ~ ~ ~ ~ ~ ~ ~ ~ ~ ~ ~ ~ ~ ~ ~ ~ ~ ~ ~ ~ ~ ~ ~ ~ ~ ~ ~ ~ ~ ~ ~ ~ ~ ~ ~ ~ ~ ~ ~ ~ ~ ~ ~
% LNA block
function out = LNA(in, theta_vec, phi_vec, parameter_vec)

matrix_in = in;
theta = theta_vec;
phi = phi_vec;

% Parameter vector
% tot_x = parameter_vec(1);
% tot_y = parameter_vec(2);
% dx = parameter_vec(3);
% dy = parameter_vec(4);
% m = parameter_vec(5);
% theta_0 = parameter_vec(6);
% phi_0 = parameter_vec(7);

% Parameters and matrixes out
out = matrix_in;

% ~ ~ ~ ~ ~ ~ ~ ~ ~ ~ ~ ~ ~ ~ ~ ~ ~ ~ ~ ~ ~ ~ ~ ~ ~ ~ ~ ~ ~ ~ ~ ~ ~ ~ ~ ~ ~ ~ ~ ~ ~ ~ ~ ~ ~ ~ ~ ~ ~ ~ ~ ~ ~
% Phase shifter block
function out = phase_shifter(in, theta_vec, phi_vec, parameter_vec,
exist_phase)

matrix_in = in;
theta = theta_vec;
phi = phi_vec;

% Parameter vector
tot_x = parameter_vec(1);
tot_y = parameter_vec(2);

```





```

% 3D plot with theta, phi and u,v (u=sin(theta)*cos(phi),
v=sin(theta)*sin(phi))
figure(1);
subplot(2,2,1);
mesh(theta_deg,phi_deg,output);
title('Beam function as a function of \theta and \phi');
ylabel('\phi [deg]');
xlabel('\theta [deg]');
zlabel('Relative amplitude [dB]');

subplot(2,2,2);
mesh(u_new,v_new,output_new);
title('Far field pattern as function of u and v');
xlabel('u = sin\theta\cdot cos\phi');
ylabel('v = sin\theta\cdot sin\phi');
zlabel('Relative amplitude [dB]');

output = output_new;
subplot(2,2,3);
plot(u_new',output(cross_v,:),'k');
title('Cross section v = v_0');
xlabel('u = sin\theta\cdot cos\phi');
ylabel('Relative amplitude [dB]');

subplot(2,2,4);
plot(v_new,output(:,cross_u),'b')
title('Cross section u = u_0')
xlabel('v = sin\theta\cdot sin\phi');
ylabel('Relative amplitude [dB]');

```

## APPENDIX E: EMBEDDED MATLAB™ ‘EDIT\_PARAMETERS.M’

```
%clearvars -except phase_shifter exist_phase exist_attenuator, clc, clf;
close(figure(1))

%% Edit parameters
% Edit parameters for simulation
% Press SAVE before returning to the simulink model.

% Antenna geometry
tot_x = 16; % The total number of antenna elements in x direction
tot_y = 6; % The total umber of antenna elements in y direction
dx = 0.5; % Element separation in x direction [lambda]
dy = 0.5; % Element separation in y direction [lambda]
m = 1.4; % Factor used to raise cosinus, i.e. sqrt(cos^m)

% Phase shifter
theta_0_deg = 0; % Steering in theta direction, range: 0-90 [degrees]
phi_0_deg = 0; % Steering in phi direction, range: 0-360 [degrees]
mu_phase_shifter = 0; % Mean for normal distribution
sigma_phase_shifter = 0.0; % Standard deviation for normal distribution
phase_bit = 9; % Number of bits

% Attenuator
mu_attenuator = 0; % Mean for normal distribution
sigma_attenuator = 0.0; % Standard deviation for normal distribution
attenuation_bit = 9; % Number of bits
sll_x = 0; % Reduce side lobe level in x direction, set to zero if
untapered [dB]
sll_y = 0; % Reduce side lobe level in y direction, set to zero if
untapered [dB]
nn_x = 4; % Number of affected nulls
nn_y = 4; % Number of affected nulls

% Simulation parameters
% If a cross section is wanted, set one of the variables equal to one.
points_theta = 181; % Number of points in theta vector
points_phi = 181; % Number of points in phi vector

% Set 'true' if new receiver modules are wanted, 'false' if latest modules
% should be used.
regenerate_modules = 'true';

% SAVE and return to the Simulink model

run('~/home/emwawik/matlab/jenny_josefina/generate_parameters.m');
```

## APPENDIX F: EMBEDDED MATLAB™ ‘GENERATE\_PARAMETERS.M’

```

%% Calculations based on edited parameters ~ ~ ~ ~ ~ ~ ~ ~ ~ ~ ~ ~ ~ ~ ~ ~ ~ ~ ~ ~ ~
% Transformation from degrees to radians
theta_0 = theta_0_deg*(2*pi/360);
phi_0 = phi_0_deg*(2*pi/360);

% Input parameters to the simulink model
parameter_vec = [tot_x, tot_y, dx, dy, m, theta_0, phi_0];
theta_vec = linspace(0,pi/2,points_theta);
phi_vec = linspace(0,2*pi,points_phi);

% Taylor tapering
% Used in the attenuator
if sll_x > 0;
    tap_x_vec = taylortap_lin(tot_x,nn_x,sll_x);
else
    tap_x_vec = ones(1,tot_x);
end

if sll_y > 0;
    tap_y_vec = taylortap_lin(tot_y,nn_y,sll_y);
else
    tap_y_vec = ones(1,tot_y);
end

matrix_in = j*ones(tot_y*length(phi_vec),tot_x*length(theta_vec));

%
clear nn_x nn_y phi_0_deg theta_0_deg points_phi points_theta sll_x sll_y;

%% generate_receiver ~ ~ ~ ~ ~ ~ ~ ~ ~ ~ ~ ~ ~ ~ ~ ~ ~ ~ ~ ~ ~ ~ ~ ~ ~ ~ ~ ~ ~ ~ ~ ~ ~ ~

if regenerate_modules strcmp(regenerate_modules,'true');
    % LNA
    % Create one unique phase shifter for each antenna element using a normal
    % distributed random function.

    % Phase shifter
    % Create one unique phase shifter for each antenna element using a normal
    % distributed random function.

exist_phase = zeros(length(tot_y),length(tot_x));
for x = 1:tot_x
    for y = 1:tot_y
        wanted_phase(y,x) = 2*pi*sin(theta_0)*((x-1)*dx*cos(phi_0)+
            (y-1)*dy*sin(phi_0));
        if wanted_phase(y,x) > 2*pi || wanted_phase(y,x) < -(2*pi)
            wanted_phase(y,x) = mod(wanted_phase(y,x),2*pi);
        end
        if wanted_phase(y,x) < 0
            wanted_phase(y,x) = wanted_phase(y,x) + 2*pi;
        end
    end
end

ideal_vec = linspace(0,2*pi,2^phase_bit+1);

```

```

for x = 1:tot_x
    for y = 1:tot_y
        [rte,index] = min(abs(ideal_vec - wanted_phase(y,x)));
        error_vec = mu_phase_shifter + sigma_phase_shifter.*randn(1);
        exist_phase(y,x) = ideal_vec(index) + error_vec;
    end
end

pos = [find(exist_phase < 0)];
for z = 1:length(pos)
    exist_phase(pos(z)) = 0;
end
pos = [find(exist_phase > 2*pi)];
for z = 1:length(pos)
    exist_phase(pos(z)) = 2*pi;
end

clear ideal_vec error_vec x y pos;

% Attenuator
% Create one unique attenuator for each antenna element using a normal
% distributed random function

exist_attenuator = zeros(length(tot_y),length(tot_x));
wanted_tapering = tap_y_vec'*tap_x_vec;
ideal_vec = linspace(0,1,2^attenuation_bit+1);

for x = 1:tot_x
    for y = 1:tot_y
        [rte,index] = min(abs(ideal_vec - wanted_tapering(y,x)));
        error_vec = mu_attenuator + sigma_attenuator.*randn(1);
        exist_attenuator(y,x) = ideal_vec(index) + error_vec;
    end
end

pos = [find(exist_attenuator < 0)];
for z = 1:length(pos)
    exist_attenuator(pos(z)) = 0;
end
pos = [find(exist_attenuator > 2*pi)];
for z = 1:length(pos)
    exist_attenuator(pos(z)) = 2*pi;
end

clear ideal_vec error_vec x y pos;
end

% exist_attenuator = exist_attenuator';
% exist_phase = exist_phase';
clear bits attenuator x y p circular_attenuator min_value max_value;
clear wanted_tapering;

```

## APPENDIX G: *MATLAB SCRIPT ‘TAYLORTAP\_LIN’*

```
function excitering=taylortap_lin(length,nn,s1)
%TAYLORTAP_LIN Beräknar exciteringar för linjär gruppantenn med lika
%avstånd mellan antennelementen
%
% TAYLORTAP_LIN(length,nn,s1)
%   length: antal element
%   nn: antal lika stora sidlober innan dämpningen ökas
%   s1:hur många dB första sidloben ska vara dämpad
% EXEMPEL:EX=taylortap_lin(41,6,25)
%   beräknar exciteringen för 41 element
%   där de 6 första sidloberna på varje sida är dämpade 25 dB i
%   förhållande till huvudloben. Sedan dämpas efterföljande
%   sidlober ytterligare med sin(x)/x. Resultatet ges som
%   utparameter i vektor EX.
```

## Design

# Designing Next-Generation AESA Radar



**Figure 1:** Products within the NI AWR Design Environment provide circuit, system and EM analysis along with interoperability to 3rd party design flows

The complexity and cost of developing systems based on phased arrays are being addressed through new functionality in electronic design automation (EDA) software, supporting designers with the means to develop new system architectures, component specifications, implement the physical design of individual components, and verify performance prior to prototyping. This article discusses these trends and presents recent advances in EDA tools for phased array based systems.

Dr. Gent Paparisto, Joel Kirshman and David Vye,  
AWR Group, NI

## Phased Array Primer

With electronically steered antennas, an array of individual radiating elements whose phase and amplitude are controlled either digitally, through analog/RF components or by using hybrid techniques to control beam direction without the need to physically move the antenna. Phase and amplitude control of the input signal to the individual elements provides steerable directivity of the antenna beam over both azimuth and elevation.

The design considerations for an actively scanned electronic array (AESA) radar include the individual radiating elements (antenna design), the RF link budget of the feed network, which is directly tied to component performance such as insertion losses and impedance mismatch, as well as the array itself.

Given the complexity of the task, design groups need a system-aware approach that allows team members to explore phased array behavior from different levels

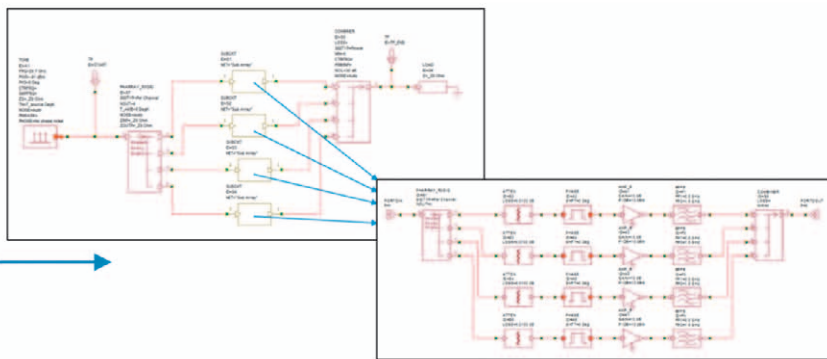
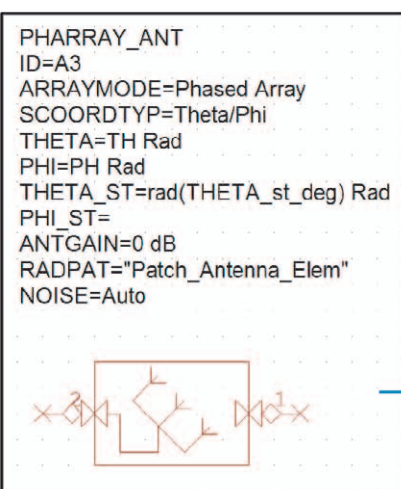


**Figure 2:** a) Single phased array element can model large scale (1000s of elements) arrays, replacing b) system designs based on individually defined elements

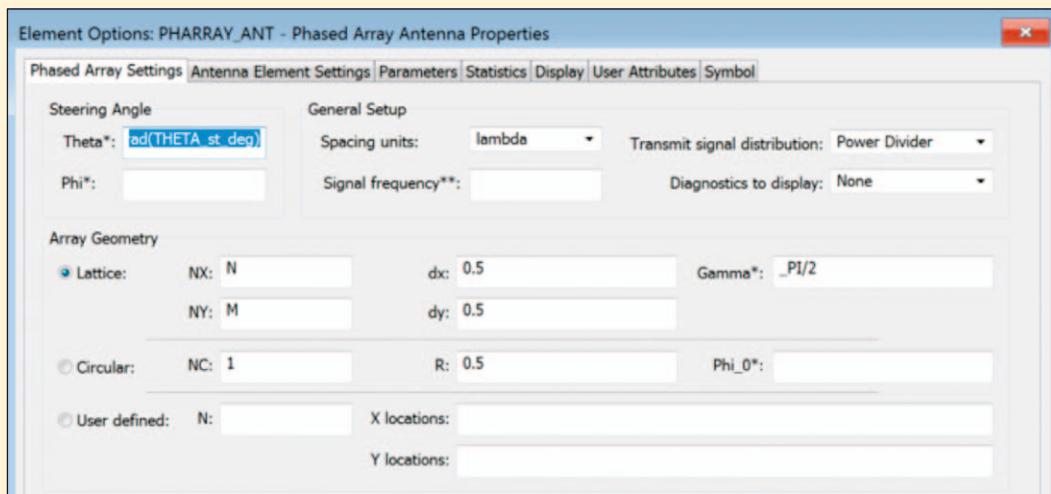


**Figure 3:** Portion of the phased array parameter dialog box showing geometry configuration options including lattice, circular and user defined configuration

of abstraction, from early conceptual models with little detail through highly-defined array models which account for true component interactions and possible impairments.

Designing the complex packaging schemes for high-frequency signaling must be addressed with circuit simulation and electromagnetic analysis specialized for RF and microwave electronics.

### Design Management and EDA Tools

While actively steered phased-array antennas have many advantages, they are extremely complex and their production, especially non-recurring development costs, is significantly higher than conventional antenna design. As the industry shifts toward highly-integrated phased array systems, it is critical to have in-house systems expertise working closely with hardware developers, both fully exploring the capabilities and trade-offs among possible architectures and integration technologies.

In addition, a start-to-finish design flow made possible with electronic design automation (EDA) has become critical in moving beyond the initial system simulation which is focused on early architecture definition, and the development of link budgets and component specifications.

A preferred phased array system design flow manages the start-to-finish front-end development, embedding RF/microwave circuit simulation and/or measured data of radio/signal-processing (behavioral) models within a phased array system hierarchy. Such software enables the system designer to select the optimum solution, ranging from hybrid modules through fully-integrated silicon core RFIC devices, addressing the specific requirements of the targeted application.

Perhaps more importantly, a system-aware approach, carried throughout the entire phased array development cycle, allows the team to continually incorporate more detail into their predictive models, observe the interactions between array components and make system adjustments as the overall performance inadvertently drifts from early idealized simulations.

Design failure and the resulting high costs of development is often due in part to the inability of high-level system tools to accurately model the interactions between the large number of interconnected channels, which are typically specified and characterized individually.

Since overall phased-array performance is neither driven purely by the antenna nor by the microwave electronics in the feed network, simulation must capture their combined interaction in order to accurately predict true system behavior. Circuit, system and electromagnetic co-simulation

allows verification throughout the design process.

### Phased Array Design Flow

A leading phased array design flow is available with Visual System Simulator (VSS), the system-level simulator that operates within the NI AWR Design Environment platform. The simulator provides full system performance as a function of steered beam direction, inclusive of the antenna design, and the active and passive circuit elements used to implement the electronic beam steering. System components can be modeled in greater detail using Microwave Office for RF/microwave circuit simulation with electromagnetic (EM) analysis for antenna design and passive device modeling using AXIEM, planar EM and Analyst, 3D EM.

These tools are fully integrated into NI AWR Design Environment, supporting seamless data sharing within the phased array hierarchy. Furthermore, individual antenna designs can be generated from performance specifications using AntSyn, with resulting geometries imported into AXIEM or Analyst for further EM analysis and optimization. Capabilities within this suite of tools, figure 1, include design assist add-on products and interoperability with third party PCB (layout), RFIC (design/layout) and EM (analysis) tools.

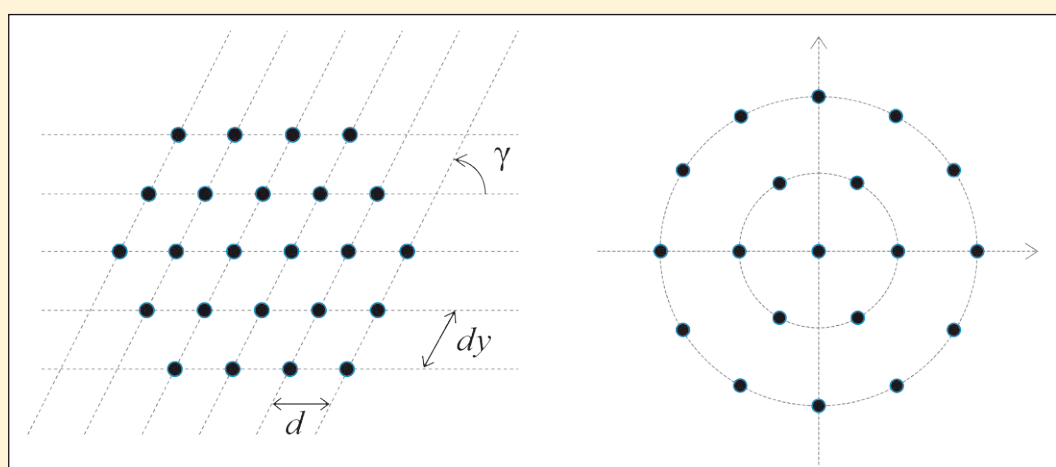


**Figure 4:** Standard array geometries for phased arrays in VSS – a) lattice, b) circular

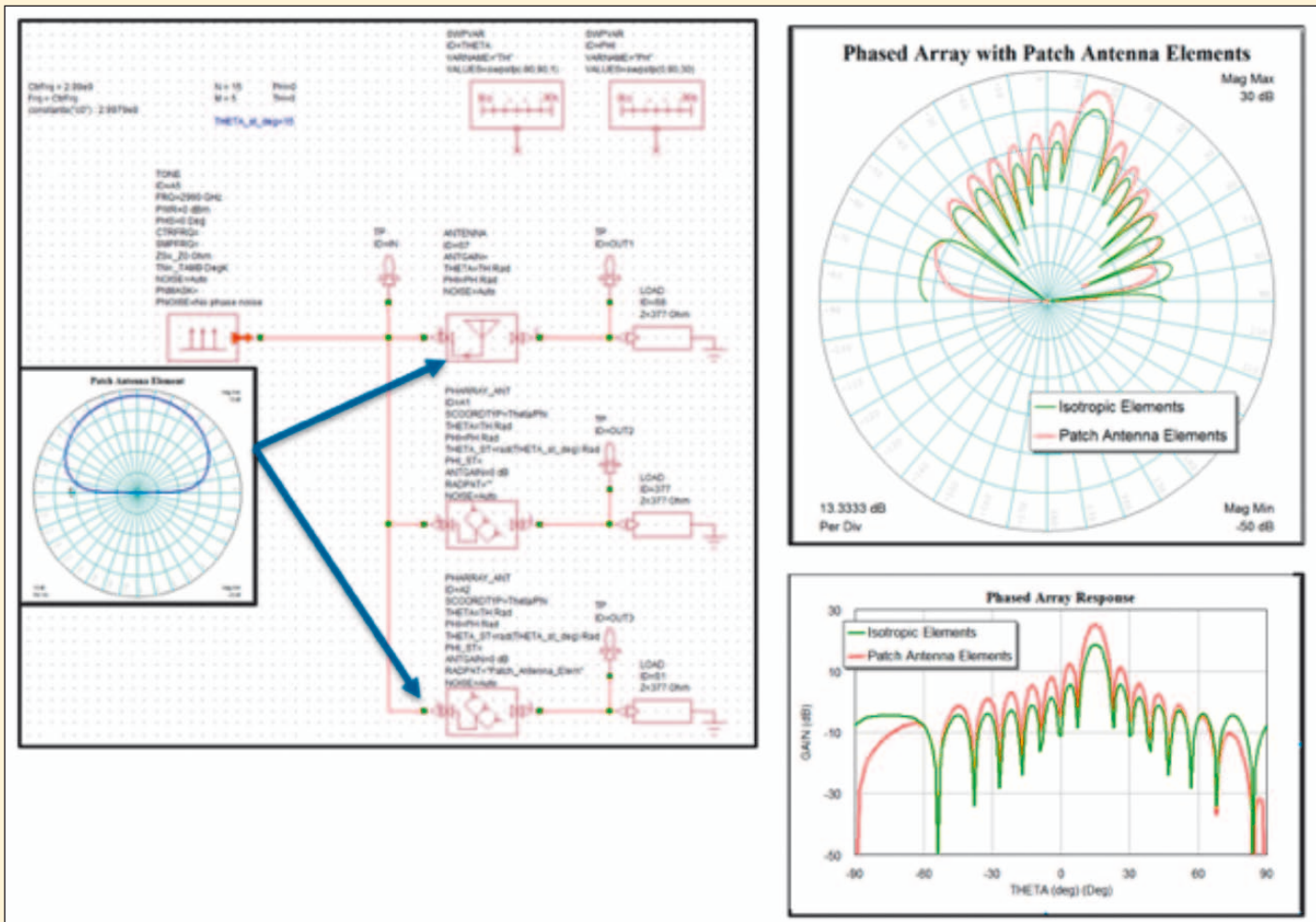


Figure 5: 2, 15 x 5 element phased arrays based on isotropic and patch antenna radiation patterns with theta angle set to 15°

## Highlights of phased array analysis in VSS includes:

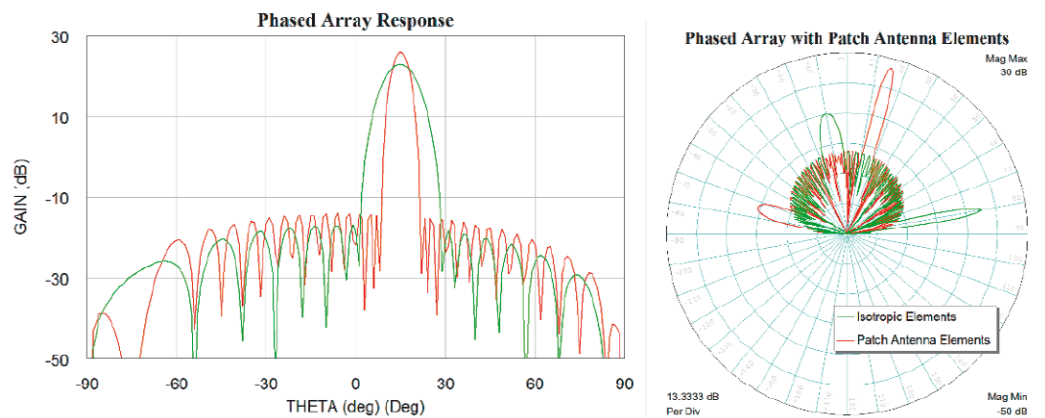
- Automate/manage the implementation of beamforming algorithms and determine phased array antenna configuration from a single input/output block

- Perform array performance for over a range of user-specified parameters such as power level and/or frequency
- Perform various link budget analysis of the RF feed network including measurements such as cascaded gain, NF, output power (P1dB), gain-to-noise temperature (G/T), etc.
- Evaluate sensitivity to imperfections and hardware impairments via yield analysis
- Perform end-to-end system simulations using a complete model of the phased array
- Simulate changing array impedance as a function of beam angle to study impact of impedance mismatch and gain compression on front-end amplifier performance

## Defining Phased Array Configurations

Specifications for any phased array radar are driven by the platform requirements and the intended application. For example, weather observation,

Figure 6: a) radiation patterns for 15 x 5 and 30 x 5 arrays, b) side lobe behavior for array (15 x 5) with element spacing = .95° at steering angle of 15° and 80°



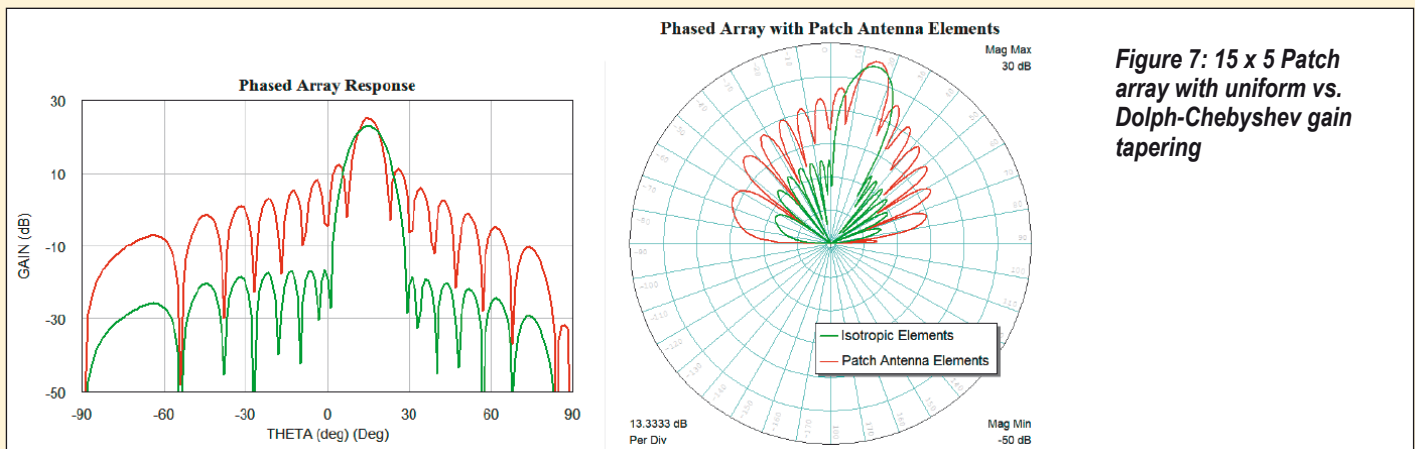


**Figure 7: 15 x 5 Patch array with uniform vs. Dolph-Chebyshev gain tapering**

which has relied on radar since the earliest days of this technology, most commonly uses airborne surveillance radar, to detect and provide timely warnings of severe storms with hazardous winds and damaging hail so that can be issued. The weather surveillance radars are allocated to the S (~10 cm wavelength), C (~5 cm wavelength) and X (~3 cm wavelength) frequency bands. While the shorter wavelength radars have the benefit of a smaller antenna size, their radiated signals are significantly affected by atmospheric attenuation.

Requirements for 10 cm wavelength (S-band) weather surveillance radars, based on years of experience with the national network of non-Doppler radars (i.e., the WSR-57), are shown in table 1 [1]. These requirements showcase some of the application specific metrics that drive range, frequency, antenna size, and gain. These factors represent the starting point for the system designer, who will also weigh cost and delivery concerns, available semiconductor and integration technologies, when considering possible architectures and defining individual component performance targets.

VSS provides system designers with the capabilities to convert these requirements into hardware specifications and work out the initial design details. Starting with the phased array configuration, VSS is able to represent thousands of antenna elements with a single model, allowing

the antenna team to quickly produce radiation patterns with basic array properties such as number of elements, element spacing, individual element gain or radiation pattern (imported measured or simulated antenna data), array configuration and gain taper. The model allows designers to specify the array's physical configuration based on various standard lattice and circular geometries, as well as custom geometries (s. figure 2).

The array behavior is easily defined through a parameter dialog box or a data file containing configuration parameters such as gain and phase offset, theta/phi angles of incidence, number of elements in both X/Y locations (length units or lambda-based), spacing and signal frequency. This model greatly simplifies early exploration of large-scale phased array configurations and individual antenna performance requirements over implementing such a model using basic individual blocks where array sizes were generally limited to several hundred elements, each modeled as a single input/single output block.

Figure 3 shows a portion of the parameter dialog box used to quickly define an antenna-array architecture using standard or custom geometries. The lattice option allows configuration of the phased array in a lattice pattern, which is configured using the number of elements along the X and Y axes, NX and NY, element spacing along these axes, dx and dy, and gamma, the angle

between these axes, figure 4b. Setting gamma to 90° results in a rectangular lattice, while setting it to 60° creates a triangular lattice. Any positive value for gamma may be used to configure the lattice while the circular option enables configuration of circular phased arrays with one or more concentric circles. The number of elements in each concentric circle and the radius of each circle can be defined as vectors by variables NC and R. Examples of lattice and circular array configurations are shown in Figures 4a and b.

To demonstrate some of the capabilities of the phased array model, an example project was constructed showing two 15 x 5 element arrays operating at 2.99 GHz, s. figure 5. One model represents an array of lossless isotropic antennas defined simply by setting the antenna gain to 0 dBi, while the elements of the other array utilize a data set containing the radiation pattern of a single simulated patch antenna. Both arrays use a lattice configuration with a 1/2" spacing between elements and uniform gain tapering - explained in more detail below. For the simulation shown, the steering angle (theta) was set to 15°, figure 5. Note that the antenna and phased array blocks support specifying the signal direction using U/V coordinates as well as THETA/PHI angles.

The VSS array model provides antenna designers with a rapid and straightforward tool to observe key antenna metrics,

providing a means to examine the main beam and side lobe behavior as a function of any number of variables including array size (figure 6a) and configuration, gain vs. steering angle, and the occurrence of grating lobes as a function of element spacing and/or frequency (figure 6b). From these results the array team can develop an optimum configuration for the given requirements such as range and overall array physical size. In addition, the array team can provide design targets for the individual antennas and incorporate subsequent antenna simulation results back into the array analysis.

Control of the amplitude excitation through gain tapering is often used to control beam shape and reduce the side lobe levels. A number of commonly used gain tapers are implemented in the phased-array block. Gain taper coefficient handling defines whether the gain taper is normalized or not. If it is, the taper is normalized to unit gain. Standard gain tapers implemented in the phased-array model include Dolph-Chebyshev, Taylor Hansen, and uniform. The earlier example (15 x 5 element patch array) was re-simulated with uniform vs. Dolph-Chebyshev gain tapering, showing the impact on the main beam and side lobes, s. figure 7. In addition, the user can define custom gain tapers by specifying the gains (dB) and phases for each array element.

**To be continued in  
hf-praxis 9**

# An AESA Development Model for Next Generation Fighter Aircraft Radar

Lars Josefsson, Lars Erhage, Thomas Emanuelsson  
Ericsson Microwave Systems AB  
Mölndal, SE-43184 Sweden

*Abstract* — An overview is presented of an ongoing study and development program which aims at the realisation of next generation radar systems for fighter aircraft. An important part of the study is the design, test, and evaluation of a breadboard array with about 100 active radiators. The array configuration, the test system, and some preliminary results are presented.

## INTRODUCTION

Active electronically scanned array antennas (or AESA for short) for fighter radars have been discussed and studied at least since the late sixties. Several experimental systems are known by the acronyms MERA, RASSR, SSPA etc [1]. It is now believed that the technology has matured to the point that AESA is a realistic and cost-effective solution to the needs of future systems for greater flexibility, increased range performance and reduced signatures.

## THE AIRBORNE PHASED ARRAY CHALLENGE

Radar systems with AESA technology have proven successful in many ground based radar systems. Our own developments include an X-band 3D radar (HARD, [2]) which now is equipped with a third generation TR module design of much reduced size and weight compared to the first versions.

In airborne applications the requirements are generally much more stringent than in ground based applications. The greatest differences are due to limitations in weight, volume, shape, and power consumption, as well as requirements for multiple functions with optimum performance in the presence of clutter and jamming signals. On top comes the environmental specifications for airborne systems.

Based on our successful results obtained with the airborne surveillance radar ERIEYE [3], we have now started a study program focussed on the technology of future AESA systems for fighter aircraft. As in the ERIEYE case solid state TR modules will be employed, but at a higher frequency and in greater numbers. The same design issues need to be addressed in both cases: power supply issues, efficiency, reference signal distribution, cooling, test and evaluation, calibration, etc. The solutions, however, are quite different in the two cases.

## DEVELOPMENT APPROACH

Starting a development program for an AESA, with possible application in a future fighter aircraft, requires careful planning for maximum cost effectiveness. This is true everywhere on the globe today, but is particularly indispensable in a small country with a decreasing defense budget.

The full program proposed includes the development of a mini-AESA for laboratory tests and a full scale AESA for flight trials, before the start of prototype development. The first phase has been approved already. It is also recognized that much of the results can be applied to similar two-dimensionally scanned systems besides the airborne one.

The mini-AESA has 108 active elements. In the design the usual electromagnetic CAD software is used extensively, such as HP HFSS etc. In addition several software and hardware models have been developed:

- Mutual coupling (infinite and finite array) prediction software.
- Waveguide simulators.
- Array antenna performance prediction software including error analysis.
- Measurement tolerance error analysis (near field tests).
- Thermal and structural analysis.
- A full scale mechanical model.
- A full scale electrical model of the aperture.
- Software for simulation of array signal processing.

An essential tool for the development of a full scale version is of course also the mini-AESA breadboard itself.

## THE BREADBOARD TEST ARRAY

### *The Breadboard Configuration*

The mini-AESA breadboard structure with a subarray of 108 active elements is shown in Fig 1. The active elements are surrounded by a ring of passive radiators. For array matching a dielectric WAIM sheet is used (not shown).

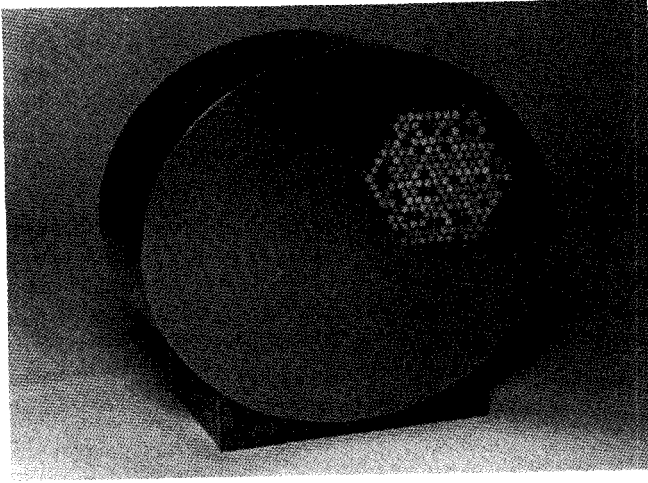


Fig. 1. Mini-AESA with breadboard subarray.

A block diagram of the antenna system is shown in Fig 2. The major microwave parts are the radiating elements and the TR modules. However, the importance of the various supporting subsystems must not be underestimated: support structure, power supply, signal distribution, cooling etc. A coherent approach to the total system design is essential in order to be able to meet typical performance levels (including reliability, maintainability, weight, power consumption etc) for an airborne application.

As shown in Fig 2 two TR (transmit/receive) functions with two radiating elements are combined in one TR unit. This reduces the number of connectors in the system. The TR units are mounted to liquid cooling channels for removal of the heat generated in the modules.

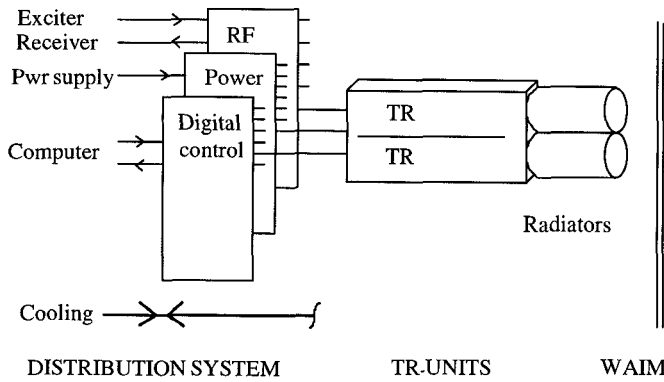


Fig. 2. Mini-AESA block diagram.

### TR Modules

The TR modules must meet a wide range of partly conflicting requirements. The power consumption must be low meaning a very high power added efficiency for the power amplifier. Furthermore, the modules must be small and light to fit in an airborne phased array radar application. Last but not least the cost must be low.

Our approach to solve these problems is to use circuits with a high degree of integration. The different types of circuit needed are shown in the block diagram (Fig. 3).

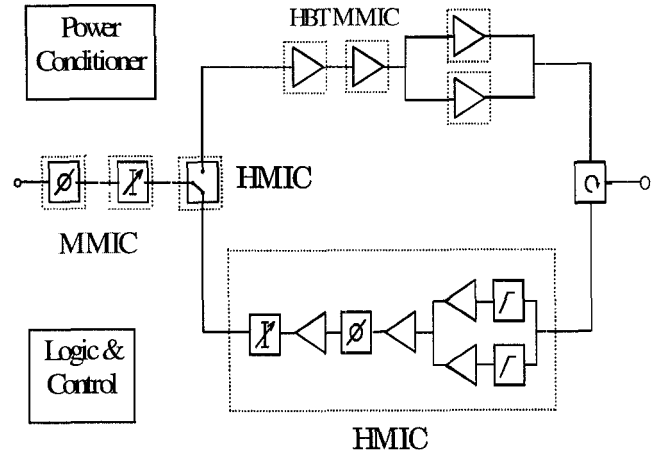


Fig. 3. TR module block diagram

To obtain the highest possible power added efficiency we use HBT technology for the design of the MMIC power amplifier. We have demonstrated an output power exceeding 5 W for one single MMIC amplifier with a power added efficiency well above 40%. The HBT technology has a potential for high volume production at low cost.

The phase shifter and the step attenuator are two compact designs using standard GaAs FET MMIC technology.

The receiver function is implemented in glass technology (HMIC) in order to obtain small dimensions and low cost. It contains a mixture of technologies: GaAs HBT to get high linearity, PHEMT to get a low noise figure, and silicon diodes for switching. Measured data for the receiver are: noise figure  $< 2.5 \text{ dB}$ , gain  $> 30 \text{ dB}$ , and  $\text{IP3}_{\text{out}} > +35 \text{ dBm}$  [5].

The logic part and the control circuits for the RF functions are mounted on a standard multilayer PCB which is integrated on the microstrip substrate. There are also power regulation circuits in the module.

The weight of the module is dominated by the weight of the housing. A preliminary trade off between weight and cost per unit has resulted in two TR functions in one common housing for the mini-AESA.

### Radiating Elements

The radiating elements are dual polarized dielectric loaded circular waveguide elements. This type was chosen for the mini-AESA because of its simple design and good electrical performance. It can be matched with reasonable ease over a wide band and within a wide scanning region.

The elements are arranged in a triangular grid at roughly half wavelength spacings.

The element exhibits a rather poor match when it is isolated, and performance has to be specified in the array environment. The basic design is made with an infinite array model, verified by waveguide simulator measurements. HFSS simulations are made for detailed analysis of the feeding structure. The final design of the matching WAIM structure is made by numerical optimization, where the mismatch is minimized over the frequency and scan regions.

We have also developed a finite array analysis program. This is used as a tool for compensation for variations in the mutual coupling environment towards the edges of the structure. For a large array (in particular with a dielectric cover) the analysis becomes very complex (Fig 4).

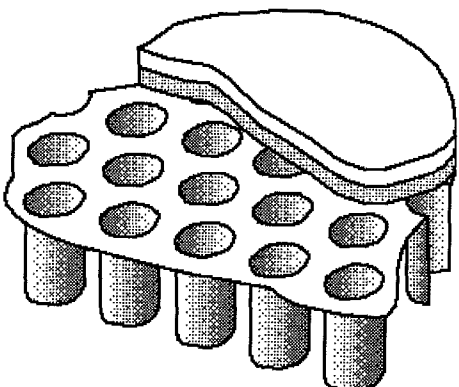


Fig. 4. The array configuration with dielectric layers.

### Beam Steering and Module Control

With individual control of the amplitude and phase of each TR module any beam shape and beam direction can be generated within the limitations of the aperture size and the achievable accuracy. Different excitations can be selected for transmit and receive. Among the beam shapes of interest are pencil beams, broadened beams, fan beams, monopulse split beams, multiple beams etc. In an advanced digital beam forming system there are virtually no limitations, besides the resulting complexity. With subarraying partial digital beamforming can be used with a reduced number of channels [4].

In the mini-AESA the design of the beam steering and control system is based on the expected requirements of a full scale array with roughly 2000 modules. Suppose 8 bit phase information is to be transferred to each module in a time frame of e. g. 10 microseconds. This would require a data rate in the Gbit/s range. Even if several parallel data buses are used the data transmission design becomes quite complex.

A practical solution is to transfer high level commands in stead of individual phase and amplitude values. Thus information about the required beam direction, beam shape, and other information is sent to the modules. Each module needs to compute its individual excitation. The computations are fairly simple. A phase calculation could be:

$$\text{phase} = Ax + By + Cx^2 + Dy^2$$

where x,y are the module coordinates and the A, B, C, D values govern beam direction and shape. With e.g. 16 bit words we will then safely be in the Mbit/s range.

The module control system also includes error detection, calibration, and other signals. The purpose of the calibration is to compensate for phase changes caused by variations in temperature and frequency. The modules can do this correction automatically. However, the calibration data may need to be updated from time to time.

### Supply and Feed Networks

In order to evaluate the functional performance of the breadboard array under laboratory conditions the supply and feeding networks can be simplified. We have, however, studied the assumed full scale requirements of a cooling system, since this is recognized to be one of the major critical parts of an airborne system. The power supply and control signal distribution is realized in a multilayer circuit board. The RF signal distribution is made in stripline (Fig. 5).

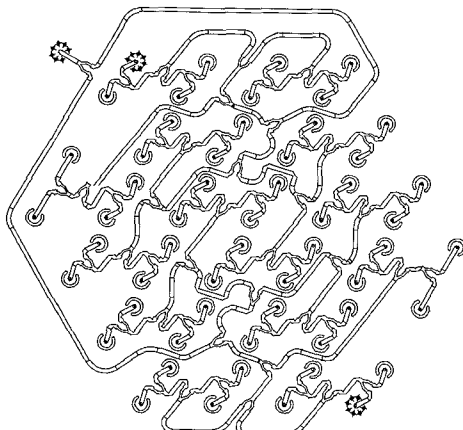


Fig. 5. The RF feed network.

## System for Test and Evaluation

Near field measurement techniques are used for test and evaluation. This method requires the sampling of the field in front of the antenna by means of a near field probe. The data is then transformed to create far field patterns, and back transformed to find the element excitations.

An active array antenna has more degrees of freedom than a passive antenna. In an AESA for a radar system the variations with time are of particular interest. Such variations are mainly due to the pulsed waveform. The antenna characteristics may depend on the waveform parameters, there may be changes during the duration of the transmit pulse, spectrum purity is of interest etc

The test system must therefore operate in a pulsed mode with a large measurement bandwidth in order to achieve a time resolution in the order of microseconds. The measurement noise is reduced by averaging a large number of samples.

The test system contains the four main blocks shown in Fig. 6. The measurements are controlled by a computer. A particular measurement sequence is initiated by start of the appropriate program. The tests are done in the transmit mode or in the receive mode. In either case the exciter/receiver sends digitized complex data at a high (Mbyte/s) rate to a buffer memory. The data can then be downloaded to the computer for later processing. The AESA is controlled by computer commands via an interface that connects to the AESA series bus.

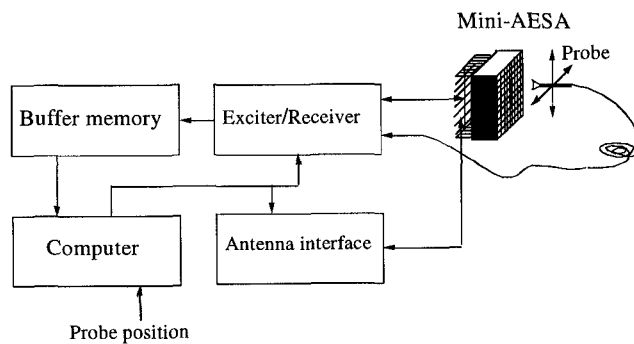


Fig. 6. System for test and evaluation using near field techniques.

## PRELIMINARY RESULTS

Both theoretical and experimental results achieved so far all point to the conclusion that the airborne active solid state array antenna is feasible and will meet the assumed performance requirements. The breadboard itself mainly demonstrates the technology, but some of the results can be extrapolated to a large array.

A major achievement is the data obtained for the TR modules discussed above. Another important parameter is the scanning performance, some of which can be inferred from the embedded element pattern. Fig. 7. illustrates computed element patterns without and with WAIM sheet matching. In this case a two-layer WAIM was used. The computations were made for a simulated infinite array environment.

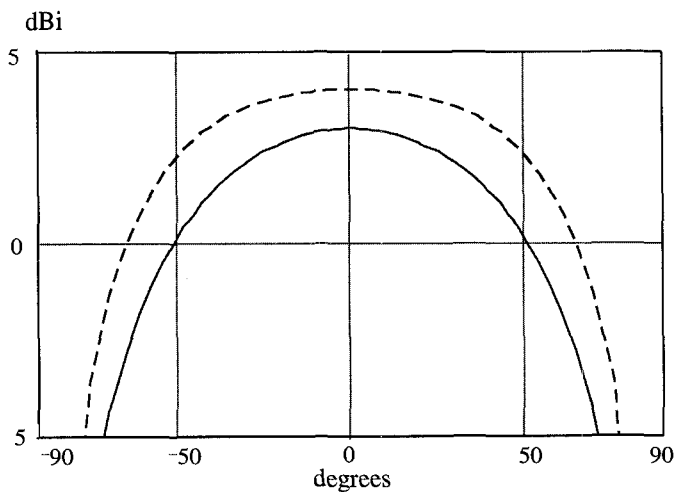


Fig 7. Active (embedded) element pattern without (solid line) and with WAIM sheet (broken line).

## CONCLUSION

We have described an active array antenna which represents a possible technology for future active arrays for fighter aircraft. This mini-AESA demonstrates the feasibility of such systems in many respects: cooling principles, packageing, antenna pattern performance, output power efficiency, waveform and radiation pattern flexibility and many more things. Last but not least it has given valuable experience in a number of important areas: design methods, production process control, system integration, test and evaluation, calibration etc. This knowledge is essential as we proceed to larger systems.

## REFERENCES

- [1] D. McQuiddy et al, Transmit/receive module technology for X-band active array radar, Proc IEEE, March 1991, p 308-341.
- [2] J-O Winnberg, Phased arrays for battlefield applications, Military Microwaves, London 11-13 July, 1990.
- [3] S. Ahlbom, P. Andersson, R. Lagerlöf, A Swedish airborne early warning system based on the Ericsson ERIEYE radar, Ericsson Review, vol. 62, 1995.
- [4] B. Johannesson, L. Steen, Partial digital beamforming using antenna subarray division, Proc Radar '94, Paris, 3-5 May, 1994, pp. 63-67.
- [5] C Vaktnäs, First pass success of a complex X-band glass receiver optimising intermodulation, noise and power consumption by a combination of PHEMT and HBT technology, Proc EUMC 95, Bologna, Sept 1995.

# 항공기용 평면형 능동 전자주사식 위상 배열(AESA) 레이더 프로토 타입 개발

## Development of Planar Active Electronically Scanned Array(AESA) Radar Prototype for Airborne Fighter

정민길 · 김동윤 · 김상근 · 전상미 · 나형기

Min-Kil Chong · Dong-Yoon Kim · Sang-Keun Kim · Sang-Mi Chon · Hyung-Gi Na

### 요 약

본 논문에서는 T/R(Transmit/Receive) 모듈을 이용한 항공기용 평면형 능동 전자주사식 위상 배열(AESA) 레이더 프로토 타입을 설계, 제작 및 시험하였다. LIG 네스원은 항공기용 레이더 개발에 필요한 핵심 기술 확보를 목적으로 AESA 레이더 프로토 타입을 개발하였다. 본 프로토 타입은 복사 소자 배열, 다수의 T/R 모듈, RF 금전기, 전원 분배, 범 조향기, 아날로그/디지털 변환기(ADC)를 가지는 소형화된 수신기 및 액냉식 냉각과 지지 구조체로 구성되어 있다. 안테나 장치는 590 mm 직경에, 536개의 능동 소자를 배열할 수 있는 크기를 가진다. 각 T/R 모듈들은 삼각 배열을 적용하여 14.7 mm×19.5 mm 간격으로 배치하였다. 송신 최대 드uty 운용시 2,310 W의 전력이 입력되며, 발열은 1,554 W를 발생하게 된다. AESA 레이더 프로토 타입은 근접 전계 챔버에서 시험하였고, 그 결과 정확하고 유연한 제어에 의한 범 조향과 범 형성을 제공하는 범 패턴을 확인할 수 있었다.

### Abstract

This paper presents a design, fabrication and the test results of planar active electronically scanned array(AESA) radar prototype for airborne fighter applications using transmit/receive(T/R) module hybrid technology. LIG Nex1 developed a AESA radar prototype to obtain key technologies for airborne fighter's radar. The AESA radar prototype consists of a radiating array, T/R modules, a RF manifold, distributed power supplies, beam controllers, compact receivers with ADC(Analog-to-Digital Converter), a liquid-cooling unit, and an appropriate structure. The AESA antenna has a 590 mm-diameter, active-element area capable of containing 536 T/R modules. Each module is located to provide a triangle grid with 14.7 mm×19.5 mm spacing among T/R modules. The array dissipates 1,554 watts, with a DC input of 2,310 watts when operated at the maximum transmit duty factor. The AESA radar prototype was tested on near-field chamber and the results become equal in expected beam pattern, providing the accurate and flexible control of antenna beam steering and beam shaping.

Key words : AESA Radar, T/R Module, Airborne

### I. 서 론

바야흐로 ‘능동 전자주사식 위상 배열(AESA: Active Electronically Scanned Array)’ 레이더 시대가 활

짝 열리고 있다. 제1차 세계대전(1914~1918년) 기간 중 무기 동기화(gun synchronization)가 공중전에 대 혁신을 일으킨 것과 같이, AESA 레이더 기술을 기반으로 한 전투기 사격 통제 장치의 출현은 향후 비

LIG 네스원 ISR 연구센터(LIG NEX1 ISR R&D Lab)

· 논문 번호 : 20100729-101

· 교신 저자 : 정민길(e-mail : mkchong01@lignex1.com)

· 수정완료일자 : 2010년 11월 12일

약적인 기술 발전을 가져올 것으로 기대된다<sup>[1]</sup>.

AESA 원리는 잠자리(또는 곤충)류의 눈에서 찾을 수 있다. 잠자리류들은 10,000~30,000개의 낱눈(lenslets)으로 구성된 복잡한 눈(복안)을 가지고 있다. 낱눈들은 3차원 구조에 흘어져 있기 때문에 높이와 각도가 다른 곳에서 움직이는 물체를 감지할 수 있다. AESA 레이더가 바로 낱눈 구조의 레이더이다. AESA 레이더의 원판 위에는 손가락 크기 정도의 T/R 모듈이 500~1,500개가 방위각, 고각 방향으로 일정하게 배열되어 있으며, 이 T/R 모듈들이 잠자리의 낱눈들처럼 각각의 목표물을 동시에 탐지, 추적한다. AESA 레이더는 일반 기계식에 비해서 뛰어난 점이 많다. 우선 기계식이 안테나 스캔 영역에 따라 시차가 발생하는데 비해서 AESA 레이더는 회전하지 않더라도 충분한 영역을 스캔할 수 있어 일정한 영역을 지속적으로 조향할 수 있고, 빔 형성 능력도 보다 균일하고 T/R 모듈이 각각 고속 프로세서에 연동되어 있기 때문에 방향 전환과 추적을 고속으로 수행할 수 있게 된다. 따라서 빠르게 기동하는 적기나 미사일도 신속하게 추적할 수 있다. 기계식 레이더는 적기나 미사일이 전투기 기체에 근접할 때 사각 지역이 생기지만, AESA 레이더는 가까이 올 경우 사각 지역 없이 모두 탐지 가능한 장점 또한 있다. AESA(능동 전자주사식 위상 배열) 레이더는 종래의 기계식 레이더처럼 송신부와 수신부가 따로 분리되어 있는 게 아니라, 작은 송수신(T/R) 모듈 수천 개가 레이더 전반부에 장착되어 여러 가지 기능을 수행한다. 익히 알려진 AESA 레이더 기술 장점으로는 높은 신뢰성과 정비성, 점진적 성능 완화(graceful degradation), 향상된 탐지 거리, 동시 다기능 그리고 표적 탐지 후 추적 및 통합 센서를 향해 다가오는 이동체 예측, 재밍 및 통신 능력 등이 있다. 최근 가격 경쟁력이 높아진 AESA 기술은 오늘날 새롭게 등장하는 대부분의 전투기 체계에 꼭 갖추어야 하는 요소라 할 수 있다<sup>[2],[3]</sup>.

전투기용 AESA 레이더 설계에 있어서 가장 우선적으로 고려되어야 하는 사항은 SWaP(size: 크기, weight: 무게, power: 소모 전력), 가격 및 방열 등이다. 무게 부분에서는 첨단 소재를 이용하여 소형/경량화되는 추세이며, 가격 부분은 GaAs MMIC 기술의 발전으로 T/R 모듈의 크기와 가격을 줄일 수 있

다. 그리고, 단위 면적당 고발열로 인해 방열에 있어서는 수냉이 대부분 적용되고 있다. T/R 모듈을 포함하는 레이더 안테나부는 전체 레이더 가격의 60~70 %를 차지하며, 계속되는 MMIC 기술 발전 추세로 비용 부분은 더욱 개선될 것으로 기대된다<sup>[4]</sup>.

능동 전자주사식 위상 배열(AESA: Active Electronically Scanned Array) 레이더는 빔을 송신하고 수신하는 T/R 모듈이 안테나에 다수 배열된 레이더로써, 각 소자가 송수신 기능을 갖고 있기 때문에 원하는 방향으로의 송신 빔을 생성하거나 특정 빔의 수신 및 모드 변경 등을 개별적으로 수행할 수 있어 빠른 빔 조향, 다수의 빔 제어를 통한 다중 모드(multi-mode) 동시 운용, 신뢰도 향상, 포착하기 어려운 목표에 대한 지속적 감시와 추적, 무게 감소, 스텔스 능력 향상, 탐지 거리와 범위 확대, 동시 다표적(multi-target) 교전 능력 향상 등의 장점이 있다. 한 가지 단점이라면 단위 면적당 열이 집중되어 발열량이 많고 냉각이 어려워서 부피가 크고 복잡한 액냉식 냉각 장치(liquid cooling system)를 갖추어야 된다. 따라서 냉각 장치가 복잡해지고, 비용이 많이 소요되는 단점이 있지만 AESA 레이더 장점을 위해 감수해야 하는 부분이다<sup>[5],[6]</sup>.

AESA 레이더는 전투기의 임무 수행에 필요한 공중전(공대공), 공대지 및 공대해의 운용 모드를 갖추고 목표물에 대한 탐지, 추적 및 화기 통제 기능을 수행한다. 특히, 조종사에게 필요한 정보를 전방 상향 시현기(Head-Up Display: HUD)나 다기능 시현기(Multi-Function Display: MFD) 등에 도시할 수 있도록 획득 정보를 전송하는 전투기의 가장 중요한 센서이다. AESA 레이더는 전투기 시스템의 주 센서로 성공적인 임무를 위해 공대공(Air-to-Air) 모드, 공대지(Air-to-Ground) 모드, 공대해(Air-to-Surface) 모드, 대전자전(ECCM) 모드, 자체 점검(Built-In-Test) 기능 및 다중화(Redundancy) 관리를 수행할 수 있어야 한다<sup>[5],[7]</sup>.

본 논문에서는 전투기용 능동 전자주사식 위상 배열(AESA) 레이더에 필요한 소요 기술을 획득하기 위해 항공기의 전기적 및 기계적 인터페이스를 고려하여 소형/경량의 AESA 레이더 프로토 타입을 자체 개발하였다. 논문의 II장에서는 AESA 레이더의 주요 전기적/기계적 인터페이스를 고려하여, 주요 구

성품을 설계한다. 주요 구성품은 T/R 모듈을 이용한 안테나 장치, RF/처리부, 전원공급기 및 냉각 장치의 설계에 대해 기술하였고, III장에서는 제작된 하드웨어 시제를 이용하여 근접 전계 시험실에서 전자적 빔 조향 특성을 시험을 통해 확인하였다. 그리고, IV장에서는 결론을 내리도록 한다.

## II. AESA 레이더 프로토 타입 설계

### 2-1 AESA 레이더 설계

본 논문의 설계 목표는 평면형 능동 전자주사식 위상 배열(AESA) 레이더 프로토 타입을 개발하여 항공기 탑재 가능성을 확인하기 위해 전기적 및 기계적 인터페이스를 먼저 확인하고, 실시간 빔 형성 및 빔 조향을 확인하는 성능 시험을 목표로 한다. 본 논문에서 제안하는 AESA 레이더 프로토 타입 구조 및 블록도는 그림 1과 같다. AESA 레이더 프로토 타입은 AESA 안테나 장치, RF/처리 장치, 냉각수 순환 장치로 구성되어 있다.

AESA 안테나 장치는 T/R 모듈과 복사 소자로 구성되는 1차원 T/R 단위 모듈, 부배열 급전기, 빔 조향기, 제어 및 타이밍 인터페이스, 지지 및 냉각 구조체, 그리고 전원 공급기로 이루어 있다.

RF/처리 장치는 여자기(exciter), 4채널 수신기, 신호 처리기로 구성되어 있다. 여자기는 다중 모드 파형 발생 신호, 보정 신호와 수신기 및 신호 처리기 기준 클럭 신호를 생성·분배하여 준다. 수신기는 4 채널을 가지고 있으며, 각 채널은 모드에 따라 광대역(공대지/해 모드) 및 레이더 모드 신호를 수신하

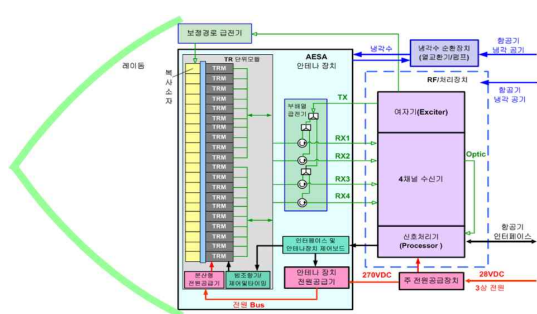


그림 1. 능동 전자주사식 위상 배열(AESA) 레이더 프로토 타입 기능 블록도

Fig. 1. Functional block diagram of AESA radar proto-type.

여 IF단까지 주파수 하향 변환을 하고, 또한 각 채널은 디지털 감쇄 소자를 두어 STC(Sensitivity Time Control) 기능을 수행한다. 신호 처리는 COTS(Commercial Off-The-Shelf) 보드를 기반으로 획득된 신호를 분석하여 상황 판단에 의한 각종 기능 수행에 있어서 성공적으로 제어되는 것을 확인하고, 차체 점검 상태를 모니터링하게 된다.

냉각수 순환 장치는 AESA 안테나 장치에서 발생하는 열과 RF/처리 장치, 전원 공급기 및 냉각제 펌프에서 발생하는 열을 방열한다. AESA 안테나 장치는 액냉식 냉각 시스템을 사용하고, 안테나 장치의 열을 냉각수 순환 장치로 전달하고, 펌프와 열교환기를 통해 열을 방출한다.

주 전원 공급 장치는 3상, 400 Hz, 115 V의 항공기 교류 전원을 270 V 직류로 변환한다. 변환된 직류 전원은 각 장치로 전달되어 각 부 체계 레벨에서 필요한 전원을 생성하여 공급된다.

본 논문에서 개발한 AESA 레이더 프로토 타입은 핵심 기술 확보가 목표이며, AESA 레이더 프로토 타입에서는 항공기에 장착되어 완전 체계 시제에 적용 가능성을 확인하기 위한 것이다. 실제 항공기 탑재되는 모델에서는 T/R 모듈이 1,000개 규모로 이루어지지만, 본 개발에서는 미래 장착될 시스템에 바로 적용 가능한 확장성 있는 구조 개발에 초점을 둔 개발이어서, 일반적인 체계 규격(탐지 거리, 추적 거리 등) 도출보다는 항공기 개구면의 전기적/기계적 인터페이스, 방열 성능 및 AESA 레이더 응용을 위한 기능적 요구사항을 표 1과 같이 도출하였다.

### 2-1-1 능동 전자주사식 위상 배열(AESA) 안테나 장치

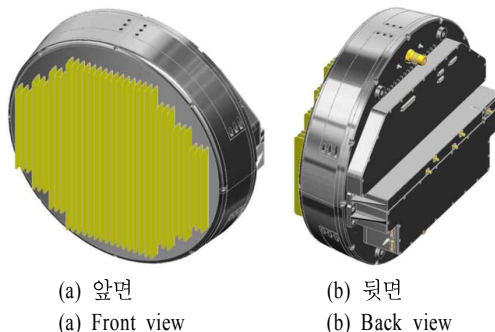
안테나 장치는 고속 빔 조향이 가능한 능동 전자주사식 위상 배열 특성을 가지고 있고, 구조는 그림 2, 3과 같다. 크기는 590 mm(개구면 직경)×258 mm(길이)로써 항공기 기계적 인터페이스에 적합한 구조로 설계하였다. AESA 안테나 장치는 536개 T/R 모듈을 가지는 T/R 단위 모듈, 부 배열 급전기, 보정 경로 급전기, 인터페이스 및 안테나 장치 제어 보드, 전원 공급기, 지지 및 냉각 구조체로 구성되어 있다.

#### 2-1-1-1 복사 소자 및 배열 구조

표 1. AESA 레이더 프로토 타입 주요 성능 파라미터

Table 1. Key performance parameters of AESA radar proto-type.

항 목		개발 목표 규격
1. 안테나 구조		능동 전자주사식 위상 배열
2. 동작 주파수		X-대역
3. 송신 드티		33 % (Max.)
4. 송신 펄스 폭		40 us (Max.)
5. PRF(Pulse Repetition Frequency)		150 kHz (Max.)
6. 송신 첨두 전력		10 W/모듈당
7. 잡음 지수		4 dB 미만 @T/R 모듈
8. 배열 수		500개급
9. 송신 빔 패턴	빔 폭(방위각/고각)	3.73°±10 % / 4.68°±10 %
	이득	32.9 dB
10. 수신 빔 패턴	빔 폭(방위각/고각)	4.3°±10 % / 5.49°±10 %
	이득	31.9 dB
11. 수신 채널 수		4 채널
12. 소모 전력	안테나 장치	2.243 kW
	RF/처리 장치	440 W
	냉각수 순환 장치	800 W
13. 크기	안테나 장치	590 mm(개구면 직경)×258 mm(길이)
	RF/처리 장치	254 mm(너비)×230 mm(높이)×457 mm(길이)
	냉각수 순환 장치	275 mm(너비)×350 mm(높이)×500 mm(길이)

그림 2. AESA 안테나 장치 구조  
Fig. 2. Structure of the AESA antenna.

능동 전자주사식 위상 배열 레이더 설계 시 그레이팅 로브(grating lobe)를 피하면서 원하는 빔 패턴을 효율적으로 방사하기 위해서는 먼저 배열 구조 및 간격을 설정해야 한다. 그레이팅 로브가 발생하는 각도를  $\theta_p$ 라고 하면, 다음의 식에서 그레이팅 로브가 발생하는 조건을 알 수 있다<sup>[8],[9]</sup>.

그림 3. AESA 안테나 배열 조립도  
Fig. 3. Exploded view of AESA antenna array.

$$\sin \theta_p = \sin \theta_0 + \frac{p\lambda}{d} \Rightarrow \frac{d}{\lambda} \leq \frac{1}{1 + \sin \theta_0} \quad (1)$$

$\sin \theta_p > 1$  이상이 되는 조건, 즉 배열 간격이 식 (1)의 우측 조건을 만족할 때, 그레이팅 로브가 발생하지 않는다. 조건식에 알 수 있듯이 그레이팅 로브가 발생하는 조건은 배열 간격( $d$ ), 파장( $\lambda$ ), 빔 조향각( $\theta_0$ )에 의해 결정되며, 2차원 배열에서는 방위각/

고각 방향으로 빔 조향과 배열 구조 및 배열 간격을 동시에 고려해야 한다. 배열 구조에서 그레이팅 로브 발생 영역을 비교하여 보면 같은 배열 간격일 경우, 사각 배열 구조에서 그레이팅 로브 발생 영역이 더욱 많이 발생하게 된다. 일반적으로 빔 조향 범위가 넓은 AESA 레이더에서는 공간을 효율적으로 사용하면서 그레이팅 로브를 피하기 위해서 삼각 배열 구조를 많이 사용한다<sup>[10]~[12]</sup>.

본 논문에서 배열을 경제적으로 구성할 수 있는 삼각형 구조를 적용하였고, AESA 레이더의 일반적인 빔 커버리지가 방위각/고각  $\pm 60^\circ$  근처인 것을 감안하여 삼각형 구조의 배열 간격이  $dx=19.5$  mm,  $dy=14.7$  mm 이하일 경우에는 그레이팅 로브가 발생하지 않는 것을 시뮬레이션으로 확인하고, 배열 간격은  $dx=19.5$  mm,  $dy=14.7$  mm로 설정하였다<sup>[13]</sup>.

단일 복사 소자는 테이퍼 슬롯(tapered slot) 구조인 비발디(vivaldi) 형태를 사용하여 T/R 단위 모듈과 일체형으로 제작함으로써 제작/조립이 용이해지고, 광대역 특성을 구현한다. 단일 복사 소자 구조는 그림 4와 같고, 모의 해석한 방사 패턴은 그림 5와 같다.

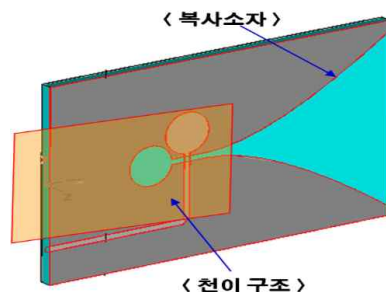


그림 4. 비발디 복사 소자 구조

Fig. 4. Structure of vivaldi radiator.

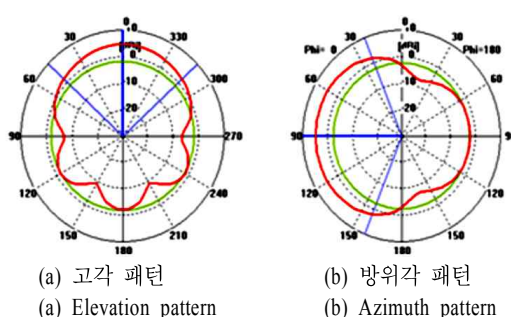


그림 5. 복사 소자 패턴 시뮬레이션 결과

Fig. 5. Simulation result of the radiation patterns.

표 2. 복사 소자 파라미터

Table 2. Parameters of radiator.

항 목	개발 목표 규격
1. 이득	4.9 dBi(최대)
2. 방사 효율	0.99
3. 반사계수( $S_{11}$ )	-15 dB 이하
4. 빔 폭(고각/방위각)	95% / 135°

복사 소자 기능적 파라미터들은 표 2와 같다. 특히, 본 논문에서 제안하는 스트립 비발디 구조는 적층 구조가 가능하여 점검 신호 경로를 추가하는데 아주 용이한 구조이다<sup>[14]</sup>.

### 2-1-1-2 T/R 단위 모듈

T/R 단위 모듈은 안테나 장치의 가장 핵심 조립체로서 그림 6에서와 같이 복사 소자, T/R 모듈, 빔 조향기, 급전기, 제어/전원 분배기, 냉각 수로 및 하우징 조립체로 이루어진다. T/R 단위 모듈은 20배열, 16배열, 12배열, 8배열 T/R 단위 모듈들이 각각 16조, 6조, 6조, 6조로 이루어진다. 급전기는 RF 신호를 각 T/R 모듈에 분배 및 결합하여 신호를 송신하거나 수신하는 기능을 가진다.

AESA 안테나에 있어서 가장 핵심 소자인 T/R 모듈의 블록도는 그림 7과 같다. AESA 레이더의 위상 배열 안테나 빔은 T/R 모듈 출력들의 합으로서 형성되고, 각각의 개별적 모듈의 위상과 크기를 조절하여 빔 스캔을 한다. T/R 모듈은 AESA 안테나 장치에서 많은 부분을 차지하고 있기 때문에 전기적/기계적 인터페이스를 간략화하여 소형화되고 경량화된 간단한 인터페이스로 구현되어야 한다. 특히, 7개 MMIC(스위치 3개, 이득 증폭기 2개, 위상변위기, 디지털 감쇠기) 기능을 대신하는 고집적화된 단일 core chip MMIC를 적용하여 소형 경량화할 수 있다. 또한,

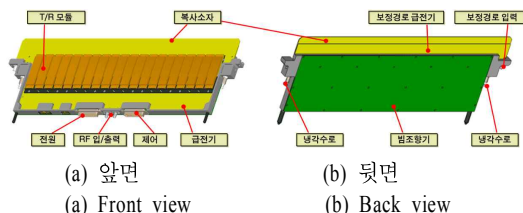


그림 6. T/R 단위 모듈 조립체(20 배열)

Fig. 6. T/R unit assembly with T/R module(20 array).

표 3. T/R 모듈 개발 목표 규격

Table 3. The specification of T/R module.

항 목	개발 목표 규격		비 고
1. 동작 대역	$F_0 \pm 5\% \text{ GHz}$		
2. 송신	1) 송신 출력	$\geq 40 \text{ dBm}$	Max.
	2) 송신 펄스 평탄도	0.6 dB 미만	
3. 수신	3) 송신 펄스 폭	40 us	Max.
	4) 송신 이득	37 dB 이상	
3. 수신	4) 드티	10 % 이상	
	1) 잡음 지수	3 dB 미만	
	2) 수신 이득	$32 \text{ dB} \pm 1 \text{ dB}$	
	3) RMS 위상 오차	$1.5^\circ$	6 bits / $5.625^\circ$ step
4. 전력 소모	$4.3 \text{ W} @ \text{duty } 10\%$		
5. 효율	26 %		
6. 발열량	$2.9 \text{ W} @ \text{duty } 10\%$		
7. 크기	16.5 mm × 5 mm × 67 mm		넓이 × 높이 × 길이
8. 무게	15 g 이하		

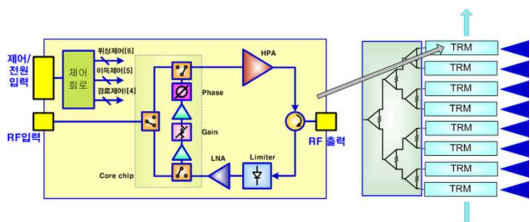


그림 7. T/R 모듈 블록도

Fig. 7. T/R module block diagrams.

단일 칩으로 위상 오차와 감쇠 오차를 획기적으로 줄일 수 있다. 항공기용으로 적용이 가능하도록 표 3과 같이 T/R 모듈 성능 파라미터를 도출하며, 무엇보다도 SWaP(size: 크기, weight: 무게, power: 전력 소모)를 고려해서 크기는 소형화, 무게는 경량, 전력 소모는 낮게 구현되도록 하는 것이 필수적이다. 본 논문에서는 성숙 단계에 있는 갈륨비소(GaAs) MMIC를 적용한 T/R 모듈을 설계/제작한다.

항공기용 레이더 시스템의 빔 제어는 특정 운영 모드에서 낮은 부엽 조건을 만족하기 위해서 정확한 위상 및 이득 제어가 요구되어진다. 또한, 빠른 빔 조향이 가능해야 되기 때문에 제어 명령 전송 및 계산시간을 줄이기 위해 분산형 빔 조향기를 적용하여

빔 계산을 수행한다<sup>[13]</sup>. 본 논문에서 전기적/기계적 인터페이스를 간략화하여 소형/경량의 LRU 단위의 빔 조향기를 최소화 하였다.

### 2-1-1-3 부 배열 급전기

부배열 급전기 설계는 쉽게 과소 평가되는 부분이지만, AESA 레이더의 전반적인 사양에 영향을 주는 중요한 부분이다. 부 배열 급전기는 송신 및 수신 동작 시 모든 T/R 모듈에 동일한 위상과 이득이 전달되도록 설계되어져야 한다. 또한, 부 배열 급전기는 일정 모듈들을 묶어서 하나의 부분 집합체를 형성하여 레이더 운용에 필요한 채널을 형성한다. 종래의 레이더에서 많이 볼 수 있는 핵, 차 채널을 이용한 모노필스 구조가 그 대표적인 예이다. 최근 적용 빔 형성 등과 같이 많은 수신 채널이 필요로 하게 되고 있으며, 부 배열 급전기 채널 수가 증가하게 되어 급전기 설계가 AESA 레이더 설계에 있어서 중요한 요소로 대두되고 있다. 특히, 다채널 부 배열 구조를 필요로 하는 항공기용 레이더에 적용 가능하기 위해서 급전기 구조는 소형화되고 있다<sup>[15]</sup>.

### 2-1-1-4 전원 공급기

AESA 레이더용 전원 공급기는 T/R 모듈에 낮은 전압을 공급하고, 빔 조향기 및 수신기에도 전원을 공급할 수 있어야 한다. 공급되는 전압은 낮은 리플과 노이즈로 반드시 안정화되어야 하고, 레이더 시스템에 요구되는 깨끗한 스펙트럼 특성을 가져야 한다. 특히, 536개 T/R 모듈에 전력을 집중적으로 공급하는 데는 항공기 탑재에 많은 어려움이 따른다. 여러 인터페이스 특성 등을 고려해 볼 때 분산형 구조 방식으로 전력을 공급하여야 하며, 신뢰성 측면에서 다중화 기능을 가지게 되어 안정적으로 동작할 수 있다<sup>[2]</sup>.

### 2-1-2 RF/처리 장치

RF/처리 장치는 RF 장치 부분인 4채널 수신기 및 아날로그 변환/디지털 변환(ADC/DDC) 모듈, 여자기(exciter), 송수신 제어기 및 전원 공급기와 처리 장치 부분인 신호 처리기로 구성되어 있다. 여자기는 다중 모드 파형 발생 신호, 보정 신호와 수신기 및 신호 처리기 기준 클럭 신호를 생성하여 분배하여 준다. 수신기는 4채널을 가지고 있으며, 각 채널은 모드에 따라 광대역(공대지/해 모드) 및 레이더 모드 신호를 수신하여 IF 단까지 주파수 하향 변환을 하고, 또한 각 채널은 디지털 감쇄 소자를 두어 STC (Sensitivity Time Control) 기능을 수행한다. 수신기부터 입력된 IF 신호는 A/D 변환기를 거쳐 디지털로 변환되고, 직접 신호 변환 방식의 디지털 복조 처리(DDC)를 거쳐 기저대역의 I/Q 신호로 복조하는 기능을 수행한다. 광 전송을 통해 전단된 I/Q 신호 처리는 COTS 보드를 기반으로 획득된 신호를 분석하여 상황 판단에 의한 각종 기능 수행에 있어서 성공적으로 제어되는 것을 확인하고, 차체 점검 상태를 모니터링하게 된다. RF/처리 장치는 VME(Versa Module Eurocard) 버스 기반의 개방형 구조로 되어 있다. RF/처리 장치 블록도는 그림 8, 수신기 블록도는 그림 9와 같다.

### 2-1-3 냉각수 순환 장치

AESA 레이더의 운용 시 열적 안전성 확보를 위하여 방열 시스템 구성이 필요하다. 방열 시스템은 장치 구성 요소인 냉각수 순환 장치, T/R 단위 모듈,

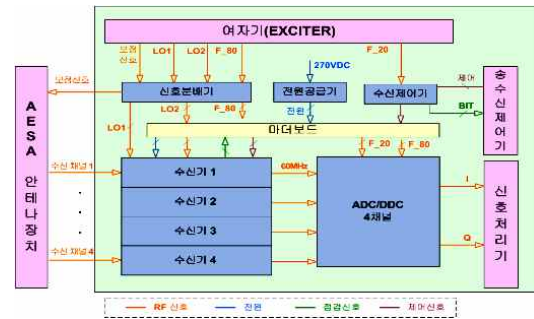


그림 8. RF/처리 장치 블록도

Fig. 8. Block diagram of RF and processor.

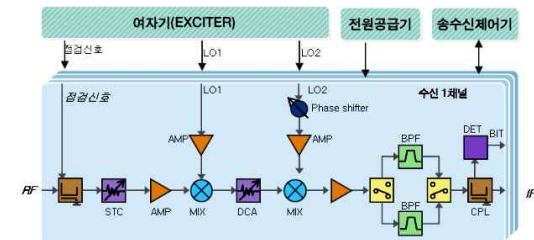


그림 9. 다채널 수신기 블록도

Fig. 9. Block diagram of multi-channel receiver.

냉각수 매니폴드로 구성된다. 냉각수 순환 장치에서 공급되는 냉각수는 안테나 장치 하우징의 상부 매니폴드에 연결되며, 매니폴드에서 각각의 T/R 단위 모듈로 분기되게 된다. 각각의 T/R 단위 모듈을 냉각시킨 냉각수는 하부 매니폴드에서 모아지며, 다시 냉각수 순환 장치로 연결되게 되는 구조로 되어 있다. 매니폴드 및 T/R 단위 모듈과 연결되는 커넥터는 자동 밀봉식(self-sealing) 커넥터를 사용하여 커넥터 분리 시 자동적으로 입구가 닫혀서 냉각수가 흐르지 않도록 하는 구조로 설계 및 제작하였다. AESA 안테나 장치의 냉각 구조는 그림 10과 같다.

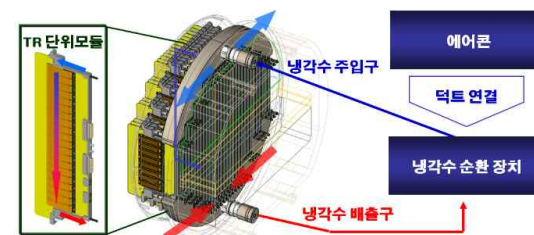


그림 10. AESA 안테나 장치의 냉각 구조

Fig. 10. Cooling mechanism of AESA antenna.

표 4. 냉각수 순환 장치의 사양

Table 4. The specification of liquid heat-exchanger.

항 목	개발 목표 규격	비 고
1. 냉각 능력	3 kW	duty 10 % 기준
2. 냉각수 순환 유량	15 LPM	
3. 냉각수 토출 압력	0.05 MPa	
4. Size	275 mm×350 mm×500 mm	넓이×높이×길이

냉각수 순환 장치의 사양은 표 4와 같다.

### III. 제작 및 시험 결과

#### 3-1 안테나 장치

본 논문에서 항공기 탑재가 가능하도록 전기적 기계적 인터페이스를 고려하여 설계/제작된 X-대역 AESA 레이더용 안테나 장치 형상은 그림 11과 같다.

제작된 안테나 장치에서 각 단위 모듈은 출력 40 dBm 이상의 T/R 모듈로 구성되며, T/R 모듈의 전원/제어/방열을 효율적으로 하기 위해서 분산형 구조의 T/R 단위 모듈 단위로 구성하였다. 20배열, 16배열, 12배열, 8배열 T/R 단위 모듈들이 각각 16조, 6조, 6조, 6조로 구성된다. 각각의 단위 모듈들은 그림 13과 같이 단일 LRU(Line Replaceable Unit)로 되어 있어 단위 모듈별로 한 번에 장착 가능한 구조로 되어 있다 특히, 안테나 장치에는 536개의 T/R 모듈을 제어하기 위한 제어 인터페이스, 공급되어야 하는 전원 인터페이스 RF 입/출력 인터페이스 및 단위 면적당 발열량이 밀집되어 있는 방열 인터페이스가 집약되

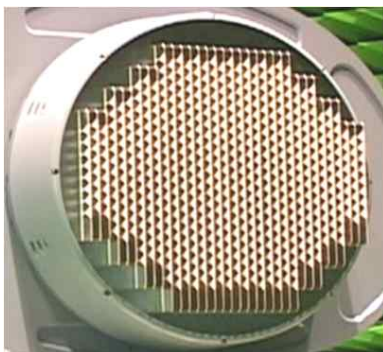


그림 11. 제작된 AESA 안테나 장치

Fig. 11. Photo of AESA antenna.

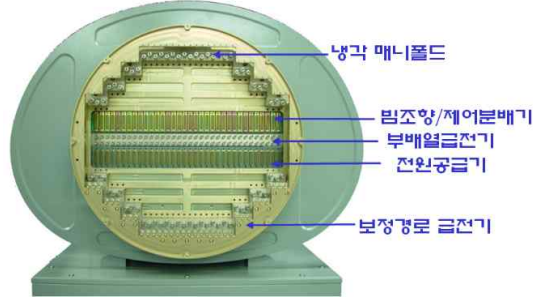


그림 12. AESA 안테나 장치 내부 구조

Fig. 12. Inside of AESA antenna.

는 구조여서 전기적/기계적 인터페이스를 보다 간략화해야 한다. 본 논문에서는 그림 12와 같이 T/R 단위 모듈에 분산형 구조의 기능들이 구현되어 전기적/기계적 인터페이스가 한 번에 체결되는 구조로 설계/제작되었다.

T/R 단위 모듈은 비발디 타입의 복사 소자(그림 13), T/R 모듈(그림 14), 빔 조향기, RF 분배/합성기 및 전원/제어 분배기로 구성되어 있다. 복사 소자는 스트립 구조의 광대역 특성을 갖고, 보정 경로 급전 구조를 쉽게 구현할 수 있는 장점이 있고, 측정 결과는 해석한 결과와 유사함을 확인하였다. T/R 모듈은 목표한 모든 사양을 만족하였으며, 특히, 그림 15와 같이 송신 출력은 40 dBm 이상을 만족함을 측정으로 확인하였다. 무게는 15 g으로 기존 개발된 T/R 모듈 보다 경량화되고, 효율은 26 %로 고효율화 되었다.

제작된 T/R 단위 모듈은 그림 16과 같다. 또한 T/R 단위 모듈에 바로 장착되는 구조여서 조립과 배열 간격을 맞추는데 아주 용이하다. T/R 단위 모듈에는 각 모듈들의 크기/위상을 제어하기 위해서 빔 조향기와 전원/제어분배기가 후면에 형성되어 있다. T/R 단위 모듈은 탈 장착이 용이하도록 모든 인터페이스가 같은 면에 형성되어 있기 때문에 쉽게 조립

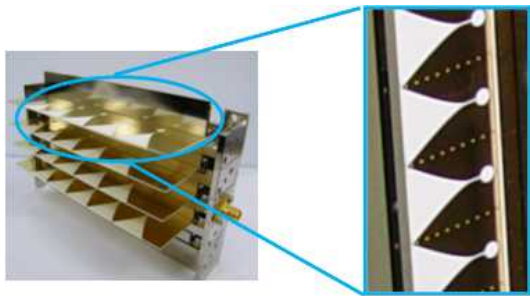


그림 13. 제작된 비발디 복사 소자  
Fig. 13. Photo of vivaldi radiator.

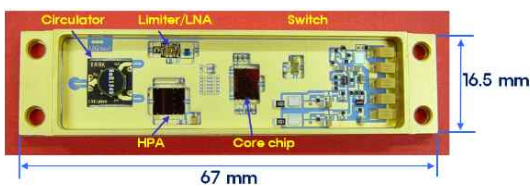


그림 14. 제작된 T/R 모듈  
Fig. 14. Photo of T/R module.

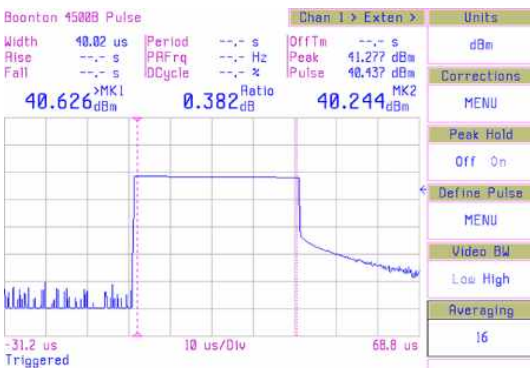


그림 15. 송신 출력 측정 결과  
Fig. 15. The result of transmit power.

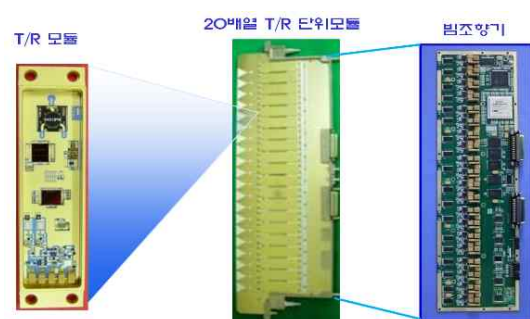


그림 16. 제작된 T/R 단위 모듈  
Fig. 16. Photo of T/R unit assembly.



그림 17. 제작된 전원 공급기  
Fig. 17. Photo of power supply.

이 가능하다.

그림 17은 제작된 전원 공급기 형상이다. 전원 공급기는 536개의 T/R 모듈에 전원을 공급하기 위해서 분산형 구조의 낮은 전압을 공급하게 된다. 특히, 전기적/기계적 인터페이스를 간략히 하여 LRU 단위의 체결이 가능한 구조로 설계되어 있는 것이 큰 특징이다.

### 3-2 RF/처리 장치

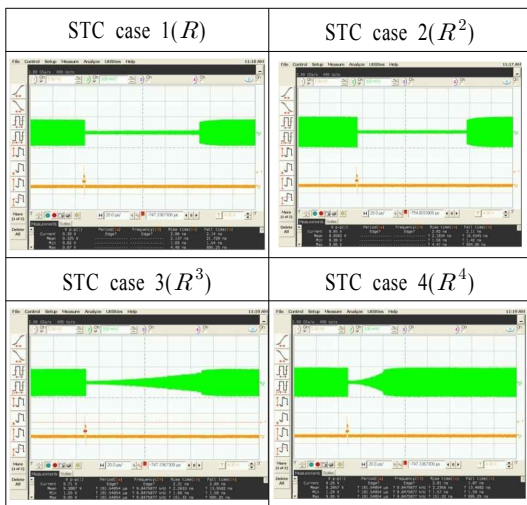
그림 18은 제작된 RF/처리 장치의 형상이다. 크기는 254 mm(너비)×230 mm(높이)×457 mm(길이)로서, 내부에 총 12개의 모듈들로 설계/제작되었다. 구조는 바닥면이 모기판 조립체로 되어 있고, 나머지 모듈들이 표준 인터페이스를 가지며, 너비가 모두 같은 크기(6U 크기)로 되어 있는 것이 가장 큰 특징이다. 모듈을 표준 크기 및 인터페이스를 적용하여 향후 확장이 가능하도록 하였다. RF 장치인 수신기, 스위치 모듈, 분배기 모듈, 여자기(파형/주파수 합성기), ADC/DDC 복조기 등은 HMIC로 소형/경량화 하였고, 전원 공급기 또한 6U 크기로 표준 인터페이스를 갖도록 제작하였다. 신호 처리기는 상용 SBC(Single Board Computer) COTS 제품을 사용할 계획이며, 이



그림 18. RF/처리 장치 형상  
Fig. 18. Photo of RF and processor.

표 5. STC 감쇄 곡선

Table 5. The attenuation curve of STC.



번 핵심 기술 확보에서는 제외되었다.

제작된 RF 장치의 수신기 STC(Sensitive Time Control) 기능 시험은 표 5에서와 같이 설계된 대로 구현됨을 확인하였다. 수신 신호는 근거리 클러터 특성

으로 인해 수신기가 포화되는 현상을 방지하기 위해 근거리 수신 처리 구간 동안 일정한 감쇄를 주어 수신기가 정상 동작할 수 있게 하는 기능이 STC 기능이다. STC는 지형 또는 클러터 특성 등 송신 펄스 신호 간의 구간 특성을 고려하여 STC 지수 곡선을 적용한다.

또한 파형 발생기에서는 다양한 운용 모드에 필요한 여러 가지 파형 또한 양호한 출력 특성을 표 6에서와 같이 확인하였다.

### 3-3 냉각수 순환 장치

그림 19는 제작된 냉각수 순환 장치의 형상이다. 크기는 275 mm(너비)×350 mm(높이)×500 mm(길이)로서 항공기 장착에 적합하도록 소형화 하였고, 항공기 외부에서 강제 공랭된 공기를 에어 덕트를 통해 냉각수 순환 장치로 받아들여 차가운 냉각수를 만들게 된다. 이 액냉식 냉각 시스템을 이용해 안테나 장치의 열을 방열하게 된다. 냉각수 순환 장치에는 펌프와 열교환기를 통해 열이 방출된다.

표 6. 파형 발생기 측정 결과

Table 6. Measurement result of waveform generator.

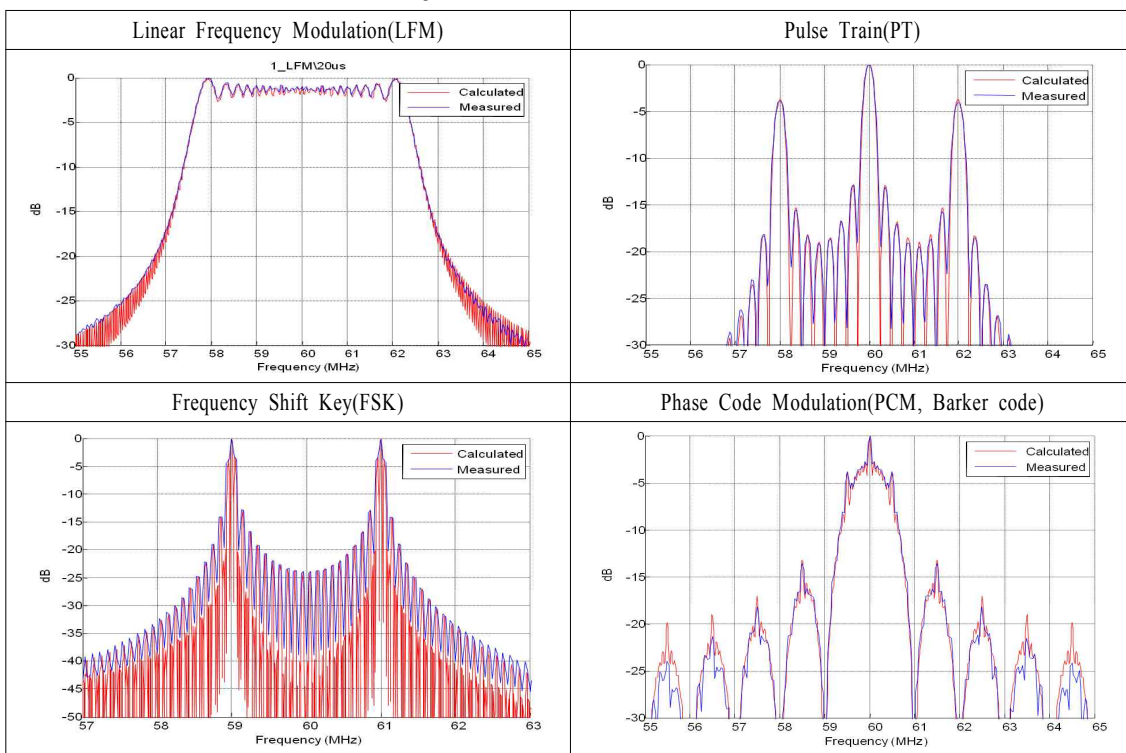




그림 19. 냉각수 순환 장치 형상  
Fig. 19. Photo of heat exchanger.

본 개발에서 제작된 냉각수 순환 장치는 536개 급의 T/R 모듈을 방열할 수 있는 냉각 능력, 유량, 냉각수 토출 압력 등이 만족하는지 안테나 장치에서 확인 시험을 하였고, 목표 성능을 만족함을 확인하였다.

### 3-4 근접 전계 시험

AESA 레이더에서 가장 중요한 시험 중 하나가 고속 빔 조향 및 빔 형성을 확인하는 것이다. 이를 위해서 근접 전계 측정 시설을 사용하여 빔 조향 기능을 확인하고, 안테나 패턴을 측정하였다. 챔버 내

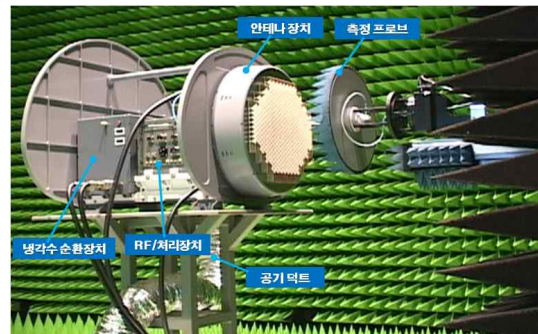


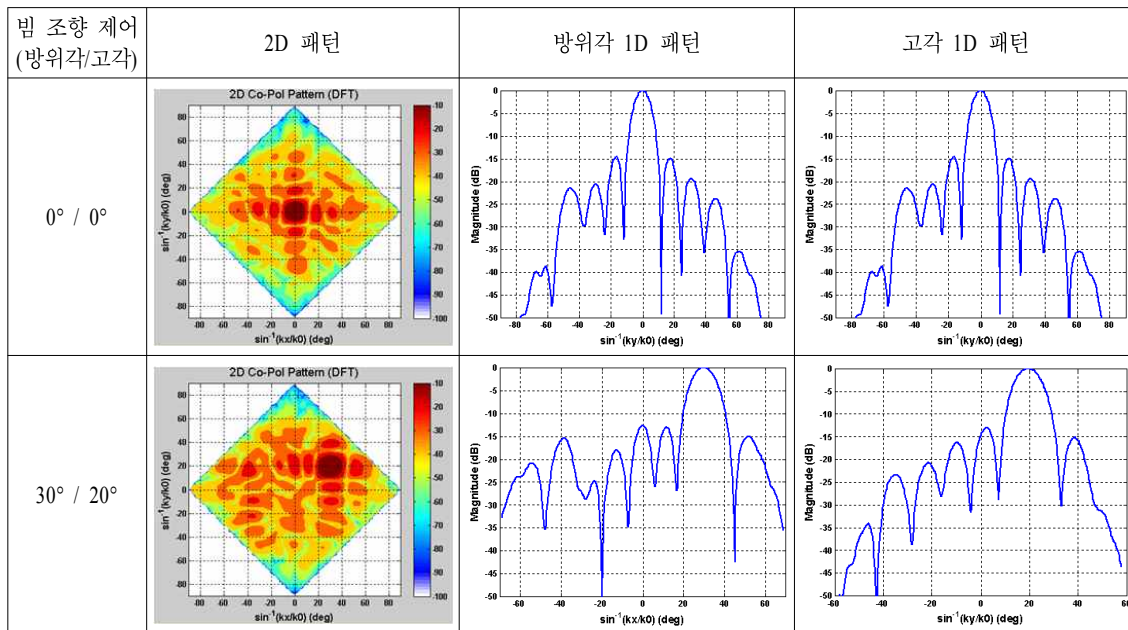
그림 20. AESA 레이더 프로토 타입의 근접 전계 측정  
Fig. 20. Near-field measurement of AESA radar prototype.

장치 구성도는 그림 20과 같다. 근접 전계 측정은 3 차원 안테나의 전기적 특성을 외부 환경을 배제하여 근거리 측정을 통해 분석하는 시스템이다. 안테나의 근접 전계를 측정하여 획득한 이득 및 위상 정보를 FFT 알고리즘을 이용하여 원 전계(far-field) 데이터로 변환한다.

본 개발에서는 AESA 레이더 안테나 장치의 성능, 구조, 제어 기능 및 인터페이스 등을 확인하기 위해서 T/R 모듈을 전체 536개급에서 실제는 19 % 정

표 7. 송신 패턴 측정 결과

Table 7. Transmit pattern results.



도 장착하고, 나머지 부분은  $50 \Omega$ 으로 터미네이션 시켰다.

### 3-4-1 송신 패턴

송신 빔은 균일(uniform) 분포를 사용하여 빔 조향의 정확도와 빔 형성 제어를 확인하였다. 또한 AESA 레이더 안테나에서의 송신 출력은 EIRP(Effective Isotropically Radiated Power)를 통해 확인하였다. 측정 결과는 표 7, 8과 같다.

측정된 EIRP와 예측된 EIRP 차이는  $0.67 \text{ dB}$  발생하였으며, 원인은 각 T/R 모듈과 복사 소자의 손실이 모두 동일하지 않고 약간의 차이가 발생하여 오차가 나타난 것으로 판단된다. 그리고, T/R 모듈의 개수가 소량이어서 더 많은 오차가 나타난 것 같다.

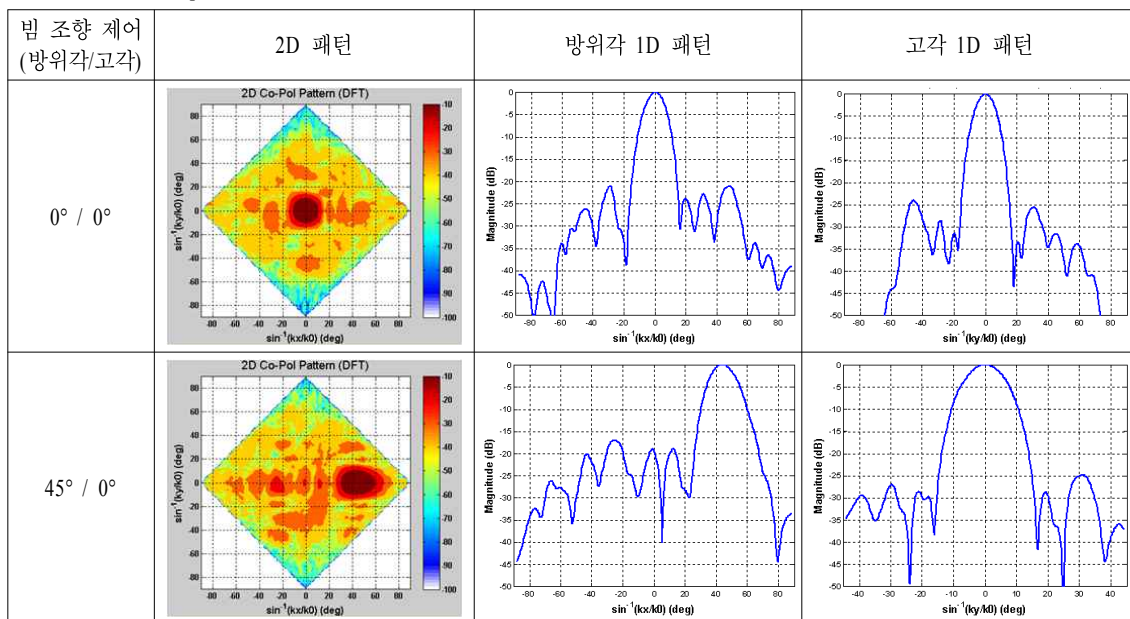
표 8. 송신 EIRP

Table 8. Transmit EIRP.

	예측값	비고
Directivity	24.7 dB	
복사 소자 손실	1.5 dB	
총 출력	$40 \text{ dBm} \times 100개 = 60 \text{ dBm}$	
예상 EIRP	$24.7 \text{ dB} - 1.5 \text{ dB} + 60 \text{ dBm} = 83.2 \text{ dBm}$	
측정 EIRP	82.53 dBm	예측값과의 차이: $0.67 \text{ dB}$

표 9. 수신 패턴 측정 결과

Table 9. Receive pattern results.



### 3-4-2 수신 패턴

수신 결과는 4채널의 부 배열로 구성되어 있으며, 각 채널의 측정 결과를 처리하여 전체 빔 패턴을 형성하였다. 측정 결과는 표 9와 같다. 높은 부엽은 배열 개수가 많지 않고 T/R 모듈 간의 이득 및 위상 오차 영향이 많이 작용한 것으로 판단된다. 하지만 배열 개수가 536개 정도로 되면 예측하는 낮은 부엽 수준으로 구현할 수 있을 것으로 판단된다.

## IV. 결 론

본 논문은 항공기 탑재 가능한 AESA 레이더의 핵심 기술 확보를 위해 프로토 타입을 자체 개발하였다. 항공기 탑재에 적합하도록 전기적, 기계적 인

터페이스를 고려하여 소형, 경량화 구조로 설계/제작하였다. 특히, 열 문제, 복잡한 인터페이스 및 제어분배에 관련된 문제를 간략화 하여 체결과 장착이 용이한 LRU 구조로 AESA 안테나 장치를 설계/제작하였고, 항공기 탑재가 가능하도록 소형, 경량화된 평면형 능동 전자주사식 위상 배열(AESA) 안테나 장치, 과형 발생 및 주파수 합성기 제작 기술, 다채널 수신기 등을 개발하였다.

레이더 프로토 타입에서는 AESA 레이더의 핵심 부품인 T/R(Transmit/Receive) 모듈을 기존 개발된 모듈보다 소형/경량화하여 항공기 탑재 가능성을 확인하였다. 출력 40 dBm 이상, 무게 15 g 이하, 효율 26 % 이상의 T/R 모듈을 개발하였다. 또한, T/R 단위 모듈도 기존 장비보다 소형/경량화하여 열 문제, 인터페이스 및 제어 분배를 LRU 단위로 구현하여 전기적/기계적 인터페이스를 보다 더 간략히 하였다. 이를 바탕으로 AESA 레이더 가장 핵심 기능인 전자적/고속 능동 빔 조향과 빔 형성을 안테나 근접 전계 패턴시험을 통해 확인하였다. 또한, 단위 면적당 출력 전력이 집중되는 항공기용 AESA 레이더에서 방열은 수냉이 적합함을 선진국 사례를 통해 알 수 있었으며, 개발된 장비의 수냉 능력이 만족함을 시험을 통해서 확인하였다. 무엇보다도 항공기 장착이 가능한 전기적 및 기계적 인터페이스 관련된 핵심 기술을 확보할 수 있었다.

본 개발에서 제외되었던 신호 처리 핵심 기술 확보는 향후 실시간 신호 처리기와 연동하여 실제 표적 탐지/추적 등 기본적인 AESA 레이더 성능 확인을 위한 추가적인 연구를 할 계획이다.

### 참 고 문 헌

- [1] 임상민, 전투기의 이해, 상, 이지북, pp. 76-90, 2005년.
- [2] D. N. McQuiddy, R. L. Gassner, "Transmit/receive module technology for X-band active array radar", *Proceedings of the IEEE*, vol. 79, issue 3, pp. 308-341, Mar. 1991.
- [3] S. Moore, "UK airborne AESA radar research", *Aerospace and Electronic Systems Magazine, IEEE*, pp. 29-35, Feb. 2010.
- [4] P. Lacomm, "New trend in airborne phased array radars", *IEEE International Symposium, Phased Array Systems and Technology*, pp. 17-22, Oct. 2003.
- [5] Merrill I. Skolnik, *Radar Handbook*, McGraw-Hill, pp. 5.1-5.46, 2008.
- [6] F. Gautier, P. Lacomm, "Future electronically steered antennas for airborne radar", *IEE Workshop, The Future of Radar in the UK and Europe*, pp. 2/1-2/6, Nov. 1999.
- [7] D. N. McQuiddy, R. L. Gassner, P. Hull, J. S. Mason, and J. M. Bedinger, "Transmit/receive module technology for X-band active array radar", *Proceedings of the IEEE*, pp. 308-341, Mar. 1991.
- [8] Hubregt J. Visser, *Array and Phased Array Antenna Basics*, John Wiley & Sons, Ltd., 2005.
- [9] Robert J. Mailloux, *Phased Array Antenna Handbook*, Second Edition, Artech House.
- [10] M. Uhlmann, J. S. Tanner, and G. Albarel, "Design characteristics of the AMSAR airborne phased array antenna", *Electronic Beam Steering(Ref. No. 1998/481)*, *IEE Colloquium on*, issue 28, pp. 3/1-3/5, Oct. 1998.
- [11] M. Scott, "SAMPSON MFR active phased array antenna", *2003 IEEE International Symposium, Phased Array Systems and Technology*, pp. 119-123, Oct. 2003.
- [12] A. B. Smolders, "Design and construction of a broadband wide-scan angle phased-array antenna with 4096 radiating elements", *IEEE International Symposium, Phased Array Systems and Technology*, pp. 87-92, Oct. 1996.
- [13] 전상미, 나형기, 김수범, 이정원, 김동윤, 김선주, 안창수, 이창의, "평면형 능동 위상 배열 레이더용 안테나 시스템 개발", 한국전자과학회 논문지, 20(12), pp. 1340-1350, 2009년 12월.
- [14] D. H. Schaubert, "Wide-band phased arrays of vivaldi notch antennas", *Conference Publication No. 436 IEE 1997, 10th International Conference on Antennas and Propagation*, pp. 14-17, Apr. 1997.
- [15] L. Josefsson, L. Erhage, and T. Emanuelsson, "An

AESA development model for next generation fighter aircraft radar", *IEEE International Symposium, Phased Array Systems and Technology*, pp. 454-457, Oct. 1996.

### 정민길



1994년 2월: 경상대학교 전자공학과 (공학사)  
1996년 2월: 경상대학교 전자공학과 (공학석사)  
1996년 7월~현재: (주)LIG넥스원 책임연구원  
[주 관심분야] 초고주파 회로 및 시스템, 능동 위상 배열 레이더

### 전상미



배열 레이더

1999년 2월: 포항공과대학교 전자전기공학과 (공학사)  
2006년 2월: 포항공과대학교 전자전기공학과 (공학박사)  
2006년 5월~현재: (주)LIG넥스원 선임연구원  
[주 관심분야] 안테나 및 능동위상

### 김동윤



능동 위상 배열 레이더

2005년 2월: 광운대학교 전자공학부 (공학사)  
2007년 2월: 광운대학교 전파공학과 (공학석사)  
2007년 2월~현재: (주)LIG넥스원 주임연구원  
[주 관심분야] 반도체 송수신 모듈,

### 나형기



[주 관심분야] 안테나 및 능동위상 배열 레이더

1991년 2월: 포항공과대학교 전자전기공학과 (공학사)  
1993년 2월: 포항공과대학교 전자전기공학과 (공학석사)  
1996년 2월: 포항공과대학교 전자전기공학과 (공학박사)  
1996년 1월~현재:(주)LIG넥스원 선임연구원, 책임연구원, 수석연구원

### 김상근



설계, 초고주파 송수신

2005년 2월: 홍익대학교 전자전기 공학부 (공학사)  
2007년 2월: 홍익대학교 전자정보통신공학과 (공학석사)  
2007년 2월~현재: (주)LIG넥스원 주임연구원  
[주 관심분야] 초고주파 능동회로



**KTH Electrical Engineering**

**Wide-angle scanning wide-band  
phased array antennas**

ANDERS ELLGARDT

Doctoral Thesis  
Stockholm, Sweden 2009

TRITA-EE 2009:017  
ISSN 1653-5146  
ISBN 978-91-7415-291-3

KTH School of Electrical Engineering  
SE-100 44 Stockholm  
SWEDEN

Akademisk avhandling som med tillstånd av Kungl Tekniska högskolan framlägges till offentlig granskning för avläggande av teknologie doktorsexamen fredagen den 8 maj 2009 klockan 13.15 i sal F3, Kungl Tekniska högskolan, Lindstedtsvägen 26, Stockholm.

© Anders Ellgardt, 2009

Tryck: Universitetsservice US AB

# Abstract

This thesis considers problems related to the design and the analysis of wide-angle scanning phased arrays. The goals of the thesis are the design and analysis of antenna elements suitable for wide-angle scanning array antennas, and the study of scan blindness effects and edge effects for this type of antennas. Wide-angle scanning arrays are useful in radar applications, and the designs considered in the thesis are intended for an airborne radar antenna. After a study of the wide-angle scanning limits of three candidate elements, the tapered-slot was chosen for the proposed application. A tapered-slot antenna element was designed by using the infinitive array approach and the resulting element is capable of scanning out to 60° from broadside in all scan planes for a bandwidth of 2.5:1 and an active reflection coefficient less than -10 dB. This design was implemented on an experimental antenna consisting of 256 elements. The predicted performance of the antenna was then verified by measuring the coupling coefficients and the embedded element patterns, and the measurements agreed well with the numerical predictions. Since the radar antenna is intended for applications where stealth is important, an absorbing layer is positioned on top of the ground plane to reduce the radar cross section for the antenna's cross-polarization. This absorbing layer attenuates guided waves that otherwise lead to scan blindness, but does not adversely affect the antenna performance for the desired scan directions and frequencies. The highest frequency limit of the tapered-slot element is set by scan blindnesses. One of these scan blindnesses is found to be unique to tapered-slot elements positioned in triangular grids. This scan blindness is studied in detail and a scan blindness condition is presented and evaluated. The evaluation of the experimental antenna shows that edge effects reduce the H-plane performance of the central elements. These edge effects are further studied and characterized, by comparing the scattering parameters for finite-by-infinite arrays and infinite arrays. In this way it is possible to divide the edge effects into two categories: those caused by finite excitation, and those caused by perturbed currents due to the geometry of the edge. A finite difference time domain code with time shift boundaries is used to compute the active reflection coefficients needed to compute the scattering parameters, but this code cannot directly compute the active reflection coefficient for all the required phase shifts. Hence, an additional method is presented that makes it possible to compute arbitrary phase shifts between the elements using any numerical code with limited scan directions.



# Preface

This work has been carried out at the Division of Electromagnetic Engineering, Royal Institute of Technology (KTH), Sweden. I express my gratitude to my principal supervisor Martin Norgren for his guidance and tireless proofreading of my manuscripts. I would also like to thank my other supervisors Hans Steyskal, Patrik Persson and Lars Jonsson for their help and encouragement, especially Patrik Persson who continued to aid me in my work after he left the division. Furthermore, I thank all present and former colleagues at the department for providing an inspiring atmosphere.

The thesis work is mainly done within two projects within the National Aviation Engineering Research Programme (NFFP3+ and NFFP4). In these projects KTH have had an industrial partner Saab Microwave Systems who among many things built the experimental antenna. I am very grateful for the great work done by Andreas Wikström at Saab who helped me with some of the practical problems that are otherwise neglected in academia. I would also like to acknowledge Anders Höök and Joakim Johansson at Saab for their input and encouragement.

I have used several different numerical codes during this work. The most frequently used code was the PBFDTD-code provided by Henrik Holter. Apart from the code itself, he has given me excellent support whenever I required it, thank you. I have also had the opportunity to visit FOI and use their FDTD-code written by Torleif Martin. I would like to thank Lars Pettersson and Torleif Martin for this opportunity. The friendly atmosphere at FOI made every visit enjoyable and informative.

Finally and most of all I would like to thank my family and friends. Without your support this work would not have been possible. I express my earnest gratitude to my parents and my sister for their love and support. Most of all, to my wife, Jin for her love and patience, I love you!

*Anders Ellgårdt*  
Stockholm, March 2009



# List of papers

This thesis consists of a General Introduction and the following scientific papers:

- I A. Ellgardt, "Study of Rectangular Waveguide Elements for Planar Wide-Angle Scanning Phased Array Antennas". *IEEE International Symposium on Antennas and Propagation (AP-S 2005)*, Washington, U.S., July 2005
- II A. Ellgardt and P. Persson, "Characteristics of a broad-band wide-scan fragmented aperture phased array antenna". *First European Conference on Antennas and Propagation (EuCAP)*, Nice, France, November 2006
- III A. Ellgardt, "Effects on scan blindesses of an absorbing layer covering the ground plane in a triangular grid single-polarized tapered-slot array". *IEEE International Symposium on Antennas and Propagation (AP-S 2008)*, San Diego, U.S., July 2008
- IV A. Ellgardt, "A Scan Blindness Model for Single-Polarized Tapered-Slot Arrays in Triangular Grids". *IEEE Transactions on Antennas and Propagation*, Vol. 56, No. 9, pp 2937-2942, September 2008.
- V A. Ellgardt and A. Wikström, "A single polarized triangular grid tapered-slot array antenna". Accepted for publication in *IEEE Transactions on Antennas and Propagation*, 2009
- VI A. Ellgardt, "Computing return loss for arbitrary scan directions using limited scan codes for infinite phase arrays". *Submitted to Journal January 2009*
- VII A. Ellgardt and M. Norgren, "A study of edge effects in triangular grid tapered-slot arrays using coupling coefficients". *Submitted to Journal March 2009*

## The author's contribution to the included papers

I did the main part of the work in the papers included in this thesis. Martin Norgren and Patrik Persson have helped me with proof reading of the manuscripts and made helpful suggestions, and in paper II Patrik wrote part of the numerical code used for the optimization. In paper V Andreas Wikström was responsible for the mechanical construction and he and his co-workers at Saab built the experimental antenna. Andreas also performed all the S-parameter measurements.



# Contents

<b>1</b>	<b>Introduction</b>	<b>1</b>
1.1	Background . . . . .	1
1.2	Some phased array antenna issues . . . . .	2
1.3	Main contribution of the thesis . . . . .	2
1.4	Thesis outline . . . . .	3
<b>2</b>	<b>Array theory</b>	<b>5</b>
2.1	Planar arrays . . . . .	9
2.2	Infinite array . . . . .	12
<b>3</b>	<b>Wide scan elements</b>	<b>17</b>
3.1	Waveguide aperture element . . . . .	18
3.2	Fragmented aperture element . . . . .	19
3.3	Tapered-slot element . . . . .	23
<b>4</b>	<b>Experimental antenna</b>	<b>31</b>
<b>5</b>	<b>Scan blindness</b>	<b>37</b>
5.1	Dielectric slab on top of a ground plane . . . . .	37
5.2	Tapered-slot triangular grid scan blindness . . . . .	38
5.3	Broadside scan blindnesses . . . . .	40
<b>6</b>	<b>Edge effects</b>	<b>43</b>
6.1	Finite-by-infinite arrays . . . . .	44
6.2	Infinite array data . . . . .	47
<b>7</b>	<b>Conclusions</b>	<b>51</b>
<b>8</b>	<b>Summary of papers</b>	<b>53</b>
8.1	Paper I . . . . .	53
8.2	Paper II . . . . .	53
8.3	Paper III . . . . .	54
8.4	Paper IV . . . . .	55

8.5 Paper V . . . . .	55
8.6 Paper VI . . . . .	55
8.7 Paper VII . . . . .	56
<b>Bibliography</b>	<b>57</b>

# Chapter 1

## Introduction

### 1.1 Background

Phased array antennas consist of multiple fixed antenna elements, which can be excited differently in order to control the radiation pattern. In a basic phased array the elements are fed coherently and at all elements phase shifters or time-delays are used to scan the beam to desired directions in space. Uniformly excited arrays with a linear phase shift will create a directive beam that can be repositioned electronically by changing the phase shifts. If the amplitude and phase of each element can be controlled individually the beam of the array can be formed to more general patterns. This technique is called beamforming and can be used to suppress side lobes, to create radiations pattern nulls in certain directions, or to create application specific patterns [1].

Phased array antenna systems can be used in numerous applications, where one of the oldest is radar systems. The first phased array radar system dates back to the second world war, and today phased array radar systems are increasingly used on naval ships and aircrafts. Modern phased array radar systems can perform several tasks simultaneously, like keeping track of ground and air targets while at the same time communicating with other units.

The second oldest application is radio astronomy, where phased arrays can be used by themselves or as a feed for a large reflector antenna. An ongoing project that may use phased arrays in both these configurations is the Square Kilometre Array (SKA) [2, 3]. SKA will probe the gaseous component of the early Universe, thereby addressing fundamental questions in research on the origin and evolution of the Universe. This is an enormous international project in which the largest radiotelescope in the world will be built.

An application on the rise is mobile communication systems, where beamforming can be used for avoiding overlap between communication cells, changing the coverage during the day or to increase the range for a single base station. Phased arrays are also used for synthetic apertures, broadcasting, and radio frequency identification (RFID) readers.

## 1.2 Some phased array antenna issues

Phased array antennas are cumbersome to analyze directly due to their large size in terms of wavelengths. An additional problem is that the arrays often are densely packed, which yields strong coupling between the elements. As a consequence of the strong coupling the active reflection coefficient changes with excitation, and therefore multiple calculations with different excitations are always required to fully characterize an antenna. To design a phased array antenna one is usually required to either disregard the coupling between the elements or to assume that the antenna elements behave as if they were positioned in an infinite array. The infinite array approximation is usually the best choice for analyzing large dense arrays, for which the approximation is good for the central elements. Several textbooks on the subject are available for the antenna engineers, and the author's personal favorites are [4–7].

A recent progress in phased array research is to solve the fields for the whole antenna in one simulation, either using clever numerical codes that utilize characteristic currents to reduce the number of unknowns, or using a method that approximates the finite array with a finitely excited infinite array with corrections for the edges [8–15]. Another approach is to solve the numerics by brute force, using large clusters of computers [16, 17], or by dividing the array into subdomains which are linked together by the boundary conditions [18, 19]. All these methods allows the engineer to solve larger and more complex problems, and the increased accuracy of the numerical methods reduces the need for measurements.

## 1.3 Main contribution of the thesis

In this thesis, the emphasis has been on reducing the complexity of the phased array antennas, and on trying to answer why specific elements work the way they do and how different design solutions affect the antenna parameters. Much of the work is done by using the infinite array approximation. The choice is partly made out of necessity, due to limited numerical resources, but also since it is a powerful method that fits the aim of the thesis.

The aim was to design and study wide-angle scanning wide-band planar phased arrays, and a specific goal was to design an antenna element for a phased array radar antenna. This antenna was intended to be carried by a military aircraft, which requires low radar cross section and lightweight construction.

In order to reach the goal, a number intermediate goals were determined, which can be summarized as:

- Investigate and find suitable antenna elements for wide-angle scanning arrays.
- Design an antenna element for a wide-angle scanning phased array radar antenna.
- Build an experimental antenna based on the design of the wide-angle scanning antenna element.

- Investigate and model scan blindesses and surface waves for the chosen design.
- Investigate and characterize edge effects for the chosen design.

## 1.4 Thesis outline

Chapter 2 gives a brief overview of the basic phased array theory for finite and infinite arrays.

In chapter 3, three types of elements for wide-angle scanning arrays are described and discussed, namely: the waveguide aperture element, the fragmented aperture element, and the tapered-slot element. The tapered-slot element is chosen for the experimental antenna and the outline for the design of this element is given.

The experimental antenna consists of 256 elements. It was built by Saab Microwave Systems and the evaluation of the results is given in chapter 4. The performance of the experimental antenna is shown to agree well with the numerical results and the active return loss and embedded element patterns are presented.

The tapered-slot element designed for the experimental antenna displays three types of scan blindesses. It is important to characterize these scan blindesses since they limit the bandwidth and wide-angle scanning performance of the antenna. In chapter 5 a brief description is given of the scan blindness phenomena and the different scan blindnesses types.

In chapter 6 the edge effects are studied for an antenna similar to the experimental antenna. The arrays studied are finite in one direction only, which simplifies the analysis and makes it possible to study the effect of a single edge. The edge effects are studied by comparing the coupling coefficients for a finite-by-infinite array and an infinite array. At the end of this chapter a method, based on a finite difference time domain code using time shift boundaries, is presented on how to compute the active reflection coefficient for a phase shift that moves the main beam outside visual space. These phase shifts are crucial for computing the infinite array coupling parameters.

Chapter 7 contains a summary of the thesis and general conclusions, and chapter 8 contains a summary of the individual papers.



## Chapter 2

# Array theory

This chapter provides an introduction for readers unfamiliar with the basic concepts of planar phased array antennas and infinite arrays. The focus will be on two questions that are of key importance. The first is: how does the antenna radiate, and the second, how efficient is the antenna. There are many other questions that are also interesting to answer, regarding the ease and cost of manufacturing, the radar cross section, the size and weight of the antenna, but without an answer to the two first questions one cannot evaluate the performance of an antenna.

In the idealized antenna design case, we consider antennas in free space. For such a case we can partition the surrounding space of an antenna into two regions, the near field region and the far field region. The far field region is the region where the angular field distribution of an antenna is essentially independent of the distance from a specified point in the antenna region [20]. A prerequisite for this condition is that the fields in the far field region are the radiated fields from the antenna. A radiated field from a finite antenna is a wave whose amplitude is proportional to the inverse of the distance from the source. That means that the power density of the field decreases as inverse of the square of the distance to the source, and that the power of the radiated fields passing through a sphere enclosing the element is constant, regardless of the radius of the sphere. In the far field region the field distribution of an antenna is called the radiation pattern, which can be expressed in several ways depending on how the surroundings of the antenna are treated. One type of radiation pattern is the embedded element pattern, which is practical when the antenna consists of a group of antenna elements. The embedded element pattern is the radiation pattern of an element in a system of several elements when this element is connected to a generator with internal impedance equal to the characteristic impedance of the port of the element and all other element ports are terminated with their characteristic impedance.

An important usage of the embedded element patterns,  $f_n$ , is that they can be used to describe the electric far field,  $E$ , of an array antenna. The electric far field in a field point,  $r$ , from a sequence of antenna elements, at the positions  $r_n$ ,

$n = 1, 2, \dots$ , has the form

$$\mathbf{E}(\mathbf{r}) = \sum_{n=1}^N A_n \mathbf{f}_n(\theta_n, \phi_n) \frac{e^{-jkR_n}}{R_n}. \quad (2.1)$$

Here,  $N$  is the number of elements,  $A_n$  is the incident voltage at the port of element  $n$ ,  $\theta_n$  and  $\phi_n$  are the individual elements spherical local description to the field point  $\mathbf{r}$ , and  $k$  is the free space wavenumber. Furthermore the distance between element  $n$  and the field point is denoted  $R_n$ , where

$$R_n = |\mathbf{r} - \mathbf{r}'_n|. \quad (2.2)$$

In Eq. (2.1),  $\mathbf{r}$ , has to be in the joint far field region, which is the intersection of the far field regions of all the antenna elements. From the field obtained in Eq. (2.1) we can compute the radiation pattern of the antenna elements as a group. The radiation pattern expresses in which direction the array antenna radiates and where zeros or non-radiation directions are localized. However, it is not sufficient to describe the efficiency or the matching properties of the array antenna.

The efficiency of an antenna is partly determined by how much of the incident power that is reflected at the antenna port, and partly by the material properties of the antenna array. The first type of loss is quantified by the active reflection coefficient,  $\Gamma_m$ , the amplitude of the reflected wave at port  $m$ , which can be calculated from quantities called the scattering parameters (S-parameters). An S-parameter,  $S_{mn}$ , relates the amplitude of an incident wave at port  $n$ ,  $A_n$ , to the amplitude of the outgoing wave at port  $m$ . It is usually the preferred quantity to measure in experimental antennas and is therefore chosen to represent coupling in this thesis. The relation between  $\Gamma_m$  and  $A_n$  is expressed as

$$\Gamma_m = \sum_{n=1}^N S_{mn} A_n. \quad (2.3)$$

With the knowledge of  $\mathbf{f}_n$  and  $S_{mn}$  we can obtain estimates of the array performance. However, for large arrays it is computationally costly to determine the embedded element patterns and the S-parameters. A way to circumvent this problem is to simplify the theory. A simplification can be obtained for the E-field in the far field region of the array antenna. The electric-field given by Eq. (2.1) is valid for a region that is larger than the far field region for the antenna elements as a group. In Figure 2.1 this is illustrated for four elements, where the boundary between the far field region and the near field region of the individual elements are conceptually depicted as circumscribing circles. To achieve a radiation pattern for this antenna the field point must be farther away from the elements, so that the fields emitted from the antenna elements seem to come from the same direction thus,  $\theta_n \approx \theta$  and  $\phi_n \approx \phi$ . This approximation holds when the antenna elements are located much closer to the origin than the field point, in which case the distance  $R_n$

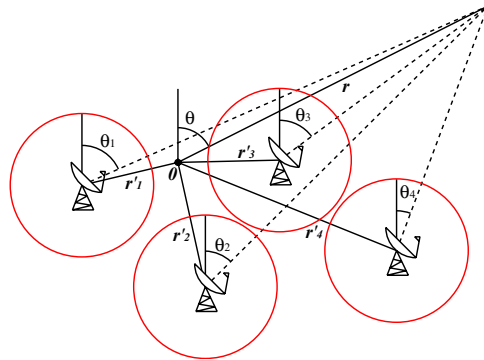


Figure 2.1: The field point  $\mathbf{r}$  is in the far field regions for the individual antenna elements but not in the far field region of the antenna elements as a group.

between the source and field point can be approximated with a Taylor series. In the far-field zone the exponential terms in Eq. (2.1) describes how the phase changes with position in space. Here the difference in phase between elements is important, which requires two terms in the Taylor series. The distance is then simplified to

$$R_n \approx r - \hat{\mathbf{r}} \cdot \mathbf{r}'_n = \left\{ \hat{\mathbf{r}} = \frac{\mathbf{k}}{k} \right\} = r - \frac{\mathbf{k}}{k} \cdot \mathbf{r}'_n, \quad (2.4)$$

where  $\mathbf{k}$  is defined as

$$\begin{aligned} \mathbf{k} &= k_x \hat{\mathbf{x}} + k_y \hat{\mathbf{y}} + k_z \hat{\mathbf{z}}, \\ k_x &= k \sin \theta \cos \phi, \\ k_y &= k \sin \theta \sin \phi, \\ k_z &= k \cos \phi. \end{aligned} \quad (2.5)$$

The denominator of the last term in Eq. (2.1) describes how the amplitude of the far field decreases with distance. In the far field zone the different distances to the elements will have a negligible effect on the magnitude of the individual element contributions, whereby it is sufficient to approximate

$$\frac{1}{R_n} \approx \frac{1}{r}. \quad (2.6)$$

The array antenna can be seen as an aperture where the elements are sample points. An efficient way to sample the aperture is to use identical elements placed in a periodic pattern, which yields similar embedded element patterns for the elements in the center of the antenna. Hence, for large array antennas it is a good approximation that the embedded element patterns are identical for all elements.

$$\mathbf{f}_n(\theta, \phi) = \mathbf{f}_0(\theta, \phi) \quad (2.7)$$

Using approximation (2.4), (2.6), and (2.7) we can in Eq. (2.1) move out the element pattern from the summation, by which the far-field becomes a product of an element pattern, a spherical wave emitted from the origin, and a factor depending only on the inter element spacing. This factor is called the array factor and unlike the element pattern it varies rapidly with the direction for large arrays.

$$\mathbf{E} = \underbrace{\mathbf{f}_0(\theta, \phi)}_{\text{element pattern}} \frac{e^{-jkr}}{r} \underbrace{\sum_{n=1}^N A_n e^{j\mathbf{k} \cdot \mathbf{r}'_n}}_{\text{array factor}} \quad (2.8)$$

Equation (2.8) is a considerable simplification of Eq. (2.1) from the analytical and computational perspective, since we only need to know one embedded element pattern.

To change the radiation pattern we use the excitation,  $A_n$ . The number of available synthesis techniques for the excitation is large, and the best choice depends on the application. One of the most basic excitations is when the amplitude of the excitation is uniform  $|A_n| = A$  and only the phase is changed to form a radiation pattern. This type of excitation can produce directive narrow beams suitable for many applications. Let's derive such an excitation for an array where one of the elements is positioned at the origin with its excitation set to  $A$ , then term in the array factor corresponding to this element is equal to  $A$ . To maximize the array factor for a specific direction, say  $\mathbf{k}_0$ , the phase of  $A_n$  must be chosen so that all the remaining terms in the array factor in this direction are equal to  $A$ . An excitation that fulfills this requirement is

$$A_n = A e^{-j\mathbf{k}_0 \cdot \mathbf{r}'_n}. \quad (2.9)$$

For the case when all the elements have identical element patterns, Eq. (2.9) is the optimal excitation to achieve the maximum gain. This excitation is a special case of the more general maximum-array-gain theorem, which holds for nonidentical elements, see e.g. [7, Ch. 1]. For the excitation given by Eq. 2.9, the far field becomes

$$\mathbf{E} = \mathbf{f}_0(\theta, \phi) \frac{e^{-jkr}}{r} A \sum_{n=1}^N e^{j\mathbf{k}' \cdot \mathbf{r}'_n}, \quad (2.10)$$

where  $\mathbf{k}' = \mathbf{k} - \mathbf{k}_0$ .

Let's consider an example, where a linear array antenna with  $N$  elements and an element spacing  $a$  is excited with the excitation (2.9). Then the antenna's main beam will be directed  $\pi/2 - \theta_0$  from the array axis, see Fig. 2.2. For this direction the phase shifts between the elements compensate for the difference in phase caused by the different lengths the waves travel to the far field point. These phase shifts can be realized either by delaying the signal between the elements or by using phase shifters that change the phase of the excitation. A time delay between elements  $n$  and  $n+1$  is equal to the time the wave travels the distance  $\mathbf{k}_0 \cdot \mathbf{r}'_n - \mathbf{k}_0 \cdot \mathbf{r}'_{n+1} = a \cos \theta_0$ . The

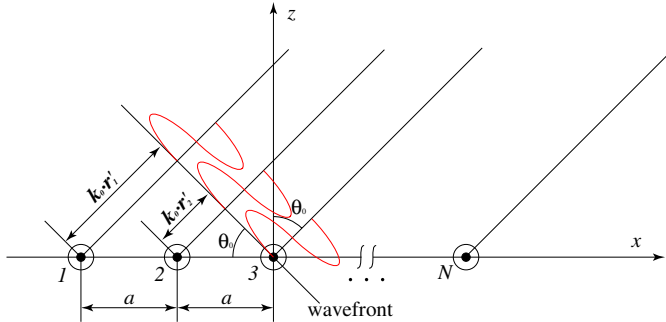


Figure 2.2: Linear array with  $N$  elements steered out to  $\theta_0$  from broadside scan.

time delay for a specific scan direction is frequency independent unlike the phase shift that changes with frequency. Therefore, if phase shifters are used the direction  $\theta_0$  of the beam will also be a function of the frequency. This effect is unsuitable for broadband applications, but could be used to steer the beam in narrow band applications.

We have above introduced the basic key quantities, the embedded element pattern, the excitation, the S-parameters, and the active reflection coefficient. These key parameters will play an important role in this thesis. We will know continue to study the excitation of the planar array and then study how the active reflection coefficient is linked to the embedded element pattern for an infinite array.

## 2.1 Planar arrays

The antennas studied in this thesis are planar and the element spacing is periodic. Planar arrays with periodic spacing will have a periodic excitation, and in this section we explain the periodicity of the excitation and show how it affects the radiation pattern.

The elements in the array are positioned in the  $xy$ -plane with the normal,  $\hat{\mathbf{n}}$ , chosen in the positive  $z$ -direction. Two primitive vectors called  $\mathbf{a}_1$  and  $\mathbf{a}_2$  are used to describe the element positions in the grid. The first of the primitive vectors,  $\mathbf{a}_1$ , is chosen to be parallel to the  $x$ -axis and the second primitive vector,  $\mathbf{a}_2$ , is directed with the angle  $\gamma$  from the  $x$ -axis in the  $xy$ -plane, see Fig. 2.3. These primitive vectors are denoted

$$\begin{aligned}\mathbf{a}_1 &= a\hat{\mathbf{x}}, \\ \mathbf{a}_2 &= c\hat{\mathbf{x}} + b\hat{\mathbf{y}}, \\ c &= \frac{b}{\tan \gamma}.\end{aligned}\tag{2.11}$$

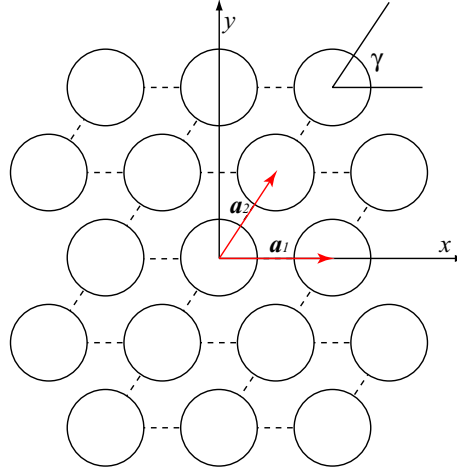


Figure 2.3: General planar array structure given by the primitive vectors  $\mathbf{a}_1$  and  $\mathbf{a}_2$ . The circles represent antenna elements.

We will now show that when the elements are configured in periodic patterns there are several different excitations that have identical radiation patterns. Consider that the element positions are given by Eq. (2.11), then the term in the array factor corresponding to element  $n$  becomes

$$A_n e^{j\mathbf{k}' \cdot \mathbf{r}'_n} = A_n e^{j\mathbf{k}' \cdot (p(n)\mathbf{a}_1 + q(n)\mathbf{a}_2)}, \quad (2.12)$$

where  $q$  and  $p$  are integers that together with the primitive vectors describe the position of element  $n$ .

As concluded above, the array factor has a maximum when the exponential terms are equal for all values of  $n$ . This occurs when  $\mathbf{k}_0 = \mathbf{k}$  but also for other values of  $\mathbf{k}_0$ . All vectors  $\mathbf{k}'$  such that

$$e^{j\mathbf{k}' \cdot (p(n)\mathbf{a}_1 + q(n)\mathbf{a}_2)} = 1 \quad (2.13)$$

will result in the same radiation pattern, due to the periodicity of the grid and the exponential function. The orthogonal components of  $\mathbf{k}'$  with respect to the normal can be expressed as

$$\mathbf{k}'_{\perp} = p'\mathbf{b}_1 + q'\mathbf{b}_2, \quad (2.14)$$

where

$$\mathbf{b}_1 = 2\pi \frac{\mathbf{a}_2 \times \mathbf{n}}{\mathbf{a}_1 \cdot (\mathbf{a}_2 \times \mathbf{n})} = 2\pi \left( \frac{1}{a} \hat{x} - \frac{c}{ab} \hat{y} \right) \quad (2.15)$$

$$\mathbf{b}_2 = 2\pi \frac{\mathbf{a}_1 \times \mathbf{n}}{\mathbf{a}_2 \cdot (\mathbf{a}_1 \times \mathbf{n})} = 2\pi \frac{1}{b} \hat{y}. \quad (2.16)$$

The vectors  $\mathbf{b}_1$  and  $\mathbf{b}_2$  are the reciprocal primitive vectors of the array grid, and  $q'$  and  $p'$  are integers. A linear phase shift of any excitation will translate the array factor in the  $k_x k_y$ -plane, and since the array factor is periodic the far field pattern will be unchanged, e.g. if  $\mathbf{k}_0 = \mathbf{0}$  is changed to  $\mathbf{k}_0 = p' \mathbf{b}_1 + q' \mathbf{b}_2$ . In Fig. 2.4 a phase diagram is shown for  $\mathbf{k}$ , this diagram is usually called a grating lobe diagram. The dot in the center of the solid circle represents the main beam direction when  $\mathbf{k}_0 = \mathbf{0}$ , and the dot in the center of the dashed circles are the other maxima directions, due to the periodicity. The dot denoted  $\mathbf{k}_{0,0}$  corresponds to the main beam direction

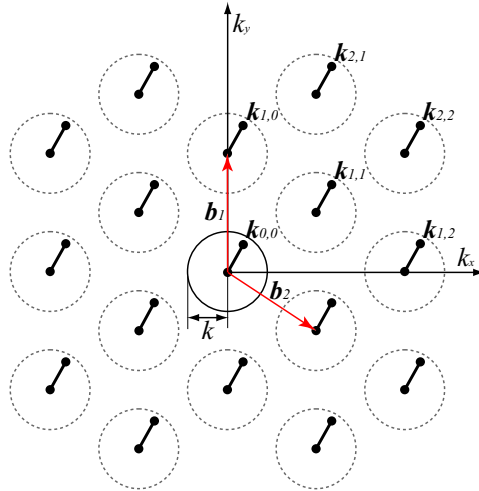


Figure 2.4: Grating lobe diagram for the array grid depicted in Fig 2.3.

when  $\mathbf{k}_0 = k_{x0}\hat{\mathbf{x}} + k_{y0}\hat{\mathbf{y}}$ , and is similarly translated for the other maxima. The solid circle has a radius equal to  $k$  and encloses the directions corresponding to visual space. Phase shifts outside this circle corresponds to directions for which  $\theta$  is imaginary and the element pattern is zero. The dashed circles represent the possible locations of the other array factor maxima when  $(k_{x0}, k_{y0})$  are in visual space.

For high frequencies the circles in the grating lobe diagram will overlap and it is possible to position more than one array factor maxima in visual space. The additional radiating beams are called grating lobes. The occurrence of grating lobes decreases the directivity of the antenna, and can also cause sudden changes in the active impedance and thereby further reduce the absolute gain of the antenna. Grating lobes are an aliasing effect due to a too sparse sampling of the surface covered by the antenna.

## 2.2 Infinite array

The previous theory describes the periodicity of the excitation of a planar array antenna and how it radiates. To put this theory to work, one needs to know the embedded element patterns and S-parameters for an array antenna, and to compute these quantities numerical methods are required. Due to the size of the computational domain it is difficult to analyze large planar arrays by numerical methods. Therefore, simplifications are needed, and a good starting point is the infinite array. When the infinite array is fed with a uniform amplitude and a linear phase shift the geometry can be reduced to a unit cell with quasi-periodic boundaries. This is a result of the Floquet theorem and the excitation used is referred to as the Floquet excitation.

In this section we will study the sources in the infinite array, when it is excited with a Floquet excitation, and show that the radiated field consists of a limited number of plane waves propagating from the antenna. Furthermore, we will discuss the relationship between the active reflection coefficient and the S-parameters and the relationship between the active reflection coefficient and the embedded element pattern for an infinite array.

Let's start with the source terms for an infinite array. Consider that element  $n$  is excited with a unit amplitude, which yields a source term in the array of the form  $f(x - x_n, y - y_n)$ . Furthermore, if the array is excited with a Floquet excitation, the source term will be a superposition of all the element contributions i.e. a current component can be written as

$$i(x, y) = \sum_{p,q} f(x - x_{pq}, y - y_{pq}) e^{-jk_x x_{pq} - jk_y y_{pq}}, \quad (2.17)$$

where

$$x_{pq} = (\mathbf{p}\mathbf{a}_1 + q\mathbf{a}_2) \cdot \hat{\mathbf{x}} \quad (2.18)$$

$$y_{pq} = (\mathbf{p}\mathbf{a}_1 + q\mathbf{a}_2) \cdot \hat{\mathbf{y}}. \quad (2.19)$$

As a consequence of the Floquet theorem the source terms and fields in the array have the same periodicity as the Floquet excitation. The array structure can be divided into unit cells, which if translated using integers of the primitive lattice vectors, reproduce the infinite array. The fields at one boundary of the unit cell will be identical to the fields at the opposing boundary multiplied with the phase shift in that direction. In numerical codes using periodic boundaries with phase shifts, this periodicity is imposed explicitly.

As an introduction to the Floquet modes we will derive the Floquet series expansion of a the current component  $i(x, y)$ . The Fourier transform of the source current is

$$\tilde{i}(k_x, k_y) = \frac{1}{4\pi^2} \int_{-\infty}^{\infty} \int_{-\infty}^{\infty} i(x, y) e^{jk_x x + jk_y y} dx dy \quad (2.20)$$

with inverse transform

$$i(x, y) = \int_{-\infty}^{\infty} \int_{-\infty}^{\infty} \tilde{i}(k_x, k_y) e^{-jk_x x - jk_y y} dk_x dk_y. \quad (2.21)$$

Inserting Eq. (2.17) into (2.20) gives

$$\tilde{i}(k_x, k_y) = \tilde{f}(k_x, k_y) \sum_{p,q} e^{j\mathbf{k}' \cdot (p\mathbf{a}_1 + q\mathbf{a}_2)}. \quad (2.22)$$

The sum in Eq. (2.22) is the array factor for an infinite array, which is equal to zero except at discrete scan angles. This can be shown by using Poisson's summation formula, whereby the sum becomes

$$\begin{aligned} \sum_{p,q} e^{j\mathbf{k}' \cdot (p\mathbf{a}_1 + q\mathbf{a}_2)} &= \\ 4\pi^2 \sum_{p,q} \delta(\mathbf{k}' \cdot \mathbf{a}_1 + 2\pi p) \delta(\mathbf{k}' \cdot \mathbf{a}_2 + 2\pi q) &= \\ \frac{4\pi^2}{ab} \sum_{p,q} \delta(k_x - k_{xpq}) \delta(k_y - k_{ypq}) \end{aligned} \quad (2.23)$$

where  $\delta(x)$  is the delta Dirac function and

$$k_{xpq} = k_{x0} + (p\mathbf{b}_1 - q\mathbf{b}_2) \cdot \hat{x} \quad (2.24)$$

$$k_{ypq} = k_{y0} + (p\mathbf{b}_1 - q\mathbf{b}_2) \cdot \hat{y}. \quad (2.25)$$

Now, if Eq. (2.22) and (2.23) are inserted into Eq. (2.21), we obtain the Floquet series expansion

$$i(x, y) = \frac{4\pi^2}{ab} \sum_{p,q} \tilde{f}(k_{xpq}, k_{ypq}) e^{-jk_{xpq} x - jk_{ypq} y}. \quad (2.26)$$

Sources of this form excite an electric field that can be written in the following form for positive  $z$  above the sources [7, Ch. 2]

$$\mathbf{E}(x, y, z) = \sum_{pq} \mathbf{C}_{pq} e^{-j(k_{xpq} x + k_{ypq} y + k_{zpq} z)}, \quad (2.27)$$

where  $\mathbf{C}_{pq}$  is a complex vector and

$$k_{zpq} = \sqrt{k^2 - k_{xpq}^2 - k_{ypq}^2}. \quad (2.28)$$

The terms in Eq. (2.27) are called Floquet modes. These modes can be divided into TE and TM-modes but here they are for brevity denoted  $\mathbf{C}_{pq}$ . These modes are plane waves that propagate from the plane of the array when  $k_{zpq}$  is real, and

are evanescent when  $k_{zpq}$  is imaginary, which leads to some interesting results. For example, it is possible to choose a phase shift for the array where no beam propagates, which happens when  $(k_x, k_y)$  are outside of all circles in the grating lobe diagram in Fig. 2.4. With such a phase shift, the incident power applied at the ports of the antenna elements must be reflected back to the ports or dissipated in the antenna due to losses. This effect would be impossible if the antenna elements within the array did not couple to each other [21].

The active reflection coefficient for an element in an infinite array is closely related to the set of S-parameters, since if one of the two are known the second can be calculated. Given that the array is excited with a Floquet excitation the active reflection coefficient for element  $m$  is

$$S'^{\text{FL}}(\psi_1, \psi_2) = \sum_{p,q} S_{m,n(p,q)} e^{-jp\psi_1 - jq\psi_2}, \quad (2.29)$$

where

$$\psi_1 = \mathbf{k} \cdot \mathbf{a}_1 = k_x a \quad (2.30)$$

$$\psi_2 = \mathbf{k} \cdot \mathbf{a}_2 = k_x c + k_y b. \quad (2.31)$$

This is a two dimensional Fourier series in which the Fourier coefficients, the scattering parameters, are given by

$$S_{m,n(p,q)} = \frac{1}{4\pi^2} \int_{-\pi}^{\pi} \int_{-\pi}^{\pi} S'^{\text{FL}}(\psi_1, \psi_2) e^{jp\psi_1 + jq\psi_2} d\psi_1 d\psi_2. \quad (2.32)$$

The active reflection coefficient,  $S'^{\text{FL}}$ , is almost always calculated numerically using periodic boundary conditions with phase shifts. By the above Fourier transform we can calculate the S-parameters for the infinite array. Once the S-parameters are known, we use Eq. (2.3) to calculate the active reflection coefficient for arbitrary excitations.

As mentioned earlier, for a specific phase shift the scan direction will change with frequency. Therefore, when analyzing the performance of an element it is usually more convenient to express the active reflection coefficient as a function of the scan direction.

$$\Gamma^{\text{FL}}(\theta, \phi) = S'^{\text{FL}}(\psi_1, \psi_2). \quad (2.33)$$

The active reflection coefficient,  $\Gamma^{\text{FL}}$ , is related to the power gain pattern (also known as absolute gain pattern) for an element in the infinite array [22]. A prerequisite is that the elements are lossless and positioned in a sufficiently dense grid in terms of wavelength, so that only one Floquet mode at a time can be excited. Then the power gain pattern is given by

$$g(\theta, \phi) = \frac{4\pi A_{\text{uc}}}{\lambda^2} \cos(\theta) \left( 1 - |\Gamma^{\text{FL}}(\theta, \phi)|^2 \right), \quad (2.34)$$

where  $A_{uc}$  is the area of the unit cell, and  $\lambda$  is the wavelength in free space. The power gain pattern is equal to the square of the absolute value of the embedded element pattern

$$|\mathbf{f}(\theta, \phi)| = \sqrt{g(\theta, \phi)}. \quad (2.35)$$

In most synthesis of antenna patterns, one is interested in a power pattern, whereas the phase changes within the pattern are of minor interest. Since for the infinite array all elements have the same embedded element patterns, the phase information is basically redundant. By using Eq. (2.32) and Eq. (2.35) for frequencies when only one Floquet mode can propagate, it is possible to answer the two fundamental questions for the infinitive array.

When the array is finite both the coupling coefficients and the embedded element patterns change with respect to the infinite array case. Such perturbations of the infinite array solution are called edge effects. Sources in the infinite array consists of superimposed element sources  $f(x - x_n, y - y_n)$  that represent the source in the array when only one element is excited with  $A_n = 1$ . The element sources extend over many antenna elements and are responsible for the coupling between elements and the embedded element patterns. When the array is truncated, so are these source terms; one could see this as making the effective radiating aperture for the edge antenna element smaller. A smaller aperture will in general result in a broader element pattern and therefore the edge element element patterns will in general be broader than the infinite array patterns.



## Chapter 3

# Wide scan elements

In this thesis three types of elements are studied, waveguide aperture elements, fragmented aperture elements, and tapered-slot elements. These elements have different properties. Compared to the other elements the waveguide aperture elements are narrow band but have been shown to be capable of wide scan angles. The fragmented aperture antenna is a thin wide-band antenna, but lacks the wide-angle performance. The tapered-slot element is a broad-band element that has shown good scan angle performance, but it is bulky. In this chapter the elements are assumed to be positioned in a very large array so that the central elements can be approximated by an element in an array antenna of infinite extent. This simplifies the design since only a unit cell with periodic boundaries needs to be considered.

In the first project, NFFP3+, the goal was to find an array element that was capable of scanning out to  $75^\circ$  from broadside with a bandwidth of 1.4:1. Here, bandwidth is defined as  $f_h/f_l:1$ , where  $f_h$  and  $f_l$  are the highest and lowest frequency limit for which the active reflection coefficient is less than -10 dB for all scan directions within the scan cone defined by  $\theta_{\max}$ .

A literature study was made [23] and three types of elements were chosen as candidates: waveguide aperture elements, stacked patch elements and tapered-slot elements. There were no elements that fully met the desired characteristics. However, there exist element designs that fulfill the bandwidth condition or the wide-scan condition but not both. Bandwidth and maximum scan-angle are conflicting design criteria and in the literature most elements that are capable of wide-scan angles are designed for a small frequency band; there are even cases when the chosen performance parameters, e.g. the active reflection coefficient or the active impedance, are only calculated for a single frequency. Phased array elements that are considered mainly as broadband elements may be suitable for wide angle scanning if the bandwidth is reduced; the tapered-slot element is such an element.

An apparent problem when we evaluated the existing elements is that there are no objective performance measure for wide-angle scanning phased array elements. In the technical report [24] three performance measures were compared

for waveguide apertures. We found that the average reflected power over the scan range normalized to unit input power was a good measure to evaluate wide-angle scanning performance. The average reflected power over the scan range is defined as

$$R_{\text{pw}}(f) = \frac{1}{2\pi(1 - \cos\theta_{\max})} \int_0^{2\pi} \int_0^{\theta_{\max}} |\Gamma(\theta, \phi, f)|^2 \sin\theta d\theta d\phi, \quad (3.1)$$

where  $\theta$  and  $\phi$  denote the scan direction in spherical coordinates,  $\theta_{\max}$  the maximum scan angle, and  $|\Gamma|^2$  the return losses, i.e. the power reflected back into the antennas port relative the incident power.

### 3.1 Waveguide aperture element

Waveguide aperture element can with irises, dielectric slabs above the apertures, and dielectric loading be match for very wide-scanning. During the 60's and 70's the waveguide aperture elements and their wide-scanning performance were the subject of many papers, see e.g. [4, 25–28], but these elements have also been studied in more recent papers [29–31]. A circular waveguide design capable of scanning out to  $70^\circ$  from broadside was presented in [31], and a square waveguide element with irises [25] has been shown to be capable of  $60^\circ$  scan from broadside. The main problem with these elements is that they have small bandwidths.

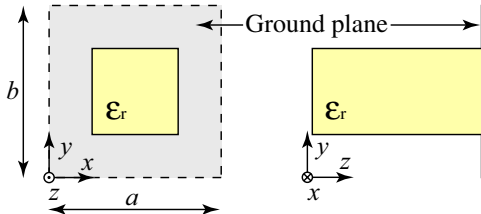


Figure 3.1: The small square waveguide aperture element.

In paper I [32], which is a condensed version of the technical report [24], we studied the performance of the basic waveguide aperture element. Three apertures were chosen for this purpose, two square waveguides capable of dual polarization and a single polarized rectangular waveguide. The elements are positioned in a square grid with the element spacing  $a = b = \lambda_h/2$  where  $\lambda_h$  is the free space wavelength at  $f_h$  the highest frequency considered. To reduce the size of the waveguide it is filled with a dielectric material. The size of the waveguide and the value of dielectric constant are chosen so that the second waveguide mode starts to propagate when  $f = f_h$ . The cross section of the square waveguides are chosen so that for the first waveguide the cross section is close to the size of the unit cell and for the second waveguide the cross section is one fourth of the unit cell area, see Fig. 3.1. The cross section of the rectangular waveguide is chosen so that the width is the same

as the large square waveguide, and the height is chosen slightly smaller than the small waveguide. The elements are excited with the first waveguide mode and this mode is matched by choosing a susceptance (conceptually) placed a distance  $\lambda/2$  from the aperture and by changing the transmission line characteristic impedance (or more correctly wave impedance) to a new value. For the square waveguides the orthogonal mode is terminated by a load with the same value as the chosen characteristic impedance, again a distance  $\lambda/2$  from the aperture. The susceptance and impedance were then chosen by minimizing the average reflected power (3.1) for one frequency using nonlinear programming.

Before the matching the largest waveguide was the best matched element for all scan directions. However, after the matching the smallest waveguide was better matched and had lower average reflected power over the scan range, see Fig. 3.2. The reason for the worse match of the large waveguide was that when the beam was scanned out in the diagonal plane the excited mode was to a greater degree reflected back to the orthogonal mode. The active reflection coefficients for the small waveguide and the rectangular waveguide were very similar, and the average reflected power was essentially the same. For these elements the active reflection coefficient was, after matching, similar to that of an infinite magnetic current sheet [33] that is perfectly matched for broadside scan.

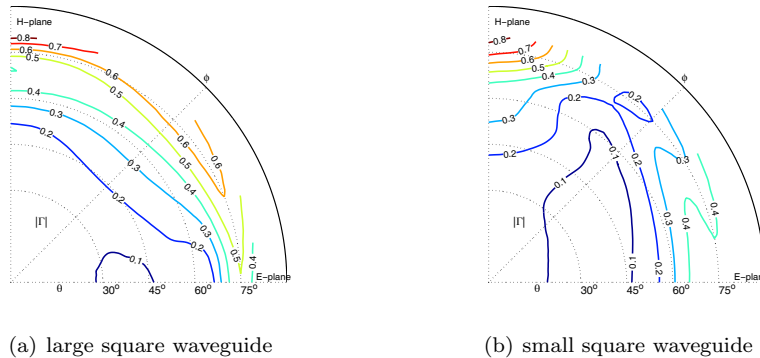


Figure 3.2: Contour plots of  $|\Gamma|$  for the waveguide apertures matched by minimizing  $R_{pw}$ ,  $f = 2.6$  GHz. The antennas are considered to be well matched when  $|\Gamma| < 0.3 \approx -10$  dB.

### 3.2 Fragmented aperture element

The average reflected power, as given in Eq. (3.1) would work well as a cost function to design wide-angle scanning array elements. However, it requires that  $\Gamma$  is known for many scan directions. For complex antenna elements it is time consuming to compute the average reflected power, which makes it practically impossible to use

this quantity as a cost function to design an element. A simplified procedure for design is to choose a few scan directions that are assumed to give a good picture of the performance of the antenna. The directions chosen are often broadside scan  $\theta = 0^\circ$  and the maximum chosen scan angle  $\theta = \theta_{\max}$  for the E plane and H plane. This strategy often works well because the active impedance for the maximum scan angle for the E plane and the H plane is close to the highest and lowest active impedance values for the antenna, e.g. for an infinite current sheet [33]  $Z_{E\text{-plane}}(\theta)/Z_0 = (Z_{H\text{-plane}}(\theta)/Z_0)^{-1}$  where  $Z_0$  is the active impedance for broadside scan.

In [34] fragmented aperture elements were designed using a genetic algorithm. The genetic algorithm is used to find the antenna geometry with the minimum reflected power for broadside scan and the maximum chosen scan angle for the E plane and H plane. The basic geometry of the fragmented aperture element is a pattern consisting of metal pixels, see Fig. 3.3. This pixel pattern is positioned on top of a dielectric slab backed by a ground plane and fed in the middle of the element with a discrete point source. Björn Thors et al. designed antenna elements by using the method presented in [34] which were capable of bandwidths of at least one octave when scanned within  $45^\circ$  from broadside. In paper II the same type of

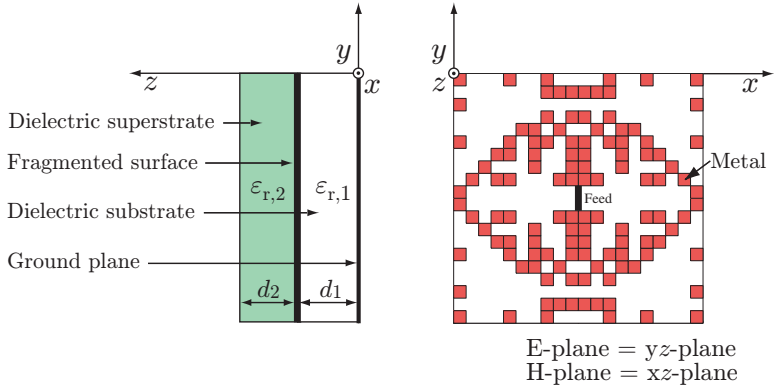


Figure 3.3: Geometry of the fragmented aperture antenna.

element was studied, with the intent to solve three specific problems: the numerical accuracy of the method, how to simplify the manufacturing of the antenna, and the wide-angle scanning performance. For the analysis, a finite-difference time-domain (FDTD) code with periodic conditions (PBFDTD) was used [35]. The model in [34] used a coarse mesh, with only one FDTD-cell to represent a metallic pixel, see Fig. 3.3. This was too few cells to guarantee that the difference between the cost function for two elements is not caused by numerical error. To improve the accuracy of the results the mesh was refined to  $4 \times 4$  FDTD-cells per pixel. The accuracy of these results was evaluated by comparing it with results computed using a mesh with  $12 \times 12$  FDTD-cells per pixel. In Fig. 3.4 the active reflection coefficient is shown

for different mesh resolutions, and even if the agreement between the  $12 \times 12$  and  $4 \times 4$  results are far from perfect the accuracy was found to be acceptable.

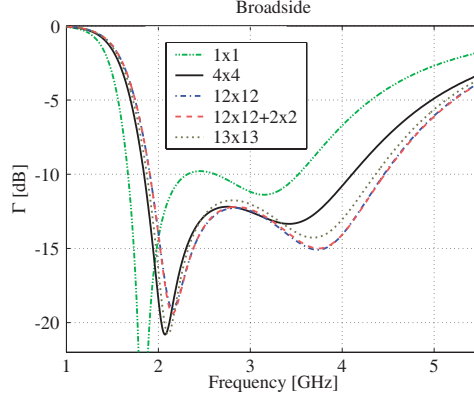


Figure 3.4: Active reflection coefficient for broadside scan for different mesh and critical corner solutions.

A problem with the metallic pattern of these elements were that the diagonal adjoining pixels could cause large current densities that would lead to ohmic losses. To prevent such losses two options were considered. The first option was to add a smaller pixel over the corners and the second was to make the pixels slightly larger so that they are overlapping, see Fig. 3.5. The two options were evaluated and the solutions are shown in Fig. 3.4, where small patch option is denoted ( $12 \times 12 + 2 \times 2$ ) and the overlapping patch is denoted ( $13 \times 13$ ). In FDTD a metal

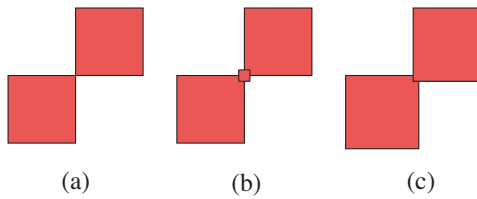


Figure 3.5: (a) Critical diagonal pixel contact ( $12 \times 12$ ). (b) Small patch covering the critical corner ( $12 \times 12 + 2 \times 2$ ). (c) overlapping pixels ( $13 \times 13$ ).

edge is slightly larger than the FDTD-cell that the material properties are assigned to, which causes the solutions to converge slowly when the mesh is refined. But if this effect is considered when the model is made, it is possible to compensate to a small degree for this effect. As a consequence the  $4 \times 4$  pixel model better agrees with the overlapping pixel model due to that they correspond to the same physical pixel width. The conclusion is that the overlapping pixel model is the best choice

to avoid the ohmic loss problems, since it is a simple solution, and it is also the model that corresponds best to the model that the genetic algorithm evaluates.

In [34] the dielectric constants were continuous variables whereby the final designs could result in non-available dielectric materials. To overcome this problem the algorithm was restricted to a list of commercially available materials. Furthermore, the maximum scan angle  $\theta_{\max}$  was changed from  $45^\circ$  to  $60^\circ$ . Two designs were made using this method, one element with a superstrate above the metallic pattern and one element without. The goal was a wide-band wide-scan design. The bandwidth for the resulting elements are good,  $\sim 2:1$  for  $|\Gamma| < -10$  dB, for scan angles within  $45^\circ$  scan from broadside, especially if the low profile of the element is considered, see Fig. 3.6. Note that the performance can be improved if the maximum

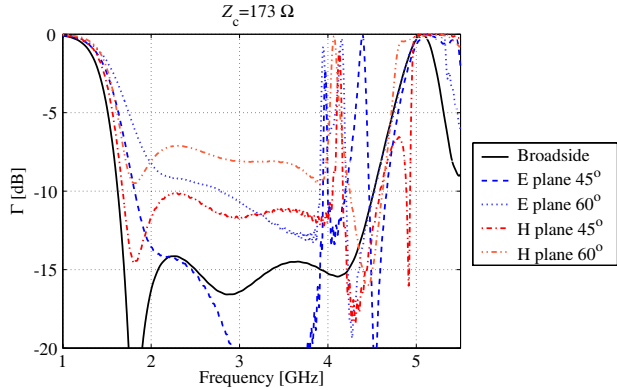


Figure 3.6: Active reflection coefficient for antenna element with a superstrate.

height of the elements is allowed to increase. However, a more important problem is that in all simulations the feed of the antenna is a discrete point source, and the ideal characteristic impedance of a transmission line connected to this source is usually much higher than the often preferred value of  $50 \Omega$ . It is not trivial to design a practical feed for this element without impairing its performance. A similar element with excellent bandwidth and wide-scan range is the dipole with arms that are strongly capacitively coupled between elements, almost physically overlapping [36]. Such an element has basically the same problem with the feed, and it has been suggested by the inventor that it could be fed by two probes through the ground plane with two connectors at the backside. However, dual probe feeds can cause scan blindness [37] and require more complex transmit and receive modules.

For the fragmented aperture antenna the largest problem is the ground plane. It is basically the ground plane that motivates many of the design choices for this element. In [34] it was shown that the fragmented aperture antenna without a ground plane has performance similar to self-complementary arrays. A self-complementary antenna of infinite extent has no lowest frequency limit and therefore the antenna

has an infinite bandwidth [38–41]. When a ground plane is added to the antenna it will introduce a frequency dependence to the active impedance [42]. This phenomena is caused by that the wave emitted from the antenna is reflected by the ground plane and depending on the frequency cause constructive or destructive interference. Since an infinite array only radiates in limited directions the destructive interference can prevent any energy to leave the antenna, which means that the antenna cannot accept any incident power. To improve the bandwidth of elements with a ground plane, both fragmented aperture antennas and the self-complementary antennas use dielectric slabs on top of the antenna and in between the antenna and the ground plane, e.g. this was done in paper II and in [3, 43]. An alternative approach is to use a ferrite loaded ground plane, which improves the bandwidth at the cost of the radiation efficiency. These designs are usually good for antennas that require a low profile, which is practical if the antenna is to be carried by an airplane and the frequencies are  $\sim 1$  GHz and lower. For these frequencies the element spacing is large enough to leave room for the extra connectors required for dual point feeds. However, for this type of elements the element spacing is in terms of wavelength often less than  $\lambda/2$  for the highest frequency, which is unacceptable in some applications.

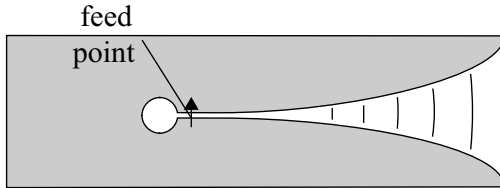


Figure 3.7: A basic tapered-slot element.

### 3.3 Tapered-slot element

The final class of elements to consider is the tapered-slot element, also known as the flared notch element, or, if the taper is exponential, the Vivaldi element. Tapered-slot elements, which can be used as a single element or in arrays, have been found to have excellent bandwidth [44, 45]. In arrays the elements have been found to have a good wide-scan performance, but they can suffer from resonances and scan blindness effects that limit both bandwidth and scan performance [46–49].

The basic tapered-slot element is a slot line that is gradually widened in one direction and terminated with an open circuit stub in the other, see Fig. 3.7. If the slotline is excited by a potential difference over the slot it creates two waves traveling along the slotline from this point. One of these waves is reflected by the open circuit, ideally without changing its sign. This reflected wave will if it is induced close to the open circuit add constructively with the other wave and

gradually leak from the slotline. There are several variants of this element that are all based on the above mentioned interference principle. The elements can either be made from a solid metal sheet or by etching a metallic pattern on a dielectric substrate. Dielectric substrates have the useful property that the feed of the element can be made on the same substrate as the tapered-slot. To shield the feeding network, two substrates are usually bonded together so that there is a tapered-slot pattern on both sides of the element. The two tapered-slot metal layers create a cavity within the substrate, which may cause resonances. To prevent these resonances vias are usually introduced between these layers [50]. The vias reduce the size of the cavities, which in turn increases the corresponding resonance frequencies so that they are moved outside the antennas frequency band. The design of the open circuit stub, feed, and the shape of the tapered-slotline vary much between different designs. Most designs are two dimensional and made from sheets of different materials, but there are also elements that are three dimensional [51–53]. The tapered-slot elements are usually used when the elements are longer than half a wavelength, which is too long for certain applications. The flared dipole [54, 55] and double-mirrored balanced antipodal Vivaldi antennas [56] are close relatives to the tapered-slot. They are shorter and do not need electrical contact between the elements, which is especially practical in dual polarized applications.

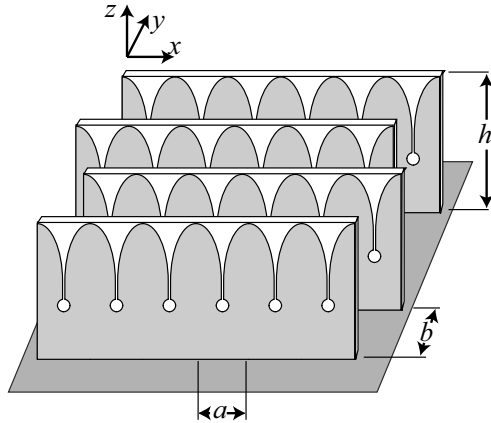


Figure 3.8: Array of tapered-slot elements positioned in a triangular grid.

In this thesis a bilateral tapered-slot fed by a microstrip line is studied. Detailed parameter studies for such elements have been made in [57–59]. The difference between the element presented in this thesis and in previous work is that the present element is designed for large arrays with the elements positioned in equilateral triangular grids, see Fig. 3.8, while previously published designs have been intended for rectangular grids; another difference is that the focus is on wide-angle scan performance rather than bandwidth. In most papers the focus is to maximize the

Band	freq. (GHz)	$ \Gamma $ (dB)	$\theta_{\max}$ (Deg)
1	9.0 – 10.0	-12	60°
2	8.5 – 10.5	-10	60°
3	4.5 – 11.5	-8	60°

Table 3.1: Requirements for the tapered-slot design.

ratio  $f_h/f_l$ , where  $f_h$  and  $f_l$  are the highest and lowest frequency limit for the element using some sort of definition of bandwidth (there are many). The highest frequency limit is set by the element spacing, i.e. grating lobes, and therefore the most important factor to minimize is the low frequency limit.

## Requirements and mechanical design

Instead of minimizing the low frequency limit the goal has been to match the element as well as possible for a radar band and fairly well for other frequencies. For the waveguide elements the goal was a very wide-scan element with moderate bandwidth. However, due to wishes from our collaboration partner Saab Microwave Systems, the goal was changed, since the expected performance of the frequency selective surface (FSS) required that the antenna would absorb most of the incident power for a certain frequency band. This requirement demands that the antenna is well matched for a much wider frequency band, see Tab. 3.1. Since bandwidth and scan performance are conflicting requirements the maximum scan angle was reduced to 60° for both the E and H planes.

The limitations of the budget for manufacturing the antenna system led to the requirement that the antenna was restricted to a single polarization. However, with no reception of the second polarization the ground plane increases the backscattered field for cross polarized incidence. To reduce this effect, an absorbing layer is positioned on top of the ground plane, wherefore the antenna element needs to be extended from the ground plane by the same length as the absorber is thick. Even though an absorber may reduce the radiation efficiency of the antenna, it is not a problem in the present case. The substrates create a parallel waveguide structure that is below cutoff for the antenna's co-polarization and operational frequencies. However, the absorber will cause losses when guided modes, that otherwise would lead to scan blindesses, are excited between the substrates. Furthermore, to add extra stability to the array, the space between the elements is filled with a foam material with a dielectric constant close to unity. Finally, a thin glass fibre layer was mounted on top of the foam for mechanical protection.

It is preferable to have as few elements as possible in the antenna. A conflicting requirement, however, is that the antenna has to be free of grating lobes up to a certain frequency, which requires a dense grid. This is important for the performance at large scan angles, and for the radar cross section (RCS). The highest frequency for which the antenna is required to be free of grating lobes is set to

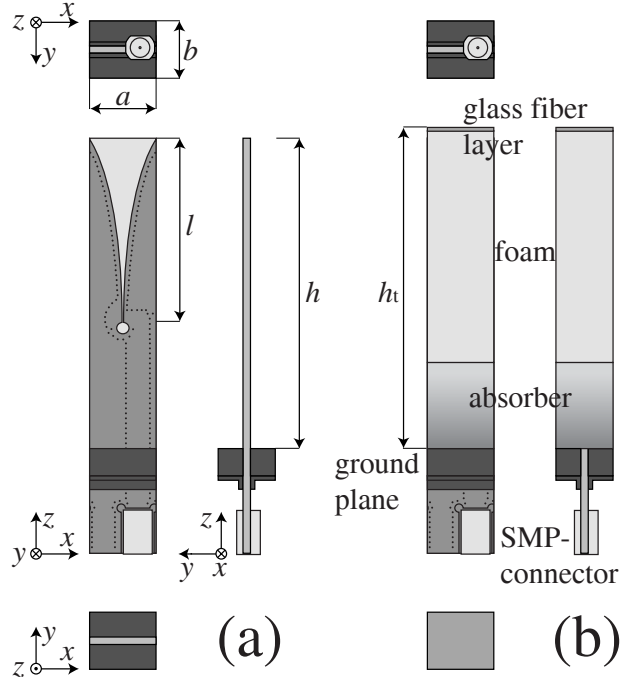


Figure 3.9: Geometry of a unit-cell of the phased array. Figure (a) depicts the antenna element without the absorber, foam and, the glass fiber layer. Figure (b) depicts the antenna element as it is in the phased array. The dimensions for the experimental antenna are  $l = 36.4$  mm,  $h = 64$  mm,  $a = 14.3$  mm,  $b = 12.5$  mm and,  $h_t = h + 2.3$  mm. Tapered-slot opening rate  $R = 0.06 \text{ mm}^{-1}$  [58].

$f_h = 12$  GHz. The sparsest grid for a grating lobe free antenna is the equilateral triangular grid also known as the hexagonal grid. The sides of the equilateral triangle are  $\lambda_h/\sqrt{3}$ , where  $\lambda_h$  is the wavelength at the grating lobe frequency  $f_h$ . Thus  $a = \lambda_h/\sqrt{3} \simeq 14.3$  mm,  $b = \lambda_h/2 = 12.5$  mm,  $c = a/2$  in Eq. (2.11).

### Electrical design

The electrical design process was divided into three steps. The first step was to create a slotline to stripline transition, the second step was to design the tapered-slot shape, and the third step was to add a stripline impedance transformer. The stripline to slotline transition is a standard transition for this type of element, using a circular short stub for the slotline and a feather shaped open stub for the stripline [57], see Fig. 3.10. Due to manufacturing tolerances the stripline impedance is chosen to  $70 \Omega$ . Hence, a stripline impedance transformer is needed

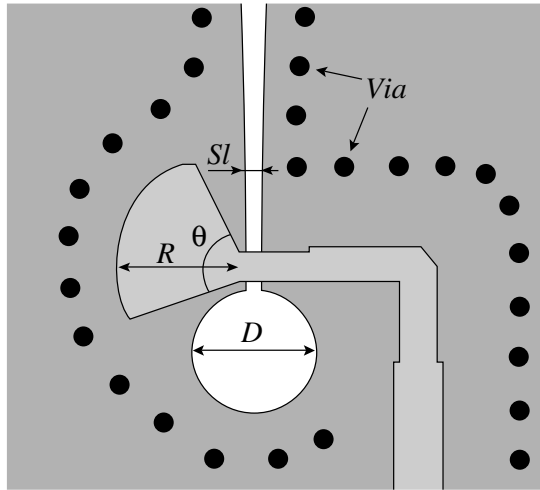


Figure 3.10: Illustration of the stripline to slotline transition.  $Sl = 0.3$  mm  $R = 2.6$  mm  $D = 2.9$  mm  $\theta = 90^\circ$ .

to get a  $50 \Omega$  interface.

The shape of the element is an exponential taper [58], and its most important parameter in this design is its length  $l$ . The tapered-slot element works basically as a tapered transmission line transformer. Because of the taper the absolute value of the active reflection coefficient will oscillate as a function of frequency. For large scan angles the local maxima of the active reflection coefficient are difficult to suppress. Therefore, the length of the tapered-slot is tuned so that a local minimum of the active reflection coefficient will be positioned at band 1, see Tab. 3.1. Furthermore, the local minimum is made sufficiently wide to match the width of band 1 for the largest scan angle in the E plane. Note, if the tapered-slot is made longer it will result in a decreased width of the minima of the active reflection coefficient. Furthermore, the maxima and minima will move with scan angle, but the antenna will be better matched for smaller scan angles.

The glass fibre layer that protects the antenna improves the electrical design. The layer acts as a wide-angle impedance matching layer (WAIM) and improves the match for the H plane [60]. The layer works as a susceptance that depends on the scan direction. The susceptance increases with scan angle in the H plane and decreases in the E plane. The dielectric constant determines the angle for which the susceptance is zero in the E plane, which makes it possible to first design an antenna for a maximum scan angle in the E plane. Then a WAIM layer is chosen that does not affect the maximum E-plane scan angle. Finally, the H-plane performance is tuned by alternating the thickness of the layer as well as the height

above the element.

The last step in the design process is to add an impedance transformer that changes the impedance interface from  $70 \Omega$  to  $50 \Omega$ , see Fig. 3.10. To avoid short period oscillations for the active reflection coefficient, the transformer is positioned close to the stripline to slotline transition.

## Numerical results

An antenna element was designed using primarily PBFDTD, the same code that was used to analyze the fragmented aperture antenna. The resulting antenna design were well within the requirements set by Saab. In Figure 3.11 the active reflection coefficient is shown for the antenna element without the absorbing layer. In this figure one can observe impedance anomalies for E-plane scan for frequencies above 11 GHz. These anomalies are caused by a scan blindness effect that will be discussed in chapter 5. To verify the design of the element a commercial finite element method code (HFSS) was used and the agreement between the HFFS and PBFDTD-model was considered to be good. In Figure 3.12 the power losses in the antenna are shown for the HFSS model when the absorbing layer is added to the numerical model. With this layer the guided waves are attenuated and the active reflection coefficient is reduced, but at the cost of the radiation efficiency. At these high frequencies the amplitude of the backscattered fields are in general lower when the absorber is included in the array, which was the primary reason why the bandwidth was increased and the absorber was added to the design.

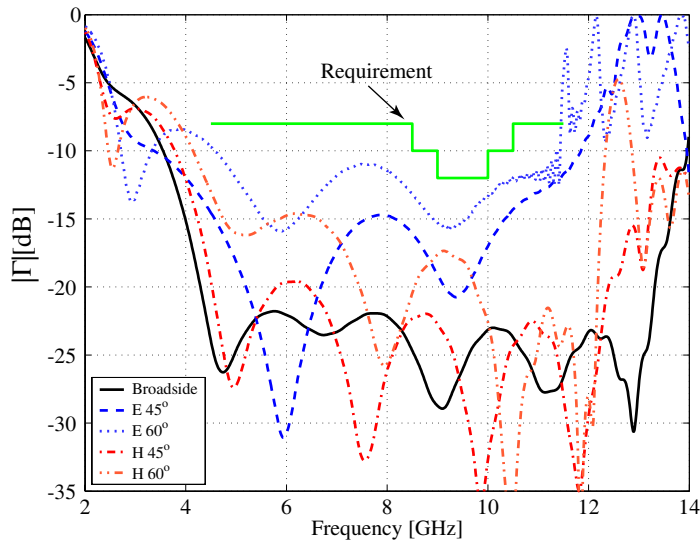


Figure 3.11: Active reflection coefficient for the PBFDTD-model, no absorbing layer.

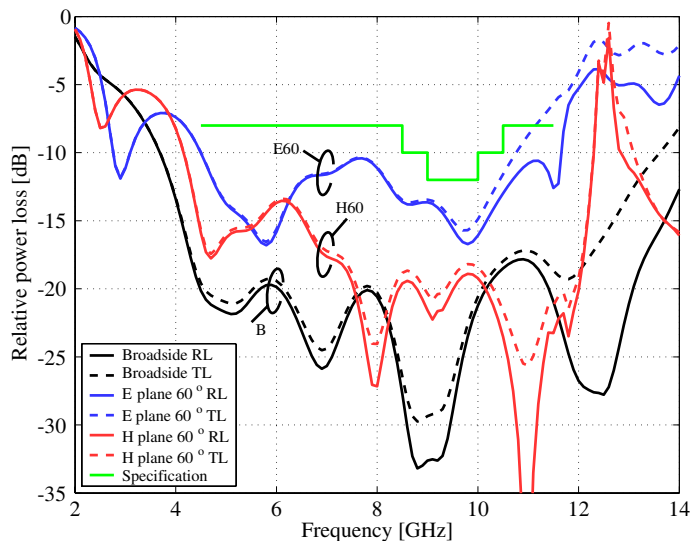


Figure 3.12: Tapered-slot antenna with absorbing layer, return loss (RL) defined as  $|\Gamma|^2$ , total loss (TL) is defined as  $(1 - \eta(1 - |\Gamma|^2))$  where  $\eta$  is the radiation efficiency.





Figure 4.1: A substrate with 16 elements.

## Chapter 4

# Experimental antenna

A  $16 \times 16$  element experimental array was built to verify the design made with the infinite array approximation. The geometry of the final element design and the dimensions are given in Figs. 3.9–3.10. The antenna consists of 16 rows; one such row is shown in Fig. 4.1. These rows protrude through the ground plane and are fastened on the backside of the ground plane, see Fig. 4.2

In Figure 4.3 the antenna array is shown without the absorbing layer and the protective foam layers. To avoid unnecessary interaction with the edges, the foam layer extends approximately one unit cell outside the elements. Furthermore, the absorbing layer covers both the top and sides of the ground plane, see Fig. 4.4.

A rule of thumb for finite antenna arrays is that the infinite array approximation is valid for the center antenna elements when the array is larger than  $5\lambda \times 5\lambda$  [16]. For the experimental antenna this corresponds to 7.5 GHz, but measurements have shown that the agreement is pretty good for frequencies below that limit. The

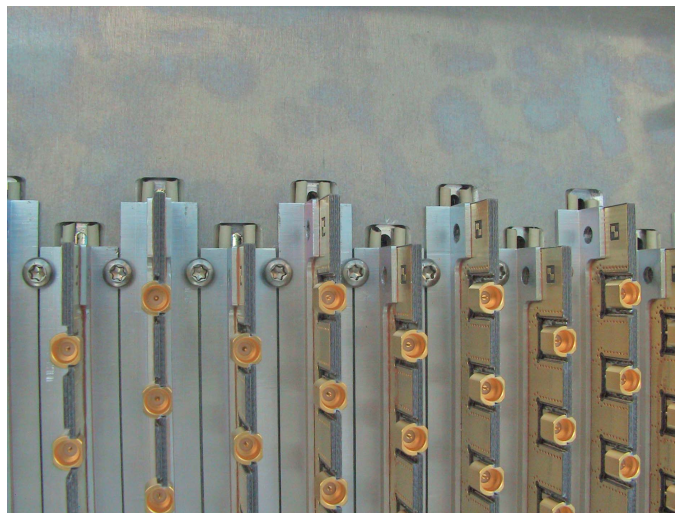


Figure 4.2: Backside of the antenna.

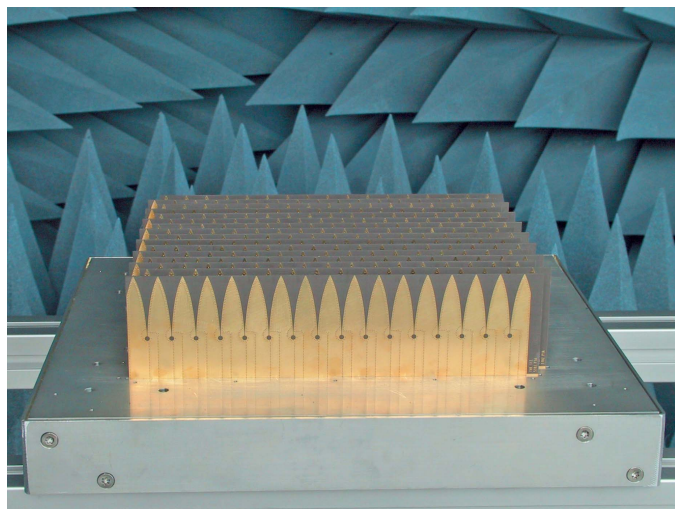


Figure 4.3: Array without the absorbing and protective layers.

experimental array was evaluated by measuring the coupling coefficients and by measuring the embedded element pattern for the central element in the array. The coupling coefficients were used to compute the active reflection coefficient using Eq. (2.3) and (2.9), with the amplitude of all elements set to unity. In Figs. 4.5(a) and 4.5(b), the contours of the active reflection coefficients are shown for the finite

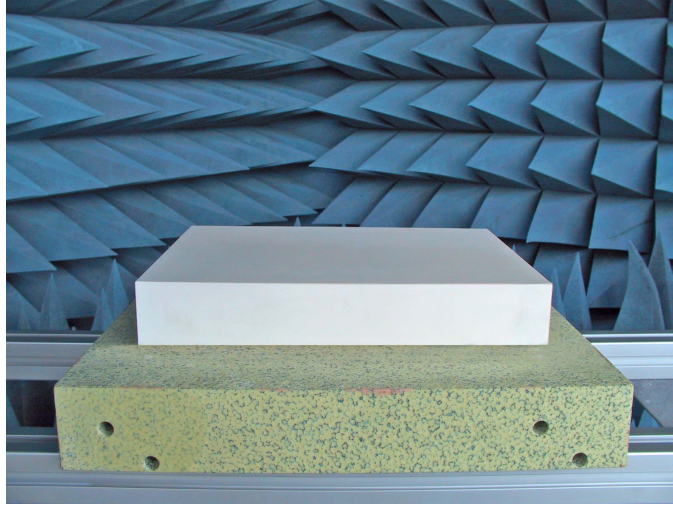


Figure 4.4: Assembled antenna with absorbing and protective layers.

array. The contours are symmetric, which is a good indication that the antenna is well built and that the surrounding elements are fully functional. For comparison, the active reflection coefficient is shown for the infinite array computations in Figs. 4.5(c) and 4.5(d). The largest difference between the measured and computed values are for the H plane, where for large angles the active reflection coefficient is larger than for the infinite array. This is a finite array effect due to a diffracted wave caused by the truncation of the infinite array.

In this case, where the antenna includes losses, the coupling coefficient data is not sufficient to answer whether the antenna radiates well, since it can be well matched due to dissipation in the absorbing layer. Therefore, it is important to verify the antenna by measuring the radiation characteristics. In Figure 4.6 the embedded element patterns are shown for two cut planes, the E plane cut and the H plane cut, for the co- and cross-polarizations. Also shown in these figures are the maximum gain for an infinite array and the embedded gain computed using Eq. (2.34) with the measured active reflection coefficient. Equation (2.34) is valid for the lossless infinite array, but in Fig. 4.6 the radiation efficiency is not equal to 1 for 12.5 GHz.

For 6.5 GHz and 9.5 GHz the agreement between the measured results is fairly good, although for the latter frequency the measured element pattern fluctuates for unknown reasons. These fluctuations could be caused by diffraction from the edges or by the measurement range.

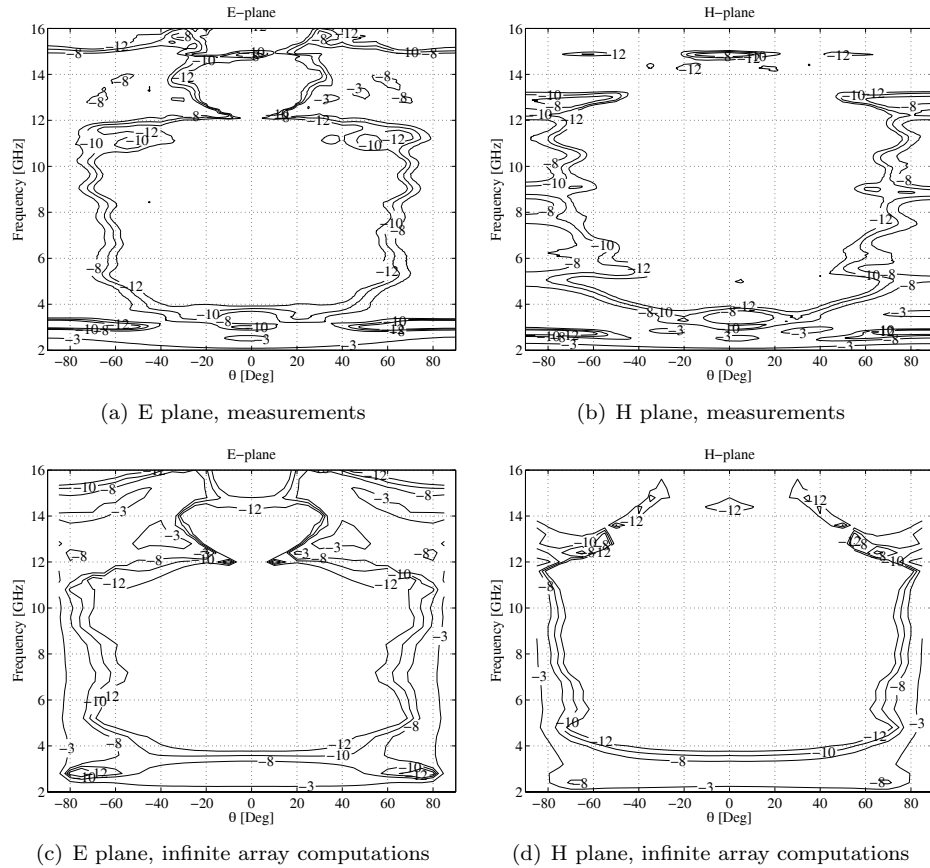


Figure 4.5: Contours of the active reflection coefficient (dB).

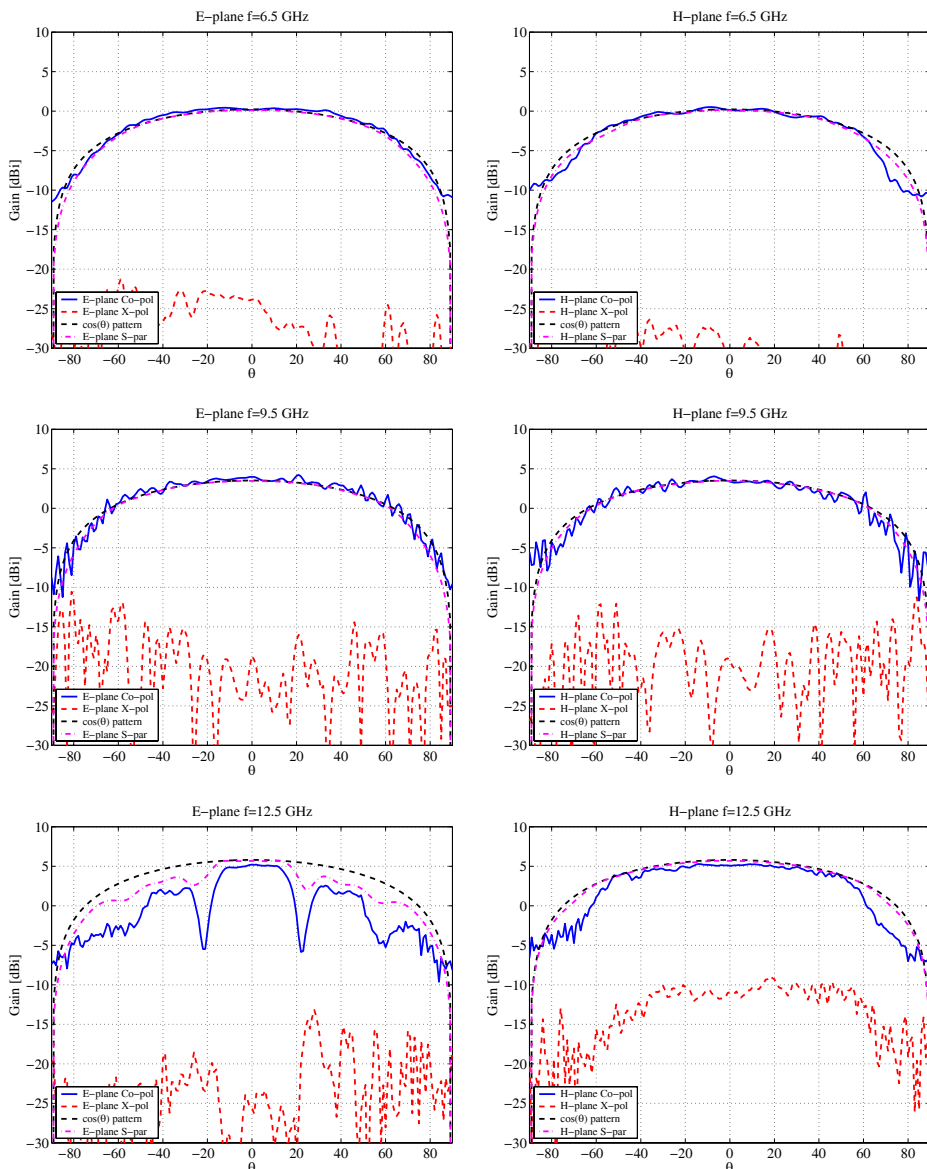


Figure 4.6: Embedded element patterns for the central element.



# Chapter 5

## Scan blindness

One of the observed effects in the previous chapters is that when scanned in the E plane the tapered-slot antenna is mismatched for frequencies close and above the high frequency limit. This type of impedance mismatch is caused by three types of scan blindness, which are discussed and modeled in papers III-V. Similarly, the fragmented aperture element with a superstrate is also mismatched for large scan angles, which is also caused by a type of scan blindness.

All these scan blindnesses have in common that they depend on the frequency as well as the phase shift between the elements. If the phase shift is changed, so is the frequency for which the scan blindness occurs. These scan blindness effects appear when guided modes are excited in the antenna structure, which occurs when the propagation constant of the guided mode coincides with that of a Floquet mode. The scan blindness condition depends on the array grid and the polarization of the guided mode.

### 5.1 Dielectric slab on top of a ground plane

The most well known cause of scan blindness is the excitation of a surface wave in a dielectric substrate on top of a ground plane [61–63]. A surface wave is a slow wave that travels along the boundary between two different media. This wave has a phase velocity that is less than the phase velocity of a wave in an unbounded medium with the same electromagnetic properties. In the surrounding media the amplitude of the surface wave decreases exponentially in the direction away from the boundary. Let's consider an example with a dielectric slab on top of a ground plane that is positioned in the  $xy$ -plane with the air/dielectric boundary at  $z = 0$ . In the air region the relation between the wave numbers for the surface wave are

$$\begin{aligned} k^2 &= \beta_x^2 + \beta_y^2 + \beta_z^2 \\ \text{Im}(\beta_z) &> 0 \\ z &\geq 0 \end{aligned} \tag{5.1}$$

which gives

$$\beta_{su}^2 = k^2 - \beta_z^2 = \beta_x^2 + \beta_y^2 \quad (5.2)$$

where  $\beta_{su}$  is the longitudinal wave number of the surface wave. To compute the transverse wavenumber,  $\beta_z$ , a dispersion relation needs to be solved that depends on the thickness and the electromagnetic properties of the dielectric slab [64, 65]. The surface wave couples very strongly to the array when the wavenumber coefficients coincide with the Floquet excitation, e.g.

$$\begin{aligned}\beta_x &= k_{xpq} \\ \beta_y &= k_{ypq}\end{aligned} \quad (5.3)$$

This scan blindness condition is depicted in the grating lobe diagram in Fig. 5.1. The surface wave longitudinal wavenumbers in Eq. (5.2) lie on a circle with a radius  $|\beta_{su}|$ , depicted in the figure as a red dot dash circle. The ( $p=-1, q=-1$ ) Floquet mode is in the figure steered so that it coincides with the surface wave circle, and if the antenna can couple to this surface wave it will cause scan blindness.

It follows from Eq. (5.2) and (5.2) that the radius of the circle depicting the scan blindness condition in the grating lobe diagram in Fig. 5.2 is larger than the visible region circle. This means that the surface wave will cause the antenna to be mismatched before a grating lobe enters visual space, which leads to that an element designer must use smaller element spacing than required by the grating lobe condition.

## 5.2 Tapered-slot triangular grid scan blindness

In paper IV the scan blindness condition in Eq. 5.3 was used for tapered-slot arrays with the elements positioned in triangular grids [49]. In this type of antenna the excited guided wave is a leaky mode that propagates in between the substrates. A leaky mode is a fast wave, and would normally radiate from the aperture. However, when the array is scanned in the E-plane the electric fields of the leaky modes are directed from the substrates, due to the symmetry of the element and excitation, and are therefore odd in the transverse direction to the E plane, see Fig. 5.2. The odd field distribution causes the radiated fields to interfere destructively for E-plane scan directions, and hence the leaky modes will not radiate unless a grating lobe directed from the E plane enters visual space. The leaky mode can be described as a TE-mode with wavenumber  $\beta_{lw}$  in the direction along the substrates and with a phase shift between the substrates of  $\phi_y = k_y b = \pi$  in the transverse direction of propagation. The lower frequency limit is set by the element spacing in the E plane, where the leaky mode ceases to propagate for a spacing smaller than  $\lambda/2$ . For these leaky modes the phase progression coincides with the Floquet modes with index  $p = \pm 1, q = n$ , in a triangular grid array, where  $n$  is any integer.

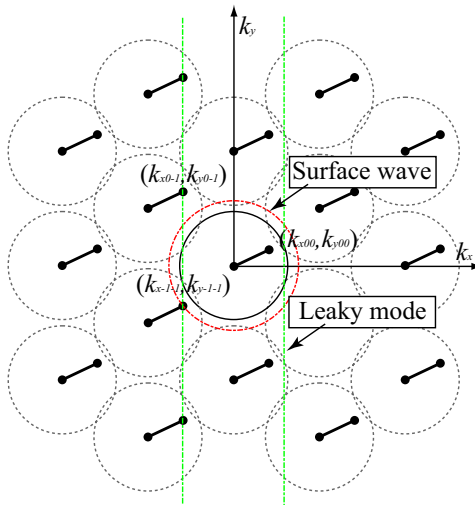


Figure 5.1: Grating lobe diagram that shows the longitudinal wavenumbers for a surface wave in a dielectric slab and the longitudinal wavenumbers for the leaky mode that causes scan blindness in the tapered-slot arrays in triangular grids. The scan blindness condition is fulfilled when the longitudinal wave numbers of a Floquet mode coincide with the longitudinal wavenumbers of the guided mode.

This type of scan blindness cannot occur for a rectangular grid tapered-slot array steered in the E plane due to the imposed symmetry of the elements and the rectangular grid. In rectangular grid arrays scanned in the E plane the fields lines must be in the same direction between two substrate regions. However, that is impossible since the symmetry of the elements and the excitation requires that the field lines have opposite directions from the substrates in the transverse direction. If  $\beta_{lw} = k_x$  for the triangular grid array for other scan directions than the E plane, there is no guaranty that scan blindness will occur, since then the leaky mode could theoretically radiate. However, this relaxed conditions often leads to that the active reflection coefficient changes rapidly and the antenna becomes mismatched. The relaxed scan blindness condition can be illustrated in the same way as the surface wave scan blindness condition, see Fig. 5.1. In this figure the Floquet modes with  $(p = -1, q = n)$  fulfil the relaxed scan blindness condition when the element spacing in the E plane is larger than  $\lambda/2$ . At the lowest frequency, the relaxed scan blindness occurs for  $\theta_0 = 90^\circ, \phi_0 = 0$  and the scan blindness angle decreases with increasing frequency, see Fig. 5.3. For this guided mode the field intensity is high close to the ground plane and therefore the absorbing layer over the ground plane in the experimental antenna will attenuate the wave, as could be observed by comparing Fig. 3.11 and 3.12. This effect is also shown in Fig. 5.3(b) where the dissipated power in the absorbing layer relative to the incident power applied at the port of the

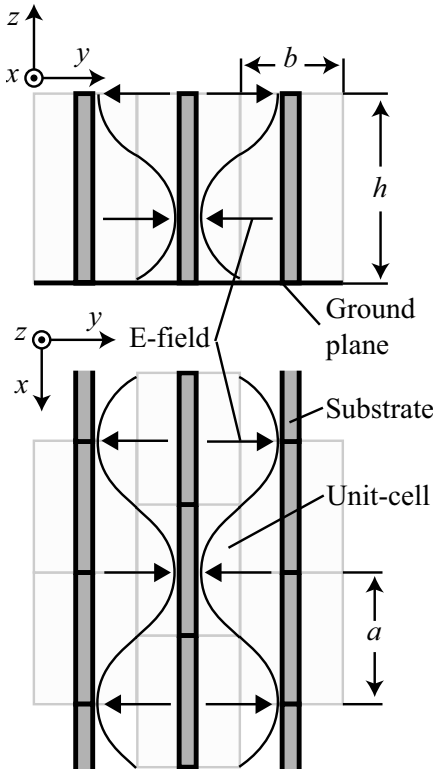
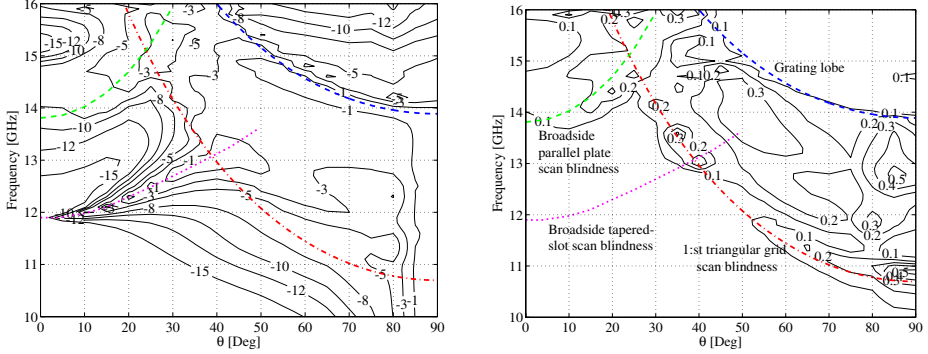


Figure 5.2: Electric field distribution of the leaky mode for the tapered-slot triangular grid scan blindness.

element is shown as a function of the scan angle in the E-plane and the frequency.

### 5.3 Broadside scan blindesses

In both rectangular and triangular grid tapered-slot arrays there exist two types of scan blindness that have the opposite frequency behavior to the previously discussed scan blindness. These scan blindesses occur for the lowest frequency for broadside scan and the scan blindness angle increases with the frequency, see Fig. 5.3. Instead of using the scan blindness condition in Eq. (5.3), to fit a known guided mode to a Floquet mode, a Floquet mode is used to calculate the guided mode. For this type of guided mode the phase progression along the E-plane is arbitrary and can be chosen equal to any Floquet-excitation. The scan blindness condition can be derived from a transmission-line circuit for propagation along the  $z$ -axis. The guided modes propagate downwards, as seen from the top of the antenna, and are reflected back



(a) Total losses (dB) (due to mismatch and reduced radiation efficiency) (b) Dissipated power in the absorbing layer relative to the incident power (-)

Figure 5.3: The three scan blindness types that occur for the experimental antenna tapered-slot design when scanned in the E-plane.

either by the ground plane or by the tapered-slot, and the scan blindness occurs when the impedance at the aperture is equal to the Floquet mode wave impedance, see Fig. 5.4. In Figure 5.4 the wave impedance of the mode in the antenna is denoted  $Z_a$  and the wave impedance of a Floquet mode is denoted  $Z_{FL}$ . Furthermore, the antenna transmission-line is terminated with an impedance  $Z_l$  at the length  $h$  from the aperture.

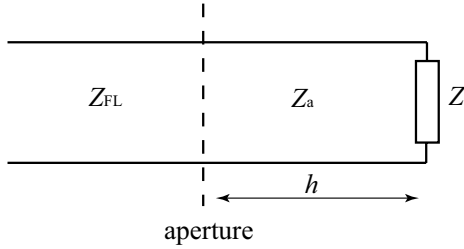


Figure 5.4: Transmission line model used for the broadside parallel plate scan blindness

### Broadside parallel plate scan blindness

The most well known of the broad side scan blindness types mentioned above occurs when the spacing between two substrates is larger than  $\lambda/2$  [46]. The antenna is modeled as a parallel plate waveguide and a  $TM_z$ -mode can be supported by this

structure. The mode propagates between the parallel plates and is reflected by the ground plane. The resonance condition with appropriate  $Z_a$ ,  $Z_{FL}$ , and  $Z_l$  in Fig. 5.4 above for this scan blindness is

$$\beta_z^a \tan(\beta_z^a h) = -jk_{zpq}. \quad (5.4)$$

Here  $\beta_z^a$  is the wavenumber along the  $z$ -axis for the guided mode and  $h$  is the height of the substrate, see Figs. 3.9 and 5.4. Equation (5.4) has solutions for the Floquet modes with index ( $p = 0, q = \pm 1$ ). These Floquet modes are the same for rectangular and triangular grids, since they do not depend on the element spacing along the E-plane. In the experimental antenna the spacing between the substrates is 10.9 mm and the scan blindness occurs for frequencies higher than 13.8 GHz. This is not a problem in the experimental antenna, since the maximum frequency requirement is 11.5 GHz. Note that this scan blindness interacts with the ground plane and the use of an absorbing layer covering the ground plane will dissipate the guided wave. This phenomenon can be seen in Fig. 5.3(b) where the scan blindness condition for the broadside parallel plate scan blindness is shown as a green line.

### Broadside tapered-slot shape scan blindness

The last scan blindness depend on the shape of the tapered-slot, and for the element design presented in paper V it limits the upper frequency bound for many scan angles in the E-plane. This scan blindness is not as well studied as the previous two [46, 49], and there is no known analytical model for the guided mode. Like broadside parallel plate scan blindness, the broadside tapered-slot scan blindness is not affected when changing between triangular and rectangular grids, from which it is likely that it also couples to the same Floquet modes as the previous scan blindness. Numerical calculations have shown that the scan blindness can be moved up in frequency if either the H-plane spacing is reduced, the slot is made shorter, the slot is made narrower, or the dielectric constant is decreased. The field intensity of the guided mode is low close to the ground plane, since the fields are reflected by the slot instead of the ground plane. This lower field intensity at the ground plane is the reason that the absorbing layer covering the ground plane has little or no effect on this scan blindness. In Figs. 5.3(a) and 5.3(b) the broadside tapered-slot scan blindness is shown as a pink dotted line, and it is clear in Fig. 5.3(b) that the dissipated power in the absorber is negligible for this scan blindness.

# Chapter 6

## Edge effects

In Chapter 4 we saw that the measured active reflection coefficient agreed fairly well with the active reflection coefficient for the infinite array. The absolute value of the measured active reflection coefficient usually oscillates around the infinite array result. However, for large scan angles in the H plane the measured active reflection coefficient will oscillate around a mean curve above the active reflection coefficient for the infinite array. Both these effects can be classified as edge effects. An edge effect is basically anything that causes the finite array element results to deviate from the infinite array results.

The edge effects are caused mainly by three factors: 1. the excitation is spatially truncated compared with the Floquet excitation, 2. the geometry close to an edge affects the electrical properties of the elements, 3. unattenuated guided waves are reflected by the edges and create a standing wave pattern over the aperture [66]. These three effects can be hard to distinguish from each other, but all of them must be included in an accurate calculation of the coupling coefficients of the array.

The coupling coefficients can be computed for the infinite array using Fourier series expansion, see Ch. 2.2 and [7, Ch. 4]. By using the coupling coefficients for the infinite array we can effectively model the truncated excitation. This is not the case for the perturbation of the current caused by the edge. To compute the edge perturbation of the currents, the finite array problem needs to be solved. The coupling coefficients can be calculated for the finite array directly if the computational resources are available. However, to analyze large finite arrays one usually require computational recourses such as computer clusters. To simplify the problem one can consider arrays that are finite in only one of the two directions. Then the computational domain is reduced and the effects of a single edge can be isolated if the finite-by-infinite array is large enough [11].

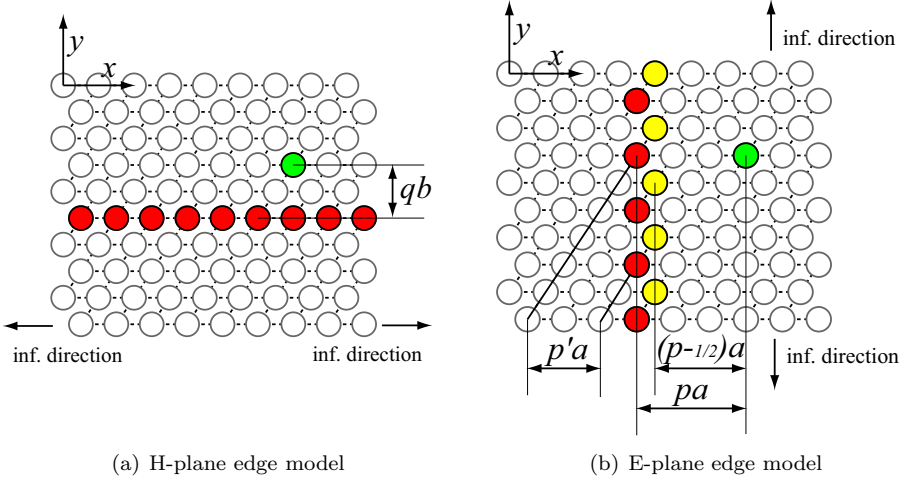


Figure 6.1: The linear arrays are chosen so that they are parallel to the edge in the finite-by-infinite array.

## 6.1 Finite-by-infinite arrays

Antennas that are finite in only one direction can be analyzed by using periodic boundaries in the infinite direction, which is equivalent with analyzing an infinite linear array of finite arrays, see Fig. 6.1. The S-parameters computed using periodic boundaries represent the coupling between a single element and an infinite linear array excited with a one dimensional Floquet excitation. The S-parameters can be calculated for the infinite array by calculating the coupling to an element by exciting the same infinite linear array as in the finite array case. In this way Eq. (2.32) can be simplified and the active reflection coefficient needs to be known for fewer scan directions. In paper VII this simplification is used to study the edge effects in a triangular grid tapered-slot array. The S-parameters are computed for infinite arrays and finite-by-infinite arrays for two types of edges. These edges are modeled after the edges in the experimental array in paper V.

We consider an  $N \times N$  finite array and will try to model it with infinite  $\times N$  or  $N \times$  infinite array models. The respective models will be denoted “the E-plane edge model” and “the H-plane edge model” as explained below.

The antenna elements are oriented so that the E-plane coincides with the  $zx$ -plane and the H-plane with the  $yz$ -plane. The phase difference between two elements along the  $x$ -axis, or  $\mathbf{a}_1$ , is  $\psi_1 = \psi_x$  and the phase difference between two elements along the other lattice axis  $\mathbf{a}_2$  can be written  $\psi_2 = \frac{1}{2}\psi_x + \psi_y$ . Note that the analysis becomes easier if the phase differences are divided into their  $x$  and  $y$  components, since the edges are parallel to the  $x$ - and  $y$ -axis. Therefore, denote the active reflection coefficient for the infinite array with  $S^{\text{FL}}(\psi_x, \psi_y) = S'^{\text{FL}}(\psi_1, \psi_2)$ .

The simplest truncation is an edge perpendicular to the H-plane. It is denoted as “the H plane edge” since, when scanning in the H-plane, the beam is scanned towards or away from that edge, see Fig. 6.1(a). The S-parameters for this edge model can be calculated using Eq. (2.32).

$$S_q = \sum_{p=-\infty}^{\infty} S_{m,n(p,q)} e^{-jp\psi_{x_0}} = \frac{1}{2\pi} \int_{-\pi - \frac{1}{2}\psi_{x_0}}^{\pi - \frac{1}{2}\psi_{x_0}} S^{\text{FL}}(\psi_{x_0}, \psi_y) e^{jq\psi_y} d\psi_y, \quad (6.1)$$

where  $\psi_{x_0} = ka \sin \theta_0 \cos \phi_0$  is the phase shift of the excitation along the  $x$ -axis.

The other edge is “the E plane edge”, when the array is truncated perpendicular to the E-plane, see Fig. 6.1(b). This edge is more difficult to analyze, since the elements are shifted half an element spacing every other element row along the edge. For this edge, two linear arrays are needed to calculate the S-parameters for the corresponding finite-by-infinite array. Along the  $y$ -axis the array is excited with a phase shift  $\psi_{y_0} = kb \sin \theta_0 \sin \phi_0$ . Then, the S-parameters for the first linear array with separation distance  $pa$  to the element are

$$S_p = \sum_{p'=-\infty}^{\infty} S_{m,n(p+p', -2p')} e^{j2p'\psi_{y_0}} = \frac{1}{4\pi} \int_{-\pi}^{\pi} e^{jp\psi_x} (S^{\text{FL}}(\psi_x, \psi_{y_0}) + S^{\text{FL}}(\psi_x, \psi_{y_0} + \pi)) d\psi_x, \quad (6.2)$$

and the S-parameters for the second array with the separation distance  $(p+1/2)a$  to the element are

$$S_{p+\frac{1}{2}} = \sum_{p'=-\infty}^{\infty} S_{m,n(p+p', -2p'+1)} e^{j(2p'-1)\psi_{y_0}} = \frac{1}{4\pi} \int_{-\pi}^{\pi} e^{j(p+\frac{1}{2})\psi_x} \{ S^{\text{FL}}(\psi_x, \psi_{y_0}) - S^{\text{FL}}(\psi_x, \psi_{y_0} + \pi) \} d\psi_x. \quad (6.3)$$

The S-parameters were computed numerically for the two edge models for the infinite array and the finite-by-infinite array, with the phase shift along the common infinite direction set to zero. The agreement between the finite and infinite array results is good for elements far from the edge, and poor for elements close to the edge, see Fig. 6.2.

To evaluate the finite and the infinite array S-parameters, the active reflection coefficient can be calculated using Eq. (2.3). The excitation is chosen to be uniform in amplitude with a linear phase shift  $\phi$  between the elements in the finite direction. In the infinite array the excitation was truncated to the corresponding elements in the finite array. In Fig. 6.3 we display the active reflection coefficients computed for four cases, namely: the truncated excitation of the infinite array, the infinite array with Floquet excitation, the finite array, and a combined solution to be discussed later. As expected, the agreement between the different cases is best for elements far

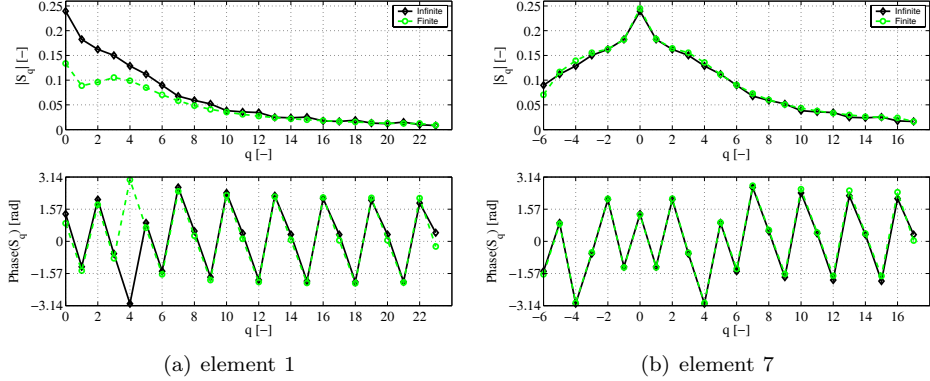


Figure 6.2: The scattering parameters for the H-plane edge model,  $f = 8$  GHz. The finite array consists of 24 elements.

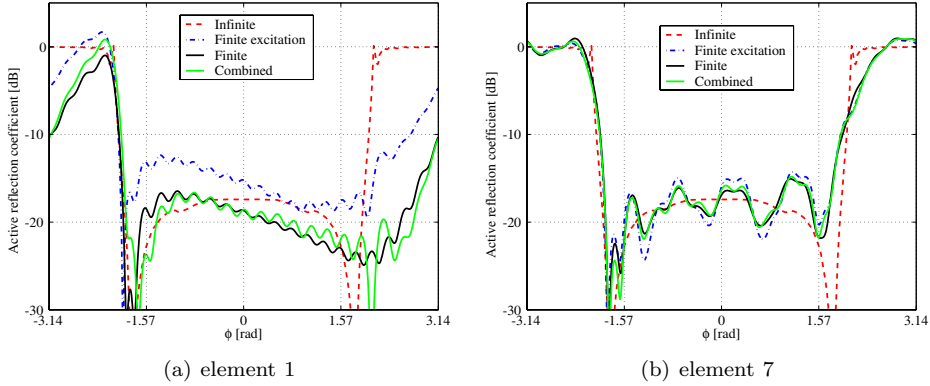


Figure 6.3: Active reflection coefficient as a function of phase shift along the  $y$ -axis,  $\phi = kb \sin \theta$ ,  $b = 12.4$  mm,  $f = 8$  GHz. The finite array consists of 24 elements. The active reflection coefficient were computed using four methods, namely: the infinite array with Floquet excitation (Infinite), the truncated excitation of the infinite array (Finite excitation), the finite array (Finite), and a combined solution (Combined).

from the edges. Furthermore, the active reflection coefficient varies similarly for the finite array and the truncated infinite array, the local maxima and minima in Fig. 6.3 are basically located at the same phase shift. These oscillations in the truncated array results are caused by the missing contributions from the elements that are not excited or not present. The small oscillations in the amplitude are caused by the edge far from the element, and larger oscillations with a longer period are caused

by the closest edge.

The currents are perturbed by the edges of the array, which causes the difference between the finite and finitely excited infinite array. Part of this perturbation can be added to the infinite array result, thereby making it possible to accurately calculate the active reflection coefficient for an arbitrary sized array. If the finite array is sufficiently large, the edge elements will not be affected by the opposite edge and the finite array S-parameters could be combined with the infinite array S-parameters. This is done by using the finite array S-parameters for coupling from elements close to an edge and the infinite array S-parameters for coupling from elements farther away from the edge. This method seems to work pretty well and reduces the largest discrepancies between the finite array and finitely excited infinite array, see Fig. 6.3.

## 6.2 Infinite array data

To calculate the S-parameters one must know the active reflection coefficient for all scan directions. Due to the periodicity of the Floquet excitation, the scan directions can be limited to the phase shifts along the primitive vectors  $-\pi < \psi_1 < \pi$  and  $-\pi < \psi_2 < \pi$ , and if these parameters are sampled close enough the required values to calculate the integral in Eq. (2.32) can be found by interpolation. Some of these phase shifts correspond to invisible space, when no beam radiates from the antenna. These scan directions cannot be computed directly using FDTD-codes based on unit-cell approaches with time shifts between the boundaries, i.e. a time-domain version of the Floquet theorem [48, 67]. In paper VI a method is presented that describes how to calculate arbitrary phase shifts for an infinite array using a numerical code that is restricted to phase shifts that correspond to visible space.

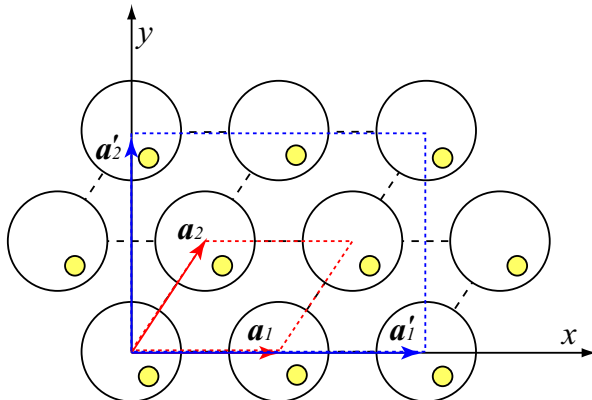


Figure 6.4: The computational domain of the unit cell compared with the larger computational domain used to compute additional phase shifts.

The basic idea is that a computational domain, with a phase shift between its boundaries, that contain more than one element can be used to calculate several different linear phase shifts for the infinite array. This can be done if the S-parameters are calculated for the elements in the computational domain and then weighted together to calculate the active reflection coefficient. This method was used to calculate the active reflection coefficient, needed for the calculation of the S-parameters for the infinite tapered-slot array. Four elements were included in the computational domain, to be able to span the required phase shift space and to keep the triangular grid, see Fig. 6.4. The computational domain containing four elements is a new unit cell of a rectangular grid, with the primitive vectors  $\mathbf{a}'_1 = 2a\hat{x}$  and  $\mathbf{a}'_2 = 2b\hat{y}$ . The phase shifts between the boundaries of this computational domain are  $\psi'_1$  and  $\psi'_2$ , and they correspond to four different phase shifts for the original unit cell defined by  $\mathbf{a}_1$  and  $\mathbf{a}_2$ . In this case the relations between the four phase shifts for the original unit cell and the new unit cell are given by  $\psi_x = \psi'_1/2 + \pi m$  and  $\psi_y = \psi'_2/2 + \pi n$ , where  $m$  and  $n$  are arbitrary integers. This means that the phase shifts spanned with the standard method, i.e. the phase shifts enclosed by the visible space circle, are translated  $\pi/a$  along the  $k_x$ -axis and  $\pi/b$  along the  $k_y$ -axis in the grating lobe diagram. The translated visual space circles are the same as the grating lobe circles for the larger unit cell, see Fig. 6.5.

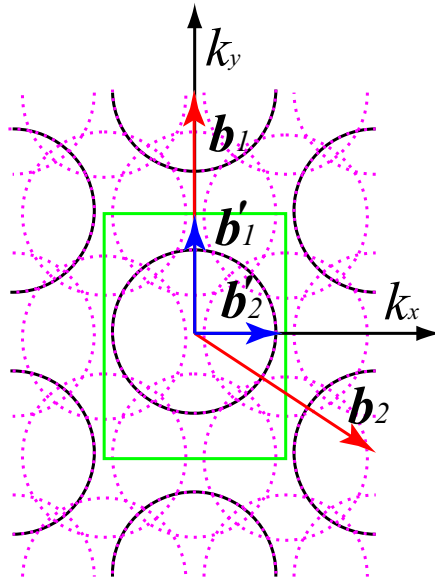
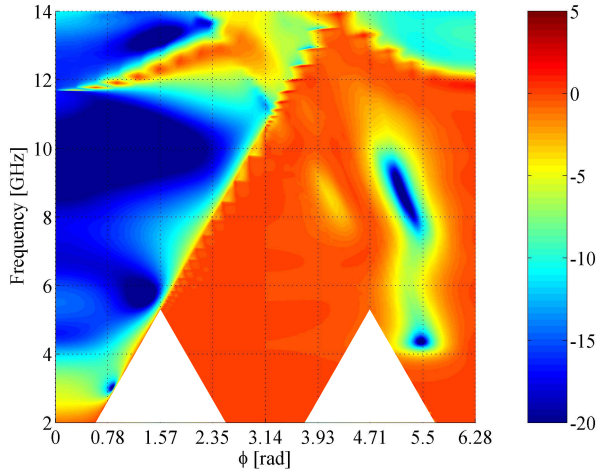


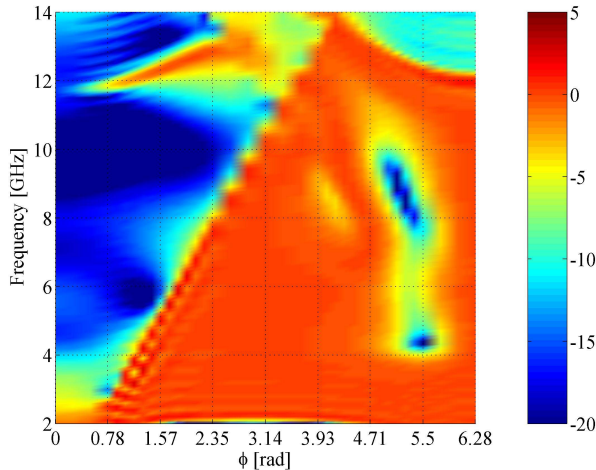
Figure 6.5: The green square represent the phase shifts that need to be spanned to compute the scattering parameters for the infinite array and the purple dashed circles represent the phase shifts that can be spanned by using the larger computational domain.

Given that the grating lobe circles of the larger computational domain cover all the possible phase shifts, it is possible to compute all phase shifts for the infinite array. However, for low frequencies there will be phase shifts that are in between these grating lobe circles. In Figure 6.6(a) the active reflection coefficient in the E-plane, for the tapered-slot element in paper VII, is shown as a function of frequency and phase shift. The white areas in this figure are the phase shifts that were outside the grating lobe circles and for which the active reflection coefficient is unknown. To solve this problem one can either expand the computational domain or use a numerical code that is capable of arbitrary phase shifts.

There are FDTD-codes that use fix phase shifts between the boundaries [68]. A fix phase shift between the boundaries means that the scan direction changes with frequency. This is perfect when calculating S-parameters, but cumbersome when one wants to design an array element for a maximum scan angle. In Figure 6.6(b) a code TFDTD, described in [69] with the periodic boundaries described in [70], was used to calculate the active reflection coefficient for the same case as in Fig. 6.6(a). Due to limited access, this code was primarily used for verification of the method described in paper VI. However, in paper VII the active reflection coefficient computed using TFDTD was used for the frequencies and phase shifts not spanned by the enlarged computational domain. The results computed using PBFDTD and TFDTD agree very well, most of the discrepancies between the results shown in Fig. 6.6 are due to interpolation errors caused by there being fewer scan directions used for the TFDTD computations.



(a) Time shift boundaries with four elements in the computational domain. (PBFDTD + extended domain algorithm)



(b) Phase shift boundaries. (TFDTD)

Figure 6.6: Active reflection coefficient as a function of frequency and phase shift along the  $x$ -axis,  $\phi = ka \sin \theta$ ,  $a = 14.1$  mm.

## Chapter 7

# Conclusions

The subject of the thesis is planar phased arrays capable of wide-angle scanning. Part of the thesis work was to design an antenna element for a phased array radar antenna. To find suitable candidates for the application a literature study was made in our report [23] to identify antenna elements with good wide-angle performance.

At the beginning of this thesis work the goal for the radar antenna to be designed was an element capable of scanning  $75^\circ$  from the aperture normal. The antenna was supposed to be a planar array antenna that was easy to manufacture and which consisted of as few elements as possible. To simplify the analysis, the array was assumed to be large enough to be modeled as an infinite structure. The requested bandwidth of the antenna was moderate, in the order of half an octave, and it was supposed to be well matched with an active reflection coefficient that was less than  $-10$  dB for all scan angles out to  $75^\circ$  from broadside.

Starting from these requirements, the wide-angle scanning limits were studied for waveguide elements in a ground plane. The elements were matched conceptually using a simple circuit model, in which parameters were chosen by minimizing the reflected power for the intended scan range. It was found with this matching method that the waveguide elements were capable of large scanning angles but required additional scan improving techniques to be able to fulfill the requirement for even a single frequency.

These difficult requirements was changed during the thesis due to the expected performance of the frequency selective surface (FSS) that will cover the antenna. A well matched antenna works as an absorber for an incident plane wave. Therefore, a wide-band antenna was preferred to reduce the radar cross section for the frequency bands for which the FSS is transparent. However, wide-angle scan performance is related to the bandwidth of the antenna and if one requirement is increased the other needs to be decreased. The new requirements were for a single polarized element capable of a 2.5:1 bandwidth for scan angles out to  $60^\circ$  from broadside.

An element that could potentially fulfill these requirements was the fragmented aperture element. The fragmented aperture element is a novel design and it was considered as a backup element in case the other option, the tapered-slot element, did not work out. A couple of practical problems related to building and analyzing

fragmented aperture elements were considered and solved. The fragmented aperture element still has some unsolved design problems; one is the design of a practical feed.

The element that was chosen for the radar antenna was the tapered-slot element. This element has two main advantages: it is easy to fabricate and it has excellent broadband qualities. The idea was that part of the broadband performance could be traded in the design to achieve a better scan performance. To improve the mechanical stability of the array, the elements are encapsulated by a foam layer that is in turn covered by a glass fibre layer. The glass fibre layer acts both as a protection and as a wide impedance matching layer that improves the performance for the H-plane scan directions. The final design was an element that fulfilled the requirements and incorporated an absorbing layer covering the ground plane, to reduce the radar cross section for the antenna's cross polarization.

The tapered-slot element design was the basis for an experimental antenna built by Saab Microwave Systems. This antenna proved to agree well with the numerical calculations, but also gave ideas for further studies. The active reflection coefficient for the H-plane scan direction is worse for the central elements in the experimental array than in the infinite array calculations. This is shown to result from the truncation of the infinite array, i.e. an edge effect.

Phased arrays often suffer from an effect called scan blindness. This effect, which impairs the performance, is caused by a guided wave in the array structure. In the experimental antenna design, there occur three types of scan blindnesses. One of these scan blindnesses occurs only for triangular grid tapered-slot elements and cannot be excited in a rectangular grid. This scan blindness sets the maximum element spacing and therefore reduces the benefit of the otherwise optimal equilateral triangular grid. The other scan blindnesses occur for the same frequencies for triangular and rectangular grids and appears first in frequency for broadside scan. The most problematic of these broadside scan blindnesses depends on the shape of the tapered-slot, and unlike the two other scan blindnesses there is today no analytical expression for the scan blindness condition. It is a challenge to find such an expression, but it would be a useful tool for an engineer when designing this type of element.

An infinite array element behaves similarly to an element within a large array. The difference between the infinite array solution and the finite array solution is usually referred to as edge effects. In this thesis edge effects for tapered-slot in triangular grids were considered. The edge effects were studied by comparing the scattering parameters for finite-by-infinite arrays with those for infinite arrays. The active reflection coefficient for a finite excitation was calculated for these two cases and showed good agreement for the central elements. The thesis ends with the description of a method that was developed for the use of finite difference time domain codes with time shift boundaries to calculate active reflection coefficients for scan directions in invisible space. This method was used to compute the raw data required to calculate the scattering parameters.

# **Chapter 8**

## **Summary of papers**

### **8.1 Paper I**

Rectangular waveguide elements in infinite planar arrays are analyzed with respect to wide-angle scanning, and results for three types of waveguide apertures are presented. The goal was to find a wide-angle scanning array element with moderate bandwidth that can excite two polarizations. The dual polarization requirement leads to the cross section of the waveguides being either circular or square shaped. Dual polarization elements can have problems due to coupling between the two polarizations. Therefore, a single polarized element was chosen as a reference. A goal was to be capable of scanning out to  $75^\circ$  from broadside. For such a large scan angle, a small element spacing is required to avoid the appearance of grating lobes, which requires that the waveguides are filled with a dielectric material to reduce the size of the waveguide cross section.

The elements were evaluated by computing the average reflected power over the scan range. Before the elements were matched, the waveguide with the largest cross section was the best element in terms of the average reflected power. The elements were then matched using a simple matching scheme which minimized the average reflected power. After the matching procedure, the waveguide with the smallest cross section achieved the best result but was similar to the single polarized waveguide. The reason why the large waveguide could not be as well matched was that when the element was steered out in the diagonal plane a large part of the incident power was reflected back in the orthogonal polarization.

### **8.2 Paper II**

Fragmented patch elements for infinite planar arrays are studied in this paper. The shape of this element is obtained by using a genetic algorithm to minimize the average reflected power over a frequency band for three scan directions. The elements consist of small metal pixels and the optimization algorithm chooses the

pattern of these pixels. Like for an idealized dipole the element is fed in the middle with a point source. At the time of the paper these elements were a new design and several issues needed to be resolved to improve the designs and to simplify the manufacturing.

Three improvements were addressed in this paper. First, the new designs were done with  $4 \times 4$  FDTD-cells per pixel, to describe the geometry, instead of a single FDTD-cell. Furthermore, the  $4 \times 4$ -model was evaluated by comparing the results with results for grids with a  $12 \times 12$  resolution. The second item that was addressed was the electrical contact between corners of two adjacent pixels. To avoid problems during manufacturing with reduced electrical contact, two solutions were proposed and evaluated. The first solution was to put a small patch over the problematic corners. The results computed using this method were identical to the results without the small patch, which shows that this is a good practical solution to avoid the reduction of electrical contact across corners. The second solution is to make the metal pixel slightly larger so that a small overlap is created. Since metal edges are effectively slightly wider than the grid in an FDTD-model, the overlapping pixel model agree better with the  $4 \times 4$  optimization model than the corner patch model. The last addressed item was a wide-angle design, in which a thin array element was designed for scan angles out to  $60^\circ$  from broadside scan. Two designs were considered, one with a dielectric superstrate on top of the metallic pattern and one without.

### 8.3 Paper III

In this paper we studied the effect of an absorbing layer covering the ground plane in an array of tapered-slot elements. The tapered-slot elements are configured in a triangular grid and designed for a radar application. To reduce the radar cross section of the polarization that is orthogonal to the antenna element, an absorber is positioned above the ground plane. The absorbing layer does not affect the antenna performance much, since fields with the same polarization as the antenna cannot reach the absorbing layer. The antenna structure works as a parallel plate waveguide structure that is under cutoff for these waves. However, there is a scan blindness effect in this array caused by a guided mode that is excited in between the elements. The absorbing layer will attenuate the guided mode that causes the scan blindness and the antennas radiation efficiency is reduced instead of becoming mismatched. An additional scan blindness is discussed, which is not affected by the absorbing layer; in this thesis it is denoted as the broadside tapered-slot scan blindness. This scan blindness is incorrectly identified in paper III as the scan blindness presented in [46], which still occurs for this antenna but for higher frequencies. The scan blindness in this paper is very similar, but unlike the scan blindness in [46] it depends on the shape of the tapered-slot. Parts of the results in this paper are also published in paper V.

## 8.4 Paper IV

This paper describes a scan blindness that exists in triangular grid tapered-slot arrays. A simple model for the scan blindness is presented and the model is evaluated. This scan blindness is important because it will for some designs set the maximum frequency limit for the antenna. The maximum unit cell size is 15% larger for triangular grids than for rectangular grids. However, the larger unit cell cannot be utilized completely due to this scan blindness.

The scan blindness depends primarily on two element parameters, the height of the element and the width of the tapered-slot element along the E-plane. The scan blindness occurs when the width is longer than half a wavelength and the scan blindness angles decreases when the frequency increases. If the element height above the ground plane is increased, the scan blindness angle occurs for a lower frequency. In the limit when the height of the element goes to infinity the scan blindness occurs for the same angle and frequency as the grating lobe in a rectangular grid with the same element spacing.

## 8.5 Paper V

This paper describes a design of a triangular grid tapered-slot array. The main focus was on the design of an array element suitable for radar applications. This element needs to be well matched for a wide frequency band but also to have a low radar cross section for the antenna's orthogonal polarization. The wide-scan performance is met due to careful modeling of the tapered-slot shape and a wide-angle impedance matching layer. To reduce the radar cross section an absorbing layer is positioned above the ground plane. This layer interferes little with the antennas performance with the exception that it reduces the scan blindness effects that exist for this design. This antenna element has three scan blindness effects, of which two are affected by the absorbing layer.

An experimental antenna consisting of  $16 \times 16$  elements was built and evaluated. The measured active reflection coefficient for the center element was compared with the active reflection coefficient for an element in the infinite array. The agreement was good for broadside scan as well as E-plane scan. The results for the H-plane scan deviated more than expected from the infinite array result. This has been shown to be a finite array effect and it does not occur from incorrect manufacturing of the antenna.

## 8.6 Paper VI

In this paper a method is presented that describes how to calculate arbitrary phase shifts for an infinite array using a numerical code that is restricted to phase shifts that correspond to visible space. This is a problem with finite difference time domain codes that use time shifts between the periodic boundaries.

The basic idea is that a computational domain, with a phase shift between its boundaries, and containing more than one element, can be used to calculate several different linear phase shifts for the infinite array. This can be done if the S-parameters are calculated for the elements in the computational domain and then weighted together to calculate the active reflection coefficient.

Two numerical examples are given in this paper. In the first example a computational domain with three dipole elements is used to calculate the three different linear phase shifts for the infinite array in a single run. The second example compares the results computed using the method with results from another numerical code.

## 8.7 Paper VII

In this paper the edge effects in tapered-slot arrays are studied and modeled using coupling coefficients. The arrays were chosen to be infinite in one direction and finite in one direction, since this reduces the size of the problem and the number of edges in the array. S-parameters for the finite-by-infinite arrays are compared with S-parameters for the infinite array for two types of edges. The edge shape was chosen to be the same as in the experimental antenna in paper V. These edges are parallel to either the E plane or the H plane.

It is shown how the S-parameters change with element position. The active reflection coefficients are computed using these S-parameters for the finite array and the infinite array by using a truncated excitation. The active reflection coefficient for these two cases is very similar but differ from the infinite array that is uniformly excited. It is therefore concluded that the dominant cause of the edge effects is the truncated excitation of the array. The difference between the coupling coefficients for the finite array and the infinite array is more prominent close to the edges. This is a secondary effect caused by the currents being perturbed by the finite array edge.

# Bibliography

- [1] A. Balanis, *Antenna theory*, 3rd ed. Wiley-Interscience, New York, 2005.
- [2] P. Patel, D. Kant, E. Wal, and A. van Ardene, “Phased array antennas demonstrator as a radio telescope - embrace,” *Antennas and Propagation Society International Symposium, 2008. AP-S 2008. IEEE*, pp. 1–4, July 2008.
- [3] S. Hay, J. O’Sullivan, J. Kot, C. Granet, A. Grancea, A. Forsyth, and D. Hayman, “Focal plane array development for ASKAP (Australian SKA pathfinder),” *Antennas and Propagation, 2007. EuCAP 2007. The Second European Conference on*, pp. 1–5, Nov. 2007.
- [4] N. Amitay, V. Galindo, and C. P. Wu, *Theory and analysis of phased array antennas*. Wiley-Interscience, New York, 1972.
- [5] R. J. Mailloux, *Phased array antenna handbook*. Artech House, Boston, 1994.
- [6] R. C. Hansen, *Phased array antennas*. Wiley-Interscience, New York, 1998.
- [7] A. K. Bhattacharyya, *Phased Array Antennas*. Wiley-Interscience, New York, 2006.
- [8] A. Ishimaru, R. Coe, G. Miller, and W. Geren, “Finite periodic structure approach to large scanning array problems,” *Antennas and Propagation, IEEE Transactions on*, vol. 33, no. 11, pp. 1213–1220, Nov 1985.
- [9] A. Skrivervik and J. Mosig, “Analysis of finite phase arrays of microstrip patches,” *Antennas and Propagation, IEEE Transactions on*, vol. 41, no. 8, pp. 1105–1114, Aug 1993.
- [10] A. Neto, S. Maci, G. Vecchi, and M. Sabbadini, “A truncated Floquet wave diffraction method for the full wave analysis of large phased arrays. I. Basic principles and 2-D cases,” *Antennas and Propagation, IEEE Transactions on*, vol. 48, no. 4, pp. 594–600, Apr 2000.
- [11] C. Craeye, A. Tijhuis, and D. Schaubert, “An efficient MoM formulation for finite-by-infinite arrays of two-dimensional antennas arranged in a three-dimensional structure,” *Antennas and Propagation, IEEE Transactions on*, vol. 52, no. 1, pp. 271–282, Jan. 2004.

- [12] W. B. Lu, T. J. Cui, Z. G. Qian, X. X. Yin, and W. Hong, "Accurate analysis of large-scale periodic structures using an efficient sub-entire-domain basis function method," *Antennas and Propagation, IEEE Transactions on*, vol. 52, no. 11, pp. 3078–3085, Nov. 2004.
- [13] D. J. Beckers, S. J. L. van Eijndhoven, A. A. F. van de Ven, P.-P. Borsboom, and A. G. Tijhuis, "Eigencurrent analysis of resonant behavior in finite antenna arrays," *Antennas and Propagation, IEEE Transactions on*, vol. 54, no. 6, pp. 2821 – 2829, June 2006.
- [14] R. Maaskant, R. Mittra, and A. Tijhuis, "Application of trapezoidal-shaped characteristic basis functions to arrays of electrically interconnected antenna elements," Sept. 2007, pp. 567–571.
- [15] ———, "Fast analysis of large antenna arrays using the characteristic basis function method and the adaptive cross approximation algorithm," *Antennas and Propagation, IEEE Transactions on*, vol. 56, no. 11, pp. 3440–3451, Nov. 2008.
- [16] H. Holter and H. Steyskal, "On the size requirement for finite phased-array models," *Antennas and Propagation, IEEE Transactions on*, vol. 50, no. 6, June 2002.
- [17] W. Yu, X. Yang, Y. Liu, L. ching Ma, T. Sul, N.-T. Huang, R. Mitral, R. Maaskane, Y. Lu, Q. Che, R. Lu, and Z. Su, "A new direction in computational electromagnetics: Solving large problems using the parallel FDTD on the BlueGene/L supercomputer providing teraflop-level performance," *Antennas and Propagation Magazine, IEEE*, vol. 50, no. 2, pp. 26–44, April 2008.
- [18] G. Paraschos, R. Kindt, D. Schaubert, and M. Vouvakis, "Radiation and coupling studies of finite-size dual polarized Vivaldi arrays using a domain decomposition FEM," *Antennas and Propagation Society International Symposium, 2008. AP-S 2008. IEEE*, pp. 1–4, July 2008.
- [19] J. Jian-Ming and R. J. Douglas, *Finite element analysis of antennas and arrays*. IEEE Press, New York, 2008, ch. 11.
- [20] "IEEE standard definitions of terms for antennas." *IEEE Std 145-1993*, Jun 1993.
- [21] P. Hannan, "The element-gain paradox for a phased-array antenna," *Antennas and Propagation, IEEE Transactions on*, vol. 12, no. 4, pp. 423–433, Jul 1964.
- [22] N. Amitay, V. Galindo, and C. P. Wu, *Theory and Analysis of Phased Array Antennas*. Wiley-Interscience, 1972, p. 27.
- [23] A. Ellgårdt and H. Steyskal, "Antenna elements for wide-angle phased arrays," Division of Electromagnetic Theory, Royal Institute of Technology, Tech. Rep., 2005, TRITA-TET 2005:04.

- [24] ——, “Study of waveguide elements for planar wide-angle scanning phased antennas,” Division of Electromagnetic Theory, Royal Institute of Technology, Tech. Rep., 2005, TRITA-TET 2005:05.
- [25] S.-W. Lee, “Aperture matching for an infinite circular polarized array of rectangular waveguides,” *Antennas and Propagation, IEEE Transactions on*, vol. 19, no. 3, pp. 332 – 342, May 1971.
- [26] S.-W. Lee and W. R. Jones, “On the suppression of radiation nulls and broadband impedance matching of rectangular waveguide phased arrays,” *Antennas and Propagation, IEEE Transactions on*, vol. 19, no. 1, pp. 41 – 51, Jan. 1971.
- [27] G. N. Tsandoulas and G. H. Knittel, “The analysis and design of dual-polarization square-waveguide phased arrays,” *Antennas and Propagation, IEEE Transactions on*, vol. 21, no. 6, pp. 796 – 808, Nov. 1973.
- [28] J. P. Montgomery, “Ridged waveguide phased arrays,” *Antennas and Propagation, IEEE Transactions on*, vol. 24, no. 1, pp. 46 – 53, Jan. 1976.
- [29] C. C. Chen, “Wideband wide-angle impedance matching and polarization characteristics of circular waveguide phased arrays,” *Antennas and Propagation, IEEE Transactions on*, vol. 22, no. 3, pp. 414 – 418, May 1974.
- [30] R. G. Schmier and M. J. Buckley, “Broadband circular waveguide radiating element for use in phased array antennas,” *AP-S*, vol. 2, pp. 1236 – 1239, June 1994.
- [31] B. J. Lamberty, W. P. Geren, S. H. Goodman, G. E. Miller, and K. A. Dallabetta, “Wide angle impedance matching surfaces for circular waveguide phased array antennas with 70 degree scan capability,” in *Proc. Antenna Applications Symp.* Allerton Park, Sept. 2003, pp. 372–390.
- [32] A. Ellgardt, “Study of rectangular waveguide elements for planar wide-angle scanning phased array antennas,” *Antennas and Propagation Society International Symposium, 2005 IEEE*, vol. 1B, pp. 815–818 vol. 1B, 2005.
- [33] H. Wheeler, “The grating-lobe series for the impedance variation in a planar phased-array antenna,” *Antennas and Propagation, IEEE Transactions on*, vol. 14, no. 6, pp. 707–714, Nov 1966.
- [34] B. Thors, H. Steyskal, and H. Holter, “Broad-band fragmented aperture phased array element design using genetic algorithms,” *Antennas and Propagation, IEEE Transactions on*, vol. 53, no. 10, pp. 3280–3287, Oct. 2005.
- [35] H. Holter, “Analysis and design of broadband phased array antennas,” Ph.D. dissertation, KTH, 2000.

- [36] B. A. Munk, T. W. Kornau, and R. D. Fulton, “Scan independent phased arrays,” *Radio Science*, vol. 14, no. 6, pp. 979 – 990, Nov.-Dec. 1979.
- [37] J. J. Schuss and J. D. Hanfling, “Nonreciprocity and scan blindness in phased arrays using balanced-fed radiators,” *Antennas and Propagation, IEEE Transactions on*, vol. 35, no. 2, pp. 134–138, Feb. 1987.
- [38] Y. Mushiake, “Self-complementary antennas,” *Antennas and Propagation Magazine, IEEE*, vol. 34, no. 6, pp. 23–29, Dec 1992.
- [39] A. Neto and J. J. Lee, “Ultrawide-band properties of long slot arrays,” *Antennas and Propagation, IEEE Transactions on*, vol. 54, no. 2, pp. 534–543, Feb. 2006.
- [40] ——, “‘Infinite bandwidth’ long slot array antenna,” *Antennas and Wireless Propagation Letters, IEEE*, vol. 4, pp. 75–78, 2005.
- [41] R. Hansen, “Comments on ‘Infinite bandwidth long slot array antenna’,” *Antennas and Wireless Propagation Letters, IEEE*, vol. 4, no. 1, pp. 497–, 2005.
- [42] X. Dardenne and C. Craeye, “Simulation of the effects of a ground plane on the radiation characteristics of self-complementary arrays,” *Antennas and Propagation Society International Symposium, 2003. IEEE*, vol. 1, pp. 383–386 vol.1, June 2003.
- [43] M. Gustafsson, “Broadband array antenna using a self-complementary antenna array and dielectric slabs,” Lund Inst. Tech., Tech. Rep., 2004.
- [44] N. Schuneman, J. Irion, and R. Hodges, “Decade bandwidth tapered notch antenna array element,” in *Proc. Antenna Applications Symp.* Allerton Park, Sept. 2001, pp. 280–295.
- [45] M. Kragalott, W. R. Pickles, and M. S. Kluskens, “Design of a 5:1 bandwidth stripline notch array from FDTD analysis,” *Antennas and Propagation, IEEE Transactions on*, vol. 48, no. 11, pp. 1733–1741, Nov. 2000.
- [46] D. H. Schaubert, “A class of E-plane scan blindesses in single-polarized arrays of tapered-slot antennas with a ground plane,” *Antennas and Propagation, IEEE Transactions on*, vol. 44, no. 7, pp. 954–959, July 1996.
- [47] ——, “A gap-induced element resonance in single-polarized arrays of notch antennas,” in *Antennas and Propagation Society International Symposium*, vol. 2. AP-S. Digest, June 1994, pp. 1264 – 1266.
- [48] H. Holter and H. Steyskal, “Infinite phased-array analysis using FDTD periodic boundary conditions-pulse scanning in oblique directions,” *Antennas and Propagation, IEEE Transactions on*, vol. 47, no. 10, pp. 1508–1514, Oct 1999.

- [49] A. Ellgardt, “A scan blindness model for single-polarized tapered-slot arrays in triangular grids,” *Antennas and Propagation, IEEE Transactions on*, vol. 56, no. 9, pp. 2937–2942, Sept. 2008.
- [50] H. Holter, T.-H. Chio, and D. H. Schaubert, “Elimination of impedance anomalies in single- and dual-polarized endfire tapered slot phased arrays,” *Antennas and Propagation, IEEE Transactions on*, vol. 48, no. 1, pp. 122 – 124, Jan. 2000.
- [51] H. Holter, “Dual-polarized broadband array antenna with BOR-elements, mechanical design and measurements,” *Antennas and Propagation, IEEE Transactions on*, vol. 55, no. 2, pp. 305–312, Feb. 2007.
- [52] ———, “A new type of antenna element for wide-band wide-angle dual polarized phased array antennas,” *IEEE International Symposium*, Oct. 2003.
- [53] E. Arnold, “A radiating element for an active airborne antenna,” in *Antennas and Propagation Society International Symposium, 1999.*, vol. 1. IEEE., July 1999, pp. 134 – 137.
- [54] J. J. Lee, S. Livingstone, and R. Koenig, “A low-profile wide-band (5:1) dual-pol array,” *IEEE Antennas and wireless propagation letters*, vol. 2, pp. 46–49, 2003.
- [55] ———, “Performance of a wideband (3-14 GHz) dual-pol array,” in *Antennas and Propagation Society International Symposium*, vol. 1. AP-S. Digest, June 2004, pp. 551 – 554.
- [56] M. W. Elsallal and D. H. Schaubert, “Electronically scanned arrays of dual-polarized, doubly-mirrored balanced antipodal Vivaldi antennas (DmBAVA) based on modular elements,” in *Antennas and Propagation Society International Symposium*. AP-S. Digest, July 2006, pp. 887 – 890.
- [57] T.-H. Chio and D. H. Schaubert, “A parameter study of stripline-fed Vivaldi notch-antenna arrays,” *Antennas and Propagation, IEEE Transactions on*, vol. 48, no. 6, pp. 879–886, June 2000.
- [58] J. Shin and D. Schaubert, “A parameter study of stripline-fed Vivaldi notch-antenna arrays,” *Antennas and Propagation, IEEE Transactions on*, vol. 47, no. 5, pp. 879–886, May 1999.
- [59] S. Kasturi and D. H. Schaubert, “Effect of dielectric permittivity on infinite arrays of single-polarized Vivaldi antennas,” *Antennas and Propagation, IEEE Transactions on*, vol. 54, no. 2, pp. 351–358, Feb. 2006.
- [60] E. G. Magill and H. A. Wheeler, “Wide-angle impedance matching of planar array antenna by a dielectric sheet,” *Antennas and Propagation, IEEE Transactions on*, vol. 14, no. 1, pp. 49 – 53, Jan. 1966.

- [61] D. M. Pozar, “Analysis of an infinite phased array of aperture coupled microstrip patches,” *Antennas and Propagation, IEEE Transactions on*, vol. 37, no. 4, pp. 418 – 425, Apr. 1989.
- [62] D. M. Pozar and D. H. Schaubert, “Scan blindness in infinite phased arrays of printed dipoles,” *Antennas and Propagation, IEEE Transactions on*, vol. 32, no. 6, pp. 602 – 610, June 1984.
- [63] D. M. Pozar, “General relations for a phased array of printed antennas derived from infinite current sheets,” *Antennas and Propagation, IEEE Transactions on*, vol. 33, no. 5, pp. 498 – 504, May 1985.
- [64] R. E. Collin, *Field Theory of Guided Waves*, 2nd ed. IEEE Press, New York, 1991, pp. 705–707.
- [65] J. Ramprecht, “Electromagnetic waves in media with ferromagnetic losses,” Ph.D. dissertation, KTH, 2008.
- [66] D. Janning and B. Munk, “Effects of surface waves on the currents of truncated periodic arrays,” *Antennas and Propagation, IEEE Transactions on*, vol. 50, no. 9, pp. 1254–1265, Sep 2002.
- [67] R. Lee and G. Smith, “An alternative approach for implementing periodic boundary conditions in the FDTD method using multiple unit cells,” *Antennas and Propagation, IEEE Transactions on*, vol. 54, no. 2, pp. 698–705, Feb. 2006.
- [68] G. Turner and C. Christodoulou, “FDTD analysis of phased array antennas,” *Antennas and Propagation, IEEE Transactions on*, vol. 47, no. 4, pp. 661–667, Apr 1999.
- [69] T. Martin, “Broadband electromagnetic scattering and shielding analysis using the finite difference time domain method,” Ph.D. dissertation, Linköpings Universitet, Linköping.
- [70] L. Pettersson, T. Martin, and L. Pettersson, “FDTD with phase shift boundaries for simulation of infinite planar arrays,” in *Computational Electromagnetics - Methods and Applications, EMB04*, Gothenburg, Sweden, Oct. 2004, pp. 58–65.

# BROADBAND ARRAY ANTENNA

Mike Stasiowski  
Cobham Defense Electronic Systems  
Nurad Division  
3310 Carllins Park Drive  
Baltimore, MD 21215

Dan Schaubert  
Antennas and Propagation Laboratory  
Electrical and Computer Engineering  
100 Natural Resources Road  
University of Massachusetts  
Amherst, MA 01003

**Abstract:** The continued convergence of radar, electronic warfare and communication applications require advances in broad band phased array antennas, including both performance improvements and development of manufacturing technology. Nurad and the University of Massachusetts collaborated to design and fabricate 3:1 and 9:1 bandwidth arrays. The first array designed and tested was a 3:1 band phased array. Using lessons learned from that antenna, a 9:1 band array antenna was designed. The results showed that acceptable electrical performance is readily available and that the manufacturing of the array was vastly more complex than originally expected. This presentation discusses the electromagnetic simulation results and compares them to the measured data, while focusing on manufacturing issues and advancements.

## 1 BACKGROUND

### 1.1 Design Baseline: University of Massachusetts Antenna

Several arrays with bandwidths up to 5:1 have been designed by the University of Massachusetts. The dual-polarized array in Figure 1 is a frequency-scaled prototype for an early design of the Square Kilometer Array radio telescope. Numerical simulations predicted this array to operate with VSWR<2 from 1-5 GHz and scanning to 45° in any plane. The 144-element array (8x9x2) in Figure 1 was extensively tested [1] and its performance was quite good, even in such a small array.

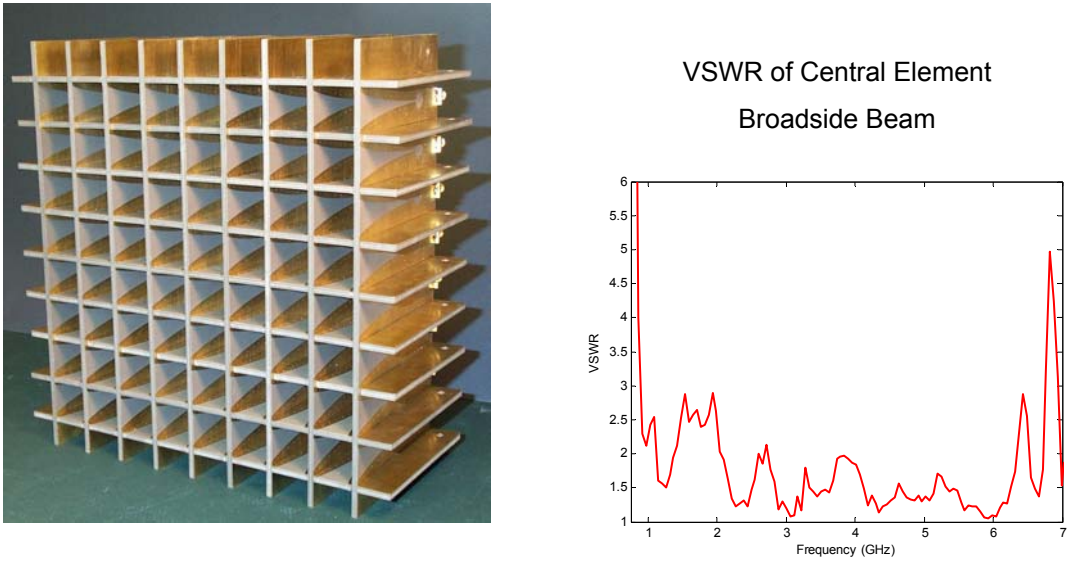


**Figure 1. Dual-polarized Vivaldi array designed for Square Kilometer Array radio telescope. VSWR for broadside beam is computed from measured coupling coefficients in 8x9x2 array. The low-frequency performance is affected by truncation - the array is only 2 wavelengths square at 2 GHz.**

Based on prior experience with single- and dual-polarized Vivaldi arrays and on the reported results of others, e.g., [2], the 9:1 bandwidth array was designed using the Vivaldi element. The Vivaldi element is very attractive for phased array applications because it can be fed directly from stripline or microstripline, the balun is an integral part of the antenna structure. The Vivaldi elements of the completed array operate over the same frequency range as the array in [2] but our elements are shorter than the design presented in [2], 45mm compared to approximately 62mm.

## 1.2 Notch & Horn Antennas

Single element notch and horn antennas have been used in a variety of military applications, most notably Electronic Counter Measure (ECM) systems that require moderate to wide bandwidth, wide angular coverage, specific polarization control, and high power handling capability. Several examples are shown in Figure 2.

Nurad offers high power horn antenna designs with characteristics such as broad frequency ranges to cover 3:1 bandwidths, lensed apertures to provide beamwidth and pattern control and unique machined/angled apertures to solve difficult installation problems. Also available are special horn designs with bandwidths up to 9:1. These offer the clear advantage of using one antenna to cover larger frequencies instead of having several antennas covering the same frequencies. Nurad currently offers existing horn antennas from 100 MHz to 96 GHz for various applications with linear, circular, dual linear, and simultaneous circular polarizations

Nurad also offers extended bandwidth horns to meet special customer requirements. Phase and amplitude tracking characteristics can be incorporated and matched sets can be provided for specific applications.

Horn antenna's featured rugged construction and a lightweight, moisture sealed design make them well suited for extreme conditions of airborne platforms. Typical applications include ECM and other direction finding systems for both airborne and shipboard systems.

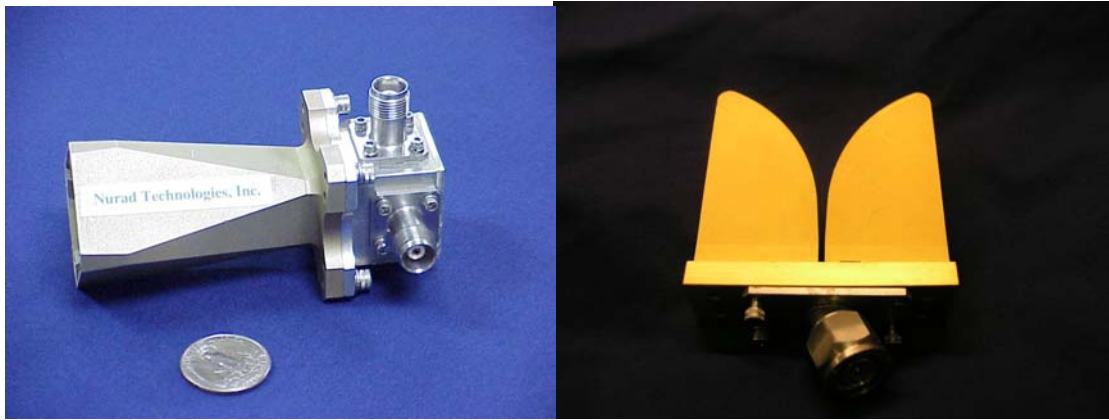


**Figure 2: Legacy ECM Antennas**

A common feature of all of these single element antennas is radiation pattern coverage of a defined (and usually wide) angular sector. The purpose of the research reported here is to develop an array antenna with that covers the same angular sector with a narrow and electronically steerable beam.

## **2 DESIGN & MODELING**

### **2.1 Design Goals (3:1)**

Nurad has threshold and objective design goals for the antenna array. The threshold is a 3:1 band width array. This array was designed not to push state of the art, but to start the process of understanding the manufacturing processes involved as well as working through the design process using the CAD resources available and creating a stepping stone design to the objective 9:1 bandwidth array.

**Table 1. 3:1 Array Threshold Design Goals**

Frequency	6-18 GHz
VSWR	2.5:1 max
Gain	$10\log(N) + ge$
Weight	Minimize
Size	16 x 8 elements (no depth requirement)
Power	5 W per element
Target Environment	Airborne Military

**Table 2. 9:1 Array Objective Design Goals**

Frequency	2-18 GHz
VSWR	2.5:1 max
Gain	$10\log(N) + ge$
Weight	Minimize
Size	128 x 64 elements 2.2" thick
Power	5 W per element
Target Environment	Airborne Military

## 2.2 CAD Tool

The arrays were designed by using efficient computer simulations to estimate the performance of candidate element geometries. The candidate elements were modified based on design curves developed at the University of Massachusetts [3] [4] [5] until satisfactory performance was achieved. Each array design requires numerous computer simulations of the array performance to optimize the element geometry, so the infinite array approximation was used. This approximation greatly reduces computation time but fails to capture truncation effects. Nevertheless, infinite array approximations have previously been shown to yield reasonably good predictions of performance for elements that are located at least two wavelengths from the array edge.

Several commercial and proprietary electromagnetic simulators can be used for the infinite array analysis. The finite-difference, time-domain (FDTD) solver for periodic boundary conditions, PB-FDTD [6], is particularly well-suited for wide-band array design. This simulator combines the efficiencies of the FDTD algorithm and unit cell modeling, and it provides a rigorous solution for beam steering in the principal planes. The input impedance of a coarse-resolution model for the 9:1 dual-polarized array can be analyzed over the frequency range of interest at a single scan angle in about 30 minutes on a typical desktop computer. Once a reasonably good design is achieved, a fine-resolution model can be evaluated to verify and tune the performance.

### 2.3 Egg Crate

The chosen design is an “egg crate” design where the boards cross at the edge of each element. A conceptual sketch is shown in Figure 3. This differs from the cross design in that the phase center of the orthogonal elements are offset from one another; however, the fabrication methods are simplified considerably over the cross design. In addition, this type of design builds on the legacy of other University of Massachusetts antenna designs so the particular characteristics are well understood.

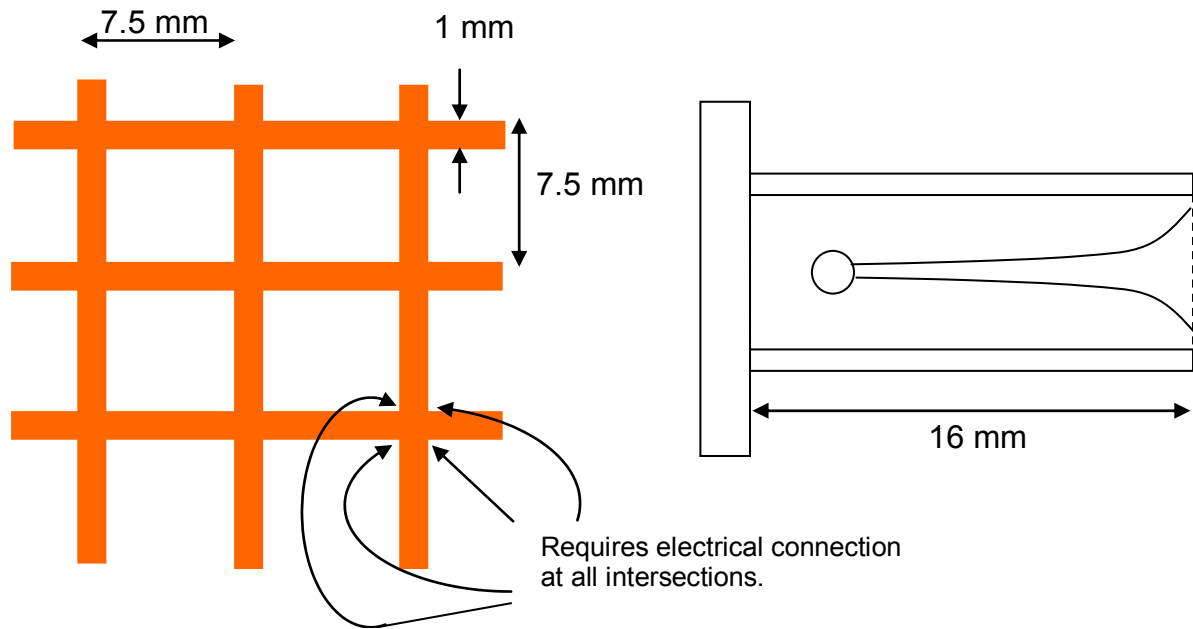


**Figure 3. Egg Crate Design**

### 2.4 Notches

The elements were designed in rows and columns for ease of assembly and positional accuracy. Since these boards would interfere with each other as they cross, notches were cut into the boards as shown in Figure 44.

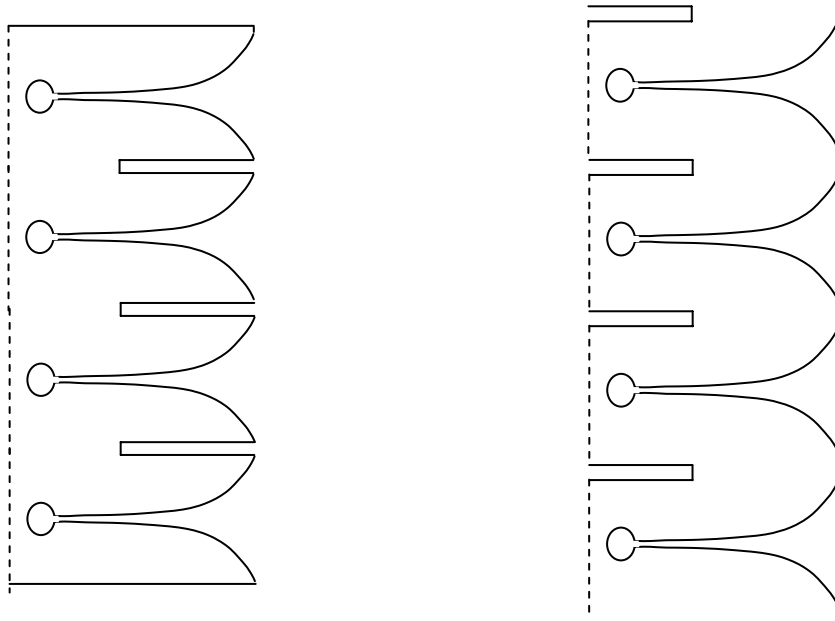


**Figure 4. Notching of Elements**

## 2.5 Notch Element Cross Section (3:1 & 9:1)

The 3:1 notch element has a cross section as shown in Figure 5. The stripline-fed Vivaldi antenna element design is reasonably standard for the required 3:1 bandwidth. The element spacing in the array was chosen to be 0.45 wavelengths at the highest frequency of operation, 18 GHz [7]. Vivaldi antenna arrays exhibit several impedance anomalies when the element spacing exceeds 0.5 wavelengths, and scan performance usually degrades for element spacing greater than 0.45 wavelengths. The desired scan range of the array was 60°.

Arlon AD-250,  $\epsilon_r=2.5$ , was initially selected for the substrate material because it is relatively low cost and has low loss. This was later changed due to manufacturing problems that are described below. The element design utilized a stripline assembly to minimize radiated effects from the transmission line and was fabricated by using two 0.020" boards, total thickness = 1mm. Element depth was not critical and was adjusted for good electrical performance. The stripline design has plated through holes or vias to keep the outer circuit layers at the same potential and suppress parallel-plate and waveguide modes in the dielectric region. Figure 5 is a diagram of the final element showing the feed line placement and approximate location of the vias. The image is not to scale, but is representative of the final configuration.

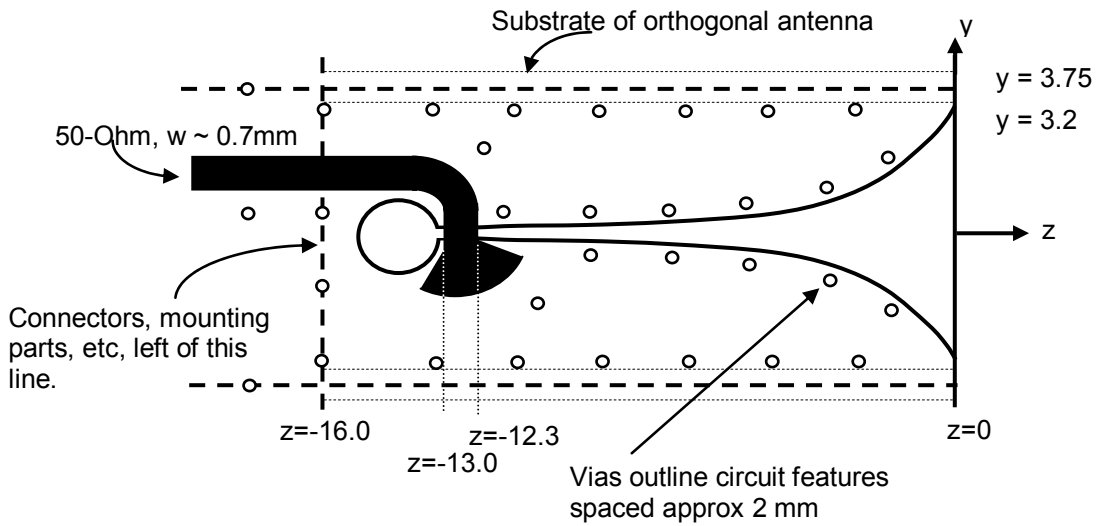
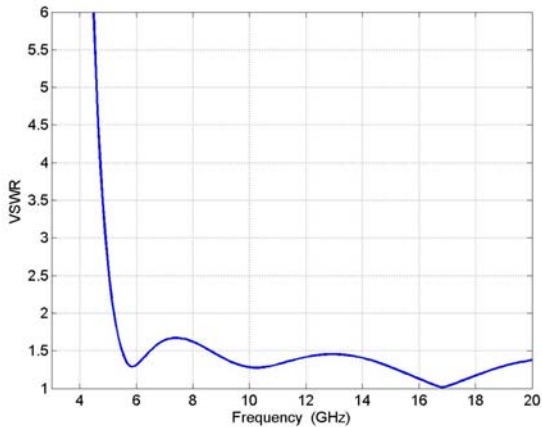


**Figure 5.3:1 Notch Element Cross Section**

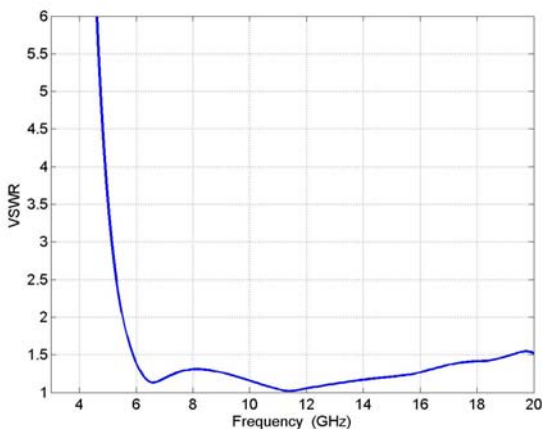
## 2.6 Predicted Results

Initial modeling of the array showed good performance over the design band. The method used for evaluation was active array impedance and VSWR plots. VSWR of the array at broadside angle is less than 1.5 over most of the design band. At  $45^\circ$  incidence angle, both E and H-plane VSWR is also excellent and no anomalous behavior is observed. Figure 6 shows the VSWR plots for broadside and  $45^\circ$  beam pointing angles. Note that all of the simulation results are based on an infinite array simulation so truncation effects are not included in the VSWR simulations. Since the simulation was of an infinite array, no pattern performance was predicted.

SWR for Broadside Beam ( $Z_0=50$ )



SWR  $45^0$  E-Plane Beam



SWR  $45^0$  H-Plane Beam

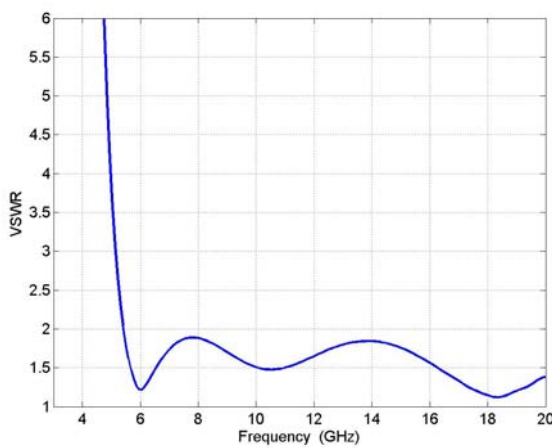


Figure 6. Predicted Infinite Array Results

## 2.7 Active VSWR Finite Array (3:1)

Active VSWR predictions for a finite array were not run. This is due to computational limitations. The very small feed lines of the array would require very small meshing to accurately simulate combined with the electrically large array,  $\sim 7.2$  lambda at 18 GHz, would create a long simulation time. The intent of the array was to demonstrate capability and was intended as a sub-array into a larger array. Therefore, Nurad felt that little was to be gained by simulating the finite array active VSWR.

## 2.8 Active VSWR Infinite Array (9:1)

The 3:1 array was relatively easy to design, and its fabrication and testing provided valuable lessons that were incorporated into that design of an array covering 2-18 GHz. The electrical design of this array was more challenging than the previous array because of the bandwidth requirement. The antenna element resembles the one for the 3:1 design, except it is much longer to operate at the lower frequencies, Figure 7.

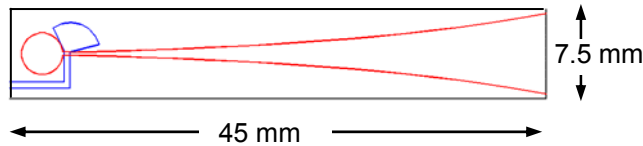


**Figure 7. Sketch of 9:1 bandwidth array element. This sketch is approximately to scale. Actual feed line was fabricated with radius bend instead of square corner**

This element was designed by using full-wave, infinite-array simulations. The predicted VSWR of the element in a large (infinite) array is shown in Figure 8. The predicted VSWR for broadside angle is mostly below 1.5 and the VSWR at  $45^0$  scan is below 2:1 except for a small excursion near 5 GHz.

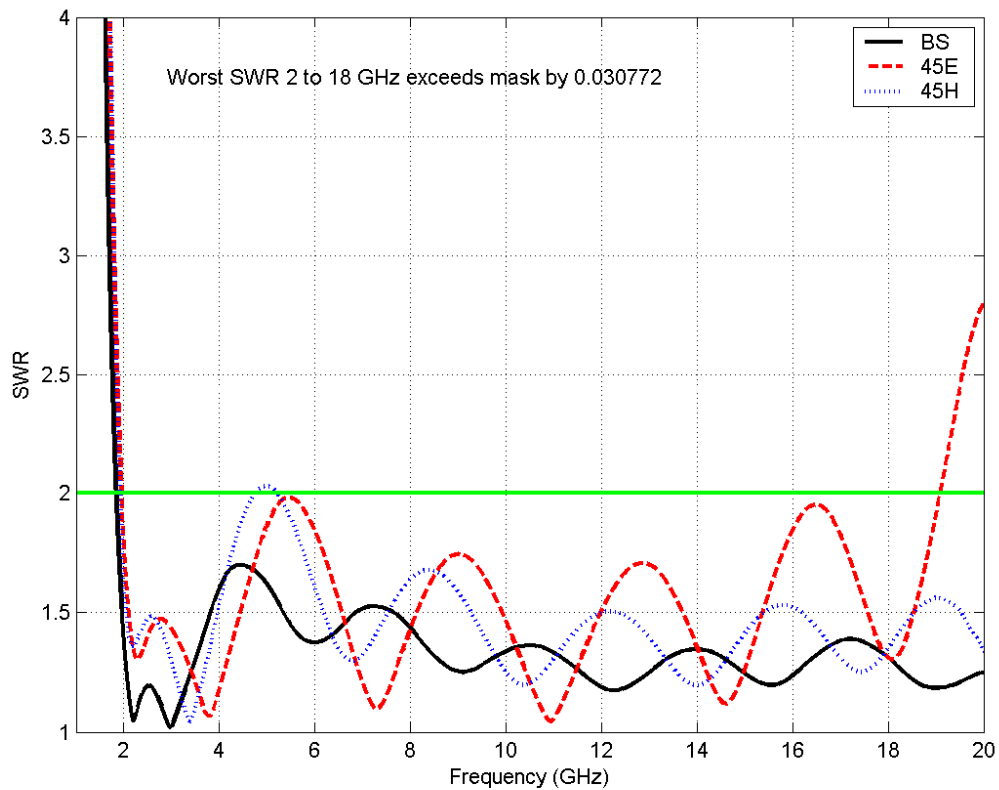


**Figure 8. Predicted VSWR of array designed for 2-18 GHz for three scan angles. Computed at 50-Ohm transmission line that feeds antenna**

The element is fed by stripline comprised of two 0.010" Duroid 5880,  $\epsilon_r=2.2$ , substrates, total element thickness is 0.5 mm. Element spacing is 7.5 mm, the same as the 3:1 array. Vias spaced approximately 2mm outline the element similar to Figure 5.

### **3 FABRICATION & MEASUREMENTS**

#### **3.1 Cross Section Views, Material & Technology**

A view of the CAD design is shown in Figure 9. The boards were notched to allow the orthogonal array apertures to be at the same plane. The design requires the elements to be soldered at the board joints. Due to the frequency range and the resultant spacing of the elements, soldering of the individual elements would be extremely difficult and time consuming. Nurad used edge plating of the slots to allow better soldering between the two circuit boards at the adjacent elements. As it turned out, the contact provided by the edge plating was sufficient to eliminate the need for soldering along the joint. This is only applicable for the lab unit, and would require some type of mechanical attachment on a flight unit.

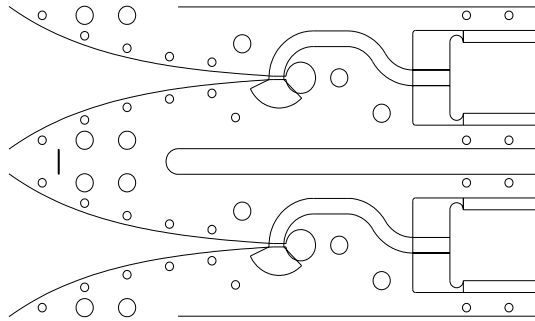


**Figure 9. CAD Model of Element**

#### **3.2 Connectors**

Because the array was to be extensively tested – impedance, coupling, radiation patterns – each element of the array was connectorized. Due to the large number of radiating elements and subsequent number of connectors, simple press-on connections were highly desirable. Simple connection to the circuit board was also required. Based on element size and the space available, SMPM connectors were the best choice. There are many different SMPM connector styles that could have been used for this application; however, the primary drivers were ease of installation and connector location tolerance. Radial misalignment due to tolerance buildup of up to 16 connectors was a concern; therefore a mechanism for alignment of the connectors to the board was important. The selected connector is shown in Figure 10. This type of connector was chosen due to the captive center conductor as well as the connector body protrusion through the board which allows the connector location to be controlled by the circuit board fabrication.



**Figure 10. Connector Type**

### 3.3        8 x 16 Array

A photo of the completed 3:1 array is shown in Figure 21. The radiating direction is up in the picture, with the connectors placed on the bottom. The array was fabricated using two layers of 0.020" thick material laminated together.

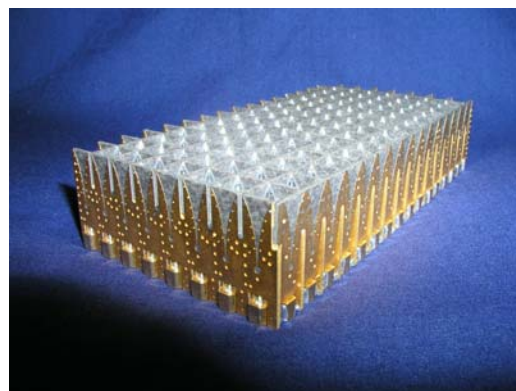


**Figure 21. Completed 3:1 Array**

### 3.4        Assembly Scheme

Notches allowing the orthogonal boards to nest together were cut into each stick. These notch lengths are arbitrary and worked out best from a mechanical layout perspective to be different lengths. For the 3:1 band array, 16 of the short boards and 8 of the long boards would be required to fully populate the array. Figure 32 shows an example of each of the board types. Note that each edge of the notches was plated allowing contact with the orthogonal board.

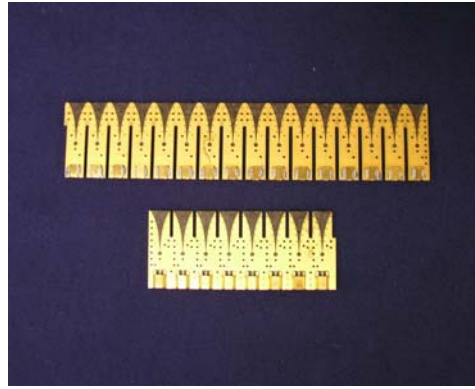


**Figure 32. Stick Array (16 short, 8 long required for array)**

### 3.5 Test Set-up

The initial concept for testing of both the 3:1 array and the 9:1 array was the same. Testing of the array involved fabrication of several fixed phase power divider assemblies. Five discrete power dividers were designed and built for the 3:1 array to provide beam positioning angles of  $0^\circ$ ,  $15^\circ$ ,  $30^\circ$ ,  $45^\circ$ , and  $60^\circ$ , see Figure 43. These power dividers all had a uniform amplitude distribution. To reduce cost, only the  $0^\circ$  and  $45^\circ$  power divider boards were designed and built for the 9:1 array. The idea behind the testing was to measure the radiation patterns in the direction of the power divider array with all surrounding elements terminated in 50 ohm loads. For the 3:1 array (256) connectors, this was done by connectorizing all antenna elements and placing 50 ohm loads on the unused connectors. Both planes could then be measured using the same power divider and rotating it 90 degrees and connecting the center elements to the antennas and terminating the unused elements. The 9:1 array posed a problem. The array size of 128 by 64 elements meant that there would be 16,384 connectors to apply to the array. The number of connectors and associated 50 ohm terminations made the attempt cost prohibitive. Another way needed to be found. Since only the center row and column of the array would be measured for pattern data, only those elements needed connectors. The remaining elements were permanently terminated in matched loads comprised of two 100 ohm surface mount resistors in parallel. Standard pick and place equipment could be used to locate the resistors on the boards.

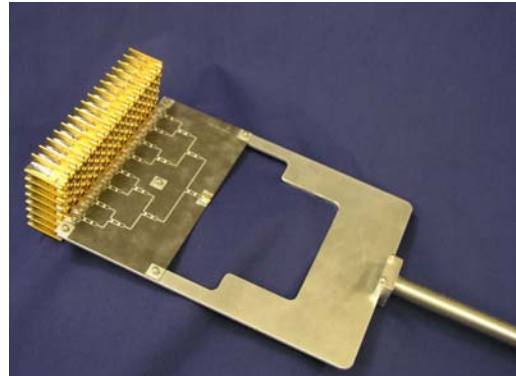


**Figure 43. 3:1 Array with 0° Power Divider**

However, this presented another issue. Due to the width of the finished circuit board (~2.125”), standard pick and place equipment was unable to handle the boards. Since the substrate material is expensive, we did not want to fabricate the boards oversize and then cut to the final width. Nurad overcame this design issue by cutting the boards in half along the length and placing the boards back to back. This required the boards to be joined along the length (64 joints), but allowed automated equipment to apply the approximately 32,000 resistors.

### 3.6 3:1 Array Test Results

Testing of the 3:1 array was to include radiation patterns of a single row, or column, and active VSWR of a single row or column. There were many issues with trying to measure the VSWR of the array. First was that the SMPM connectors do not have a calibration kit for the Agilent network analyzers. This meant that the SMA to SMPM adapter would not be calibrated out of the measurement. For individual element VSWR’s, this was not a problem as the measurement would be representative of the element performance. In order to try and calculate the active VSWR of the array however, the phase between the adjacent elements needed to be known precisely. Several concepts for the measurement technique were considered. None were actually developed though due to the possibility of error in the calibration standards as well as the cost and time needed for development. The concept used was to measure the data for each element and then mathematically generate the active VSWR. Upon taking these measurements and running the calculations, it was determined that the accuracy of the measurements was not adequate to determine the correct value for the active VSWR of the array. Much of the error resulted from the connector mating variability, especially in phase. However, the information provided did show that the modeled data provided a good indication of the performance of the fabricated array.

Pattern measurements for the 3:1 array were run using the fixed phase shifter feed boards. The measurements showed good pattern shape. Patterns for the zero degree phase card and the 45 degree phase card are shown in Figure 54 and Figure 65. Three frequencies,

6, 11 and 18 GHz are overlaid on each pattern. The gain of the patterns is not compensated for the loss of the power divider network. Based on the measurements of the power divider, the power lost in the divider assembly is 5.9 dB at 6 GHz, 12.6 dB at 11 GHz and 16.4 dB at 18 GHz. These values track within the measurement error of the theoretical loss of the divider. Therefore, to determine the gain of the array, without the power divider, the peak gain of the assembly should be added to the loss of the power divider.

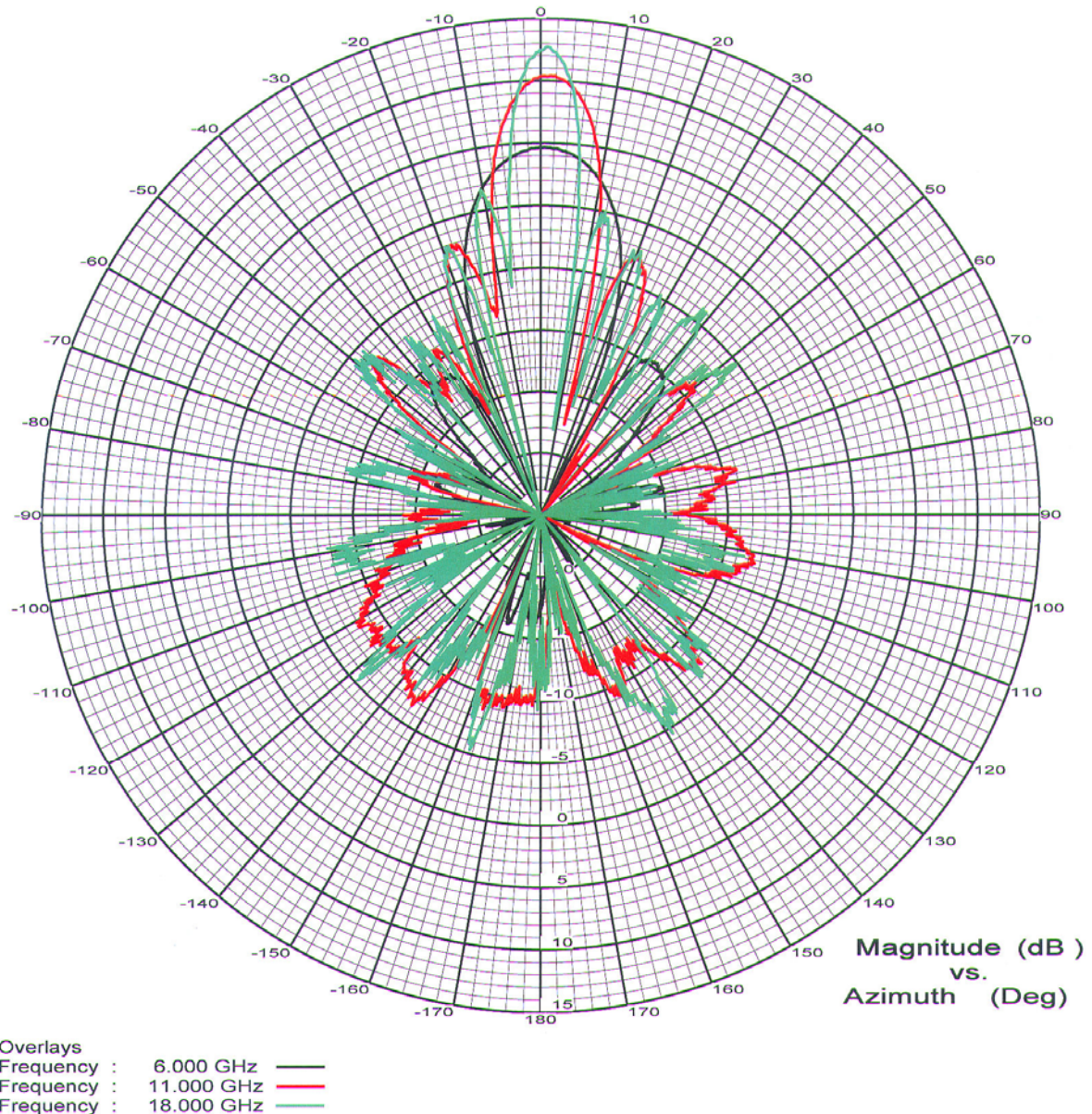


**Figure 54. 0° Card Patterns**

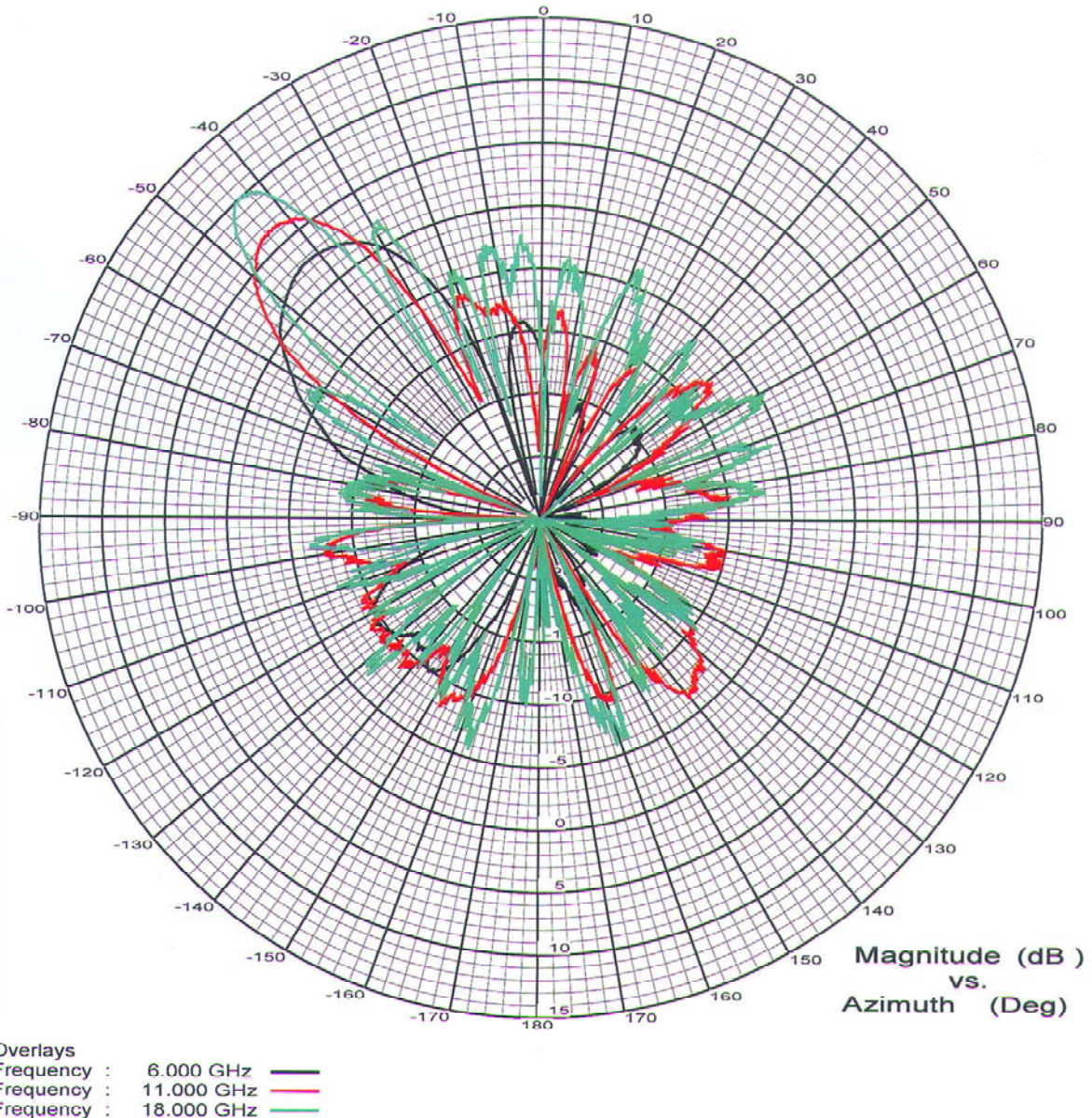


**Figure 65. 45° Card Patterns**

### 3.7 Fabrication of the 9:1 Array

The 9:1 array was intended to be built upon the success of the 3:1 array. The manufacturing processes and materials were initially intended to be the same for both. However, as the 3:1 array was being designed and built it was realized that a variety of issues would make it difficult to build them the same. Due to the increased frequency band, the antenna boards needed to be thinner than on the 3:1 array. A positive of using the thinner board was a reduction in the material cost for the antenna array; however, the

thinner boards caused several issues. Two 0.010" thick boards are sandwiched together to make the final antenna board. The connector mounts on the top surface of one of the boards, which is halfway through the laminated assembly. The method of fabrication requires the pocket to be machined after lamination. The pocket is only 0.010" deep and the copper cannot be milled off of the board, making depth control critical.

Unfortunately, the board flexes due to the thickness causing the pocket milling to be very difficult. In addition, the thin boards change dimensionally due to the heating and cooling required during processing. This caused other issues with the placement of the plated through holes. This dimensional change is random in nature and even changes in different areas of the same board. This challenge was overcome by the incorporation of targets etched onto the board during fabrication. These targets were then used to scale the locations for the plated through holes rather than using the CAD file to determine the locations. The end result is that each board is very slightly different from all others due to the unique shrinkage of the material used for fabrication. However, while the resolution to the problem is a great engineering solution, the customized nature of each board has a considerable cost impact.

Nurad worked all of the issues out for the fabrication of the 9:1 antenna array. The manufacturing process was proven by fabrication of one of each of the different board types required for fabrication. However, due to the cost of fabrication and the large number of boards required for the 9:1 array the development effort was placed on hold.

#### 4 CONCLUSION

Two different broadband phased array antennas were designed and built. The 3:1 array was characterized as both individual radiating elements as well as patterns using fixed power divider assemblies. The 9:1 array CAD design was straightforward and based on the successful measurement to prediction correlation of the 3:1 array provides confidence the measurement of the larger antenna would also be successful. A number of challenges were identified and overcome in the design, layout, material selection and fabrication of the antenna array.

#### References

- [1] H. Holter, T-H. Chio and D.H. Schaubert, "Experimental Results of 144-Element Dual-Polarized Endfire Tapered-Slot Phased Arrays," *IEEE Trans. Antennas and Propagat.*, vol. 48, pp. 1707-1718, November 2000.
- [2] N. Schuneman, J. Irion and R. Hodges, "Decade Bandwidth Tapered Notch Antenna Array Element," *Proc. 2001 Antenna Applications Symposium*, pp. 280-294, September 2001, Monticello, IL.
- [3] J. Shin and D.H. Schaubert, "A parameter study of stripline-fed vivaldi notch-antenna arrays", *IEEE Trans. Antennas & Propagat.*, vol.47, pp. 879-886, May 1999.

- [4] Tan-Huat Chio and D.H. Schaubert, “Parameter study and design of wide-band widescan dual-polarized tapered slot antenna arrays”, *IEEE Trans. Antennas & Propagat.*, vol.48, pp. 879-885, June 2000.
- [5] S. Kasturi and D.H. Schaubert, “Effect of Dielectric Permittivity on Infinite Arrays od Single-Polarized Vivaldi Antennas,” *IEEE Trans. Antennas & Propagat.*, vol. 54, pp. 351-358, February 2006.
- [6] H. Holter and H. Steyskal, “Infinite Phased-Array Analysis Using FDTD Periodic Conditions – Pulse Scanning in Oblique Directions,” *IEEE Trans. Antennas & Propagat.*, vol. 47, pp. 1508-1524, October 1999
- [7] C. A. Balanis, “Modern Antenna Handbook”, Chap 12, Wiley, 2008



Roos Instruments

## Active Electronically Scanned Array Radar Module Test



# Active Electronically Scanned Array Radar Module Test

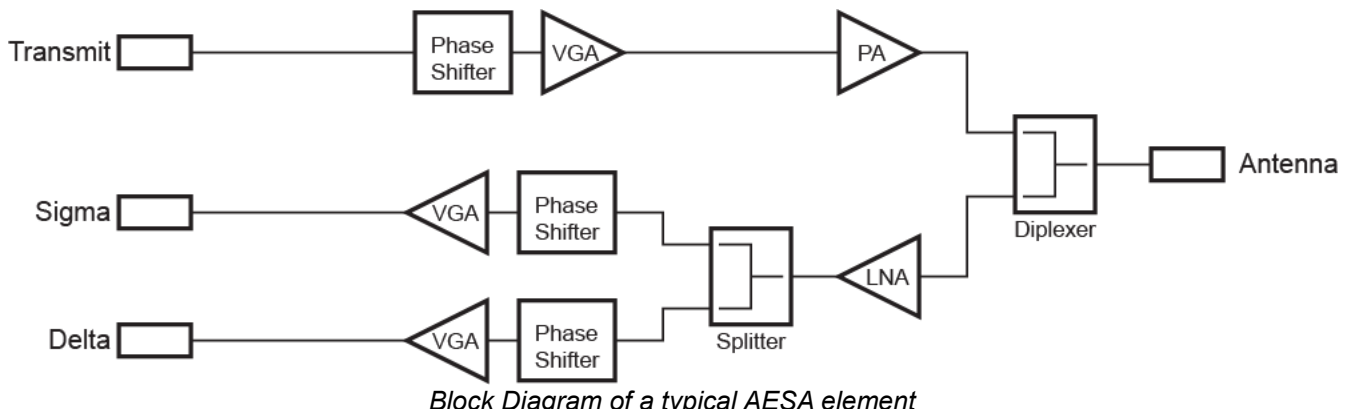
The architecture of Roos Instruments' Cassini High Speed Precision RF & Microwave Automated Test Equipment (ATE) system delivers exceptional value in the production testing of Active Electronically Scanned Arrays (AESA), also called Active Phased Array Radar, for both aircraft and shipboard programs.



Thales APAR on a Dutch LCF De Zeven Provincien class frigate

Image source: Royal Netherlands Navy / Koninklijke Marine

gain amplifiers. The interaction of these components at each of their respective control states must be measured, checked against valid limits, and calibration data stored to control the electronic steering of the antenna's focused beam. Depending on the design, this typically encompasses thousands of individual measurements.



Block Diagram of a typical AESA element

The accuracy required for measuring multiple states in each module is frequently only a few tenths of a dB and a few degrees of phase. The module is combined with a fixture interface that quickly switches the many signal paths to the required instrumentation and provides reliable connections to the module. The added losses, mismatches, and side effects in the fixturing interface must be characterized and removed from the final module test results. To accomplish this task, S-parameter vector measurements and advanced calibration techniques are used to calibrate and mathematically remove errors of the fixture. The vector math allows a complete model of the actual measurement to be made in software. Due to the accuracy required, complexity of the math, and the calibration techniques needed, typical ATE systems are not up to the task.

# Active Electronically Scanned Array Radar Module Test

A "rack & stack" measurement system could be designed that uses accurate bench test equipment to overcome the measurement accuracy issues, but the test time for a rack & stack solution would range from several hours to a few days for each module, depending on specific requirements. Therefore, a rack & stack system is not a viable or cost effective solution for volume production.

Roos Instruments brings 20 years experience to RF module test. In 1989, RI developed a production test solution for the US government focused on accuracy and repeatability for monolithic microwave integrated circuits. RI leverages that technology to create economical solutions for production level testing of AESA modules and packages.

RI's latest generation test systems feature highly configurable hardware and software combined with integrated vector calibration technology to deliver the fastest and most accurate systems available today.

- Single Channel Receiver is used for coherent measurements to provide exceptional repeatability.
- Compiled Vector Calibration ensures accuracy on multiple ports.
- Extendable Calibration all the way to the device ports ensures accuracy at the DUT.
- Graphical User Interface simplifies test plan development.

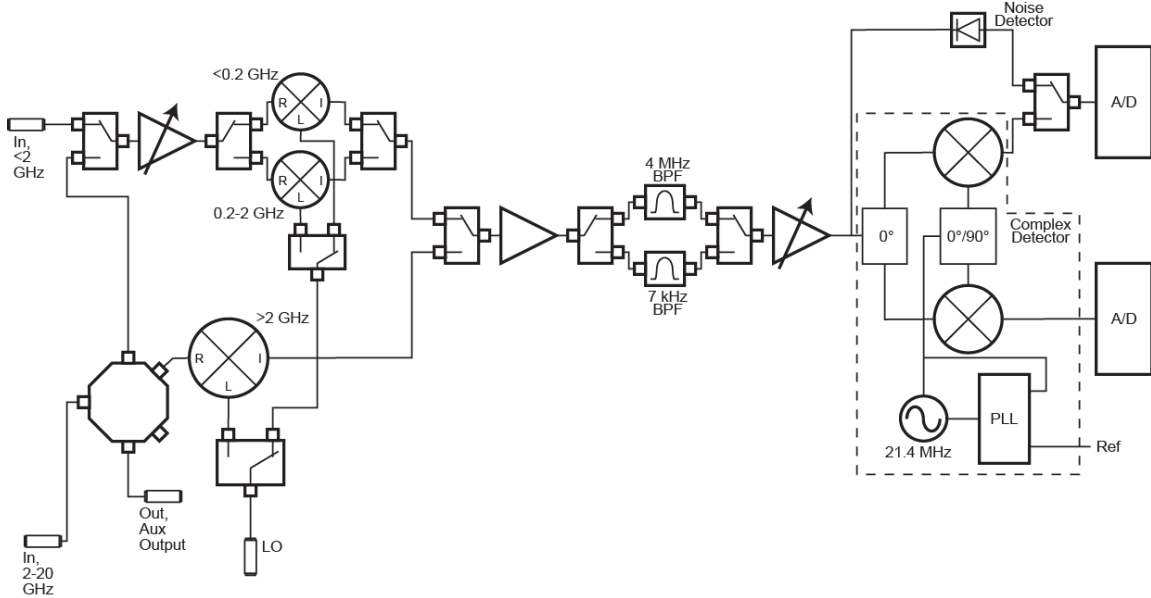


*RI's latest generation ATE systems provide unequalled configurability while maintaining speed and accuracy*

RI hardware is designed to be highly reliable, tolerant to temperature fluctuations, and extremely fast. Other test solutions must constantly calibrate to remove the drift factors, but RI has been successful in minimizing them. As a result, RI engineers are able to use a simple block diagram to produce accurate models that consistently produce the highest possible measurement speed while still maintaining accuracy. This innovative system architecture allows a flexible combination of graphical software user interfaces and standard hardware device interfaces.

RF measurements are made with a single channel vector receiver that uses advanced computing power of the system controller to translate those direct measurements into the desired scattering parameters, power measurements, or noise measurements. Vector S-parameter measurements are executed extremely fast and with high accuracy using an innovative time reference approach with the single channel receiver. This design eliminates the need for extensive error correction in matching two sets of I & Q demodulators. Normally, S-parameters ratios are typically measured with two receivers that must be matched perfectly in order to make the same accurate measurements RI does with a single channel. Any small drifts due to time or temperature are canceled out by common mode rejection.

# Active Electronically Scanned Array Radar Module Test



*The RI vector receiver can make up to 80,000 complex voltage measurements per second*

The simplified hardware is under direct control of the software instead of cascading layers of firmware found in off-the-shelf bench instruments. A low overhead command and control interface replaces the commonly used GPIB bus to enable fast communication with the sources, switching and measuring devices. The incredible processing power of modern PC hardware is used to calculate the desired result from the raw measurement data.

A typical Active Array Radar Module manufacturer will be able to accurately measure their modules while dramatically reducing their test time. Actual test time reductions of up to 420% have been seen in previous applications. For example, a five hour test time using bench equipment can be reduced to only seven minutes with RI ATE. The US government was looking for a single order of magnitude improvement to make Active Array Radar Module testing an economic reality and RI delivered over 4 orders of magnitude improvement in test time!

RI's ability to make accurate relative phase and amplitude measurements on multiple RF & Microwave ports makes the production process of Active Array Radar Modules economically feasible. Our single channel receiver design combined with an extensible, all inclusive, calibration technique increases the repeatability by using the same receiver for coherent measurements and increases the accuracy with multiple port vector calibrations. Our latest generation of RI test solutions helps our customers dramatically reduce cost and test time.

Make sure your program is using an RI Microwave ATE system for lowest life cycle cost and highest precision measurement throughput available!

Contact Roos Instruments, Inc. at 408-748-8589, at [Sales@roos.com](mailto:Sales@roos.com) or visit our web site at [www.roos.com](http://www.roos.com)



# F/A-18 & EA-18G Program

Capable, Affordable & Joint Interoperable...Today & Tomorrow



CAPT "BD" Gaddis  
F/A-18 Hornet & EA-18G Program Manager  
24 April, 2007



# Key Messages

**F/A-18E/F Super Hornet:** It's the most capable, affordable, and effective multi-mission fighter-attack aircraft in the world. It will fly and fight from carrier flight decks thru 2030.

The F/A-18E/F and EA-18G, and its advanced sensors, pinpoint targeting, computing and connectivity capability, and precision weapons, has already started to transform the way Navy fights (e.g. AAW, ASUW, NTISR and TST).

Next generation capability -- cooperative, multi-moving, and multi-spectral targeting, Combat ID, IP-based networking, and networked enabled weapons -- is on the F/A-18E/F Super Hornet & the EA-18G Growler “Flight Plan.”



# Navy Carrier Strike Groups & F/A-18 Hornets

- Carrier flight decks are now filled with Hornets, Super Hornets and USMC F/A-18A+ only
- Production continues 3 months ahead of schedule
- “Flight Plan” in place to ensure Super Hornet paces the threat past 2024
- Super Hornets will fly and fight from carrier flight decks until 2030
- Long term support in place
- Long term complement to F-35 LITENING II Strike Fighter



The F/A-18E/F is the key element of the USN's long-term force structure



# The Multi-Mission Super Hornet Flexible Air Power

**Survivability:** IDECM Block 2 & ALR-67 (V)3  
ALQ-214 and ALE-50/55



Towed decoy



Air-to-Ground  
Close Air Support



Road RECCE mission



JDAM 500  
JSOW  
GBU-24B/B  
GBU-16  
GBU-32  
BRU-55  
HARM  
HARPOON  
SLAM\_ER

Digital network connectivity (MIDS L16 and DCS radio with VMF)

Unprecedented multi-mission flexibility...  
First day of the war capable and everyday thereafter



## Advanced Crew Station (ACS)

- Advanced Situational Awareness
- 8x10 Large Display

All-Weather Precision Attack  
Air Defense Suppression



Active Electronically Scanned Array (AESA) Radar



JHMCS  
(front and aft seat)



Unprecedented multi-mission flexibility...

First day of the war capable and everyday thereafter

Air Dominance  
Electronic Attack

OCA/DCA

CMD

NTISR

## Advanced Computing Architecture

F414-GE-400  
Time-on-wing >600 hr



Advanced mission computer

- Open architecture, portable, scalable
- HOL/C++ OFP
- Commercial SEE
- Fiber channel switch/OI



## Digital solid state recorder

- COTS
- Annotated Image Transfer
- JMPS compatible

Fighter Escort

Tanker

Air-to-Air



IR Search & Track Pod

AIM-9  
Sidewinder  
AIM-120A/B/C  
AMRAAM



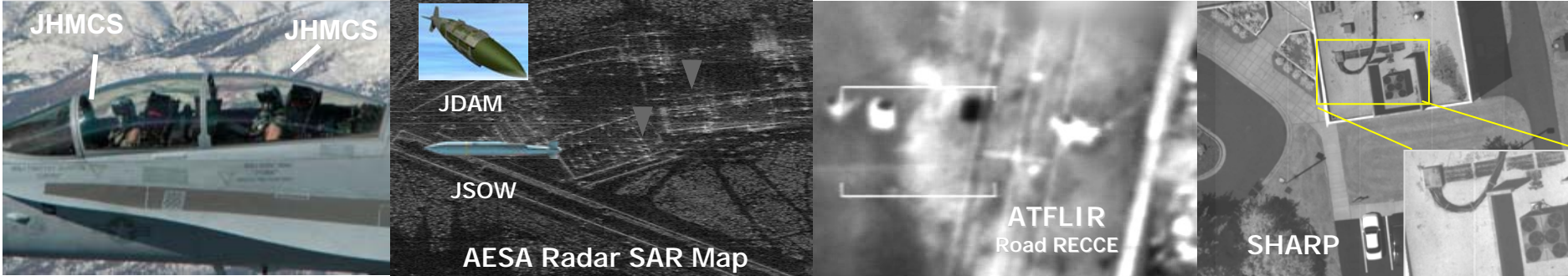
Reconnaissance



Tanker



# Super Hornet Links the Power of the Network to the Warfighter



## AIRCRAFT SENSOR INTEGRATION



DCS/VMF  
nine-line brief



MIDS/L16



ATFLIR VIDEO DATA LINK



SHARP DATA LINK

## CONNECTIVITY PATHS



E-2D



SOF



Ground Station  
(CAOC)



F-15



Rover III



Carrier  
Strike Group



# F/A-18E/F "Flight Plan" Next Generation Capability Paces the Threat

POM08/PR09

POM10

POM12

POM14

## Distributed Targeting

Onboard Geo-Registration      Multiple Movers      Combat ID  
IRST      Distributed Targeting Processor

## Sensor Integration

Electronic Surveillance      Electronic Attack      Combat ID Fusion  
Cooperative Targeting      Emitter Geo-Location

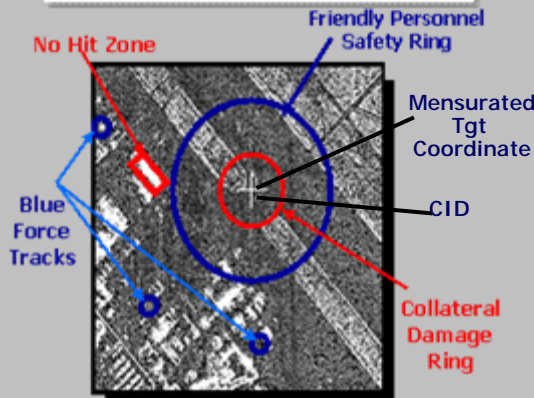
## Airborne Networking

Mode "5" IFF      MIDS-JTRS w/TTNT      Network Applications & Services      SATCOM  
UAV Connectivity

## New A/A and A/G Weapons Integration

Networked Enabled Weapons      AMRAAM HOBS      Dual Mode Weapons

## Information Superiority on the Battlefield



Real Time Information In and Out of the Cockpit



## Developed with Open Architecture Principles

- Modular Design
- Reusable Application Software
- Life Cycle Affordability

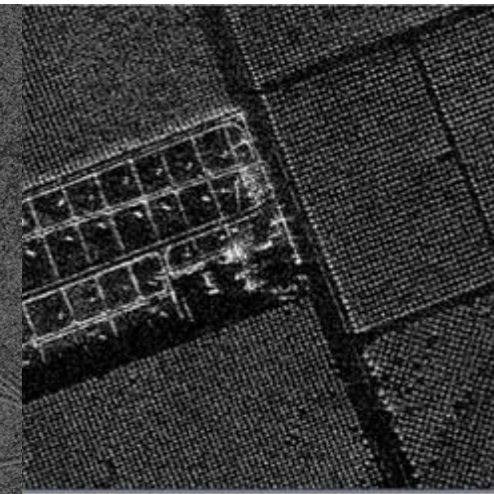
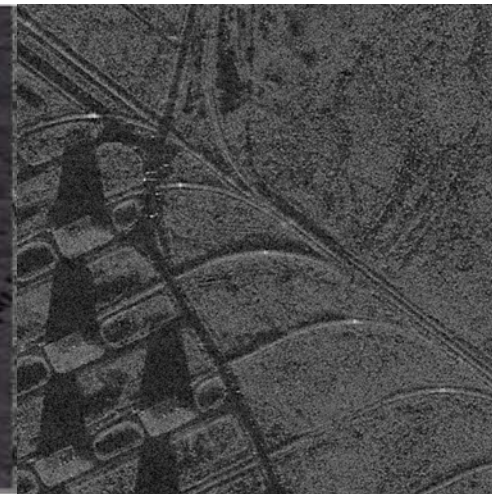


# AESA Radars in Production

## Beginning Full Rate Production in 2007

### Facts and Figures

- First Fleet deliveries began in Jan '06
- First fleet introductions complete!
- First AESA equipped squadron already flying today – VFA-213
- (31) AESA equipped aircraft currently in the Fleet
- (84) APG-79 radars already on order
- Over 5000 Flt Hrs in Fleet & Test
- VFA-213 deploys in 2008



The high resolution APG-79 is changing the game for the warfighter



# AESA/JDAM/Link 16

## Precision Strike Capability Over the Network

F/A-18E/F  
AESA SAR  
map and  
aircrew  
designated  
targets

Target designation  
received by  
AESA aircraft  
via Link16

Major component of NCO  
strategy roadmap

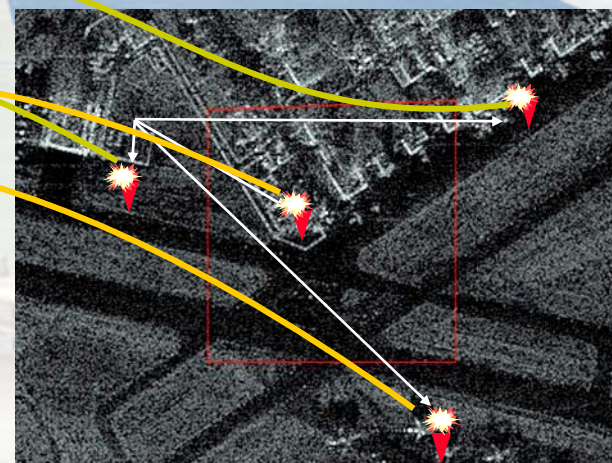


Link 16

Link 16

- AESA precision self-targeting thru the weather in a networked environment
- Integrated weapon system performance
- AESA is a force multiplier
- Thru link 16 network and future networks all joint forces have AESA capability

- Targeting coordinates sent over MIDS from AESA aircraft to non-AESA strike aircraft
- Multiple target attack in single pass
- Machine-to-machine targeting
- High volume precision fires



All four MK-84 JDAM hit their targets  
well within specification limits



# ATFLIR



- Long-range, high resolution sensor for positive target identification and accurate targeting with high power laser
- Geo-Point accuracy for self-targeting with precision weapons delivery
- High Resolution sensor for Non-Traditional Intelligence Surveillance Reconnaissance in support of ground forces
- Integrated with AESA and APG-73 Radar, JHMCS, MIDS, and Solid State Recorder
- Imagery sent to ground forces thru aircraft data link to Rover III with streaming video, annotated imagery transfer over Link 16, or digital radio with 9-line brief



Rover III  
Streaming Video To JTAC



Link 16 Image Transfer  
- Fielded -



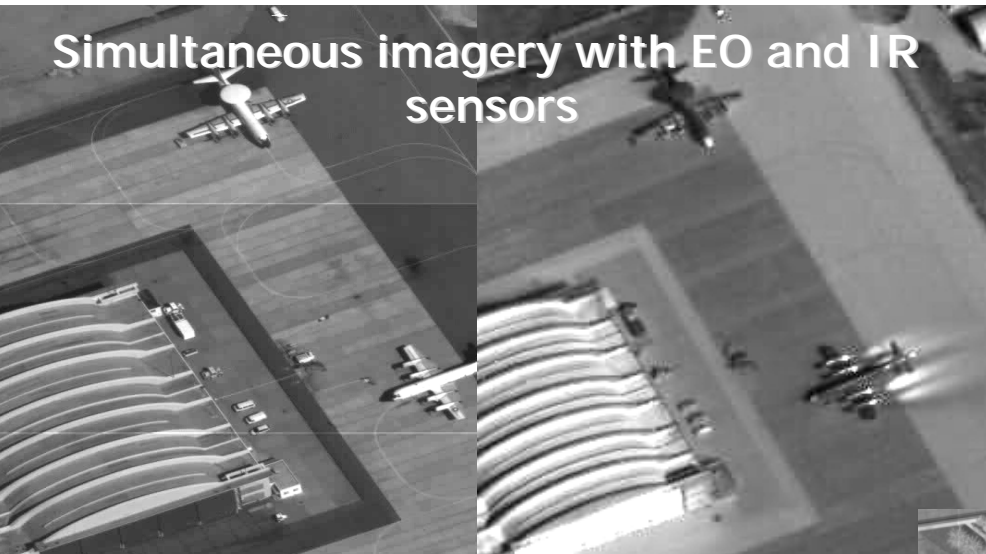
VMF Image Transfer - Fielded





# SHARP Recon Pod with Common High Bandwidth Data Link – Deployed in OIF II

Simultaneous imagery with EO and IR sensors



Simultaneous data link down to multiple ground stations (e.g. Navy CVN, Army TES-F, Marine Corps TEG)





# F/A-18E/F Sensor Integration

AESA SAR



ALR-67(v)3



SEID



Geo-Locate



- ALR-67(V)3 antenna coverage enables 360° geolocation

## Targeting Options:

- HARM/AARGM
- Georegistration of mensurated target coordinate
- JDAM
- JSOW Target Template
- HGEA w/ALQ-214 & AESA (POM10)

AESA APG-79 High Gain  
ESM in FWD Sector at  
for greater ranges



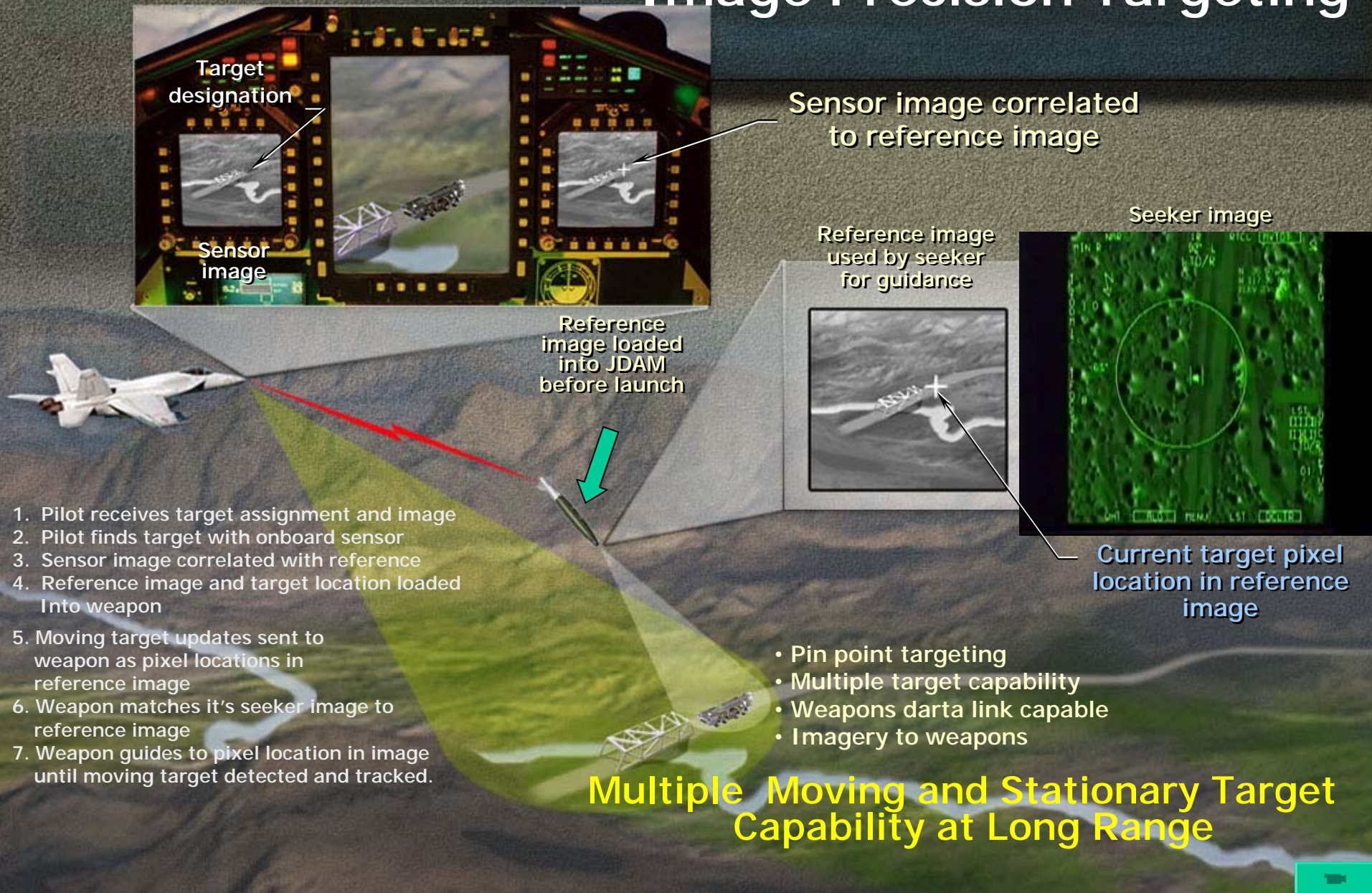
Faster and more accurate target location sufficient for:

- Data made available to EOB Enterprise
- Reduces ambiguity and increases precision
- Threat situational awareness
- Targeting for SEAD (HARM, AARGM)

## Sensor Integration Roadmap

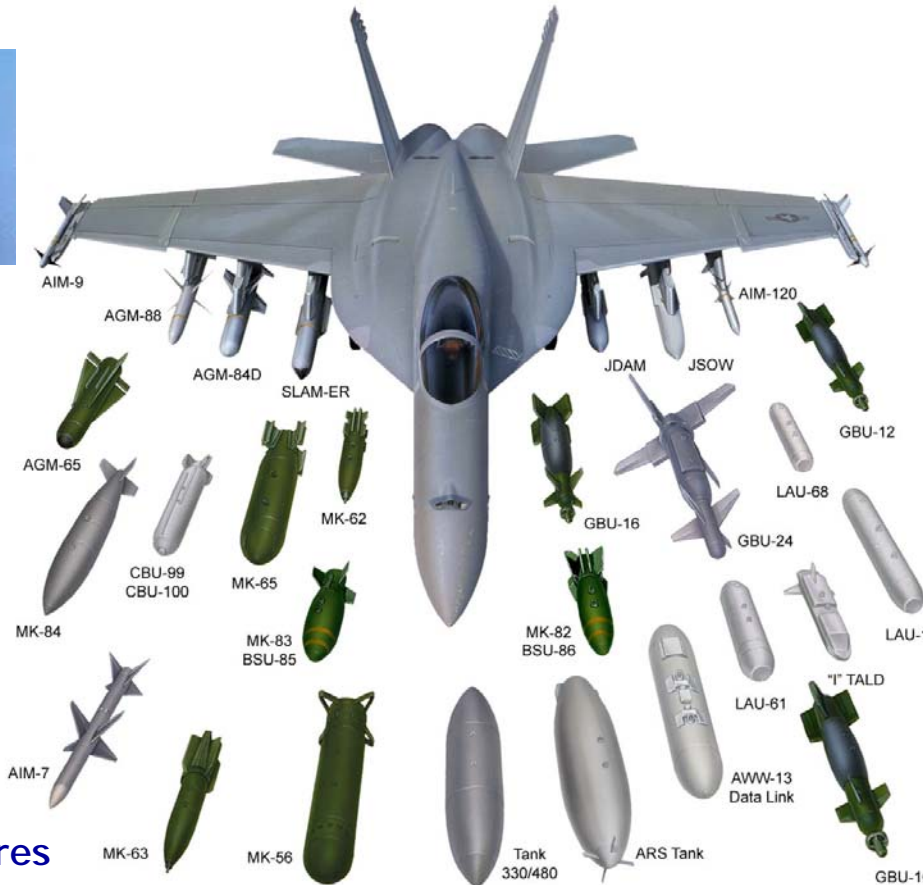
- Digitally cued ALR-67(V)3 receiver
- AESA and ALR-67(V)3 integration
- Specific Emitter Identification
- Single Ship Geolocation
- Multi-ship Geolocation
- ELINT recording

# Air Interdiction Image Precision Targeting





# Large Payload Capability and Multi-Mission Flexibility



Precision weapon delivery  
Survivability  
Advanced countermeasures



High Volume Precision Fires  
Largest Payload, Significant Mission Flexibility

AIM-9X



SLAMER



JDAM

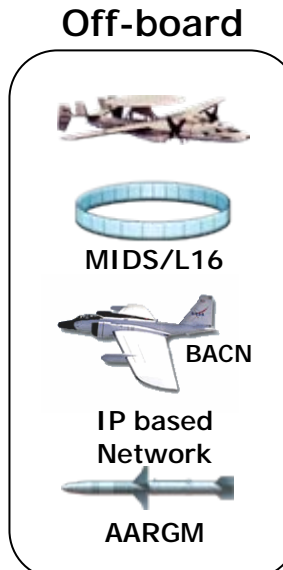
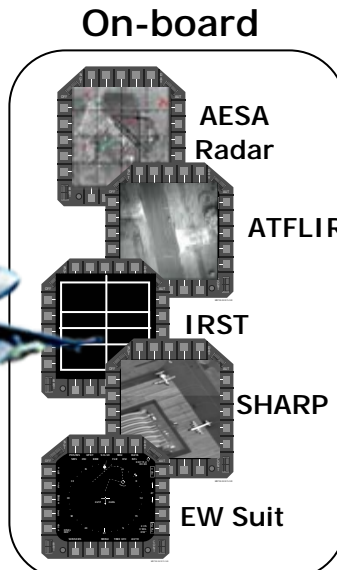


NAV AIR



# Multi-Source Integration - Sensor Fusion & Combat ID -

Multi-source integration enhances situational awareness for increased lethality and survivability

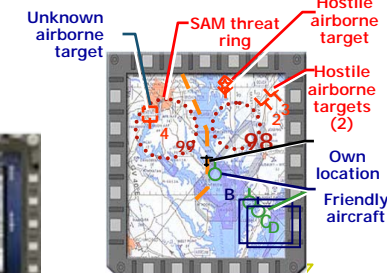


A/A, A/G and Maritime MSI

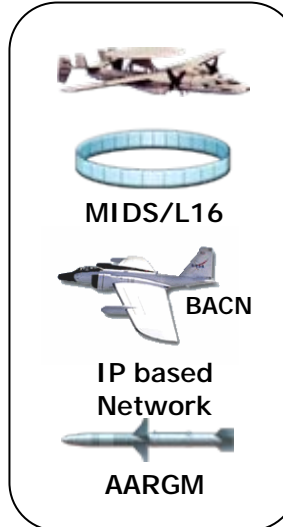
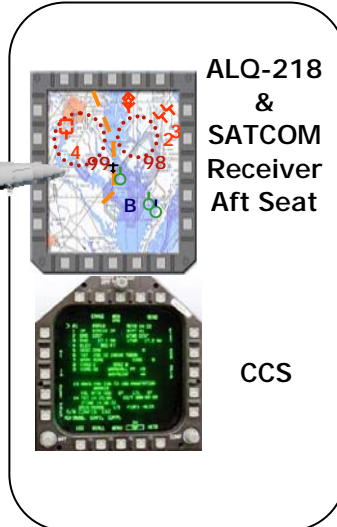


Front Seat Cockpit

Knowledge-Based SA & Targeting



Aft Seat Cockpit

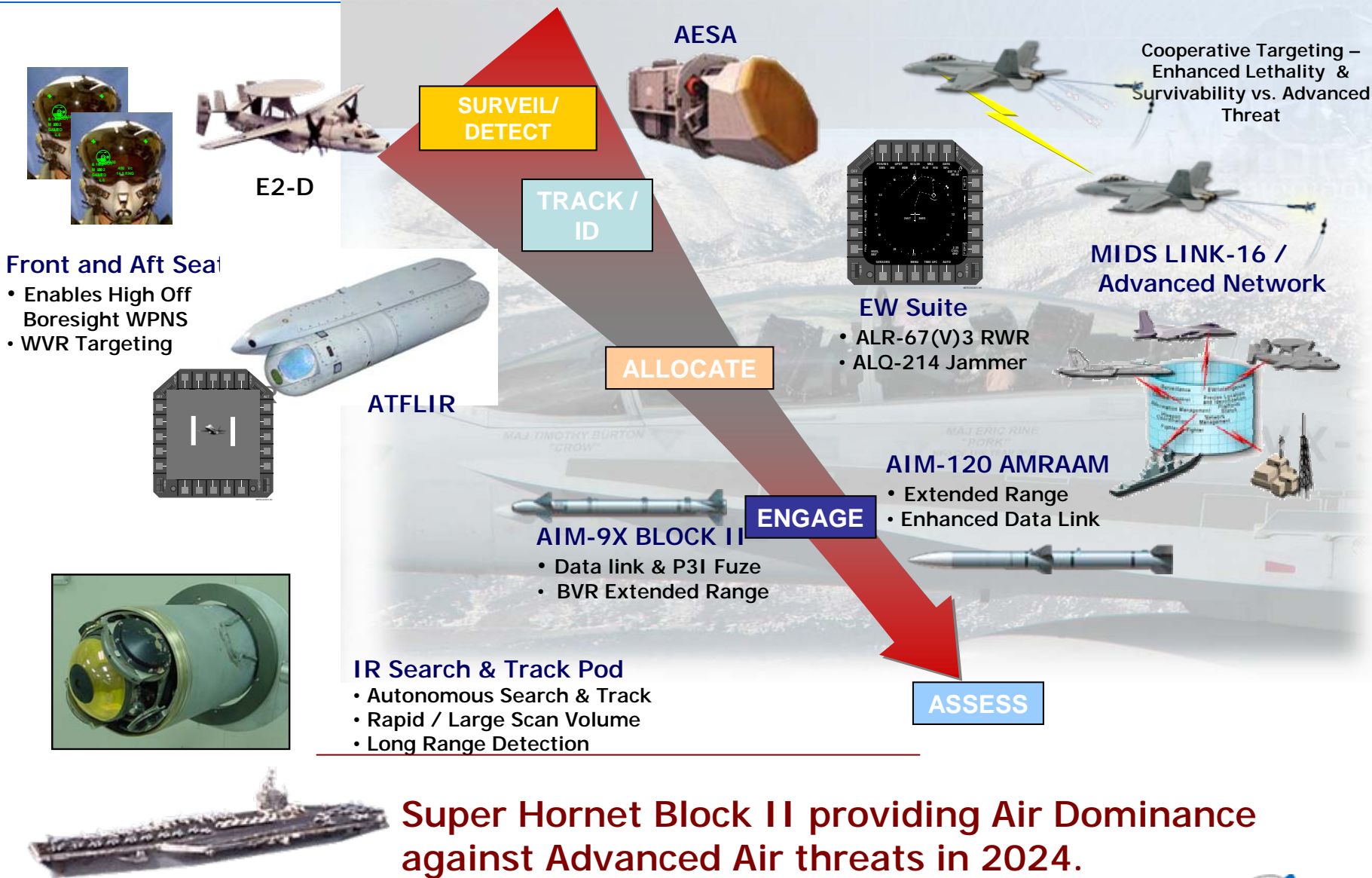


## Warfighting Capability:

- Pinpoint target location error for land and maritime targets
- Combat ID from multiple onboard and offboard sources
- Employment of longer range, precision weapons
- Engagement of Stationary and Moving Targets
- Common Operational Air Picture



# Multi-Spectral Air Dominance



# Vision



UAV's are destined to become  
the next evolution of the  
worlds air combat forces.



The integration between  
manned and unmanned systems  
will be the first step in meeting  
those future systems, today.



# Questions?



**PRIORITY:**

**"Build a Fleet for the Future"**

*... balanced, rotational, forward deployed, and surge capable – the proper size and mix of capabilities to empower our enduring and emerging partners, deter our adversaries, and defeat our enemies"*

*- CNO (CNO Guidance 2007)*

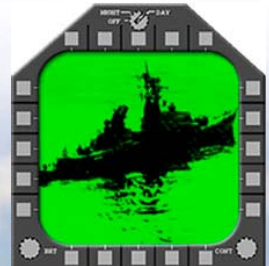


# Anti-Surface Warfare

## AESA Sea Surface Search (SSS)



Optimized for the  
Maritime Mission



"Flight Plan" includes  
capability for Maritime  
MSI and ID



Search



Track

- Cooperative Targeting
- Long Range Detection and Track
- Precision targeting of small vessels in sea clutter

- Network Enabled Weapons
  - HARPOON Block III
  - SLAM-ER
  - JSOW-C

---

**Sea surface search mode detects surface ships at long range in any weather**



# F/A-18E/F Balanced Approach to Survivability

## EFFECTIVENESS



## SURVIVABILITY

Hard to See, Hard to Hit, Hard to Kill



# Joint Interoperability and Networking

## Multiple Platforms



The platform must seamlessly move its sensor and weapon information on/off the aircraft, then into and across a joint, networked Battle Space

Information Superiority achieved in a machine-to-machine environment ensures distributed sensors on the tactical edge of Battle Space deliver combat power from the right platform, at the right time with the right weapon

### Information flow thru/into Battlespace

- |   |   |   |
|---|---|---|
| <ul style="list-style-type: none"><li>• COTP</li><li>• BHI</li><li>• Onboard Mensuration Coordinates</li><li>• BFSA</li></ul> | <ul style="list-style-type: none"><li>• Images</li><li>• Streaming Video</li><li>• Electronic Order of Battle (EOB)</li><li>• Surface Picture</li></ul> | <ul style="list-style-type: none"><li>• CID:</li><li>• Fixed Target</li><li>• Moving Targets</li><li>• Single and Multi-ship Geo-locate</li></ul> |
|---|---|---|



Radar &amp; Advanced Targeting

## MULTI-MODE SURVEILLANCE RADAR

Osprey MM multi-mode surveillance radar provides second generation Active Electronically Scanned Array (AESA) surveillance capability as the primary sensor on airborne assets to meet the challenges of the 21st century.

Osprey MM AESA radars are at a high technology readiness level (TRL) and are in production for fixed and rotary wing applications. Osprey MM's forerunners, the mechanically scanned (M-Scan) and first generation AESA Seaspray radars have been delivering a high performance surveillance capability to armed forces and paramilitary users for more than 45 years. Osprey MM brings together wide azimuth and elevation electronically scanned (E-Scan) fixed antenna(s) with a compact, state-of-the-art Processor and multi-channel Receiver.

### KEY BENEFITS

- Class-leading maritime surveillance capability
- AESA-enabled small target mode (STM)
- Very high resolution, wide swath SAR Mapping
- Small radar cross section (RCS), low minimum detectable velocity (MDV), multi-channel moving target indication (MTI)

- Air-to-Air surveillance, track and intercept
- Instantaneous multiple mode interleaving
- Difficult target detection from high altitude
- High reliability for persistent operations
- Flexible configuration, installation and integration
- Multiple fixed antennas, choice of antenna sizes
- Belly-free, obscuration-free 360° coverage
- Open standards interfaces
- Compact, lightweight LRUs.

### KEY FEATURES

Osprey MM provides a genuine multi-domain capability, with high performance sea surveillance, notably against 'difficult targets', land surveillance with wide swath, very high resolution ground mapping, small and low speed ground target indication, high performance air-to-air surveillance, tracking and intercept.

These capabilities, combined with the radar's ability to rapidly interleave modes and provide scan-independent beam steering, make Osprey MM ideally suited to mixed environment operations, such as in the littoral.

# OSPREY MM

Osprey MM is a low size, weight and power (SWaP) radar system, offered with a range of antenna sizes that may include up to four fixed antennas, depending on the azimuth coverage requirement, and which leave the belly of the aircraft free for operation to and from unprepared surfaces; or for other antennas, sensors or weapon systems.

Osprey MM is particularly well suited to unmanned air systems (UAS) operations, with very high reliability for persistent surveillance, and difficult target detection capability from high altitude, facilitating platform line of sight (LoS) communications and improved platform fuel efficiency.

Osprey MM's flexible configuration, with antenna size and installation options, its low SWaP, air cooled line replaceable units (LRU), and its open standard interfaces all simplify its integration.

## Technical Specification

### CHARACTERISTICS

Frequency	X-Band
Scan coverage	Installation dependant
Maximum range	200NM
Mean Time Between Critical Failure (MTBCF)	>2000 hours
Cooling	Unconditioned air
Weight (Approx. installation dependent)	28kg/62lbs (Single Antenna, Processor and Receiver LRUs, and IMU)
Interface standards	Ethernet, RS422, ARINC 708, ARINC 429
Video outputs	Multiple options for Mission System and cockpit display compatibility

### DIMENSIONS (H X W X D APPROX.)

Processor	200x125x230mm (8x5x9 inches)
Receiver	206x255x175mm (8x10x7 inches)
Antenna	200x510x140mm (8x20x6 inches)

### FUNCTIONS

Track While Scan	Up to 1000 tracks, with Automatic Track Initiation (ATI)
Track Identification	AIS and Inverse Synthetic Aperture Radar (ISAR)
Mode Interleaving	Simultaneous multi-mode operation

### CAPABILITIES

Maritime Surface Surveillance	Maritime surveillance Small target mode
Strip and Spot SAR Ground Mapping	High resolution wide area ground mapping
Moving target detection	Ground, Maritime and Air MTI Air-to-Air Intercept
Navigation	Land mass discrimination
	Weather detection
	Turbulence detection
Beacon detection	Search and Rescue Transponder (SART)
Target imaging/classification	ISAR
	Range profiling

## Performance Benefit of AESA Radar

E-Scan enables simultaneous multi-domain wide area search and Target of Interest (ToI) focus, and ultra-fast beam scanning to provide vastly improved clutter cancellation and superior detection performance. This performance is maintained from high altitudes typically encountered by UAS operating at the full extent of LoS data links.

## Superior Reliability and Operational Availability

At the core of the AESA radar design is the ability to tolerate individual element failure. Component failures within the array result in graceful performance degradation rather than complete system failure, delivering high operational availability when compared with conventional radar systems.

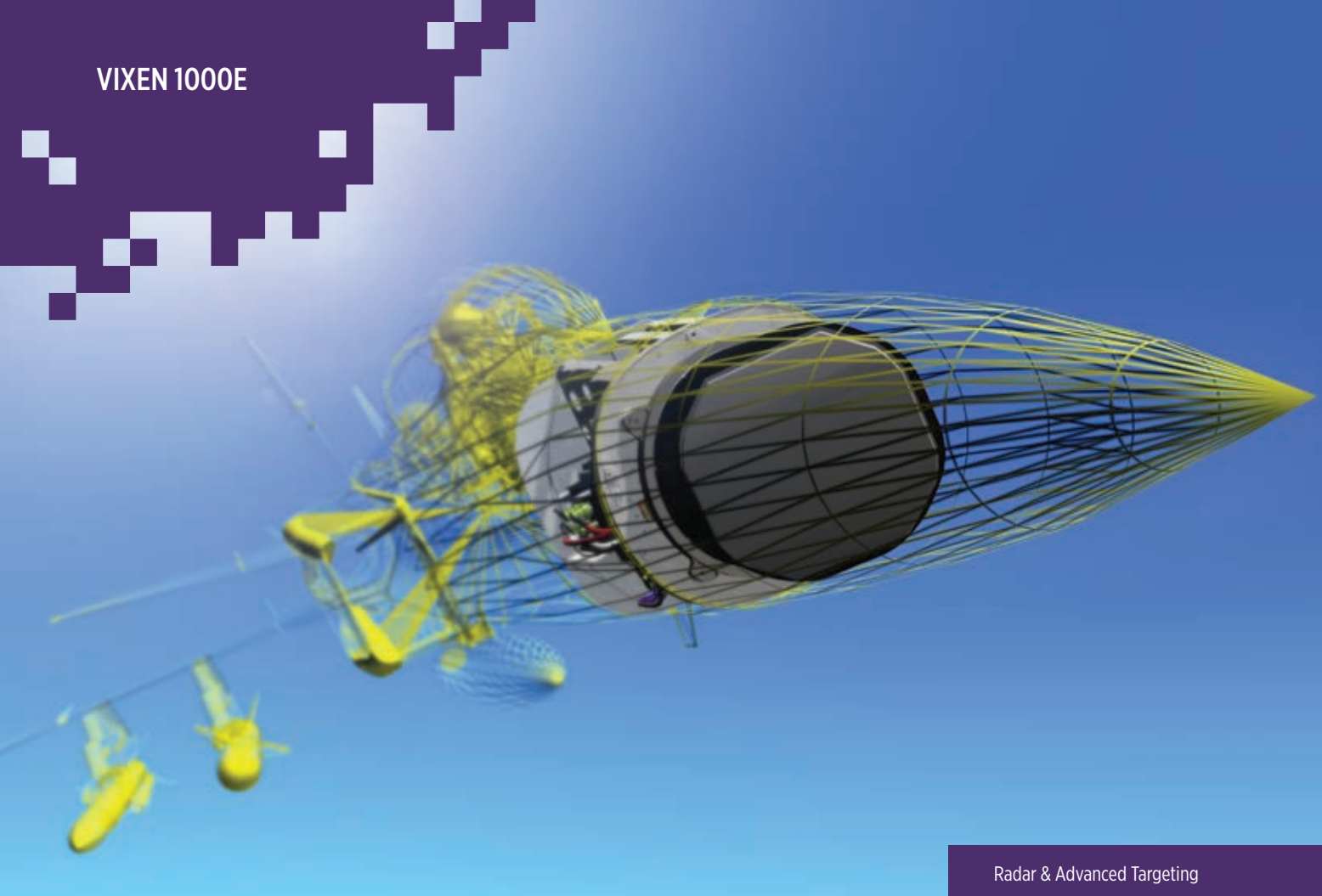
Its high reliability and availability result in a reduced maintenance requirement and provides the option to reduce spares holding, resulting in significant cost benefits over the life of the system.

## Background

The company has been at the forefront of the airborne radar market since the 1950s when the Al23 radar became the world's first high power monopulse radar to enter squadron service. Maintaining our leading position in the market, we have been developing AESA technology since the early 1990s and now offer a world-leading range of AESA radar products that meet the requirements of the airborne radar market.

Within our radar Centre of Excellence, we have designed, developed and supported radar systems for more than 65 years. Our software development capability meets the requirements of CMM Level 5. More than 3000 radar systems have been supplied for manned and unmanned fixed and rotary wing aircraft in surveillance, fire control and ground attack roles. We have extensive experience of surveillance radar and have produced more than 800 systems. Osprey MM is our latest addition to our family of AESA surveillance radars, which includes Seaspray 5000E, Seaspray 7000E, and Seaspray 7500E, and PicoSAR.





Radar &amp; Advanced Targeting

## ACTIVE ELECTRONICALLY SCANNED ARRAY (AESA) FIRE CONTROL RADAR

Vixen 1000E is a high performance AESA radar designed for fighter/interceptor aircraft building on over 60 years of fire control radar experience. Vixen 1000E features an innovative roll-repositionable AESA antenna to provide a full  $\pm 100^\circ$  field of regard allowing maximum situational awareness and platform survivability. This Wide Field of Regard (WFoR) allows the aircraft to turn away after missile launch, whilst still maintaining datalinks to the missile.

The highly reliable AESA transmit-receive module technology incorporated in Vixen 1000E significantly improves system availability leading to reduced lifecycle costs.

Vixen 1000E is part of a family of AESA Radars delivering greater performance and higher reliability than comparable mechanically scanned radars and offers all the advantages of multi-function AESA arrays with significant through life cost savings.

### KEY FEATURES

The Vixen 1000E Radar has been designed from the outset to meet worldwide fire control radar detection and target tracking needs combined into one efficient modular system. The Vixen 1000E builds on common modular units for a scaleable system architecture to meet the needs of fire control and intercept radar operational requirements whilst remaining resistant to radar countermeasures.

The AESA antenna is coupled to fully digital multi-channel exciter/receiver and processor Line Replaceable Units (LRUs). These provide a comprehensive mode suite which includes air-to-air, air-to-surface, interleaved and support functions, which can be readily adapted or extended in software to meet future needs.

# VIXEN 1000E

The radar makes use of AESA alert-confirmed techniques to confirm targets on first detection. This combined with optimised AESA waveforms results in increased track initiation ranges, whilst simultaneously maintaining situational awareness. The instantaneous scanning ability of the AESA also provides a comprehensive suite of interleaved air and surface modes, thus providing the pilot with all round situational awareness.

## Reliability

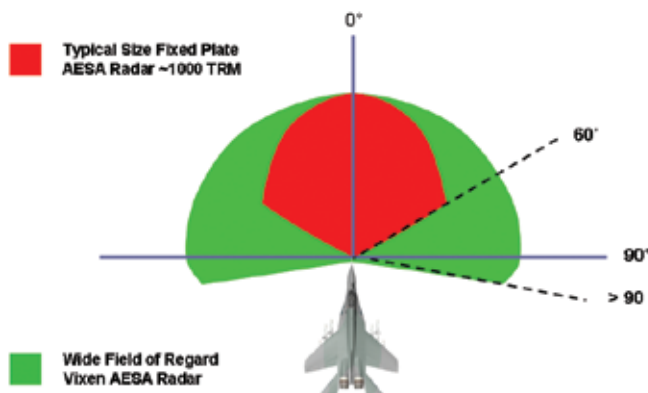
At the core of the AESA radar design is the ability to tolerate individual item failure. Component failures in the array result in graceful performance degradation rather than complete system failure, delivering high operational availability when compared with conventional radar systems. Significant cost benefits over the life of the system are realised due to the high reliability, increased availability and reduced maintenance requirements.

## Modes and capabilities

The mode set allows the system to deliver all of the functional capabilities of a Fire Control Radar within an acceptable platform volume. This is combined with the full capabilities of a detection, tracking and prosecution system to meet the needs of emerging new world threats.

The system utilises all the benefits of an electronically scanned array to deliver:

- Significantly enhanced performance relative to similar sized systems with the same weight, volume and power
- Comparable performance to larger mechanically scanned system whilst offering reduced weight and power.



## TECHNICAL SPECIFICATION

Frequency	X Band
Scan Coverage	+/- 100°
Scan Velocity	Instant beam switching
Cooling	Liquid and Air
Weight	215kg
Key Interfaces	Ethernet, I553B

## MODES AVAILABLE

Air-to-Air Modes	Search While Track
	Single Target Track
Air Combat	Modes HUD search
	Vertical scan
	Slewable scan
	Boresight
Air-to-Surface modes	Real beam ground map
	Doppler Beam Sharpening
	Sea Surface Search and Track
	Ground Moving Target Indication and Track
	Spotlight & Stripmap Synthetic Aperture
	Radar
	Inverse Synthetic Aperture Radar
	Imaging
	Air to Surface Ranging
Interleaved Modes	Customer configurable
	interleaved Air & Surface modes
Support Functions	Passive Search
	While Track
	Missile Datalinks
	Cued Search
	Non-Cooperative Target Recognition
	Comprehensive ECCM suite
	Weather mode

